Università degli Studi dell'Insubria

Dipartimento di Scienza e Alta Tecnologia

Corso di Dottorato in Fisica e Astronomia XXXIII ciclo

Search and study of blazars in the early Universe

PhD candidate:
Silvia Belladitta
Matr.733846

Supervisors: **Dr. Alberto Moretti**
Dr. Alessandro Caccianiga

a long time ago in a galaxy far,
far away...

Contents

List of Figures

List of Tables

Introduction

Active Galactic Nuclei (AGNs) are powered by accretion of matter onto a supermassive black hole (SMBH) placed in the center of the host-galaxy. AGNs are the most luminous, non-transient sources in the sky, and therefore they can be observed at extremely large cosmological distances (up to z$\sim$7.6, $<$1 Gyr after the Big Bang) across the entire electromagnetic spectrum. Studying AGNs at high redshift allows us to understand the formation and growth of SMBHs (e.g., Yang et al. 2020) and of their host galaxies (e.g., Fabian 2012), to learn about the chemical composition of the intergalactic medium (IGM, e.g., Jiang et al. 2016), and to probe the role of AGNs in driving the cosmic reionization process (e.g., Fan et al. 2006).
A low percentage of AGNs ($\sim$10%) are powerful radio sources, and are called radio-loud (RL) AGNs. The origin of AGNs radio emission is synchrotron radiation, which is produced by charged particles accelerated and collimated relativistically in a strong magnetic field, mostly along bipolar jets emitted from the central SMBH. Therefore, RL AGNs provide a unique opportunity to study the role of relativistic jets in the accretion of SMBHs (e.g., Volonteri et al. 2015). Particularly important is the sub-class of *blazars*, that are constituted by RL AGNs whose relativistic jet is seen at a small angle from our line of sight. Since the radiation produced by relativistic jets is strongly boosted along the jet direction, blazars are very bright and are visible up to high redshifts[1], allowing the study of the RL population across cosmic time. Indeed, the peculiar orientation of blazars has a high statistical relevance: for each observed blazar there must be $\sim 2\Gamma^2$ sources, with the same characteristics, whose jets are pointing elsewhere (e.g., Volonteri et al. 2011), where Γ is the bulk Lorentz factor of the emitting plasma (typically, $\sim$5-15, e.g., Saikia et al. 2016, see Sect. 1.1 and Sect. 1.2 for details). Therefore with blazars we can properly trace the entire population of SMBHs hosted by RL AGNs, including obscured objects, at any redshift, also providing critical constraints on the accretion mode, the mass and spin of the first seed black holes (e.g., Kellermann 2016).
The study of high-z RL AGN population based on blazars has been performed in the last ten years by many authors (e.g., Volonteri et al. 2011; Sbarrato et al. 2015; Ghisellini et al. 2016) and it has led to several interesting results and potential issues. For example, these studies revealed that the most massive black holes ($>10^9 M_\odot$) hosted in RL AGNs evolve faster than the total AGN population, suggesting a critical role of the relativistic jet in the black hole accretion. Another result obtained by these studies is that at z$>$3 there is a disagreement between the number of observed blazars and the number of mis-aligned RL AGNs (i.e., the parent population) expected from models, suggesting an evolution of the jet or of AGN properties. Finally, high-z RL AGNs seem to have a more intense X–ray emission with respect to similar objects at lower redshift (z$<$4, e.g., Wu et al. 2013). Although this difference is already under investigation, it could be due to the interaction between the jet electrons and the photons of the Cosmic Microwave Background (CMB), whose number density increases with redshift as $(1+z)^4$. However all these aforementioned studies have been carried out with a handful of blazars (5 between redshift 4 and 5.5) or

[1]In this thesis with the term *high redshift* I always mean z$>$ 4, when the Universe was $\sim$1.5 Gyr or less.

with a dozen of z> 4 RL AGNs and without using statistically complete samples.
To provide more stringent results on the properties of high-z blazar (and RL AGN) population (e.g., luminosity function, mass distribution, space density) larger sample of blazars suitable for statistical studies and more blazars at the highest redshift are needed. In this thesis I present a systematic work aimed at creating the largest well-defined sample of blazars at redshift above 4, pushing the search into a range of redshift (z≥5.5) not yet explored for this type of AGNs.
To this aim, I have exploited all of the wide field radio/optical/IR surveys available to date. Indeed blazars are rare sources and their search require radio and optical-IR catalogs that cover large fractions of the sky at a reasonable depth. In this work I combined these surveys to perform the search of z>4 blazar candidates all over the sky, by using the so-called *dropout* method.

This thesis is structured as follows: in the **first chapter** I describe the general properties of AGNs (especially blazars), I describe the different methodologies used to estimate the SMBH mass hosted by AGNs and I review the concept of black hole growth; in **chapter 2** I illustrate the importance of finding blazars at high-z, the selection method (the dropout technique) and the wide field surveys used in this work; in **chapter 3**, **chapter 4**, **chapter 5** and **chapter 6** I describe the selections of blazar candidates using different combinations of surveys and I analyze in details the properties of the newly discovered sources; finally in **chapter 7** I summarize the results of the work and the conclusions. In the following chapters I always use a flat ΛCDM cosmology with $H_0 = 70$ km s^{-1} Mpc^{-1}, $\Omega_m = 0.3$ and $\Omega_\lambda = 0.7$ and all errors are reported at 1σ, unless otherwise specified.

Chapter 1

Active Galactic Nuclei

The term Active Galactic Nuclei (AGNs) generally refers to the highly energetic phenomena that can be observed in the nuclei of some galaxies (called *active galaxies*) of any morphological type. Active galaxies form a family of many different types of AGNs which differ both in their spectral properties and luminosities along the entire electromagnetic spectrum. AGNs are the most luminous non-transient sources of electromagnetic radiation in the Universe. Due to their high luminosity, AGNs can be observed up to high redshifts (the current record being at z=7.6, Wang et al. 2021) allowing us to explore the farthest regions of the Universe and to draw conclusions about the properties of the *early* (i.e., *young*) Universe.
The current model explains the AGN emission as due to an accretion process of matter onto a SuperMassive Black Hole (SMBH), in the center of the host galaxy, with a mass that ranges between 10^6 and $10^{10}M_\odot$ (e.g., Kormendy & Ho 2013). The energy emitted by an AGN is thought to be produced by the gravitational infall of matter inside an accreting structure. The huge energy released by the accretion process affects the environment and the matter in the immediate vicinity and contributes to the emission over the whole electromagnetic spectrum. Therefore, AGNs provide a powerful tool for studying SMBHs properties and evolution both in the local and in the early Universe.
In this chapter I present the main characteristics of AGNs, the unified model that encloses all their different characteristics and I focus on the class of *blazars*, which are the main subject of this thesis. Finally I describe the methods for computing the SMBH mass of an AGN and I review the concept of the growth of SMBHs across cosmic time.

1.1 AGN structure and unification model

Between the 70s and the 80s, AGNs were classified in many different groups on the basis of optical and radio properties mainly, that at the beginning were not connected to the same physical process. A large collection of spectroscopically different sources were studied as different objects, leading to the proliferation of phenomenological classes (the so-called AGN *zoology*). Later on (in the '90s), it was understood that most of the differences between various AGN types can be ascribed to geometric or projection effects. This is the assumption on which the *unified model* of AGN is based (Blandford & Rees 1978; Antonucci 1993; Urry & Padovani 1995): this model try to explain the different spectral manifestations of AGNs with a single physical object, viewed from different angles. According to this unification scheme (Fig. 1.1), AGNs are formed by the same components (the SMBH, the accretion disk, the X–ray corona, the Broad Line Region, the dusty structure and the Narrow Line Region; see below for details of each components), and ∼10% of them (e.g., Bañados et al. 2015; Retana-Montenegro & Röttgering 2017; Liu et al. 2021) present

relativistic jets (see the subsection *relativistic jet*), i.e. two collimated structures of plasma moving at velocities close to the speed of light launched directly from the central SMBH. These AGNs are called *radio-loud* (RL)[1]. The first RL AGNs were discovered in the '60s by Matthews & Sandage (3C 48; Matthews & Sandage 1963) and by Martin Schmidt (3C 273; Schmidt 1963), both objects belonging to the 3C/3CR radio catalog (Edge et al. 1959, Bennett 1962). These two powerful radio sources were associated to two point-like optical objects, which showed strong and broad emission lines in their spectra. Schmidt recognized these as the lines of the Balmer series and, by using the Hubble's law, he found that the distance of those radio sources had to be very large. Therefore their high luminosity should be produced by very energetic phenomena, different from those generated by stellar activity, in a small region, due to their point-like shape in the optical images.

Actually there are two separate unification schemes based on orientation: optical and radio. In the optical regime the obscuration of the central regions of the AGN due to the surrounding dusty structure, explains the presence or absence of broad emission lines in AGNs spectra (see the *Obscuring dusty structure* subsection). Moreover it seems that the ionization of the Narrow Line Region by the continuum radiation of the AGN is not isotropic but instead depends strongly on the direction (see the *Broad Line and Narrow Line Regions* subsection). Instead, at radio wavelength, the emission from the relativistic jet is highly anisotropic because of relativistic beaming (see the *Relativistic Jet* subsection), and therefore its observed flux will be very different under different viewing angles.

The AGN structure is described in the following. The different viewing angles under which we observe the single objects are responsible for the observational differences among AGNs.

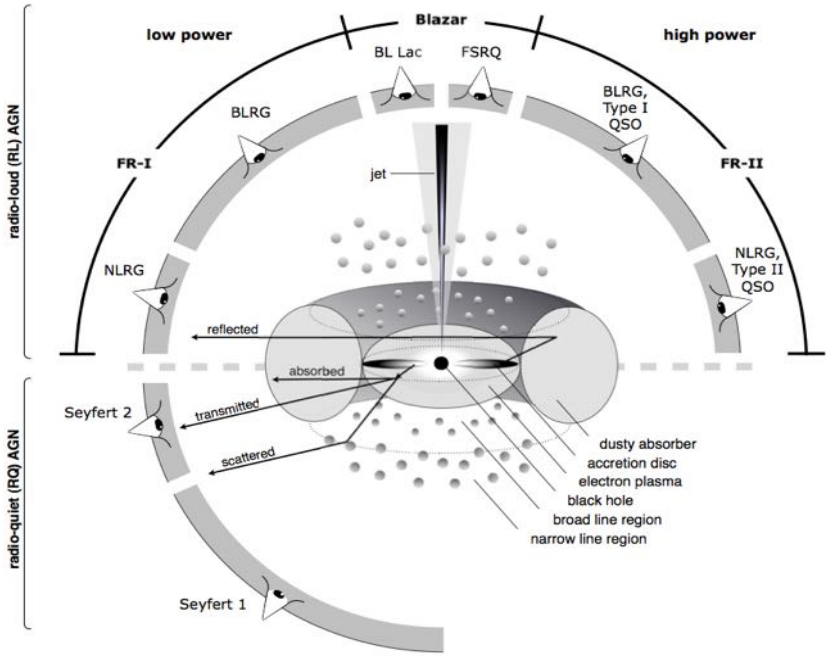

Figure 1.1: Schematic view of the AGN unified model. The AGN type depends on the viewing angle. Please note that the relativistic jet is thought to be launched symmetrically from the central black hole, but here, for illustrative purpose, the jet is shown only in the upper part of the scheme. Image credit: V. Beckmann & C. R. Shrader, 2013]

[1]Recently, Padovani (2017) proposed to change the nomenclature in *jetted AGNs*, since the presence or the absence of a relativistic jet of particles is the main observational difference between AGNs.

SuperMassive Black Hole and accretion flow

A SMBH of about 10^6-10^{10} $M_\odot$ is the *central engine* of an AGN: the accretion process of the surrounding orbiting gas is thought to be one of the main responsible for the AGN overall emission. Many models have been proposed for the accretion process, describing both high- (or *cold*) and low- (or *hot*) accretion rate processes. High accretion flows consist of cool optically thick gas accreting in a disk-like geometry. The simplest models are the geometrically thin, optically thick accretion disk (Shakura & Sunyaev 1973, hereafter SS73; Novikov & Thorne 1973) and the slim disk occurring at super–Eddington rates (e.g., Abramowicz et al. 1988; Ohsuga et al. 2005).
According to the SS73 model, the matter is moving in Keplerian motion, induced by the SMBH gravitational force, and approaches the center of the accretion disk by losing angular momentum thanks to viscous or magnetic processes. The motion of matter in the thin disk makes the system release gravitational energy, which turns into thermal energy and is radiated from the disk surface. The luminosity of the accretion process, i.e. the total energy released, is determined mainly by the mass accretion rate, $\dot{M}$, according to the formula:

$$L = \eta \dot{M} c^2 \tag{1.1}$$

where η is the efficiency of the process (~ 0.1 in the original SS73 model). However, there is an upper limit to the luminosity emitted from the accretion process in the SS73 model: the Eddington luminosity ($L_{\rm Edd}$). In fact, in order for matter to fall onto the SMBH, the radiation force needs to be smaller than the gravitational force.

$$F_{rad} = \sigma_T \frac{L}{4\pi r^2 c} < F_{grav} = \frac{G M_{\rm BH} m_p}{r^2} \tag{1.2}$$

Where r is the distance from the central SMBH, G is the gravitational constant, m_p the proton mass, σ_T the Thompson cross section and c the speed of light. Therefore:

$$L < \frac{4\pi G c m_p}{\sigma_T} M_{\rm BH} \sim 1.3 \times 10^{38} \frac{M_{\rm BH}}{M_\odot}\ erg\ s^{-1} = L_{\rm Edd} \tag{1.3}$$

The Eddington luminosity is the luminosity at which radiation pressure stops the gravitational infall, and therefore the accretion itself. Therefore it is generally assumed as an upper limit of the SS73 disk stability. The condition $L<L_{\rm Edd}$ can be translated into a minimum mass of the SMBH, required for its gravity to dominate the total force at a given luminosity.

$$M_{\rm BH} > M_{Edd} = \frac{\sigma_T}{4\pi G c m_p} L \sim 8 \times 10^7 \left(\frac{L}{10^{46}\ erg\ s^{-1}}\right) M_\odot \tag{1.4}$$

Corresponding to $L_{\rm Edd}$, an *Eddington accretion rate* can be defined as:

$$\dot{M_{\rm Edd}} = \frac{L_{\rm Edd}}{c^2} \tag{1.5}$$

When $\dot{M} > \dot{M_{\rm Edd}}$, the accretion is defined *super–Eddington*. The super–Eddington accretion range is described by the aforementioned slim disk model. According to this model, the accreting gas becomes too optically thick to radiate all the dissipated energy locally. Therefore, radiation is trapped and transferred inwards with the accretion flow. This trapping effect operates when the radial gas inflow speed is faster than the outward photon diffusion speed. In this case a *trapping radius* can be defined: $R_{tr} \sim 5 \frac{\dot{M}}{\dot{M_{Edd}}} R_S$, where R_S is the Schwarzschild radius[2]. This trapping effect

[2] R_S is defined as $\frac{2GM_{\rm BH}}{c^2}$, where $M_{\rm BH}$ is the SMBH mass.

lowers the radiative efficiency, and therefore the disk luminosity becomes progressively smaller relative to the associated $\dot{M}$.
Instead in the case of low (*hot*) accretion rates the accretion flow may be more like a geometrically thick, optically thin stellar corona described by a very hot, two-temperature *advection dominated accretion flow* (ADAF, e.g., Narayan & Yi 1994, 1995a, 1995b; Abramowicz et al. 1995). The process is more inefficient because the particle density is so low that the energy exchange time scale between electrons and protons becomes larger than the accretion time scale.

Broad Line and Narrow Line Regions

Gas and dust are thought to populate a very high number of clumpy clouds orbiting around the black hole. The clouds which are closer to the black hole (at ∼0.1-1 pc) populate the so-called Broad Line Region (BLR). Here the gas density is very large ($n_e \sim 10^9$-10^{10} cm^{-3}). The interaction between these gas clouds and the photons emitted mainly by the accretion structure leads the gas to emit Doppler broadened permitted lines[3] with typical widths of ∼10^3-10^4 km s^{-1}.
The kinematics of the clouds are not completely known: we do not know whether the clouds are rotating around the SMBH, whether they are infalling or streaming outwards or, finally, whether their motion is rather chaotic. It is also possible that different regions within the BLR exist with different kinematics properties (as it was proposed for example for the Hβ and CIV broad emission lines).
The fraction of accretion luminosity that ionizes the plasma in the BLR, i.e. the photo-ionizing luminosity, L_{ion}, depends on the properties of the accretion disk. The fraction of the radiation emitted by the disk that is intercepted and re–emitted through the broad emission lines (the covering factor C) is thought to be ∼10% (e.g., Baldwin & Netzer 1978; Antonucci et al. 1989):

$$L_{\rm BLR} = 10\% L_{\rm ion} \simeq 10\% L_{disk} \tag{1.6}$$

Therefore the luminosity emitted by the BLR can be used to trace the ionizing luminosity of the accretion disk.
At distances of ∼100 pc another region of less dense gas clouds ($n_e \sim 10^3$-10^6 cm^{-3}) is present: the Narrow Line Region (NLR). The higher distance from the central black hole prevents the NLR from being gravitationally bound to the SMBH itself. As a consequence of this distance, the velocities of the clouds in this region are one order of magnitude lower then the BLR velocities distribution, and therefore the Doppler broadening of the emission lines is lower (typical widths of ∼ 100-500 km s^{-1}.) Along with the different width, these lines can be clearly distinguished from those emitted by the BLR because they include also *forbidden* lines, that can be produced only thanks to the lower-density (and temperature) conditions of the NLR, where recombination can happen by spontaneous de-excitation. The NLR is located externally with respect to the dusty torus, and therefore it is always not obscured. The morphology of the NLR is not spherical, but appears as two cone-shaped regions (e.g. NGC 5728, Fosbury 2006). This is an indication of the fact that the ionizing radiation of the AGN is not isotropic, but it is emitted in two preferred directions (the so-called *ionization cones*).
Broad and narrow emission lines are superimposed to a blue optical spectrum[4] that can often be described, over a broad frequency range, by a power law of the form $S_\nu \propto \nu^{-\alpha}$ (where α=0.44 e.g., Vanden Berk et al. 2001). In Fig. 1.2 a typical AGN optical spectrum with broad and narrow

[3] If the emission of the lines occurs in gas at a distance r from a SMBH, the characteristic velocity of the gas is: $v_{rot} \sim \sqrt{\frac{GM_{\rm BH}}{r}} = \frac{c}{\sqrt{2}}(\frac{r}{R_S})^{-1/2}$.

[4] The AGN continuum emission in the optical band is attributed mainly to the accretion disk surrounding the SMBH, that is a black body emission. The details of the accretion disk emission can be found in Sect. 1.3.2.

emission lines is shown: lines of the Balmer series (Hβ, Hγ), Ly-α of hydrogen, and metal lines of ions like MgII, CIII], CIV. Lines in squared brackets in Fig. 1.2 are *forbidden* narrow lines, for example [OII], [OIII].

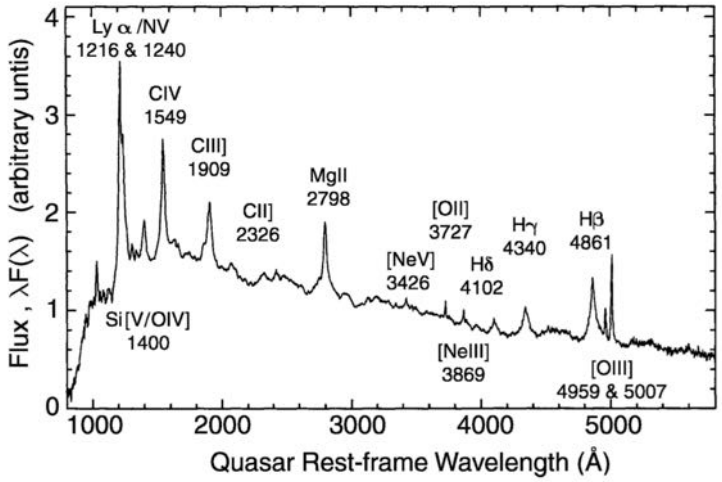

Figure 1.2: Combined spectrum of a sample of ∼700 individual AGN taken from the Large Bright Quasar Survey. The most prominent broad and narrow emission lines are marked. Image credit: Schneider P. (2006).

Obscuring dusty structure

At ∼1-10 pc from the central black hole an obscuring dusty structure is present. Dust reprocesses the accretion disk emission into the infrared band, dominating the AGN emission from wavelengths longer than ∼1μm up to a few tens of microns (in the MIR[5] at T∼10^3K).
The original unified model described this structure as a torus of dust. However, at present, different models are taken into consideration. The most discussed model (e.g., Krolik & Begelman 1988; Elvis 2000; Nenkova et al. 2008a, 2008b) describes a clumpy distribution of dust all around the nucleus, possibly outflowing (or inflowing). The obscuration would therefore be a statistical effect, linked to the possibility of finding a clump along the observer's line-of-sight.
By obscuring the optical emission from the innermost structures (i.e. BLR, accretion continuum emission) under some viewing angles, and re-emitting it in the infrared, this dusty structure is responsible for the different spectral features across the various AGN sub–classes, as the case of Seyfert I (or Type I, with both broad and narrow emission lines) and Seyfert II (or Type 2, with only narrow lines) galaxies. This would mean that, for example, the presence or absence of broad emission lines could be directly linked with the AGN viewing angle.
Indirect evidences for the dusty structure around the central SMBH came from spectro-polarimetric observations of Type 2 sources (e.g., Young et al 1996; Tran 2003; Moran 2007; Ramos Almeida et al. 2016), which reveal hidden broad permitted emission lines (typical of Type 1 objects) via reflection off material situated above the torus opening. The first spectro-polarimetry study was perfomed by Antonucci & Miller (1985) on the bright Type 2 Seyfert NGC 1068. The polarized light coming from this source showed broad emission lines (the broad Hα and Hβ lines) that were missing from the total light spectrum. This led to the idea that all Seyferts were intrinsically

[5]The infrared regime can be divided in three part: near-IR (NIR, 1–3 μm), mid-IR (MIR, 3–50 μm) and far-IR (FIR, 50–500 μm)

equal, with the dusty torus intercepting the optical-UV continuum and the broad lines for large viewing angles.

X–ray corona

The intrinsic X–ray primary emission from AGNs is thought to be inverse Compton (iC) scattering of accretion disk photons to X–ray energies by the electrons present in a *corona* surrounding the accretion disk itself (e.g., Haardt & Maraschi 1991). This iC process produces a power-law emission, with a photon index typically of ∼1.8-2. Part of the primary X-ray emission is reprocessed by the dusty torus, the BLR and the disk, giving rise to reflection features: a Compton hump peaking around 30-40 keV, and an iron Kα emission line at 6.4 keV. Finally a large fraction of AGNs show an excess over the power-law continuum below ∼1-2 keV (the so-called *soft excess*), which origin is still debate (e.g., Done et al. 2007).
As for the dusty torus, the exact geometry of this *corona* is unknown. It is supposed to be a hot layer, or an ensemble of clumpy regions particularly active in the inner parts of the disk. The intrinsic *corona* emission is connected to the accretion disk emission as demonstrated by the tight correlation observed between UV and X–ray luminosities (e.g., Strateva et al. 2005; Steffen et al 2006; Lusso & Risaliti 2016). This demonstrates that the X–ray primary emission of AGNs is universal.

Relativistic Jet

About 10% of AGN show intense radio emission (with radio luminosity between 10^{41}-10^{45} erg s^{-1}, e.g., Kellerman 1988). For this reason, they are classified as radio-loud (RL) AGNs. The criterion traditionally followed in order to classify these objects refers to the ratio between the rest-frame radio (ν∼5 GHz) and optical (blue band B at 4400Å) fluxes, the so-called *radio-loudness*: R = $\frac{S_{5\ GHz}}{S_B}$ (Kellerman et al. 1989). Another definition of R has been given by Jiang et al. (2007): R = $\frac{S_{6cm}}{S_{2500\text{Å}}}$. Therefore, the R parameter measures how much the radio emission is important with respect to the accretion luminosity. In both definitions, an AGN is defined as radio-loud when R>10 (Wilson & Colbert 1995), otherwise it is classified as a radio-quiet (RQ).
The physical process responsible for the radio emission is synchrotron radiation, i.e. radiation by particles gyrating at relativistic velocities through a magnetic field. This emission is usually described by a power law of the form $S_\nu \propto \nu^{-\alpha}$, where S_ν is the radio flux density and α the spectral index.
The radio emission in RL AGNs is generally associated to the presence of a relativistic jet, a structure formed by two collimated relativistic outflow of plasma, a jet and a counter-jet, emitted symmetrically with respect to the central AGN nucleus that transport energy and mass from the sub-parsec central regions to Mpc-scales. Therefore RL AGNs are also called *jetted AGNs*: they are able to accrete matter and to expel part of it in two oppositely directed jets.
Jets can have a size in a range from a few tens of kpc to Mpc (e.g., Blandford et al. 2019 for a recent review), tens of times the radius of their host galaxies, and usually terminate with extended structures called *lobes*, where the jets decelerate likely because of their interaction with the surrounding matter.
Following the approach of Blandford et al. (2019), AGN jets can be considered on three scales (see Fig. 1.3):

- **black hole jets** are the inward part of the jets, extending from the gravitational radius of the black hole (r_g) to the radius at which the gravitational influence of the black hole is negligible (R_{inf}). Here, the environment is dominated by the black hole potential and

the accretion process and particles (electrons, protons and positrons) are accelerated and collimated in the jets. Black hole jets structure are very rich and complex (see Fig. 1.3 for the example of M87 black hole jets), but they are all dominated by a strong helical magnetic field.

- **galaxy jets** extend from R_{inf}, to $\sim 0.1 R_{lobe}$, where R_{lobe} is the maximal extension of the radio lobes. The dynamical environment in which the jet moving, is dictated by the stellar/dark matter potential within the host galaxy and the interstellar medium. The jet plasma is expanding away from the core at superluminal speeds (v_{app} from 0.03 c to 0.4 c, e.g., Zensus & Pearson 1987).

- **lobe jets** are the outward part of the jets, extending from $0.1 R_{lobe}$ to R_{lobe}. Here, the environment is controlled by the backflow from the end of the jet and the circumgalactic medium. Radio maps of AGNs showed that many radio sources are double-lobed like Cygnus A (see Fig. 1.4) and that they have fairly compact regions, or hot spots, which support continuous energy supply from the nucleus to the lobes by jets. Thanks to the plasma deceleration and interaction with the circumgalactic medium, lobes emit a strong, isotropic radio emission.

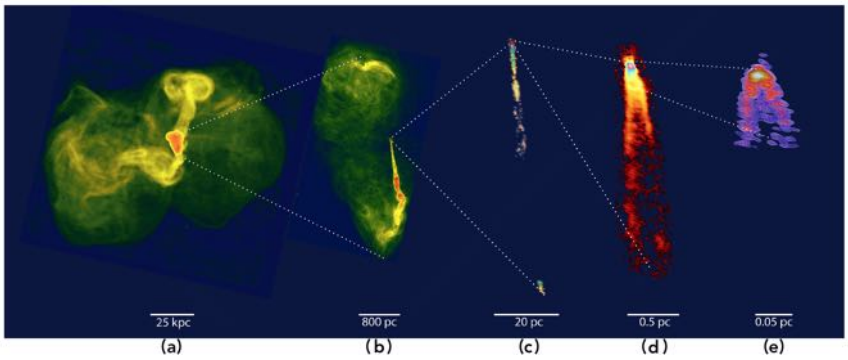

Figure 1.3: Jets of the radio galaxy M87, on scales from the outer lobes to near the black hole. From *left*: lobe jets and outer lobes (a), galaxy jets and inner lobes (b), full view of the black hole jet (c), innermost jet (d), jet launching region near the SMBH (e). Image credit: Blandford et al. (2019).

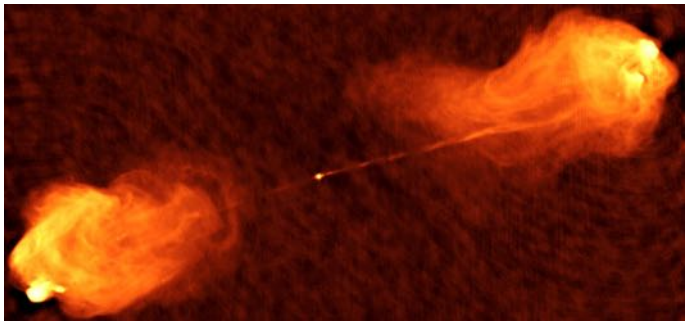

Figure 1.4: The radio galaxy Cygnus A as seen by the Very Large Array at 5 GHz. The radio lobes are clearly seen distant from the bright radio core. Image credit: Carilli & Barthel (1996).

The relative intensity of core, jet, and extended components varies with frequency, since they all have different spectral shapes. The radio core, characterized by a flat spectrum (α<0.5) and

usually located at parsec-distances from the black hole, is classically interpreted as marking the transition between synchrotron self-absorbed regions and optically thin regions (Blandford and Koönigl 1979). The flatness of the spectrum is explained as the result of the superposition of different synchrotron self-absorbed components in a conical geometry (e.g., Marscher 1996).
Jets are asymmetric (see Fig. 1.3). Due to the relativistic nature of the flow, the emission from the jet side approaching the observer can be highly enhanced as a consequence of relativistic Doppler boosting (i.e. beaming). By applying the Lorentz transformations, it can be shown that the observed flux density (S_{obs}) differs from the intrinsic one (S_{em}) by a factor:

$$S_{obs} = S_{em} \times \delta^{n-\alpha} \tag{1.7}$$

where δ is called *Doppler factor*, α is the spectral index, and n is a parameter varying between 2 and 3 (2 for a stationary cylindrical jet, 3 for a jet with distinct blobs, e.g., Blandford & Königl 1979; Giovannini et al. 1994). The Doppler factor depends on the speed of the flow β=v/c, which determines the bulk Lorentz factor

$$\Gamma = \frac{1}{\sqrt{1-\beta^2}} \tag{1.8}$$

and on the jet orientation, defined by the angle θ between the direction of propagation of the outflow and the line of sight of the observer

$$\delta = \frac{1}{\Gamma[1-\beta cos(\theta)]} \tag{1.9}$$

Therefore the jet appearance depends on the viewing angle. What we see is therefore amplified if the jet points at us, and depressed if the jet points elsewhere. AGNs whose jets are pointing at us are called *blazars* (see Sect. 1.2).
The mechanism launching, accelerating, and collimating relativistic jets is not clearly identified (see Czerny et al. 2015 for a recent review). The current consensus is that jets arise from a combination of magnetic fields and rotation. The two main processes considered to be connected to the jet formation are the electromagnetic extraction of energy and angular momentum from an accretion disk (likely thanks to magnetic reconnection, Blandford and Payne 1982), and/or the extraction of rotational energy from the spinning SMBH (e.g., Blandford & Znajek 1977).

1.2 Blazars

According to the AGNs unification model, blazars are RL AGNs whose relativistic jets are seen at a small angle to the line of sight. Usually a blazar is defined to have $\theta \leq 1/\Gamma$, with $\Gamma \sim 5-15$ (e.g., Ghisellini et al. 2010; Saikia et al. 2016) Since the radiation produced by the jets is strongly boosted and not obscured along the jet direction, blazars are the most powerful persistent objects in the Universe, and also visible up to high redshifts (the most distant being at z>6). This allows us to study the properties of SMBHs hosted by RL AGNs in the early Universe, as will be described at the beginning of chapter 2.
The sub-classification of blazars is rather complex, reflecting either the way they were discovered (radio or X–rays) or the presence or absence of broad emission lines.
Blazars are generally divided in Flat Spectrum Radio Quasars (FSRQs) and BL Lacertae objects (BL Lacs), which were originally distinguished according to the rest-frame equivalent width (EW)[6] of their broad emission lines: BL Lacs have EW<5Å, while FSRQs have EW>5Å (Stickel et al.

[6]The EW quantify the strength of an emission or absorption line and it is defined as EW = $\int_{\lambda_1}^{\lambda_2}(\frac{F_{cont}-F_\lambda}{F_{cont}})d\lambda$ where F_{cont} is the flux of the continuum under the line and F_λ is the flux density subtended to the line.

1991; Stocke et al. 1991). This EW division implies that, while FSRQs show broad emission lines just like normal (RQ) AGNs, BL Lacs instead display at most weak emission lines, sometimes exhibit absorption features, and in many cases are completely featureless (see Fig. 1.5). Nevertheless, this EW-based classification has a limitation. There are many examples of BL Lacs that show faint (in terms of EW) emission lines in their optical spectra, along with FSRQs whose broad emission lines disappear or become fainter. This is because the continuum emission in blazars is mainly due to the jet variable emission and, therefore, a change in the continuum emission implies a possible change in the EW. For example, Stocke et al. (1991) found that most BL Lacs of their sample have very weak emission lines, D'Elia et al. (2015) observed Hα lines with a EW>5Å in few z>0.7 BL Lacs, and the multi-epoch spectral study of more than 300 BL Lacs of Ruan et al. (2014) highlighted that for few of them the EW of their emission lines crossed the 5Å dividing line in different observations. All these studies confirm that the EW-based classification may not be adequate and may lead to an erroneous determination of the blazar type.
For these reasons a different classification method was suggested, for example by Ghisellini et al. (2011) and Sbarrato et al. (2012a): since the EW defines the importance of the line emis-

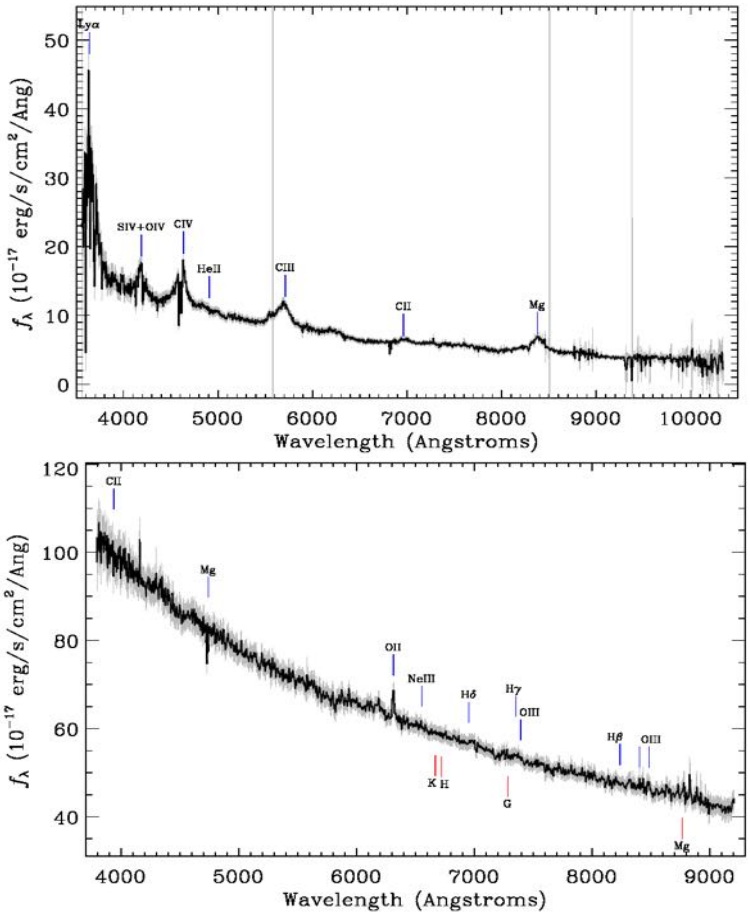

Figure 1.5: Typical observed optical spectra of a FSRQ (*upper panel*, SDSS J091512.53+305014.9 at z=1.9) in which several broad and narrow emission lines are marked over a blue continuum, and of a BL Lac (*bottom panel*, SDSS J130925.52+430505.5) in which, instead, only weak (EW<5Å) emission lines are detected. Broad emission lines in FSRQ optical spectra suggest the presence of the strong BLR; instead the weakness or the absence of emission lines in BL Lac spectra suggest that the BLR is absent or weak in this type of source. Image credits: the Sloan Digital Sky Survey Navigate Tool.

sion over the underlying continuum, the descriptive EW-based classification could correspond to a difference in the accretion mechanism. In fact, the BLR is irradiated by the ionizing photons produced by the accretion structure and therefore a difference in the broad emission lines could reflect a difference in the accretion luminosity. In the case of an efficient accretion, the BLR produces extremely luminous emission lines. On the other hand, a radiatively inefficient accretion mechanism would not induce the BLR to produce emission lines. FSRQs show strong emission lines, being therefore linked to a radiatively efficient accretion process, while the lineless BL Lacs are connected to radiatively inefficient accretion flows, like the ADAF.

Blazars at milli-arcsecond (mas) scale, probed by very long baseline interferometry (VLBI), show a compact flat spectrum radio structure, with apparent superluminal motion and a high brightness temperature (T_b[7]) larger than the inverse Compton equipartition limit ($T_b > 10^{10}$ K, e.g., Readhead 1994; Homan et al. 2006) in their center. Blazars are also dominated by high variability at all frequencies, from the radio (e.g., Ciaramella et al 2004; Aller et al. 2011), to the optical (e.g., Pian et al. 2005; Isler et al. 2017), X–ray (e.g., Pian 2002; Marscher et al. 2004) and γ–ray (e.g., Jorstad et al. 2013; Rajput et al. 2020) bands, on a wide range of time scales, from minutes to years (e.g., Chandra et al. 2011).

According to the AGNs unification model the large population of mis-directed blazars, i.e. the so-called *parent population*, is formed by the classical double-lobed radio galaxies. In particular, as reported in several works (e.g., Padovani & Urry 1990; Urry, Padovani & Stickel 1991; Maraschi & Rovetti 1994; Bai & Lee 2001; Giommi et al. 2012, Chen et al. 2015) low luminous radio galaxies (Fanaroff-Riley type I [FR I]; Fanaroff & Riley 1974) appear to be the parent population of BL Lacs, while high luminous radio galaxies (Fanaroff-Riley type II [FR II]) are believed to be the parent population of FSRQs. The AGN unification scheme predicts that all the un-beamed (i.e. isotropic) characteristics of FSRQs/BL Lacs (i.e. large-scale radio structures, host galaxies type, and emission lines properties.) should be similar to that of the parent population (FR II / FR I). The distinction between FR I and FR II was based on the relative position of the hot spots on the radio map using the ratio between the hot spot distance and the overall size of the galaxy (R_{FR}). FR I are galaxies which show a rather compact emission arising close to the core ($R_{FR} \leq 0.5$), while FR II objects have the structure dominated by the radio lobes and most of the emission appears to come from the far end of the extended emission. The first (second) are often described as core- (edge-) brightened. The FR morphology is thought to be linked to jet dynamics: the edge-brightened FR IIs are thought to have jets that remain relativistic up to the hot-spot, while the core-brightened FR Is are known to have initially relativistic jets that decelerate on kpc scales (e.g., Bicknell 1995; Laing & Bridle 2002; Tchekhovskoy & Bromberg 2016). Figure 1.6 shows a schematic view of these two classes. Fanaroff & Riley found that this first morphological classification actually corresponds to a marked difference in the luminosities of these two classes. Observing at 178 MHz all the FR-I have luminosities below 10^{32} erg s^{-1} Hz^{-1} sr^{-1}, while the FR-II lie above this threshold. Recently, it has been found that this classification is not sharp, but radio galaxies seem to be distributed continuously between the two classes. Recently a third class, FR 0, has been suggested to include FR I lacking prominent extended radio emission (see Baldi, Capetti & Giovannini 2015). The differences in radio properties between FR 0s and FR Is might be ascribed to their lower jet Lorentz factor with respect to FR Is. The slower jets in FR 0s are more subject to instabilities, which causes their premature disruption. While the radio structure of FR 0s and FR Is is different, the nuclear and host galaxy properties of these two classes are very similar (Baldi et al. 2018a; Torresi et al. 2018).

[7]The brightness temperature of individual components (core and jet) is obtained after estimating their flux density S_ν and angular dimension Θ as: $T_b = 1.22 \times 10^{12} \frac{S_\nu (1+z)}{\Theta^2 \nu^2}$.

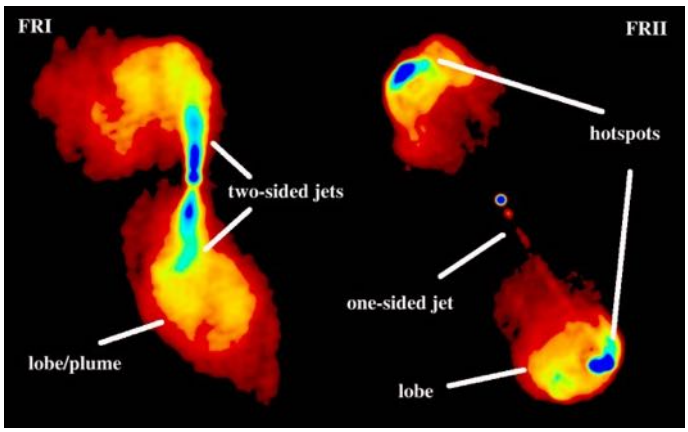

Figure 1.6: Schematic view of FR I and FR II radio galaxies. FR I are brightest close to the core and the surface brightness decreases outwards. In contrast the surface brightness of FR II increase outwards. Credit: Croston et al. 2012, EPIC consortium meeting.

1.2.1 Spectral Energy Distribution of Blazars

As already mentioned, blazar emission covers the entire electromagnetic spectrum, from radio to γ-rays and it is dominated by the Doppler boosted non-thermal processes of the relativistic jets. However the blazar global emission is produced not only by the relativistic jets, but all the elements included in the AGN structure described according to the unified model make their own contribution, even though not dominating the bolometric luminosity.
To better understand the blazars emission, it is useful to consider their Spectral Energy Distribution (SED). It represents the distribution of the energy of the source as a function of frequency (or wavelength). It is usually represented by a plot of the νf_ν or νL_ν as a function of frequency ν.[8] The SED of blazars (both FSRQa and BL Lacs) presents two characteristic prominent peaks (or *broad bumps*, see Fig. 1.7). The first peak is at rest-frame frequencies in the range 10^{13}-10^{18} Hz

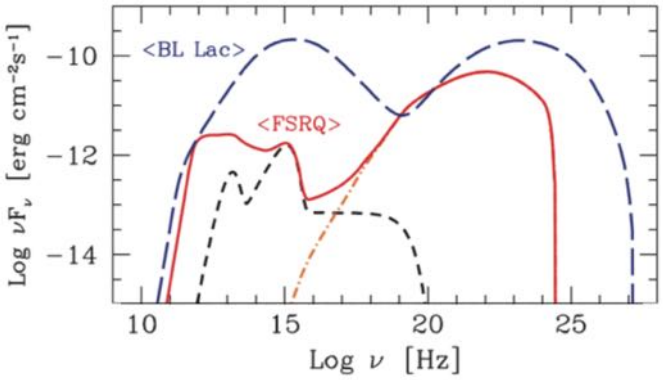

Figure 1.7: Examples of the characteristic SED of a FSRQ (solid red curve) at z=1 and a BL Lac object (long-dashed blue curve) at z=0.1. The black dashed curve represents the thermal emission from the torus and the accretion disk. This emission is only present in FSRQs, which typically have most of the UV/optical emission produced by the accretion disk and BLR, while the emission from the relativistic jet is relatively less important at these wavelengths. This seems to be particularly true for high-z blazars, as discussed, for instance by Ghisellini et al. (2010).
Both SEDs are characterized by the two-bump shape. Image taken from Ghisellini et al. (2010).

[8] The quantity f_ν (L_ν) is the source flux density (luminosity) at a given frequency.

(between IR and X–ray bands), the second at about 10^{21}-10^{24} Hz (extending well into the γray band). The low energy component is typically ascribed to synchrotron radiation produced by relativistic electrons moving in a magnetic field. Sources where this component peaks at low energies ($\nu_{synch\_peak} < 10^{14}$ Hz) are called *low synchrotron peaked* (LSP), while objects with $\nu_{synch\_peak} > 10^{15}$ Hz are called *high synchrotron peaked* (HSP) and objects with ν_{synch_peak} located at intermediate energies are called *intermediate synchrotron peaked* (ISP, e.g., Padovani & Giommi 1995; Abdo et al. 2010). The nature of the second hump is still debated. In leptonic models, the most frequently invoked process to account for the high-energy peak is the inverse Compton (iC) scattering of soft photons by the population of relativistic electrons forming the jet. Depending on which photon population is involved in the iC process, two models can be considered: Synchrotron-Self Compton (SSC) and External Compton (EC). In the SSC mechanism, the same synchrotron photons emitted by the jet are up-scattered to higher energies (e.g., Maraschi et al. 1992; Ghisellini & Madau 1996). The EC models (e.g., Sikora et al. 1994), instead, assume that the photons involved in the iC interaction include optical/UV photons from the accretion disk and from the BLR, IR photons from the torus, and, on larger scales, CMB photons. The two mechanisms are likely both present in blazars, maybe with different weight depending on which sub–class of blazar is considered. Since FSRQs have thermal components that can be the source of seed photons for the EC process, they are likely EC dominated objects. Instead the absence of any evident thermal emission in BL Lacs suggests that their iC emission is more likely produced by the SSC mechanism.
Although these are the mostly accepted emission processes, alternative models have been introduced in the last decades: proton-synchrotron radiation, curvature radiation, cyclotron masers, plasma waves (see Blandford et al. 2019 for other examples).
Another important feature of the blazar SED is its variability across the whole electromagnetic spectrum. Quasi–simultaneous variability in different spectral bands is often (but not always) observed, suggesting that most of the flux is produced in a single region of the jet (for example the simultaneous variability in the mm band and in the gamma–rays, e.g., Ackermann et al. 2011).

1.3 Measuring the AGN black hole mass

A reliable estimate of SMBH masses is necessary to determine the mass function of AGNs, and hence to understand their evolution, parallel to the evolution of their host galaxies.
Various methods to estimate SMBH masses have been proposed in the last years. They can be primarily divided into direct and indirect methods. Direct measurements are those for which the mass is derived from the dynamics of stars or gas accelerated by the black hole itself. Indirect methods are based on observables that are correlated with the central black hole mass. This includes methods based on correlations between the black hole and its host galaxy properties, such as the well known connection with the velocity dispersion of bulge stars (M_{BH}-σ relation; e.g., Ferrarese & Merritt 2000) or the relation between black hole and bulge luminosity (e.g., Magorrian et al. 1998) or the relation between BLR radius and AGN luminosity (e.g., Kaspi et al. 2000, 2007, the so-called *single epoch method, SE*).
In the following, I will detail the two methods used for this work: the single epoch (SE) virial method and the modeling of the accretion disk emission, both included in the category of indirect measurements.

1.3.1 Single Epoch virial mass estimation

A widely used method to measure black hole masses in AGNs is based on the *virial theorem*. The virial approach assumes that the BLR dynamics is dominated by the central black hole gravitational potential. Therefore the central black hole mass ($M_{\rm BH}$) is directly connected with the size of the broad line region (R_{BLR}) and with the velocity dispersion (v_{BLR}) of the particles that composed the BLR gas:

$$M_{\rm BH} \sim \frac{R_{BLR} \times v_{BLR}^2}{G} \tag{1.10}$$

R_{BLR} is estimated by studying the variability of the BLR (reverberation mapping technique, e.g., Blandford & McKee 1982; Peterson 1993, 2014) or, alternatively, from the continuum luminosity through specific statistical R_{BLR}-luminosity scaling relations (e.g., Bentz et al. 2013). On the other hand the velocity dispersion of the gas clouds can be inferred from the broad emission lines width: $v_{BLR} = f \times (line\_width)$, where f is a geometrical factor that accounts for the unknown geometry, kinematics and orientation of the BLR (e.g., Decarli et al. 2008). There is a large uncertainty on the value of f (e.g., Onken et al. 2004; Batiste et al. 2017) and it is not clear if it depends on luminosity and/or other line properties (e.g., Mejía-Restrepo et al.(2017) et al. 2017). The line width can be parametrized by the Full Width at the Half-Maximum (FWHM) or with the line dispersion (σ_{line}), i.e. the second moment of the line profile as defined in Peterson et al. (2004):

$$\sigma_{line}^2 = \langle \lambda^2 \rangle - \lambda_0^2 = \frac{\int \lambda^2 P(\lambda) d\lambda}{\int P(\lambda) d\lambda} - \frac{\int \lambda P(\lambda) d\lambda}{\int P(\lambda) d\lambda} \tag{1.11}$$

where $P(\lambda)$ is the emission line profile.
Reverberation mapping (RM, Blandford & McKee 1982; Peterson 1993) is the most accurate method for estimating the R_{BLR}. This observational technique uses the fact that heating and ionization of the gas in the BLR are both caused by the central black hole. Since the UV radiation of AGNs varies, we expect corresponding variations of the emission line intensity. The BLR responds to the variation of the AGN continuum only after a delay of $\Delta t \sim R_{BLR}/c$, which is the light travel time necessary to reach the BLR. From the observed correlated variations of continuum and line emission, Δt can be determined for different line transitions, and so the corresponding values of R_{BLR} can be estimated.
RM is now a well-established technique to measure the black hole mass of nearby AGNs. However the accuracy of the RM black hole mass estimates is fundamentally limited by unknown geometry and kinematics of the BLR. Moreover the RM technique is extremely time-consuming and complex because a monitoring of the AGN continuum light and, simultaneously, of the line fluxes over a long period is needed. The RM technique has been applied in the last two decades to hundred of sources (e.g., Kaspi et al. 2000, 2007; Peterson et al. 2004; Bentz et al. 2006, 2013; Lira et al. 2018), spanning a wide range of redshift (until z$\sim$3) and of luminosity ($\lambda L_{\lambda 5100\text{Å}}$ between $\sim 10^{42}$ and $\sim 10^{47}$ erg s^{-1}.) The masses of the central SMBHs of these AGNs are found to be between $\sim 10^6$ (for the less luminous sources) to $\sim 10^9$ $M_\odot$ (for the most luminous ones).
RM studies performed up to now allow to draw important conclusions about BLR structure and dynamics (see e.g., Peterson et al. 2004; Bentz et al. 2006; Kaspi et al. 2000, 2007; Shen et al. 2015; Lira et al. 2018). One of the main results of the RM campaigns is that the time delay between line and continuum variations is longer for more luminous objects. This suggests a strong relationship between the source luminosity and the size of the BLR of the type: $R_{BLR} \propto L^\alpha$, with $\alpha \sim 0.533 \pm 0.033$ (Bentz et al. 2013, but also see Kaspi et al. 2000, 2007 for slightly higher value $\sim$0.7). The typical intrinsic scatter of this relation is $\sim$0.13 dex. Therefore once the continuum luminosity of an AGN has been measured, it is possible to infer the BLR radius

through the R–L relation; This relation is consistent with the theoretical expectation deriving from photo–ionization models (e.g., Kaspi et al. 2000).
According to the R-L relation, the black hole mass can be written as:

$$M_{\rm BH} \sim \frac{L^{\alpha} \times (line\_width)^2}{G} \tag{1.12}$$

The R–L relation became the basis of an alternative method to estimate an AGN black hole mass: the single epoch (SE) method, so named because it is possible to obtain a reliable estimate of $M_{\rm BH}$ from a single AGN optical or infrared spectrum. The main advantage of this method is that it is remarkably less difficult and time–consuming than RM that requires large observational campaigns. Moreover it can be applied at sources at any redshift (e.g. until z=7.6, Wang et al. 2021).
The most established R–L relation is the one between the $R_{BLR(H\beta)}$ and the AGN continuum luminosity at 5100Å rest-frame, the only one calibrated on a ∼hundred of sources. However at z>2-3 Hβ falls outside the typical wavelength range of observation of the optical (4000-10000Å) ground based telescopes. Therefore other empirical relations between emission lines and continuum luminosities have been calibrated. In particular for measuring the SMBH mass of high-z AGNs the most commonly used relations are the MgII2798Å-$L_{3000Å}$ and the CIV1549Å-$L_{1350Å}$ (e.g., Vestergaard & Peterson 2006; Shen et al. 2011; Shen et al. 2019). It has been already tested that the MgII2798Å-$L_{3000Å}$ relation gives similar results of the Hβ-$L_{5100Å}$ relation (e.g., McLure & Jarvis 2002; Shen et al. 2008). Instead, some works have questioned the reliability of CIV1549Å as a good virial mass indicator (e.g., Sulentic et al. 2007; Shen & Liu 2012; Trakhtenbrot & Netzer 2012) due to its observed blueward asymmetry and velocity shifts of the line profile. However other authors have shown that there are no large inconsistency between the SE black hole mass computed from CIV1549Å and Balmer lines (e.g., Vestergaard & Peterson 2006; Greene et al. 2010; Assef et al. 2011; Dalla Bontá et al. 2020).
In any case, large intrinsic scatters are related to the SE method (∼0.4-0.5 dex, e.g., Shen et al. 2019 and references therein) and these affect inevitably the $M_{\rm BH}$ estimate.
In this thesis the relations used to compute the black hole mass of the discovered high-z blazars are:

- **CIV 1549Å**: relations from Vestergaard & Peterson (2006, hereafter VP06):

$$log(\frac{M_{\rm BH}}{M_{\odot}}) = 6.66 + 2 \times log(\frac{FWHM}{10^3\ km\ s^{-1}}) + 0.53 \times log(\frac{\lambda L_{\lambda_{1350Å}}\ erg\ s^{-1}}{10^{44}\ erg\ s^{-1}}) \tag{1.13}$$

$$log(\frac{M_{\rm BH}}{M_{\odot}}) = 6.73 + 2 \times log(\frac{\sigma_{line}}{10^3\ km\ s^{-1}}) + 0.53 \times log(\frac{\lambda L_{\lambda_{1350Å}}\ erg\ s^{-1}}{10^{44}\ erg\ s^{-1}}) \tag{1.14}$$

- **MgII 2798Å**: relation from Shen et al. (2011, hereafter Sh11)

$$log(\frac{M_{\rm BH}}{M_{\odot}}) = 0.74 + 0.62 \times log(\frac{\lambda L_{\lambda_{3000Å}}\ erg\ s^{-1}}{10^{44}\ erg\ s^{-1}}) + 2 \times log(\frac{FWHM}{km\ s^{-1}}) \tag{1.15}$$

These relationships are calibrated on the results obtained from RM method on ∼30 low-redshift (z<0.4) AGNs, with $\lambda L_{\lambda_{1350Å}}$ between $10^{41.37}$ and $10^{46.57}$ erg s^{-1} (Peterson et al. 2004). These relations are strictly valid for sources in this range of luminosity. In principle, the extrapolation of these relations to much higher/lower ranges of luminosity could produce biased results if the R-L relation changes significantly outside the observed range. The objects studied in this thesis, to which we apply these mass scaling relations, have a $\lambda L_{\lambda_{1350Å}}$ similar (∼10^{45-46} erg s^{-1}) to

the brightest AGNs of the reference sample of Peterson et al. (2004) or have a slightly higher ($>10^{46.6}$) luminosity. Therefore, the application of the relations 1.13, 1.14 and 1.15 should provide reasonable results in particular for the least luminous objects in the sample.
To improve the reliability of the black hole masses computed for high-z/high-luminosity AGNs, more RM studies of very luminous quasars would be needed.
Since this thesis is focused on blazars, i.e. objects observed under a small viewing angle, it is important to take into account the potential problematic related to the use of the SE method on this type of sources.
The first potential issue is that the BLR may not be isotropic and, therefore, the resulting black hole mass could be systematically underestimated in objects observed face-on. Indeed there is a large consensus in the literature (e.g., McLure & Dunlop 2002; Decarli et al. 2008, 2011) concerning to a disk-like structure of the BLR. However it is not already clear if the width of the broad emission lines (including CIV and MgII) depends on the orientation. For instance, Runnoe et al. (2014, and reference therein) found this dependence in RL AGNs for Hβ, but not for the CIV line. Similarly, Fine et al. (2011) in a sample of RL AGNs did not find a correlation between the line width of the CIV and the AGN orientation. These authors concluded that the high ionization lines are produced in isotropic inner parts of the BLR. Regarding the MgII line, for instance, Jarvis & Mc Lure (2006) found that the distribution of the MgII line width of FSRQs is similar to that of RQ AGNs, suggesting no dependence of orientation.
A second potential issue connected with the source's orientation is the fact that the AGNs continuum luminosity could be contaminated by the relativistic jet. Therefore, a continuum-luminosity based relationship may lead to a mass overestimate (e.g., Decarli et al. 2011). In the following chapters we evaluate source by source this potential bias on the SE masses of our newly discovered blazars (see Sect. 4.6.3, Sect. 5.5.4 and Sect. 6.6.6).
However, to verify the reliability of the SE masses, we also use an independent method, based on the accretion disk modeling, for estimating the black hole masses of the blazars reported in this thesis. I describe this method in the following section.

1.3.2 Accretion disk model

Assuming that the disk emission of an AGN it is well described by a geometrically thin and optically thick Shakura and Sunyaev accretion disk model (SS73) and assuming that the disk emission is clearly visible at UV-optical wavelengths, the black hole mass of AGNs can be estimated by modelling directly the disk emission (e.g., Sbarrato et al. 2012b; Calderone et al. 2013; Ghisellini et al. 2015a). Therefore, this approach can allow us to check in an independent way the black hole mass computed with the SE method.
According to the SS73 model, as described in Sect. 1.1, the accretion disk plasma moves following a Keplerian motion, spiraling toward the inner part of the disk, getting closer the central SMBH, thanks to an efficient mechanism able to transfer angular momentum (i.e. viscous friction). The matter falling onto the SMBH releases gravitational energy that it is transformed into thermal energy and radiated from the disk surface (according to Eq. 1.1). Because of the density and optical depth of the accretion structure, each emitting element of a SS73 disk, at radius R from the central engine, emits as a black body, with a temperature T(R). The overall disk emission is therefore an integral of the single black body spectra (i.e. a multicolor black body spectrum) emitted at different temperatures and distances from the central black hole. Therefore, the overall disk profile can be derived starting from a black body emission, described by the Planck's equation:

$$B_\nu d\nu = \frac{2h\nu^3}{c^2} \frac{1}{e^{\frac{h\nu}{kT}} - 1} d\nu \tag{1.16}$$

where h is the Planck constant and k is the Boltzmann constant. The temperature of each emitting element is therefore a function of the distance from the central SMBH (R), of the black hole mass ($\mathrm{M_{BH}}$) and of the accretion rate ($\dot{M}$):

$$T(R, M_{BH}, \dot{M}) = [\frac{3G}{8\pi\sigma_S}\frac{M_{BH}\dot{M}}{R^3}[1 - (\frac{R_{in}}{R})^{0.5}]]^{0.25} \tag{1.17}$$

where σ_S the Stefan-Boltzmann radiative constant and R_{in} is the inner radius of the disk, i.e. $\mathrm{R_{ISCO}}$, the Innermost Stable Circular Orbit (ISCO), the nearest point to the central black hole on which the matter can follow a stable orbit. Assuming a Schwarzschild metric, i.e. assuming a non-rotating black hole, the $\mathrm{R_{ISCO}}$ is expected at three times the Schwarzschild radius (R_S):

$$R_{in} = R_{\mathrm{ISCO}} = 3R_S = 3 \times \frac{2GM_{BH}}{c^2} \tag{1.18}$$

Assuming a Kerr geometry in case of a spinning black hole, instead, the ISCO would have a different value: in the maximally spinning cases $\mathrm{R_{ISCO}} = \mathrm{R}_S/2$ if the disk and the black hole are co-rotating, and $\mathrm{R_{ISCO}} = 9\mathrm{R}_S/2$ if they are counter-rotating. Usually RL AGNs are associated to spinning black holes (e.g., Blandford & Znajek 1977; Tchekhovskoy et al. 2011). However for the cases discussed in this thesis a Schwarzschild metric (i.e. valid for non-rotating BH) is always assumed. This choice is justified by the results of Campitiello et al. (2018) who found an equivalence between the accretion disk fit with an SS73 model and a KerrBB model with spin$\sim$0.8 and a viewing angle of 0°.

As can be noticed from the explicit expression for the emitting temperature (Eq. 1.17), the innermost regions of the disk are hotter than the outer ones, hence they are responsible for the most intense emission, that peaks at the higher frequencies. On the other hand, the elements in the outer radius provide the lowest temperatures and their Planck spectra peak at the lowest frequencies.

In order to obtain the spectrum of the whole SS73 accretion disk, the Planck spectra emitted from all the disk elements (Eq. 1.16) have to be integrated, i.e the emitted disk luminosity has to be integrated on the whole disk surface:

$$L(\nu, M_{BH}, \dot{M})d\nu = 2\int_{R_{in}}^{R_{out}} 2\pi R dR \int_{0°}^{90°} 2\pi \sin(\theta)\cos(\theta) d\theta B_\nu[T(R, M_{BH}, \dot{M})]d\nu \tag{1.19}$$

where R_{out} is the outer edge of the disk, that is not constrained. A large value for this parameter is generally assumed. Following Abramowicz et al. (2013) in this thesis we used $2\times10^3\mathrm{R}_S$. In any case, the calculated accretion disk spectrum in the optical-UV band (rest-frame) is usually insensitive to the value of the outer radius. It contributes more at the spectral shape in the infrared wavebands (see Fig. 1.8). The integral over angle θ accounts for the directions in which each surface element of a single face of the disk emits. The fact that each element of the disk emits on both the disk sides is accounted for with the factor 2 that opens the formula.

Therefore the final shape of the multicolor black body spectrum is given by the relation:

$$L(\nu, M_{BH}, \dot{M})d\nu = 4\pi^2 \int_{R_{in}}^{R_{out}} R B_\nu[T(R, M_{BH}, \dot{M})]d\nu dR \tag{1.20}$$

$\mathrm{M_{BH}}$ and $\dot{M}$ are the two fundamental parameters of the model. Both can be connected with observable features. In fact, $\dot{M}$ is obtained from its relation with the total disk luminosity (Eq. 1.1). If we measure L_{disk} (hence $\dot{M}$), we are left with $\mathrm{M_{BH}}$ as the only remaining free parameter: it can be obtained by fitting observational data with the above relation of $\mathrm{L}(\nu, \mathrm{M_{BH}}, \dot{M})\mathrm{d}\nu$.

The emitted disk spectrum presents three different behaviors according to Eq. 1.20:

- **Low frequencies**: $h\nu \ll kT(R_{out}) \Longrightarrow L(\nu) \propto \nu^2$
- **Intermediate frequencies**: $kT(R_{out}) < h\nu < kT(R_{in}) \Longrightarrow L(\nu) \propto \nu^{1/3}$
- **High frequencies**: $h\nu \gg kT(R_{in}) \Longrightarrow L(\nu) \propto \exp(-\frac{h\nu}{kT})$
  The spectrum presents an exponential cut-off brought by the high frequencies component of the black body spectrum emitted in the inner regions of the disk.

The multicolor black body spectrum shape is clearly visible in Fig. 1.8, along with the asymptotic behaviors. As already mentioned, there are three fundamental parameters that control the specific shape of the multicolor black body spectrum: R_{out}, $\dot{M}$, directly traced by L_{disk}, and M_{BH}. Changes in these parameters lead to variations in the multicolor black body spectrum, leaving the asymptotic behaviors unaltered (see Fig 1.8):

- **Black hole mass**: for fixed values of accretion rate and outer radius, changes in M_{BH} produce only temperature variations through the relation $T \propto M_{BH}^{-1/2}$ (see Eq. 1.17, assuming constant $\dot{M}$). Therefore a change in M_{BH} leads to a simple rigid shifts in frequency of the whole spectrum (*upper left panel* in Fig. 1.8).
- **Accretion rate**: variations in $\dot{M}$ correspond to variation in L_{disk}. For fixed values of R_{out} and M_{BH}, variations of the accretion rate intervenes in the variation of the temperature of the emitting region, following the relation $T \propto \dot{M}^{1/4} \propto L_{disk}^{1/4}$ (see again Eq. 1.17, for a fixed M_{BH} value). *Upper right panel* of Fig. 1.8 shows the shift of the multicolor black body spectrum by varying $\dot{M}$.
- **Outer radius** For fixed values of $\dot{M}$ (L_{disk}) and M_{BH}, a variations in R_{out} implies a change in the length of the intermediate frequency branch of the multicolor black body spectrum. In fact at the distance represented by R_{out} the lowest temperature black body is emitted, and hence the emitted spectrum accounts for the first break in the multicolor black body slope (*lower central panel* of Fig. 1.8).

From a practical point of view, the low frequency range of the disk emission is most likely not visible, superposed to other components or simply not luminous enough to be well sampled. Therefore, variations given by R_{out} are not observable in a fitting process. The other two defining parameters, instead, can be used as free parameters to fit this model to suitable data. In particular, if the data to be modelled in the IR-optical-UV range cover the peak of the emitted spectrum, the total disk luminosity can be directly derived from the peak luminosity $\nu_p L_p$ ($L_{disk} = 2\nu_p L_p$; Calderone et al. 2013). In this specific case, the only free parameter left would be M_{BH}. In some cases, a reliable estimate of $\nu_p L_p$ cannot be obtained. This happens if the available data do not cover properly the whole wavelength range, or if the IR-optical-UV continuum is not purely emitted from the accretion disk, but is contaminated by other components, such as the jet emission. In this case, BLR luminosity can provide an estimate of L_{disk} according to Eq. 1.6. Indeed the total L_{BLR} can be derived from the luminosity of the individual broad lines (e.g., CIV, MgII) visibile in a optical or infrared spectra, following a spectral templates that report line ratios, such as Francis et al. (1991) or Vanden Berk et al. (2001). In this case, the uncertainty on L_{disk} would be influenced by the uncertainty on the covering factor of BLR, generally assumed to be 10%.

1.4 The growth of black holes

Accurate measurements of black hole masses of high redshift AGNs help us constraining formation scenarios of the first SMBHs formed in the Universe. Indeed a fundamental question in the present

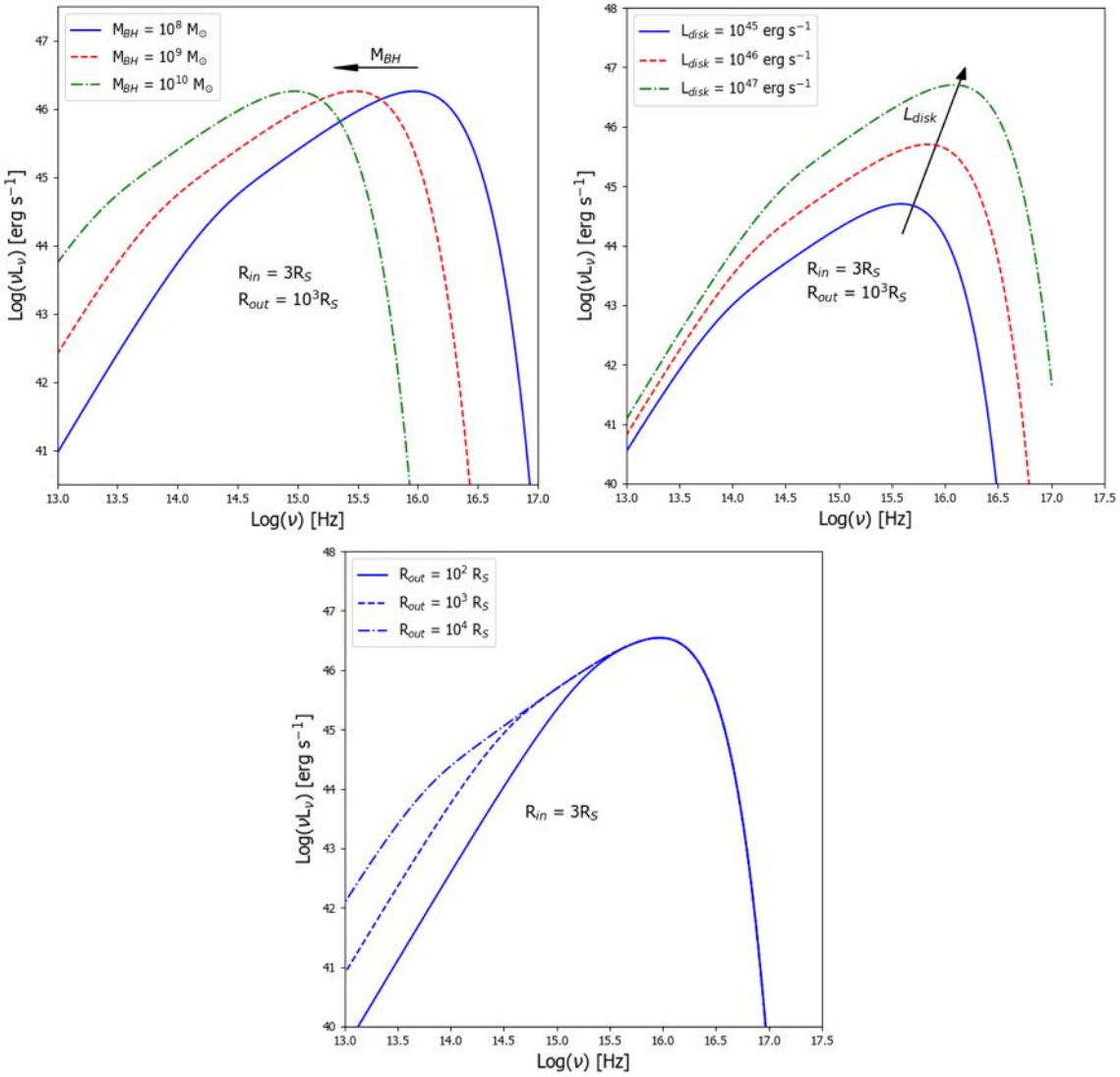

Figure 1.8: The SED (in Log(ν) versus Log(νL$_\nu$)) of a multicolor black body spectrum, emitted by a SS73 accretion disk. The arrows show how the spectrum varies by varying the values of M_{BH} and L_{disk} (i.e. $\dot{M}$). *Top left*: effect of variations in black hole mass on the multicolor blackbody spectrum, for constant disk luminosity (i.e. accretion rate). A higher mass value provokes a rigid shift toward lower frequencies of the whole spectrum, while the asymptotic trends remain unaltered. *Top right*: effect of disk luminosity variations, that correspond to variations in accretion rate, for a constant black hole mass. A larger $\dot{M}$ corresponds clearly to a more luminous disk, and also shifts the peak of the emission towards larger frequencies. *Bottom center*: effect of variations in R_{out} of the accretion disk. The outer radius emits the coldest black body in the whole structure, and therefore determines the frequency of the break between the ν^2 and $\nu^{3.5}$ trends.

day astrophysics is to understand when and how the first SMBHs formed in the Universe, how they are related to early galaxy formation and what is their role in driving the re-ionization process (e.g., Merloni 2016). Moreover high-z RL AGNs provide a unique opportunity to study the role of jets in the accretion of early SMBHs (e.g., Volonteri et al. 2015).
Observations of dozens of high-z AGNs show that they host black holes with mass larger than 10^8-10^9 $M_\odot$ (e.g., Jiang et al. 2007; Kurk et al. 2007; Wu et al. 2015; Mazzucchelli et al. 2017; Kim et al. 2018; Shen et al. 2019; Onoue et al. 2019), hence as massive as the most massive black holes we detect in today's galaxies. These discoveries indicate a fast and efficient growth of black holes that challenges the currently accepted theoretical model of SMBH formation (e.g., Volonteri 2010; Latif & Ferrara 2016). For those AGNs that are strong radio sources the problem is even more critical. Indeed the presence of a relativistic jet is usually associated to a highly spinning black hole, that is expected to have a large radiation efficiency ($\eta \sim 0.3$, Throne et al. 1974) and, therefore, a longer growth time with respect to black holes hosted by RQ AGNs. This implies that to explain observed million or billion solar masses SMBHs hosted in RL AGNs at high redshift, in a standard Eddington-limited accretion scenario, requires a very massive seed black holes ($M_{BH} > 10^{5-6} M_\odot$), that, to date, are not predicted from theoretical models (see below the description of the possible SMBH seeds). This supports the possibility of super-Eddington accretion for high-z RL AGNs (e.g., Volonteri et al. 2016; Begelman & Volonteri 2017).
There are different theoretical possibilities regarding the physical processes that can lead to the formation of the first massive black holes. The key common ingredient for the formation of a seed black hole at high redshift is the rapid collapse of baryons, i.e. stars and gas, in dark matter halos. Three are the most discussed theoretical scenarios:

- **Population III stars and stellar remnant BHs** (e.g., Bond 1984; Madau & Rees 2001; Valiante et al. 2016). POP III stars were formed from zero-metallicity gas in dark matter halos (or mini-halos) of about 10^6 $M_\odot$ at z = 20-40. Pop III stars had high masses ($M_* > 100$ $M_\odot$) and therefore a very short ($\sim 10^6$ yr) lifetime. Low-metallicity stars of ~ 100 $M_\odot$ are thought to form black holes directly, with masses that are roughly half their initial mass. At larger masses, ~ 200 $M_\odot$, pair production becomes important and leads to supernova explosion without a dense remnant. At still higher mass, ≥ 250 $M_\odot$, black holes with about half of the initial mass (~ 100 $M_\odot$) are the final result of the stellar evolution.
  For several years, this formation scenario was considered the most promising mechanism to form massive black holes at high redshift. However recent simulation results (e.g., Turk et al. 2009; Stacy et al. 2012) have put this picture into question, making Pop III stars rather unattractive candidates for being the precursors to the observed high-z SMBHs.

- **Direct collapse** of a very massive cloud of dense gas, existing at the center of proto-galaxies (e.g., Haehnelt & Rees 1993; Begelman et al. 2006; Latif & Schleicher 2015). The collapse of the gas cloud occur thanks to a low cloud's angular momentum. Moreover fragmentation and copious star formation must not occur: the gas cooling has to be inhibited. The evolution of such clouds involves various types of collapse, disk and bar instabilities and ends with the formation of a quasi-static, radiation-pressure supported supermassive star. Such star evolves and produces a black hole that continue to accrete from the surrounding envelope created from the gas inflow, leading to the formation of a seed black hole of 10^4-10^5 solar masses.

- **Stellar dynamical processes** (e.g., Devecchi & Volonteri 2009; Davies et al. 2011). Galaxies that host massive BHs, usually also host nuclear star clusters. If a rapid inflow of gas occurs, the potential well of the cluster will deepen rapidly. The result is a runaway collapse

of compact cluster objects, at the center of the potential well, which may form directly a massive black hole of $\sim 10^5$ $M_\odot$ (called Intermediate-mass BHs).

Regardless of the formation scenario, the growth of the seed black holes is determined by their mass and by mass supply from the galaxy. Let's take in consideration only growth via radiation efficient processes. The loss in gravitational energy of a falling particle onto the central black hole is converted into radiation according to Eq. 1.1. From this equation it is clear that, out of the total mass per unit of time falling towards the black hole, $\dot{M}$, only a fraction, $\eta\dot{M}$, is converted into luminosity, while the remaining fraction, $(1-\eta)\dot{M} = \dot{M_{BH}}$, feeds the black hole.
A simple case of black hole growth assumes that the time in which a black hole of mass M_{BH} is grown continuously from an initial seed $M_{BH,seed}$, assuming a constant Eddington ratio for the accretion process for all the time, can be written as (Shapiro 2005; Volonteri & Rees 2005):

$$t_{growth} = \tau \times ln(\frac{M_{BH}}{M_{BH,seed}}) \tag{1.21}$$

where τ is the e-folding timescale of

$$\tau = 0.45(\frac{\eta}{1-\eta})(\frac{1}{\lambda_{Edd}})(\frac{1}{f_{act}(M,t)})Gyr \tag{1.22}$$

where λ_{Edd} is the Eddington ratio[9] and f_{act} is the *duty cycle* of the black hole, i.e. the mass and redshift dependent fraction of time when the black hole is active ($f_{act}(M,t)$=[0,1]). Indeed to date theories suggest that the evolution of seed black holes can be an alternation of accretion and long quiescence phases and it can be largely influenced by sudden and isolated events, such as the merger with another black hole (e.g., Volonteri et al. 2003; Hopkins et al. 2008). Therefore the growth time of a seed black hole is probably not continuous.

[9]In this work the Eddington ratio is defined as: $\lambda_{Edd} = L_{bol}/L_{Edd}$, the total luminosity of the AGN divided by the Eddington luminosity. This parameter quantifies how fast the black hole is growing with respect to the Eddington limit.

Chapter 2

Blazars in the early Universe

In this chapter I explain the importance of finding blazars at high redshift, due to their statistical relevance, and I outline the aim of this thesis. Finally I describe the method used to select high-z (z> 4) blazar candidates in this work: the *dropout* technique.

In Sect. 1.2 I described the fact that, due to their peculiar orientation, blazars[1] radiation is strongly boosted, not obscured along the jet direction and is less affected by the attenuation due to the interaction of radio photons with the cosmic microwave background (see e.g., Ghisellini et al. 2015b; Wu et al. 2017). These particular characteristics make blazars very bright and visible up to high redshifts, and make them good tracers for the whole family of jetted AGNs (see, e.g., Volonteri et al. 2011; Ghisellini et al. 2013; Sbarrato et al. 2015), ensuring the census, free from obscuration effects, of all the of SMBHs hosted in RL AGNs at a given redshift, as described in the following. Therefore, the identification and detailed characterization of blazars at high redshifts will provide us with better constraints on the physical properties of the black holes hosted in RL AGNs in the early Universe.
Indeed, wide field optical surveys, like the Sloan Digital Sky Survey (SDSS, York et al. 2000), even if detecting large numbers of objects, are sensitive only to the un-obscured AGN population, while they miss the large majority of obscured AGNs. Usually obscured AGNs are assumed to have the same space density as the un-obscured population, but there are several evidences that the their fraction could be dependent to the luminosity and/or to the redshift (e.g., Liu et al. 2017; Ni et al. 2019). With blazars we can overcome all these problems related to obscuration effects.
For each blazar observed and studied we can infer the presence of a number of similar RL AGNs with their jets oriented in other directions but with the same intrinsic physical properties (black hole mass, accretion rate, jet power, etc., e.g., Volonteri et al. 2011). Indeed, if we define a blazar as a source observed within a viewing angle (θ) equal to $1/\Gamma$, from the number of observed blazars we can estimate the number of objects with the same properties but pointing elsewhere (N_{parent}):

$$N(\theta \leq 1/\Gamma) = \frac{2\Omega}{4\pi} \times N_{parent} \tag{2.1}$$

where 4π is the all sky surface and Ω is the solid angle subtended by the jet. The factor 2 takes into account both jet and counter-jet in the calculation (see Fig. 2.1). Therefore, assuming symmetry

[1] In the following, by the term *blazar* I am referring to quasar-like blazars, that is, FSRQs.

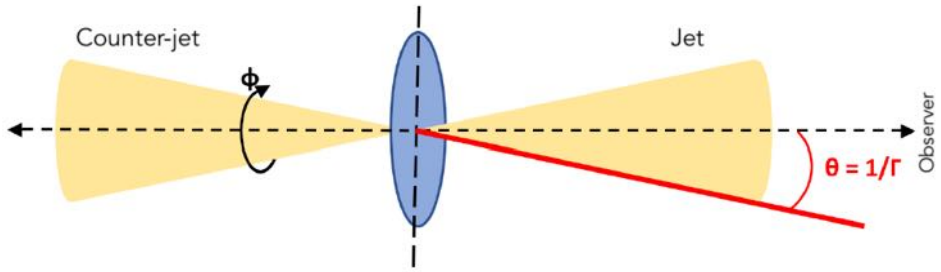

Figure 2.1: Schematic 2D view that summarizes how we can infer the number of the parent population of a blazar observed with a viewing angle $\theta \leq 1/\Gamma$.

around ϕ (Fig. 2.1), the number of blazars is given by:

$$\begin{aligned} N(\theta \leq 1/\Gamma) &= \frac{2\int_0^{2\pi} d\phi \int_0^{1/\Gamma} sin(\theta) d\theta}{4\pi} N_{parent} = \\ &= \frac{2 \times 2\pi \int_0^{1/\Gamma} sin(\theta) d\theta}{4\pi} N_{parent} = \\ &= N_{parent} \int_0^{1/\Gamma} sin(\theta) d\theta \end{aligned} \tag{2.2}$$

Solving the integral and approximating for relativistic velocities ($\Gamma \rightarrow \infty$), we obtain:

$$N(\theta \leq 1/\Gamma) \simeq N_{parent} \frac{1}{2\Gamma^2} \tag{2.3}$$

Therefore, the space density of the entire population of RL AGNs oriented in the others directions is: $N_{parent} \simeq N_{blazar} \times 2\Gamma^2$. Assuming a reasonable value of Γ (10, Saikia et al. 2016), the number of parents expected from a single blazar observation is very large (∼200).

2.1 The blazar approach: previous results and potential issues

The approach based on the class of blazars previously described has been recently proposed and used in many works, which have produced several interesting results that we summarize in the following.

Ajello et al. (2009), using an X–ray selected complete sample of 26 FSRQs at 0≤z≤3.7, have studied the cosmological evolution of blazars finding that the space density of the most luminous ones ($L_X > 10^{46}$ erg s^{-1}) has a peak at redshift ∼4. This peak is found to be at higher redshift with respect to the one derived for the total AGN population (z∼2-2.5, e.g., Hopkins et al. 2007) and implies that the black holes that grow in jetted AGNs seem to be born earlier, and/or to grow faster. Based on the blazar sample of Ajello et al. (2009) and on 5 blazars discovered at redshift between 4 and 5.5, Volonteri et al. (2011), Ghisellini et al. (2013) and Sbarrato et al. (2015) derived the space density of RL AGNs with mass $\geq 10^9 M_\odot$ as a function of redshift. The authors assumed two different values of the bulk Lorentz factor Γ (5 and 15) to perform the calculation. These results seem to suggest that the presence of a relativistic jet has a relevant influence on the growth of the accreting SMBHs and on the host-galaxy evolution. If this observed different cosmological evolution is true, then RL AGNs would be more abundant at high redshift, making the ratio between RQ and RL AGNs (the so-called *radio-loud fraction*, RLF) redshift-dependent.

Therefore another way to test if RL and RQ AGN follow different cosmological evolutions is to study the RLF as a function of z. At low redshift, the fraction of RL AGNs with respect to the RQ population is ∼10% (e.g., Ivezić et al. 2002). Several works (e.g., Anderson et al. 2001; Bañados et al. 2015) do not show any significant dependence of the RLF with redshift. On the other hand, Jiang et al. (2007) found evidence of an evolution both in redshift and luminosity. All these works computed the RLF starting from samples of RL AGNs directly observable in the wide field surveys, which are mainly Type I, excluding the contribution of dust reddened and obscured (Type 2) sources. Using blazars, instead, an unbiased (not affected by obscuration effects) measurement of RLF can be done. For example, Volonteri et al. (2011) computed the number of expected RL AGNs with $M_{BH} \geq 10^9 M_\odot$ starting from the blazars sample of Ajello et al. (2009) and from 5 blazars at z>4, assuming different value of Γ (5 and 15). The authors found that the RLF increases with z, with the number of RL AGNs becoming comparable to that of RQ at z∼3-4.
Moreover Volonteri et al. (2011) also found that the number of RL AGNs predicted from blazars is too large (an order of magnitude at z>3) with respect to that directly observed in the common area between SDSS (optical) and FIRST[2] (in the radio). Also Ghisellini et al. (2016) found an inconsistency between the number of RL AGNs at z≥4 detected in the SDSS+FIRST sky area and the number of RL AGNs at the same redshift predicted from the observed blazars in SDSS+FIRST surveys. These authors suggested different possible solutions to such a large discrepancy: an evolution of the bulk Lorentz factor Γ (decreasing for increasing redshift), a structured jet (namely only part of the jet is actually highly beamed), a compact and self-absorbed structure (that prevents the detection at GHz frequencies), possible observational biases related to strong optical absorption and compact self-absorbed radio emission.
Another interesting result on high-z RL AGNs has been firstly pointed out by Wu et al. (2013). Highly radio-loud quasars (HRLQ, with log(R)≥2.5) at z>4 have stronger X–ray emission (by a factor of ∼3) than those at lower redshift with similar values of R. This result has been obtained from the analysis of Chandra observations of 17 HRLQs, without a distinction between blazar and non blazar sources. The authors suggest, as a possible explanation, that this X–ray enhancement could be due to the interaction of the jet electron with the photons of the Cosmic Microwave Background (the so-called iC/CMB model, e.g., Tavecchio et al. 2000; Celotti et al. 2001) or with the photons emitted by intense star formation activity in the host galaxy (e.g., Hardcastle & Croston 2011).

2.2 Going beyond: extending the samples of blazars

To confirm or disprove the interesting results reported in the previous section, we need to select larger and better samples of high-z (z≥4) blazars, suitable for reliable statistical studies, and we need to increase the number of blazars at z>5, where only an handful (4) has been discovered before this work (see Table A.1). Indeed even if the number of high-z RQ AGNs is increased exponentially in the last two decades (∼200 at z> 6, e.g., Andika et al. 2020, among which 7 at z> 7, Mortlock et al. 2011; Bañados et al. 2018a; Wang et al. 2018; Yang et al. 2019b; Matsuoka et al. 2019; Yang et al. 2020, Wang et al. 2021), the number of RL AGNs (and blazars) remained limited. Before 2018 (i.e., before this thesis) only 160[3] RL AGNs have been discovered at z>4,

[2]The Faint Images of the Radio Sky at Twenty-cm (FIRST, Becker et al. 1994) is a radio flux limited (S_{lim} = 1 mJy) survey carried out at 1.4 GHz with the JVLA covering 10000 deg^2 of the North and South Galactic Caps.

[3]114 out of 160 have been found in the SDSS DR 7 (Shen et al. 2011) and SDSS DR 12 (Pâris et al. 2017) Quasar Catalogs. The other 46 sources have been reported independently in different papers: Shaver et al. (1996); Zickgraf et al. (1997); Hook & McMahon (1998); Stern et al. (2000); De Breuck et al. (2001); Péroux et al. (2001);

with the most distant being at z=6.21 (Willott et al. 2010a). Among these 160 RL AGNs, only 27 have been classified as blazars (see Table A.1). Their distribution is reported in Figure 2.2. This is because RL AGNs (and blazars) are rare sources and for discovering them wide field surveys ideally covering the entire sky (or, at least, a significant fraction of it) at a reasonable depth (e.g., few mJy sensitivity in the radio and mag∼21-22 in the optical) are needed.
The aim of the work discussed in this thesis is that of using a multiwavelength approach based on the wide field surveys available to date (see Sect. 2.4.1 and 2.4.2), to select blazars at z≥ 4 for answering the open issues reported in the previous section. In particular, firstly, a statistically complete sample of radio-selected blazars in the redshift bin between 4 and 5.5 (the so-called *g-dropout*, *r-dropout* and *i-dropout* sources, see the following section) was built. This selected sample is, to date, the largest statistically complete sample of blazars at z>4. It is described in chapter 3 and it has laid the basis for the search of blazars at higher redshift (between 5 and 6.5, *r* and *i-dropout* objects), for increasing their number thanks to the exploitation of recent and deep optical and near-IR large photometric databases (chapter 4, chapter 5 and chapter 6).

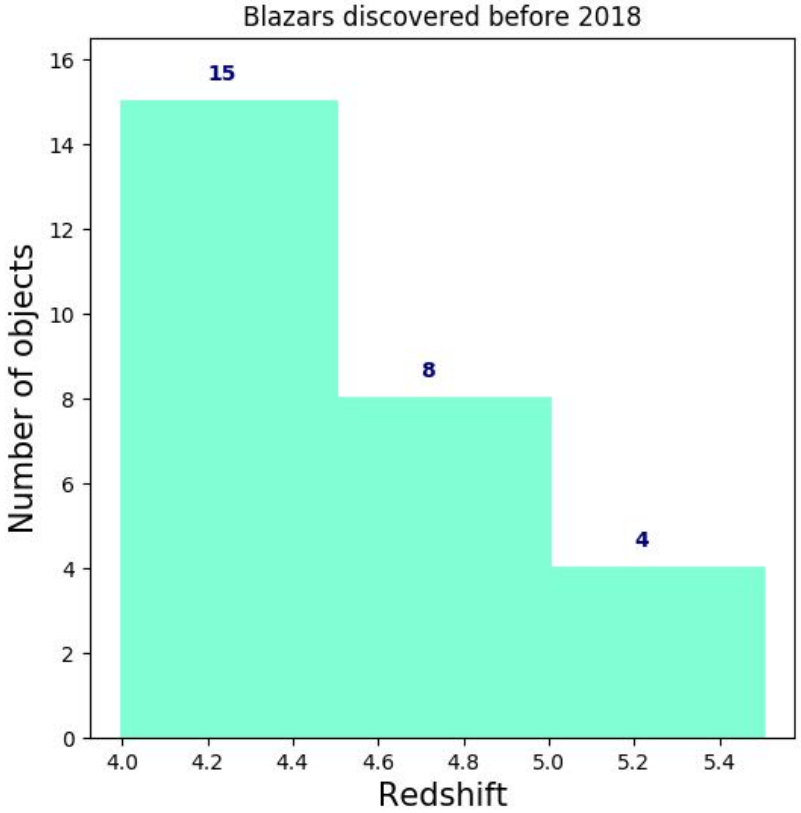

Figure 2.2: Distribution of blazars discovered before 2018 at z≥4. The criteria adopted to classify a source as a blazar are not unique and they can be based on both radio and X–ray properties. Here all the sources defined as blazars in the literature (see Table A.1) were considered.

Fan et al. (2001) ; Benn et al. (2002); Hook et al. (2002); Sowards-Emmerd et al. (2003,2004); Romani et al. (2004); Amirkhanyan & Mikhailov (2006); Kopylov et al. (2006); McGreer et al. (2006); Carballo et al. (2008); Healey et al. (2008); McGreer et al. (2009); Jiang et al. (2009); Glikman et al.(2010); Willot et al. (2010a,b); Zeimann et al. (2011); Titov et al. (2013); McGreer et al. (2013); Flesch et al. (2015); Bañados et al.(2015); Wang et al. (2016)

2.3 Selection method: the dropout technique

In this thesis I describe the search for blazar candidates at high-z (z>4). Blazars are strong radio emitters. Therefore, the starting point for the selection of this type of objects are the available wide field radio catalogs (for a detailed list of the radio surveys used in this work see Sect. 2.4.1). Then, the selected radio catalogs have been cross-matched with optical and near-IR databases, because the most commonly used method to find high-z AGNs is the color selection technique, i.e. the *dropout method*, which relies on multi-wavelength broadband photometric observations. This method is based on the fact that the flux of high-redshift sources at wavelengths shorter than the Ly-α emission line (1216Å rest-frame) is strongly absorbed by the intervening HI clouds along the line of sight (Gunn & Peterson 1965). Indeed the light of a distant object has to pass through different gas clouds, close to the source itself or distributed in the intergalactic medium (IGM, see Fig. 2.3). Photons emitted by the source with a $\lambda < \lambda_{Ly-\alpha}$ are absorbed by neutral

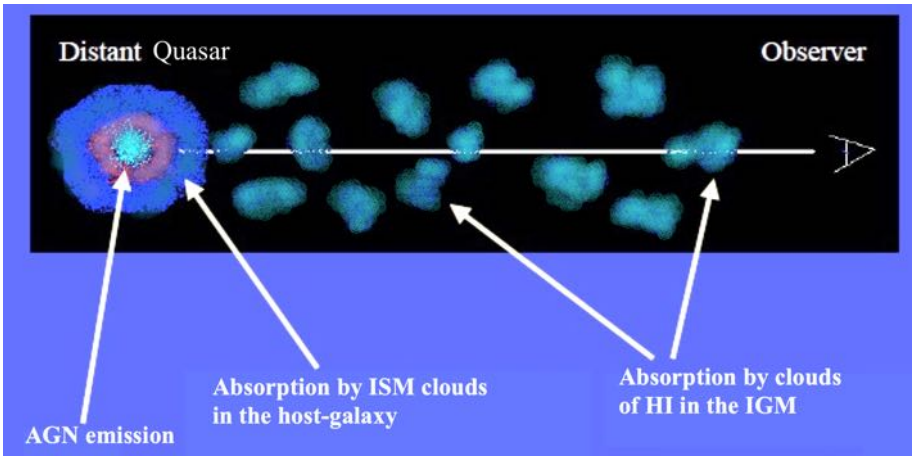

Figure 2.3: The light travel of a distant AGN to the observer. The presence of absorbing material in the AGN itself or in the intervening gas along the line-of-sight originates absorption lines in the AGN spectrum. Image adapted from https://wwwmpa.mpa-garching.mpg.de

hydrogen; instead the light emitted with wavelength longer than that of Ly-α passes through the HI clouds and can reach the observer. The flux absorbed by the gas clouds depends on redshift and on the amount of fraction of neutral hydrogen present along the line of sight: $F_{abs} = F_{em} \times (1\text{-}e^{\tau_{HI}})$, where τ_{HI} is the opacity of the hydrogen clouds[4]. Therefore, the UV-optical spectrum of a low-redshift source shows lower absorption features (called *Ly-α absorbing clouds* or *Ly-α forest*[5]) with respect to a high redshift object, due to the increasing HI column density along the line of sight (see Fig. 2.4). The absorption feature at the position of the Ly-α line creates a *drop* (i.e. the Ly-α break), which can be recognized with broad-band photometry.
In the last decades, a large fraction of the optical and near-IR sky has been observed in different photometric bands, with wide filters that cover a specific range of wavelengths, which depends on the particular survey (see Sect. 2.4.2). Due to the cosmological redshift, these filters cover a

[4] τ_{HI} is related to the abundance of absorbing neutral hydrogen atoms as $\tau_{HI} = \frac{\pi e^2}{m_e c} f_\alpha \lambda_\alpha H^{-1}(z) n_{HI}$, where f is the oscillator strength of the Ly-α line, H is the redshift-dependent Hubble parameter and n_{HI} is the neutral number density (Fan et al. 2006).

[5] The Ly-α forest is further subdivided, according to the strength of the absorption features, into narrow Ly-α lines, Lyman-limit systems, and damped Ly-α systems. Narrow Ly-α lines are caused by absorbing gas of neutral hydrogen column densities of $N_H < 10^{17}$ cm^{-2}. For the Lyman-limit systems the column densities of neutral hydrogen is $N_H \sim 10^{17}$ cm^{-2}. Damped Ly-α systems occur if the column density of neutral hydrogen is $N_H \sim 10^{20}$ cm^{-2}

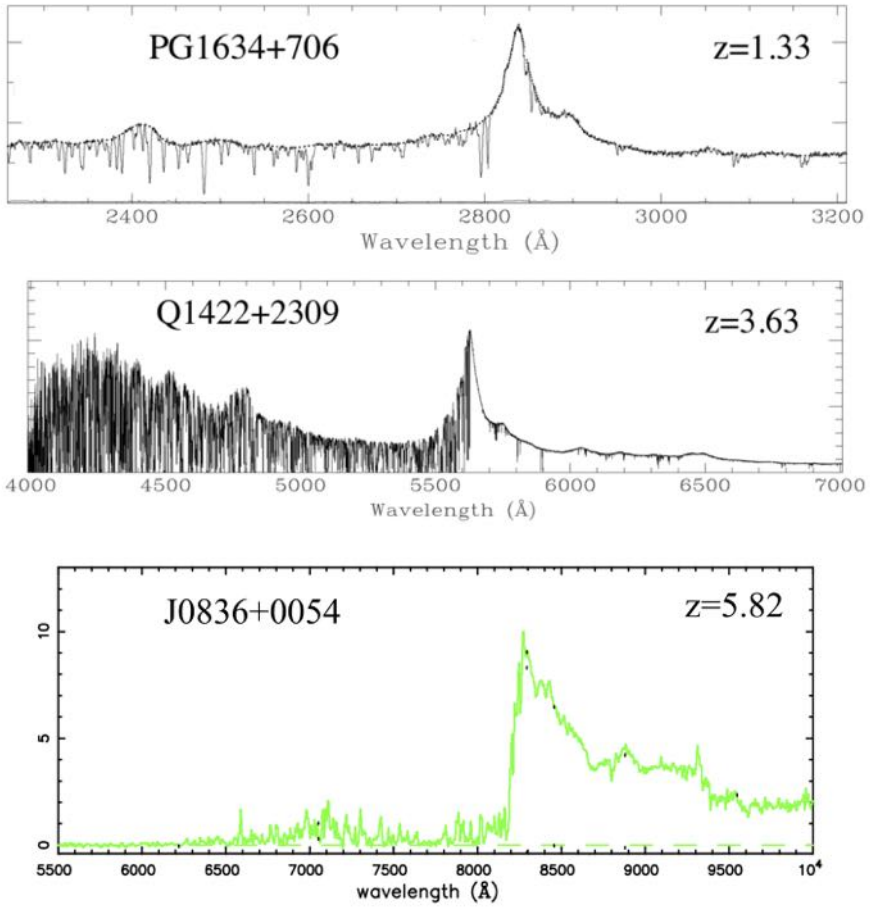

Figure 2.4: Ly-α absorption features in three AGN spectra at different redshift. The flux bluer than Ly-α emission line is absorbed by neutral hydrogen clouds along the line of sight. At z$\sim$1 absorptions are not strongly marked, due to the fact that the gas in the today Universe is completely ionized; at z$\sim$3 stronger and frequent absorption lines are clearly shown (i.e. the so-called Ly-α forest); finally at z$\sim$6, where the gas in the IGM is almost neutral the AGN flux at $\lambda<\lambda_{Ly-\alpha}$ is completely absorbed and a break in the spectrum is easily seen at the position of the Ly-α line. Image credit: Charlton & Churchill (2000) and Becker et al. (2001).

different part of the source's electromagnetic spectrum and, as a result, the Lyman break falls between two different filters, depending on the redshift. For example if the source is at z$\sim$5 the Lyman drop falls between filters r and i (and the object is called *r-dropout*); if the redshift of the source is larger than $\sim$6 the object is called *i-dropout* as the spectrum break falls between i and z filters. An example of *i-dropout* AGN is shown in Fig. 2.5. Lyman break causes a very red color (i.e. a large difference in magnitude) between the flux density measured by filter before the drop and that measured by the filter after the Ly-α break. Therefore for an high-z AGN little or no flux density in the bluer bands and a strong flux density at the wavelength of the Lyman break and above are expected to be recovered.

In summary, the two main steps of high-z blazar candidates selection described in this thesis are the cross-matching between a radio catalog and an optical/infrared one, and the selection of the dropout sources, according to the redshift we are interested in.

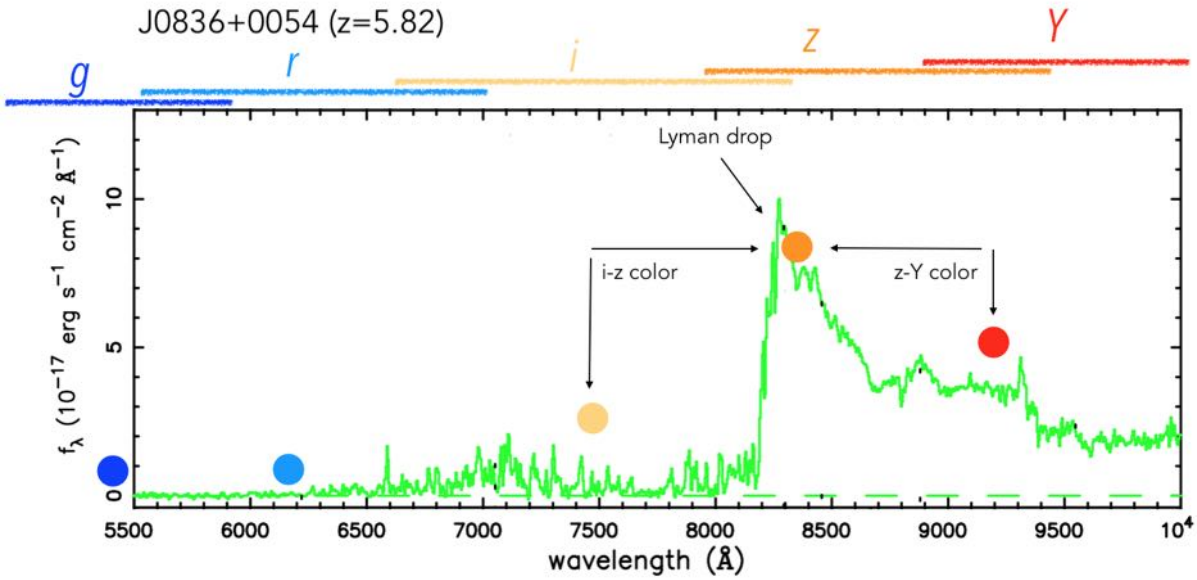

Figure 2.5: Example of a $i-dropout$ source with broad band photometry. On the top we have shown the different wavelengths covered by the common optical near-IR filters. The filled colored points correspond to the flux density expected in each filter. As the Lyman break falls between i and z-bands, the expected flux in g, r and i filters will be very low (or absent), and a strong flux in z-band and a flux also in the last filter (Y) will be measured. The object has a red $i-z$ color and a blue $z-Y$ color. Image adapted from Becker et al. (2001).

2.3.1 Contaminants

Two are the main types of contamination in the search for RL AGNs at high redshift: brown dwarf stars and low redshift (z∼1-2) AGNs:

- **brown dwarfs**, especially late M, L, and T dwarfs in our Galaxy. They are point-like in optical and near-IR bands and they can have optical colors similar to AGNs. Indeed the optical spectra of this type of stars present very red colors (see Fig. 2.6), which can mimic the Ly-α drop in AGNs spectra.
  These stars usually do not emit in the radio band at the flux levels considered in this work (a few mJy). However the radio surveys available in the literature, and used in this thesis, are characterized by large positional errors (sometimes up to tens of arcsecond). Therefore, stars can fall in the radio positional error box with a high probability, since their sky density is very high. This contamination is difficult to remove. Usually two methods can be used to reduce it: 1) to search for objects outside the Galactic plane and 2) to set a blue color, i.e. a small difference in magnitude, between two filters on redward side of the Lyman break. Indeed, as shown in Fig. 1.2, AGNs show a blue continuum, with respect to stars. Hence a blue color between two filters after the Lyman break is expected in case of true high-z AGN. A blue continuum allows the selection of un-obscured AGNs but excludes the possibility of selecting also obscured (moderately red) high-z AGNs. However the radiation of blazars, as already said in Sect. 1.2, is not obscured along the line of sight, making this potential bias less relevant.

- **low redshift (z∼1-2) AGNs**, both compact elliptical radio galaxies and Type I AGNs whose spectra are reddened by dust. The red color of the spectrum of these sources (see

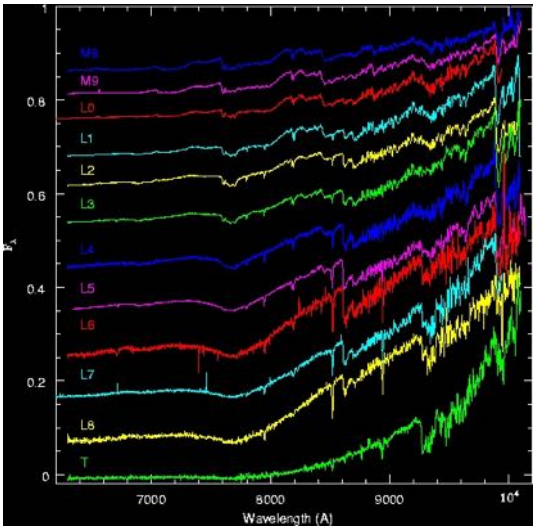

Figure 2.6: M,L,T-dwarf optical spectral sequence. The red color of these spectra can mimic the Ly-α break. Image credit: https://www.stsci.edu/ inr/ldwarf.html

e.g., Fig 2.7 for an example of low-z elliptical galaxies) can mimic the Lyman drop. This contamination can be kept at minimum using mid-IR data, since low-z reddened AGNs typically have stronger 3μm (observer's frame) emission than high-z sources with the same optical magnitude (e.g., Carnall et al. 2015).

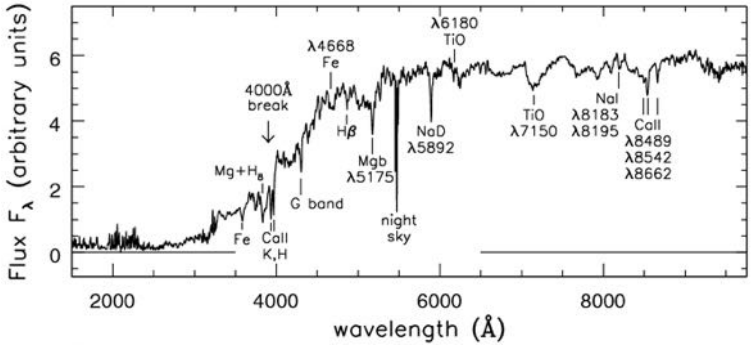

Figure 2.7: Rest-frame UV-optical spectrum of an elliptical radio galaxy. Image credit: http://www.astro.wisc.edu/ sparke/book/webfigs.html

2.4 Wide Field Surveys

In this section I describe the wide field surveys used in this thesis for selecting high-z blazars candidates. I used radio, optical and infrared surveys that cover a large fraction of the sky, due to the very low sky density of blazars.

2.4.1 Radio surveys

In this section the characteristics of the radio surveys used in this work to select blazar candidates are summarized, together with the description of some radio surveys that have been useful to

characterize the radio properties of the sources discovered and studied in this thesis. Table 2.1 reports a summary of the main properties of these surveys.

Cosmic Lens All Sky Survey

The Cosmic Lens All Sky Survey (CLASS; Myers et al. 2003; Browne et al. 2003) is a flux density limited survey at 4.85 GHz ($S_{4.85\ GHz}$>30 mJy) covering almost the entire northern hemisphere (16300 deg^2), spanning the declination 0°≤δ≤75°, excluding the Galactic plane (|b|≥10°). Figure 2.8 shows the sky area covered by the survey. CLASS was built by combining the NRAO VLA Sky Survey, NVSS, at 1.4 GHz (Condon et al. 1998), with the Green-Bank Survey, GB6, at 5 GHz (Gregory et al. 1996) and by selecting only objects with a flat spectrum between these two radio frequencies (α<0.5, with $S_\nu \propto \nu^{-\alpha}$). The number of flat spectrum radio sources contained in the CLASS is ∼11000. All these sources have been then followed up at 8.4 GHz using the Very Large Array (VLA) in its most extended configuration (i.e. the A-array, which gives the best resolution) providing a resolution of 0.2″ and, therefore, a very accurate radio position.

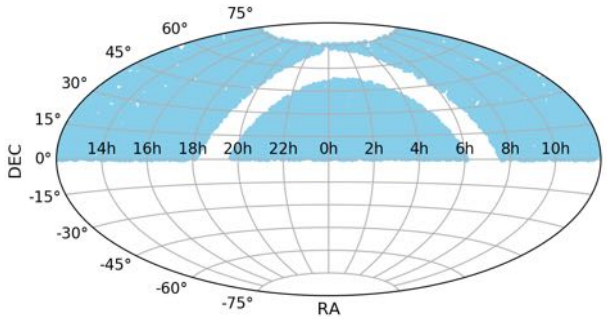

Figure 2.8: CLASS sky coverage.

NRAO VLA Sky Survey

The NRAO VLA Sky Survey (NVSS, Condon et al. 1998) is a radio imaging flux limited (S_{lim} ∼ 2.3 mJy at 5 times the rms) survey covering ∼82% of the celestial sphere (δ>-40°, see Fig. 2.9). It was carried out, between 1993 and 1996, at 1.4 GHz with the the Karl Guthe Jansky Very Large Array (JVLA, Fig. 2.9) telescope with an angular resolution of about 45″ (D and DnC configuration). The survey is based on 217446 *snapshot* observations from which a catalog of ∼2×10^6 sources was created. The rms noise of the NVSS images is ∼0.45 mJy beam^{-1}. The rms uncertainties in right ascension and declination vary from ≤1″ for the 10^5 sources stronger than 15 mJy to ∼7″ at the survey limit.

Sidney University Molonglo Sky Survey

The Sidney University Molonglo Sky Survey (SUMSS, Bock et al. 1999, Mauch et al. 2003) is a radio imaging flux limited (S_{lim} = 5 mJy at 5σ) survey of the southern sky at δ<−30°, covering a total area of 8100 deg^2 (see Fig. 2.10), carried out at 843 MHz with the Molonglo Observatory Synthesis Telescope (MOST, Fig. 2.10). The survey consists of 629 4.3°×4.3° mosaic images with a resolution of 45″ by 45″×cosec(δ), and a limiting peak brightness of 6 mJy beam^{-1} at declinations δ≤-50°, and 10 mJy beam^{-1} at δ >-50°. The mean rms noise level is ∼1 mJy beam^{-1}. SUMSS is therefore similar in sensitivity and resolution to the northern NVSS. Positions in the catalog are

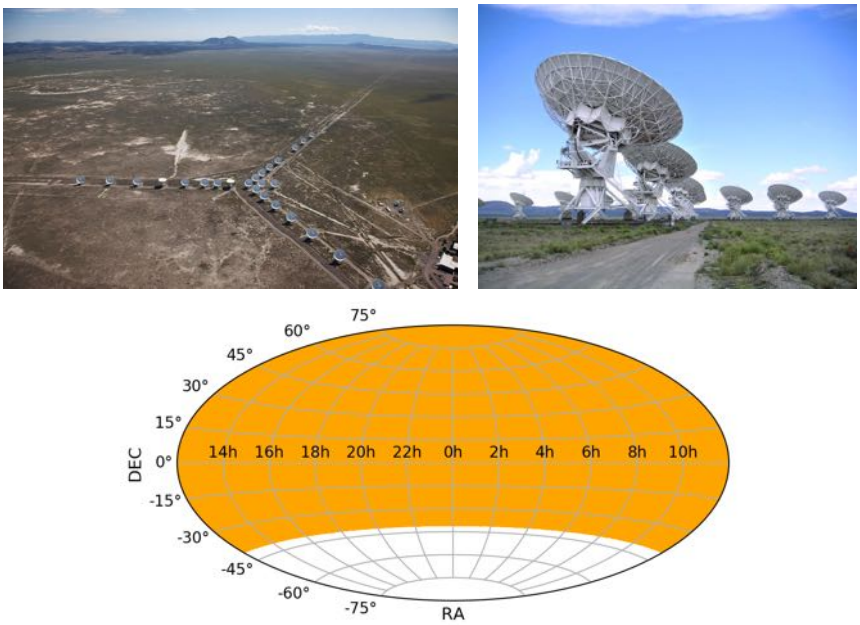

Figure 2.9: JVLA telescope and NVSS sky coverage. *Top panel*: the JVLA telescope located in Socorro, New Mexico, used to carry out the survey. It is composed by twenty-eight 25-m antennas deployed in a *Y-shaped* array. The antenna receivers cover the frequency range from 1.0 to 50 GHz, with an angular resolution from 0.04″ to 46″ depending on the array configuration: A, B, C or D. The A-configuration provides the longest baselines (36 km) and thus the highest angular resolution for a given frequency. The D-configuration provides the shortest baselines (1 km), translating to a high surface brightness sensitivity at the cost of angular resolution. Images taken from the NRAO webpage. *Bottom panel*: the sky coverage of the NVSS.

accurate to within 1-2″ for sources with peak brightness ≥20 mJy beam^{-1}, and are always better than 10″.

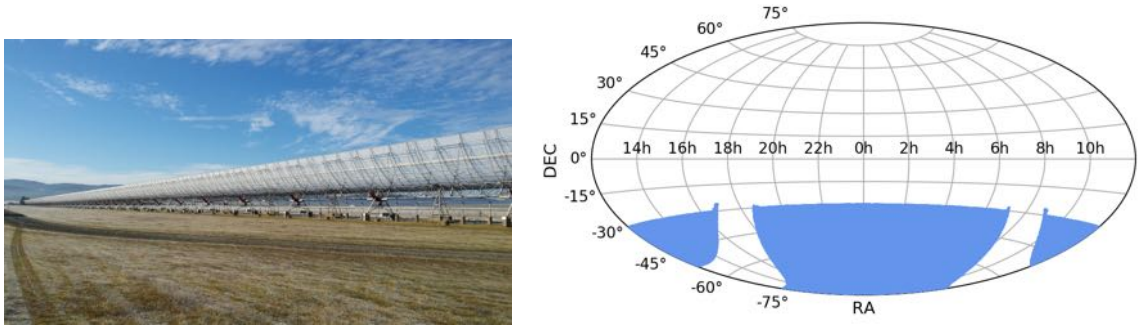

Figure 2.10: MOST telescope and SUMSS sky coverage. *Left panel*: the Molonglo Observatory Synthesis radio Telescope (MOST) located near Canberra, Australia, used to carry out the survey. It is a parabolic cylindrical antenna consisting of 352 independent antennae grouped in 4 identical modules. MOST has the largest collecting area (∼18000 square meters) of any telescope in the southern hemisphere to date. Image taken from https://sciencesprings.wordpress.com. *Right panel*: the sky coverage of the SUMSS survey.

Other radio surveys

There has been several radio surveys available in the literature, carried out at different frequencies (from few MHz to 20 GHz), which have been used to estimate the radio properties of the sources discovered and studied in this thesis. Here I briefly summarize them, from the low frequency survey to the high frequency one.

- **GaLactic and Extragalactic All-sky MWA Survey**: GLEAM (Hurley-Walker et al. 2016) is a low frequency radio survey carried out with the Murchison Widefield Array (MWA), located in Western Australia, with a resolution (beam) of $100''$. The first release of the extragalactic catalog covers the entire high Galactic latitude sky south of $+30°$ of declination (24831 deg^2). The catalog contains flux density measurements in 20 separate intervals between 72 and 231 MHz with a flux density limit at 5σ equal to 50 mJy.

- **TIFR GMRT Sky Survey**: TGSS (Intema et al. 2017) was carried out at 150 MHz, between 2010 and 2012, with the Giant Metrewave Radio Telescope (GMRT). TGSS is the first continuum full-sky radio survey at meter wavelengths (below 200 MHz) with angular resolution comparable to existing centimeter surveys. To date, the data collected by the TGSS project team remained largely unpublished. The first alternative data release (ADR1) covers 36900 deg^2 (or 3.6π steradians, 99.5% of the sky) of the sky between $-53°$ and $+90°$ in declination and includes images at a resolution of $25''\times25''$ north of $19°$ and $25''\times25''/\cos(\delta-19°)$ south of $19°$. The majority of pointing images have a median rms noise of 3.5 mJy beam^{-1} (and always below 5 mJy beam^{-1}). The extracted radio source catalog contains positions, flux densities, sizes for 0.62 Million radio sources down to a 7-sigma peak-to-noise threshold. For the bulk of the survey, the measured overall astrometric accuracy is better than $2''$ in RA and DEC, while the flux density accuracy is estimated at $\sim$10%.

- **Westerbork Northern Sky Survey**: WENSS (Rengelink et al. 1997) is a low-frequency radio survey that covers the whole sky north of δ=30° at a wavelength of 92 cm (325 MHz) to a limiting flux density of $\sim$18 mJy (5×rms). This survey has a resolution of $54''\times54''\mathrm{cosec}(\delta)$ and a positional accuracy of $5''$ for the faint sources to better than $1''$ for the stronger ones. To carry out this survey the Westerbork Synthesis Radio Telescope (WSRT) was used. As a result the final catalog consists of 300000 sources for which a high, medium and low resolution maps ($1'$, $2.5'$ and $4'$ resolution) has been made.

- **Very Large Array Sky Survey**: VLASS (Lacy et al. 2020) is a radio survey of the entire sky visible at the JVLA ($\delta>-40°$, 33885 deg^2) carried out at 3 GHz, with an angular resolution of $\sim2.5''$. The survey is still in progress. The data will be acquired in three epochs to allow the discovery of transient radio sources. The 1σ sensitivity goal for a single pass is 120 μJy, and 69 μJy when all three passes are combined. VLASS Epoch 1 is already finished and quick look images are available. VLASS Epoch 2 is started in June 2020 and several quick look images have been available from Autumn 2020.

- **4.85 GHz PARKES-MIT-NRAO survey**: The PMN database contains 36640 sources of the Parkes-MIT-NRAO Southern, Zenith, Tropical and Equatorial surveys (Wright et al. 1994). These surveys were made using the Parkes 64 m radio telescope at a frequency of 4850 Hz, covering the sky from $-87.5°$ to $+10°$ in declination and with a spatial resolution of approximately $4.2'$. The PMN surveys were divided into several zones: Southern ($-87.5°<\delta<-37°$, flux limit from 20 to 50 mJy), Zenith ($-37°<\delta<-29°$, flux limit of

72 mJy), Tropical ($-29°<\delta<-9.5°$, flux limit of 42 mJy) and Equatorial ($-9.5°<\delta<+10°$, flux limit of 42 mJy).

- **Australia Telescope-PMN survey** (ATPMN, McConnell et al. 2012): Following the PMN survey, the Australian Telescope Compact Array (ATCA) was used to re-observe at 4.8 and 8.6 GHz a sample of 8385 sources in the PMN catalog with a flux density at 4.8 GHz larger than 70 mJy. The ATPMN survey cover the southern sky under $-38.5°$ with an angular resolution of $0.03''$ and $0.02''$ at 4.85 and 8.4 GHz respectively, until a flux limit of 7 mJy. The ATPMN source catalog contains 9040 distinct objects.

- **Combined Radio All-sky Targeted Eight GHz Survey** (CRATES): Healey et al. (2007) have assembled an 8.4 GHz catalog of bright ($S_{4.8\ GHz} \geq 65$ mJy), flat-spectrum radio sources with nearly uniform extragalactic ($|b| > 10°$) coverage. CRATES is designed as an extension of the CLASS. Indeed the catalog was assembled from existing observations from CLASS, and from PMN surveys, by reprocessing of archival JVLA and ATCA data and by new observations to fill in coverage gaps. The resulting catalog provides precise positions, sub-arcsecond structures, and spectral indexes for 14467 sources.

- **Australia Telescope 20 GHz Survey (AT20G) and the AT20G high-resolution follow-up ($\mathbf{AT20G}_{follow-up}$)**: AT20G (Murphy et al. 2010) is a blind 20 GHz survey of the entire southern sky with $|b|>1.5°$ (20086 deg^2). Observations were carried out using ATCA from 2004-2008. The final AT20G catalog consists of 5890 sources above a 20 GHz flux density limit of 40 mJy and includes near-simultaneous observations at 4.8 and 8.6 GHz for most sources south of -15°. The AT20G is the largest blind survey done at such a high radio frequency. A second part of the survey consisted of a high angular resolution follow-up at 20 GHz using ATCA with the maximum baseline of ∼6 km. The follow-up observations reaches an angular resolution of $0.3''$ (Chhetri et al. 2013).

Survey	Frequency (GHz)	Sky coverage (deg^2)	flux density limit (mJy)	Resolution (arcsec)
GLEAM	0.072-0.231	∼10000	50 (5σ)	100
TGSS	0.150	∼36900	24.5 (7σ)	25
WENSS	0.325	∼10200	18 (5σ)	15
SUMSS	0.843	8100	5 (5σ)	45
NVSS	1.4	∼33800	2.3 (5σ)	45
VLASS	3	33885	0.069 (1σ)	2.5
CLASS*	4.85	16300	30	0.18
PMN	4.85	∼14800	42-42-50-72 (5σ)	252
ATPMN	4.8 - 8.6	∼7400	7 (5σ)	1.8-1.2
CRATES*	8.4	∼32000	65	1.2-0.18
AT20G	4.8 - 8.6 - 20	20086	40 (at 20 GHz, 4σ)	∼10 (at 20 GHz)

Table 2.1: Summary of the radio surveys used in this work. For the TGSS survey the values of the first data release (ADR1) are reported; the two surveys marked with $*$ contains only FSRQs. Col (1): survey acronym; Col (2): Frequency (in GHz) at which the survey has been carried out; Col(3): Covered area in square degrees; Col (4): Flux limit (in mJy) and in parenthesis the level of sensitivity. For the VLASS survey I reported the limit that will be reached after the end of the survey, and for the PMN survey the fluxes of the Equatorial, Tropical, Southern and Zenith surveys respectively are shown.

2.4.2 Optical surveys

The dropout method previously described is based on optical and infrared (NIR/MIR) photometric data. In this work data from two optical surveys, the Dark Energy Survey and the Panoramic Survey Telescope and Rapid Response System and from one MIR survey (WISE) have been used. Table 2.2 reports a summary of the main properties of these surveys.

Dark Energy Survey

The Dark Energy Survey (DES, Flaugher 2005) is a survey in the visible/NIR bands, which covered 5000 deg^2 of the southern Galactic cap (roughly 1/8 of the total sky, see Fig. 2.11), by using the Dark Energy Camera (DECam; Honscheid, K. & DePoy 2008) mounted on the 4 m Victor M. Blanco Telescope (Fig. 2.11). The survey took 758 observing nights spread over six years to complete (from August 2013 to January 2019), covering the survey footprint ten times in five broad photometric bands (g,r, i, z and Y, see Fig. 2.13). The first public data release DES DR1 (Abbott et al. 2018) consists of reduced single-epoch images, coadded images, coadded source catalogs, and associated products over the first three years of DES science operations. DES DR1 has a median delivered point-spread function of g = 1.119, r = 0.958, i = 0.880, z = 0.836 and Y = 0.904 arcsec FWHM, a photometric precision better than 1% in all bands, and an astrometric precision of 151 mas. The nominal median co-added catalog depths for a 1.95″ diameter aperture at signal-to-noise ratio (S/N) = 10 are g = 24.33, r = 24.08, i = 23.44, z = 22.69, and Y = 21.44 mag. Thanks to its depth, this survey offers new possibilities to discover high-z AGNs that are less luminous, and therefore, on average, with a smaller SMBH, with respect to those found with previous shallower surveys (like the SDSS, r∼22 mag).

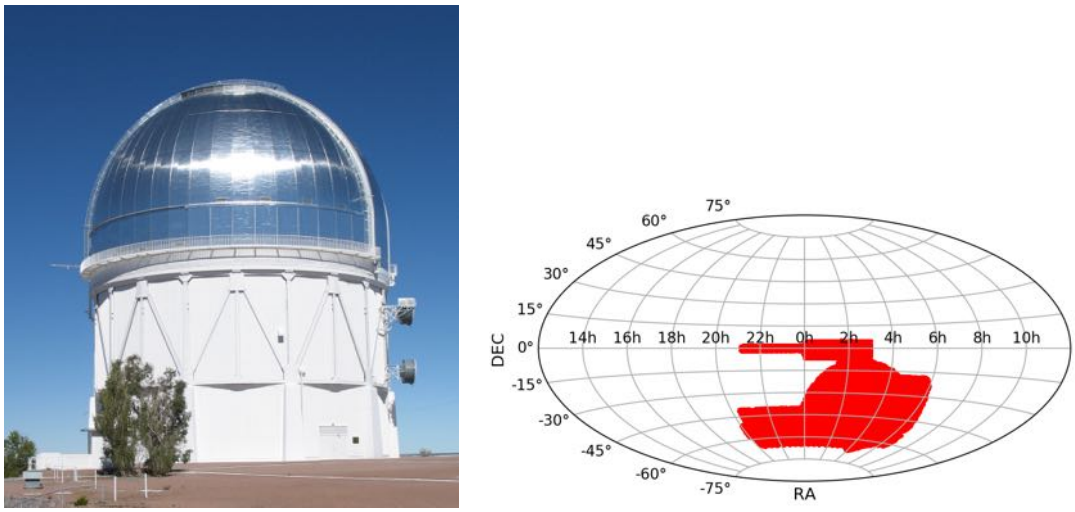

Figure 2.11: *Left panel*: the 4 m Victor M. Blanco Telescope located at the Cerro Tololo Inter-American Observatory (Chile) used to carry out the survey. It is equipped with DECam, a high-performance, wide-field CCD imager mounted at the prime focus. DECam contains 62 CCDs with 520 megapixels and images 3 deg^2 at 0.263 ″/pixel resolution. Image taken from https://www.darkenergysurvey.org. *Right panel*: the sky coverage of the DES survey.

Panoramic Survey Telescope and Rapid Response System

The Panoramic Survey Telescope and Rapid Response System (Pan-STARRS, Kaiser et al. 2002, 2010; Chambers & Pan-STARRS Team 2016) is an innovative wide-field astronomical imaging

and data processing facility developed at the University of Hawaii's Institute for Astronomy. Pan-STARRS1 (PS1) is the first part of Pan-STARRS to be completed and is the basis for both Data Releases 1 and 2 (DR1 and DR2). The PS1 survey used a 1.8 m telescope located at Haleakala Observatories (see Fig. 2.12), and its 1.4 Gigapixel camera (GPC1) to image the sky in five broadband filters (g, r, i, z and y, see Fig. 2.13). PS1 covers the whole sky above a declination of -30° (70% of the entire sky, Fig. 2.12) for about four years. The nominal median coadded catalog depths at a S/N of 5 are $g = 23.3$, $r = 23.2$, $i = 23.1$, $z = 22.4$, and $y = 21.4$ mag (Chambers & Pan-STARRS Team 2016). The mean uncertainty of the astrometric position is 2.3 mas in RA and 1.7 mas in Dec.

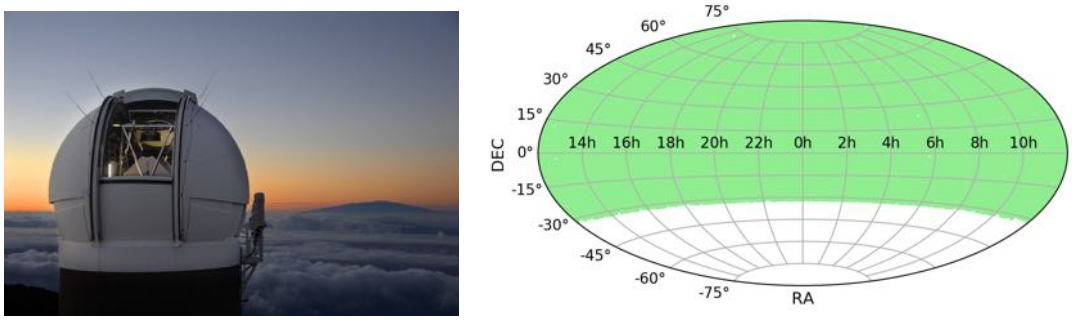

Figure 2.12: Pan-STARRS telescope and sky coverage. *Left panel*: the 1.8 m Pan-STARRS PS1 alt-az telescope, situated at Haleakala Observatories near the summit of on the island of Maui (Hawaii) used to carry out the survey. Image taken from https://panstarrs.stsci.edu. *Right panel*: the sky coverage of the Pan-STARRS survey.

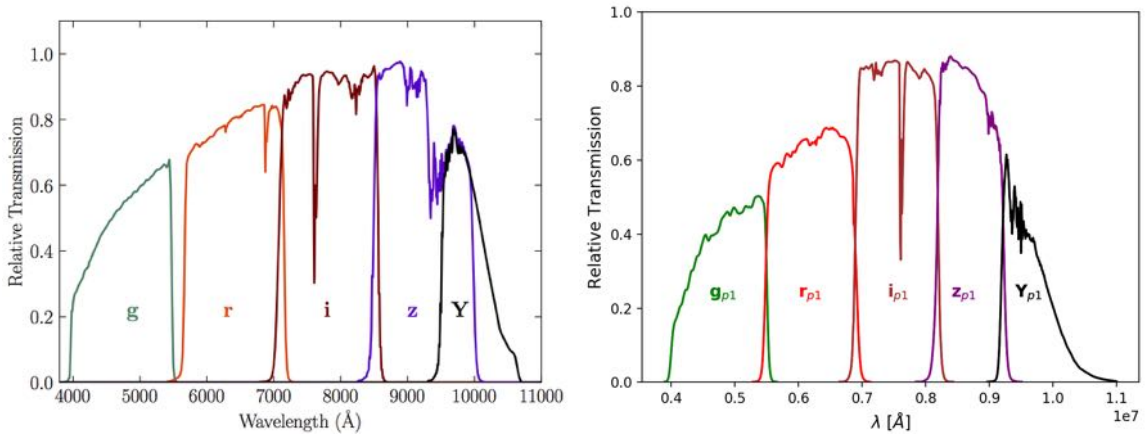

Figure 2.13: *Left*: DES DR1 Standard bandpasses for the DECam g, r, i, z and Y filters. The bandpasses represent the total system throughput, including atmospheric transmission (airmass = 1.2) and the average instrumental response across the CCDs. The effective wavelength of each filter are: $g = 5270$Å ; $r = 6590$Å; $i = 7890$Å; $z = 9760$Å ; $y = 10030$Å. Image credit: https://www.darkenergysurvey.org. *Right*: Pan-STARRS PS1 g, r, i, z and Y filters trasmission curves (airmass = 1.2). The effective wavelength of each filter are: $g = 5460$Å ; $r = 6800$Å; $i = 7450$Å; $z = 8700$Å ; $y = 9780$Å.

2.4.3 Infrared survey

In Section 2.3.1 it was mentioned that one of the most important type of contamination in the case of a radio selected blazars sample are low-redshift (z∼1-2) *red* (i.e. moderately absorbed)

AGNs. To reduce these contaminants mid-IR data can be used. In this thesis the mid-IR catalog of the Wide-field Infrared Survey Explorer mission has been used to this purpose.
The Wide-field Infrared Survey Explorer (WISE, Wright et al. 2010, Fig. 2.14) is a NASA infrared-wavelength space telescope launched in December 2009. By early 2011, it had finished scanning the entire sky twice in four wavelengths of the infrared band: 3.4 (W1), 4.6 (W2), 12)W3) and 22 (W4) μm (see Fig. 2.14). WISE achieved at least 68, 98, 860, and 5400 μJy 5-sigma sensitivity at 3.4, 4.6, 12, and 22 microns. This is a factor of ∼500 times better sensitivity than the survey completed in 1983 by the IRAS satellite at 12 and 23 μm. Upon completing its surveys in 2011, WISE was placed in hibernation mode. However in 2013, NASA reactivated the mission with the primary goal of scanning for near-Earth objects, or NEOs, through a project called NEOWISE (Mainzer et al. 2014).

The photometric system used to catalog the sources detected by WISE is the Vega system,

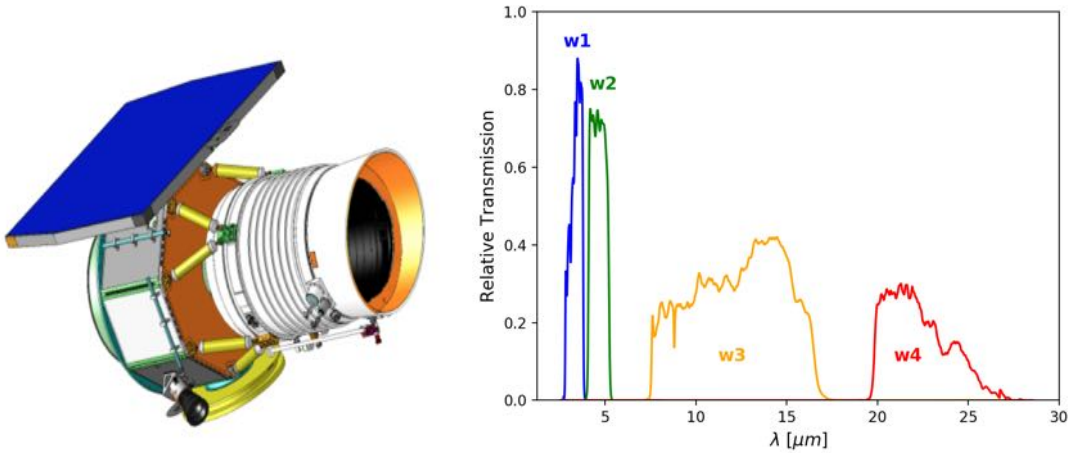

Figure 2.14: *Left panel*: Image of the WISE spacecraft. Image taken from NASA website. *Right panel*: W1, W2, W3, W4 filters transmission curves. The effective wavelength of each filter are: 3.368, 4.618, 12.082 and 22.194 μm.

different from those used in optical near-IR surveys (the AB system). Vega magnitude can be converted to AB magnitude with the following relation:

$$mag_{AB} = mag_{Vega} + \Delta_m \tag{2.4}$$

where Δ_m is the characteristic off-set for each WISE filters. In this work the Δ_m found in Cutri et al. (2012) have been used: 2.683 (W1), 3.319 (W2), 5.242 (W3) and 6.604 (W4).

Survey	Sky coverage (deg^2)	filters and magnitude limits				
		g	r	i	z	Y
DES	∼5000	24.33	24.08	23.44	22.69	21.44
Pan-STARRS PS1	∼28800	23.3	23.2	23.1	22.4	21.4
		W1	W2	W3	W4	
WISE	all sky	19.6	19.3	16.7	14.6.	

Table 2.2: Summary of the main properties of the optical and near infrared surveys used in this thesis. Col(1): survey acronym; Col(2): Sky coverage in square degrees; Col(3): filters and magnitude limits (in AB system) for each band.

Chapter 3

Searching for z≥4 blazars in the CLASS+PS1 surveys

This chapter is based on the following papers:
- Caccianiga A., Moretti A., ***Belladitta S.****, Della Ceca R., Antón S., Ballo L., Cicone C., et al., 2019, MNRAS, 484, 204, hereafter C19*
- Ighina L., Caccianiga A., Moretti A., ***Belladitta S.****, Della Ceca R., Ballo L., Dallacasa D., 2019, MNRAS, 489, 2732, hereafter Ig19*
My contribution to the works: discussion of the results; student (Luca Ighina) co-supervision bachelor thesis in physics.

The use of blazars to study the high-redshift (z>4) Universe requires the selection of well-defined and sizable samples suitable for reliable statistical analyses, as it was already mentioned in Sect 2.2. Starting from the combination of CLASS and Pan-STARRS PS1 (Fig. 3.1) we decided to efficiently select a radio-flux limited sample of z≥4 blazars to be directly comparable with radio samples selected at lower redshifts and to be useful for a statistical study of the properties of blazars (and RL AGNs) at high-z (e.g., space density, luminosity function, black hole mass distribution, etc.). In this chapter I summarize the selection of such sample, the multi-wavelength properties of the sources and the results also used for the analysis of the new z≥5 blazars discovered in this thesis and reported in the other chapters.

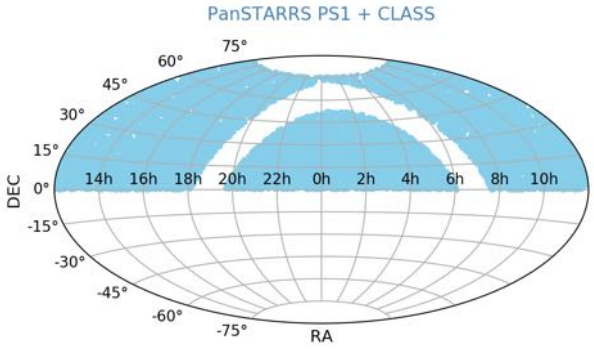

Figure 3.1: The common area of the sky between Pan-STARRS PS1 and CLASS. It consists of 16300 deg^2 (the northern sky with |b|>10°). In this area we searched for z≥4 blazars.

3.1 Sample selection

The sub-arcsec JVLA position of the CLASS sources (see Sect. 2.4.1) guarantees the detection of the correct optical counterpart of the radio objects, even at faint optical magnitudes, without significant spurious contamination. In particular, we used a search radius of 0.6″ to find the optical counterpart of the CLASS sources cross-matching the CLASS list (∼11000 objects) with the Pan-STARRS1 (PS1) catalog. We then used the dropout method described in Sect. 2.3 to select z≥4 blazar candidates. The adopted selection criteria are summarized in Fig. 3.2. In the

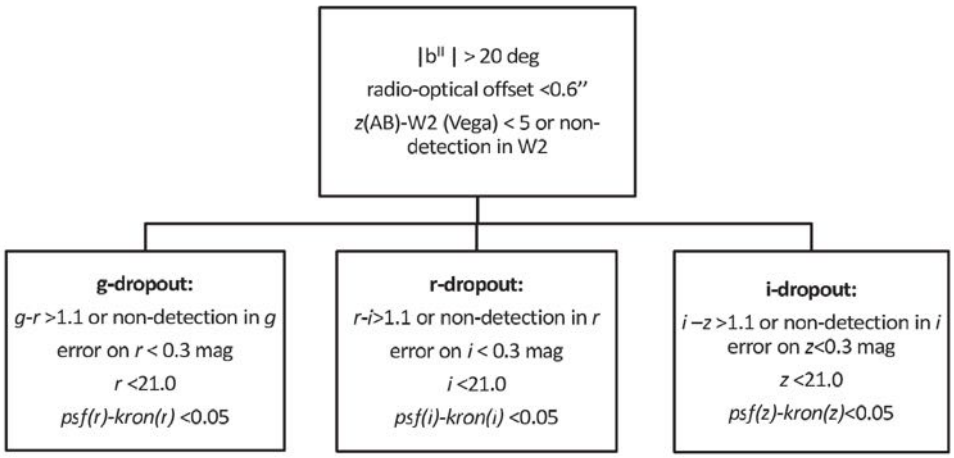

Figure 3.2: Summary of the criteria adopted to select high-z blazar candidates from the CLASS survey. Figure taken from C19.

specific:

- We required that the $g-r$, $r-i$ or $i-z$ colors (for the range of redshift between 4 and 6, considered) are larger than 1.1. This threshold is suggested by the expected colors of a typical quasar template (see Fig. 3.3). It has been set in order to include the large majority (>99%) of the z≥4 AGNs discovered to date.

- We decided not to apply a blue continuum filter, as this can introduce some incompleteness in the selection, excluding the possibility of selecting moderately red AGNs.

- To remove the contamination of low-z *red* AGNs (see Sect. 2.3.1), we imposed that the object is either undetected in WISE (W2) or, if detected, we require that z(AB)−W2(Vega)<5.0 (see Fig. 3.3); this threshold is similar to the one adopted by Carnall et al. 2015.

- We required that the source is star-like in the optical bands: PSF magnitude − Kron magnitude < 0.05 (see Chambers & Pan-STARRS Team 2016).

- We imposed that the magnitude in the reddest filter of each selection (i.e. r magnitude for $g-r$ selection, the i magnitude for the $r-i$ selection and the z magnitude for the $i-z$ selection) is brighter than 21. This last constraint guarantees that the dropout is significant when the object is not detected in the bluest filter.

- To reduce the number of possible spurious optical counterparts (i.e. stars), we restricted the search area to the high Galactic latitudes (|b|≥20°). This requirement reduced the area

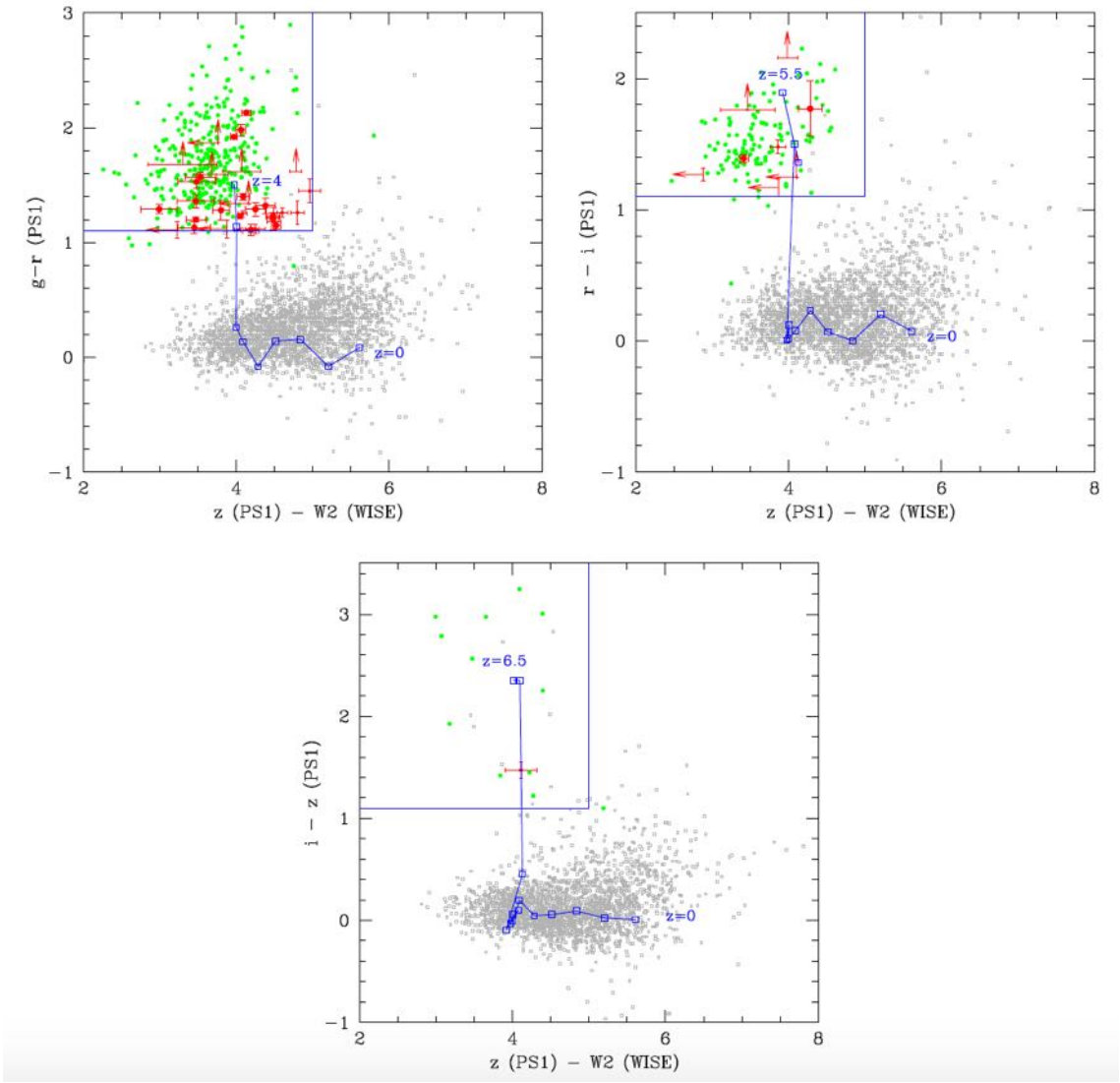

Figure 3.3: Diagnostic diagrams used to select z≥4 candidates from CLASS. We plot the three different PS1 colors ($g-r$, $r-i$, and $i-z$) versus mid-IR colors (z−W2). Red points are the CLASS objects that fulfill the selection criteria. Grey points show all the CLASS sources with a star-like PS1 counterpart and detected in WISE. Green points are 4<z<4.5, 4.6<z<5.5, and 5.6<z<6.5 high-z AGNs from the literature (including RQ AGNs). For reference, we also plot the paths (blue lines) of the AGN template from Polletta et al. (2007) for redshifts ranging from 0 up to the maximum values indicated in each panel by steps of 0.5. Finally, the blue boxes indicate the regions used to select the candidates. Figure taken from C19.

covered by the CLASS sample to 13120 deg^2 with respect to the total CLASS area (16300 deg^2).

After this selection criteria, we visually inspected the high-z candidates and removed all the problematic cases (i.e. sources close to bright stars and/or with photometric problems). We remained with a list of 37 candidates (see Table 3.1). 25 of these already have either a spectroscopic redshift from the literature or an available optical spectrum in the SDSS catalogue (see Ref. in Table 3.1). However 10 out of 25 have a z<4 (typically with z between 3 and 4), therefore we discarded them from the sample. For the remaining 12 candidates without a spectroscopic identification in the literature and without an optical spectra in the SDSS database we performed a spectroscopic follow-up to assess their redshift.

Name	class	z	Coordinates (J2000)	Mag (AB)	Dropout	Drop value (mag)	$z-W2$ (mag)	Ref.
(1)	(2)	(3)	(4)	(5)	(6)	(7)	(8)	(9)
GB6J001115+144608	QSO	4.96	00:11:15.24 +14:46:01.8	18.28	r	1.39	3.41	(1)∗
GB6J001307+205335	QSO	3.53	00:13:11.10 +20:53:42.7	17.79	g	1.11	4.02	LBT06/18
GB6J002121+155127	QSO	3.70	00:21:20.06 +15:51:25.8	19.59	g	1.23	4.48	(1)
GB6J003126+150729	QSO	4.29	00:31:26.80 +15:07:39.5	20.23	g	1.36	3.47	(1)∗
GB6J004348+342617	QSO	0.97	00:43:48.85 +34:26:26.1	19.06	g	1.32	4.38	(2)
GB6J010135+153845	QSO	1.50	01:01:36.09 +15:38:38.2	20.33	i	1.47	4.11	LBT11/17
GB6J012126+034646	QSO	4.13	01:21:26.15 +03:47:06.7	18.77	g	1.25	4.08	LBT11/17
GB6J012202+030951	QSO	4.00	01:22:01.91 +03:10:02.4	20.86	g	1.12	<3.88	(3)
GB6J012921+310303	QSO	3.56	01:29:21.85 +31:02:58.5	19.26	g	1.20	3.47	(1)
GB6J024612+182334	QSO	3.59	02:46:11.82 +18:23:30.1	19.22	g	1.15	4.52	(3)
GB6J040738+001713	QSO	3.70	04:07:36.61 +00:17:26.3	19.60	g	1.26	4.60	TNG03/18
GB6J042423+144230	QSO	3.55	04:24:23.49 +14:42:16.7	20.14	g	1.26	4.80	TNG03/18
GB6J061110+721814	-	-	06:11:09.17 +72:18:15.6	19.78	g	1.45	4.96	LBT02/18
GB6J064057+671228	-	-	06:40:58.19 +67:12:25.1	20.94	r	>1.76	3.46	TNG03/18
GB6J083548+182519	QSO	4.41	08:35:49.43 +18:25:20.1	20.93	g	>1.87	<3.76	(1)∗
GB6J083945+511206	QSO	4.40	08:39:46.22 +51:12:02.8	19.28	g	1.98	4.06	(1, 4)∗
GB6J090631+693027	QSO	5.47	09:06:30.75 +69:30:30.8	20.54	r	>2.16	3.98	(5)
GB6J091825+063722	QSO	4.22	09:18:24.38 +06:36:53.4	19.68	g	1.40	4.09	(1, 4)∗
GB6J100724+580201	QSO	3.77	10:07:24.88 +58:02:03.5	17.59	g	1.23	4.05	(1)
GB6J102623+254255	QSO	5.28	10:26:23.62 +25:42:59.4	20.06	r	1.77	4.28	(6)∗
GB6J132512+112338	QSO	4.42	13:25:12.49 +11:23:29.8	19.45	g	2.13	4.13	(1, 4)∗
GB6J134811+193520	QSO	4.40	13:48:11.26 +19:35:23.5	20.64	g	1.53	3.48	(1)∗
GB6J141212+062408	QSO	4.47	14:12:09.97 +06:24:06.8	20.19	g	1.29	2.99	(1, 4)∗
GB6J143023+420450	QSO	4.72	14:30:23.74 +42:04:36.5	19.79	r	1.27	<2.88	(7)∗
GB6J143533+543605	QSO	3.81	14:35:33.78 +54:35:59.3	20.20	g	1.13	3.45	(1)
GB6J151002+570256	QSO	4.31	15:10:02.93 +57:02:43.4	20.52	g	1.21	4.48	(8, 1)∗
GB6J154929+170853	BL	1.2:	15:49:29.27 +17:08:28.0	18.77	g	>4.03	3.80	(1)
GB6J155930+030444	QSO	3.89	15:59:30.98 +03:04:48.3	20.12	g	1.29	4.25	(1)
GB6J161216+470311	QSO	4.36	16:12:16.76 +47:02:53.6	20.53	g	1.28	3.80	(1)∗
GB6J162956+095959	QSO	5.00	16:29:57.28 +10:00:23.5	20.77	r	1.17	<3.87	LBT05/18
GB6J164327+410359	QSO	3.86	16:43:26.24 +41:03:43.5	20.05	g	1.11	4.19	(1)
GB6J164856+460341	QSO	5.36	16:48:54.53 +46:03:27.4	20.31	r	1.48	3.86	LBT01/18
GB6J171103+383016	QSO	4.00	17:11:05.54 +38:30:04.3	20.53	g	1.12	4.25	LBT01/18
GB6J205332+010307	QSO	3.59	20:53:31.73 +01:03:42.2	19.72	g	1.18	4.49	TNG05/18
GB6J223927+225959	QSO	2.93	22:39:27.69 +23:00:18.1	18.17	g	1.92	3.97	(1)
GB6J231449+020146	QSO	4.11	23:14:48.71 +02:01:51.1	19.64	g	1.57	3.53	(9)
GB6J235758+140205	QSO	4.35	23:57:58.56 +14:02:01.9	20.40	g	1.11	<3.22	LBT07/18

Table 3.1: The list of dropout candidates selected from CLASS. Col(1): name; Col(2): classification (QSO = broad emission line AGN; BL = BL Lac object); Col(3): redshift (':'=tentative redshift); Col(4): radio (8.4 GHz, VLA-A array) position (J2000.0); Col(5): PS1 magnitude in the reddest filter of the dropout (i.e. r filter for g-dropout sources, i filter for r-dropout sources, z filter for i-dropout sources; Col (6): type of dropout; Col (7): dropout value; Col (8): $z-W2$; Col (9): reference for the optical spectrum or for the spectroscopic identification: 1 = SDSS DR 12; 2 = Ackermann et al. (2011); 3 = Sowards-Emmerd et al. (2003); 4 = Sbarrato et al. (2013); 5 = Romani et al. (2004); 6 = Sbarrato et al. (2012b); (7) = Hook & McMahon (1998); 8 = Hook et al. (1995); 9 = Hook et al. (2002). Please note that some of the objects with an SDSS spectrum have been already published in the literature. The spectra of the candidates observed during our spectroscopic follow-up are reported in Appendix B. Instead with ∗ we mark the objects with a spectrum also published in C19 paper. Table adapted from C19.

3.2 Spectroscopic observations

During 2017-2018, we have carried out dedicated spectroscopic observations of the high-z blazar candidates of CLASS without an available redshift from the literature (12 objects), using the Large Binocular Telescope (LBT) and the Telescopio Nazionale Galileo (TNG) both shown in Fig. 3.4. We used LBT coupled to the Multi-Object Double Spectrograph (MODS; Pogge et al. 2010).

Figure 3.4: *Left*: LBT, located at Mount Graham, Arizona (USA). It has a binocular design with two identical 8.4 m telescopes. Image taken from https://www.oas.inaf.it. *Right*: TNG is a 3.58 m telescope located in the island of San Miguel de La Palma (Spain). Image taken from http://tmtlapalma.org/

The observations were taken during the period 2017 November - 2018 July with the red grating (G670L, 5000-10000Å) and using slit widths of 1″-1.2″. Data reduction was performed at the Italian LBT Spectroscopic Reduction Center through scripts optimized for LBT data. Each spectral image was independently bias subtracted and flat-field corrected. Sky subtraction was done on 2D extracted, wavelength calibrated spectra with a fit. Wavelength calibration was obtained from spectra of arc lamps (rms=0.08Å on MODS1 and 0.1Å on MODS2), while flux calibration was achieved from observations of spectro-photometric standard stars. With LBT we observed 8 out of 12 candidates (see Col 9 of Table 3.1).
In 2018 March-May period we carried out the TNG observations of the remaining 4 candidates using DOLORES (Device Optimized for the LOw RESolution) installed at the Nasmyth B focus of the telescope. We used the LR-R/LR-B grisms and a long-slit with a width between 1″ and 1.5″, depending to the actual seeing conditions, oriented along the parallactic angle. For the data reduction, we used the IRAF[1] long-slit package (Tody 1993). The spectra have been wavelength calibrated using Ar, Ne+Hg, Kr reference spectra. The flux calibration was obtained by observing spectrophotometric standard stars.
In total, we observed all the 12 sources without a spectroscopic redshift in the literature, but only in 10 cases the data were good enough to obtain a firm classification and redshift, while for 2 sources the S/N was too low and they should be considered still unidentified[2]. Therefore these two objects were not taken into account for building the final high-z CLASS sample. With these observations we found two new $z \geq 5$ AGNs (GB6J162956+095959 at z=5.0 and GB6J164856+460341 at z=5.36), 3 AGNs with a redshift above 4, 4 objects with $3 \leq z \leq 4$ and 1 low-z source. The optical spectra of these 10 objects are reported in Appendix B.
We have not found high-redshift featureless blazars (i.e. BL Lac objects) even though our selec-

[1]IRAF (Image Reduction and Analysis Facility) is a software developed at National Optical Astronomy Observatories (NOAO) to analyze optical and infrared astronomical images, using a series of program called tasks.

[2]We do not provide a complete data reduction on these spectra, since from a quick look to the data confirms the high level of noise for both of them.

tion is potentially sensitive also to these objects. This lack of high-z BL Lac is likely due to their peculiar cosmological evolution (very weak or even negative, i.e. their space density decreases with redshift; e.g., Ajello et al. 2014; Paliya et al. 2020) that makes their detection at high-z very unlikely.
In total we obtained 20 FSRQs with z≥4 (5 from our spectroscopic follow-up and 15 from the literature or from the SDSS database) among the 37 candidates selected with the dropout method. Six sources are in common with the sample of high-z blazar candidates selected by Sbarrato et al. (2013).

3.3 Completeness of the sample

To check the completeness of our sample we have searched through the literature and in the SDSS spectroscopic database for high-z AGNs among all the ∼11000 CLASS sources, independently from their photometric colors, magnitudes, or sky positions. We found six additional z>4 AGNs (see Table 3.2). Two of them were not selected because they have a low Galactic latitude (|b|<20°). The other three objects have a magnitude fainter than the adopted limit (mag≤21). Only one source (GB6J153533+025419) was not recovered in our selection because of a low dropout value ($g-r = 0.79\pm0.07$) and, therefore, it can be considered as missed from our selection. However we noted that in the SDSS, this source has a higher dropout value ($g-r = 1.18\pm0.08$). This suggests that the low dropout value observed in PS1 can be related to some photometric problem in Pan-STARRS[3]. With this six additional sources, our CLASS sample consists of 26 high-z objects. The fact that we have found only one source outside our selection confirms that our method is highly complete for z≥4. While most (95%) of the z>4 objects are recovered, for redshifts below 4 this fraction decreases significantly, being around 25% for 3.6<z<4 and below 5% for 3<z<3.6. After the publication of the C19 paper, we discovered that the object GB6J160608+312504 has an incorrect spectroscopic redshift (z=4.56, Healey et al. 2007)) reported in the literature: it is a low-z AGN (z=0.88, private communication from R. W. Romani). This source has been therefore considered in the radio analysis of the sample and in the calculation of the space density of CLASS blazars reported in Sect. 3.5, but it was removed for the X–ray analysis (Sect. 3.6). We removed this source for building Table 3.3, in which the multi wavelength properties of the CLASS sample (25 objects in total) are reported. Finally we considered as *complete sample*, the one defined at high Galactic latitude (|b|>20°) and at a magnitude limit of 21 (in r, i, or z filter depending on the redshift of the source). The objects of the complete sample are marked with a letter c in Table 3.3.
A detailed discussion on the problems that can affect the completeness of the CLASS sample are reported in C19 and are mainly related to the radio variability of blazars (estimated to be ∼14%, C19)[4].

3.4 Contamination from GPS sources

By definition, CLASS contains sources with a flat radio spectrum between 1.4 and 5 GHz (observed frame). However sources that do not have a genuinely flat spectrum across the entire radio band could be also included. An example are the so-called Giga-Hertz Peaked Spectrum (GPS) sources (O'Dea 1998), AGNs that appear compact at arcsecond resolution and with an apparent flat

[3]In this particular case, the problem is visible on the r band image of this source.

[4]We expect that variability in the optical band has a lower impact on the completeness of the CLASS sample compared to that at radio frequencies. Indeed, as already explained in Fig. 1.7 in Sect. 1.2, FSRQs typically have most of the UV/optical emission produced by the accretion disk.

Name	z	Coordinates (J2000.0)	Mag (mag)	Dropout	Drop value (mag)	$z-W2$ (mag)	Ref.	b (deg)
(1)	(2)	(3)	(4)	(5)	(6)	(7)	(8)	(9)
GB6J025758+433837	4.07	02:57:59.08 +43:38:37.7	19.86	g	1.04	3.25	(1)	−13.5101
GB6J102107+220904	4.26	10:21:07.58 +22:09:21.6	21.46	g	>1.34	<4.16	(2)∗	55.6110
GB6J153533+025419	4.39	15:35:33.88 +02:54:23.4	20.72	g	0.79	3.33	(2)∗	43.9170
GB6J160608+312504	4.56	16:06:08.52 +31:24:46.5	21.32	r	>1.38	5.57	(3)	47.6632
GB6J171521+214547	4.01	17:15:21.25 +21:45:31.7	21.51	g	>1.29	-	(4)	30.3650
GB6J195135+013442	4.11	19:51:36.02 +01:34:42.7	20.56	g	1.16	3.65	(3)	−12.6097

Table 3.2: This table includes other z>4 AGNs present in the CLASS survey that have not been selected mostly because they have a low Galactic latitude or because they have magnitude below the adopted limit. Only one object (GB6J153533+025419) is missed by the selection method because of a low dropout value. Table caption is the same of Table 3.1 except for the Col (9) that contains the Galactic latitude. In this case reference (Col 8) for the optical spectrum are: 1 = Amirkhanyan & Mikhailov (2006); 2 = SDSS DR12; 3 = Healey et al. (2007); 4 = Hook & McMahon (1998).

radio spectrum simply because we are observing its self-absorbed part. These are intrinsically small radio sources, possibly because of their young age. Interestingly, RL AGNs at high redshift often show these characteristics (e.g., Frey et al. 2003, 2005; Coppejans et al. 2017). At mas scales their radio emission is usually resolved, often showing a Compact-Symmetric Objects (CSO) morphology, i.e. a small-scale version of a radio galaxy with lobes, hot-spots, jets, and relatively weak cores. Two examples are J2102+6015, at z = 4.57 (Frey et al. 2018) and J1427+3312, at z = 6.12 (Frey et al. 2008), one of the most distant RL AGN ever discovered. The CSO morphology is an indication that the relativistic jet is mis-aligned with respect to the observer. However, this is not always true: the source Q0906+6930 at z = 5.47 (Romani et al. 2004), which is also part of the CLASS complete sample (GB6J090631+693027) shows a clearly peaked radio spectrum (Coppejans et al. 2017) with a turnover frequency of 6.4 GHz (observed frame). At the same time, VLBI data found evidence of Doppler boosting (Zhang et al. 2017, Frey et al. 2018, An. et al. 2020). These results suggest that Q0906+6930 is a GPS source likely oriented towards the observer, i.e. a blazar. Therefore, the simple observation of a peaked radio spectrum does not firmly exclude the presence of beaming.

In order to detect possible hints of spectral curvature and distinguish between truly flat spectrum sources and GPS it is important to extend the analysis of the radio spectrum at higher and lower frequencies. If a source is a GPS we expect that the two-point spectral index computed at very high frequencies would appear steeper than the one computed at lower frequencies (convex spectrum).

To this purpose we have used the TGSS first data release (ADR1) at 150 MHz and the high-frequency data at 8.4 GHz that are available for the CLASS objects, in order to cover the widest range of frequency. Out of the 26 high-z sources in the CLASS sample, 17 are present in the TGSS catalog. For the remaining objects not included in the TGSS source catalog we found a detection (at least 2σ) in seven out of the nine sources. For the two undetected objects, we considered an upper limit of the 150 MHz flux density of 15 mJy (= 3rms). From this spectral analysis we found that 18 CLASS sources have a radio spectrum that is well represented by a flat power law between 150 MHz and 8.4 GHz, without significant curvatures. This fact strongly supports the idea that these are beaming dominated objects, i.e. blazars. In eight cases, instead, the $\alpha_{0.15}^{1.4}$ is significantly flatter than $\alpha_{1.4}^{8.4}$, typical of GPS-like sources. These objects could be mis-aligned AGNs, although we cannot completely exclude their blazar nature, as in the case of Q0906+6930. In Table 3.3, we reported the radio spectral type ("Flat"/"Peaked") as derived from this analysis.

For seven CLASS sources we also carried out a proper spectral analysis thanks to the availability

of several simultaneous data points taken from the GLEAM survey. Overall, the spectral analysis of the few CLASS objects with data from GLEAM supports the results obtained with TGSS, based on few, non-simultaneous, data points, giving us confidence on the reliability of our radio spectral classification.

3.5 The space density of the CLASS high-z blazars

Thanks to its completeness, the CLASS sample can be used to derive, for the first time, the space density, i.e. the number of objects with a given luminosity as a function of redshift, of blazars at z>4, with a radio power at 5 GHz between 10^{27} and 1.3×10^{28} W Hz^{-1} (the observed range of luminosities of CLASS sources). The complete sample contains 21 objects with redshift between 4 and 5.5, 14 of which have been classified as *flat spectrum sources*, i.e. blazars. Since we cannot exclude that some of the remaining seven objects, with a peaked radio spectrum, are blazars, we considered the total complete sample as an upper limit on the number of blazars.
In order to compute the space density of CLASS blazars, we used the following method. For each object with redshift between z_1 and z_2 we computed

$$V_{obs} = \frac{A}{4\pi} V_{max} \tag{3.1}$$

the volume of the Universe within which it could have been discovered. A is the sky area (in steradians) covered by the survey and V_{max} is the co-moving volume of Universe between z_1 and the minimum value among z_2, z^R_{max} and z^O_{max}. The quantities z^R_{max} and z^0_{max} are, respectively, the redshift at which the observed flux from the source would be equal to the radio (R) or optical (O) flux limit of the survey. The reason for taking the minimum of these three values of redshift is that the V_{max} must be computed on the most stringent among the radio/optical constraints. The space density then can be computed as:

$$\rho_{bl} = \sum \frac{1}{V_{obs}} \tag{3.2}$$

with an error of:

$$\rho_{bl\_err} = \frac{err}{N} \rho_{bl} \tag{3.3}$$

where N is the observed number of blazars in the given redshift bin and *err* is the Poissonian uncertainty on N. Using this method, we found a space density of blazars (14 objects) at 4<z<5.5 and with radio powers at 5 GHz between 10^{27} and 1.3×10^{28} W Hz^{-1} of $\rho_{bl} = 0.13^{+0.05}_{-0.03}$ Gpc^{-3}. Considering all the 21 objects of the complete sample the space density become $\rho_{all} = 0.17^{+0.05}_{-0.04}$ Gpc^{-3}.
On this estimates, there are two potential sources of incompleteness, one related to the lack of spectroscopic confirmation of two high-z candidates and one related to the radio variability. Taking into account these two problems, i.e. considering the two unidentified objects as true high-z sources and considering the possible fraction of missing objects due to radio variability (see Sect. 3.3), we obtained marginally higher space densities ($\rho_{bl} = 0.15$ Gpc^{-3} and $\rho_{all} = 0.19$ Gpc^{-3}).

3.5.1 Comparison with theoretical predictions

We compared the space densities computed with CLASS objects with the predictions of Mao et al. (2017, hereafter M17), who used a a radio selected sample of FSRQ at z<3 to predict the space density of blazars at all redshifts.

We used the analytical luminosity function (LF) presented in M17 to derive the expected space density as a function of redshift of the FSRQs in the same luminosity range of the high-z CLASS objects ($\log(L_{1.4\ GHz})$ = 43.04 - 44.43 erg s^{-1}). The luminosity function $\Phi(L,z)$ is defined as the number of object (N) per luminosity interval (dL) and per unit of comoving volume (dV) at redshift z. It specifies in which way astronomical sources are distributed with respect to their luminosity at a given redshift. The change of $\Phi(L,z)$ with redshift can be described by a *pure luminosity evolution*, $\Phi(L,z) = \Phi(L/L_*(z),0)$, a *pure density evolution*, $\Phi(L,z) = \mathrm{N(z)}\Phi(L,0)$, or a combined *density and luminosity evolution*, $\Phi(L,z) = \mathrm{N(z)}\Phi(L/L_*(z),0)$, where both luminosity and space density decreasing with time. A luminosity-dependent density evolution (LDDE) is often considered for AGNs (e.g., Ueda et al. 2003; Ajello et al. 2012).
The radio LF of M17 is described by a double power law, with a LDDE evolution:

$$\Phi(L,z) = \frac{A}{(ln10)L}[(\frac{L}{L_*})^{\gamma_1} + (\frac{L}{L_*})^{\gamma_2}]^{-1} \times e(z,L) \tag{3.4}$$

where A = 7.35 Gpc^{-3} erg^{-1} s, γ_1 = 0.67, γ_2 = 1.69 and L_*= 6×10^{43} erg s^{-1}. The dependence with redshift is included in the term

$$e(z,L) = [(\frac{1+z}{1+z_c(L)})^{-p_1} + (\frac{1+z}{1+z_c(L)})^{-p_2}]^{-1} \tag{3.5}$$

where p_1 = 4.54 and p_2 = -7.81. The maximum of the $e(z,L)$ is set at z_c=$z_{c_*}(L/L_{factor})^{0.08}$, with z_{c_*} = 1.94 and L_{factor} = 10^{43} erg s^{-1}.
Integrating the LF of M17 over a range of luminosity for a given redshift the space density is obtained. The result of the comparison between M17 space density and the CLASS values is reported in Fig. 3.5. We also added the upper limit at 5.4≤z≤6 based on the fact that none of the CLASS candidates in this range of redshift turned out to be true FSRQ. Figure 3.5 shows that the CLASS data points, both from the complete sample (21 objects) and from the truly flat spectrum sources (14 objects), follow the predictions of M17 that are based on sources at lower redshift. According to this Figure, the peak of the space density of FSRQs, in this luminosity bin, is at z∼2, a value similar to that found for the total AGN population (e.g., Hopkins et al. 2007). This is significantly different from the evolution estimated, for example, by Ajello et al. (2009) using an X–ray selected sample of blazars at z≤3 derived from the *Swift*–BAT survey (see also Sect. 2.1). The author found a peak at much higher redshifts (z∼4). To further evaluate this difference in the peak position, we computed the value of the space density of CLASS objects at z∼3 and in the same bin of luminosity, finding a value of 1.4 Gpc^{-3}. This is a lower limit since the identification level of CLASS at this redshift is relatively low (15%). However the position of this limit in Fig. 3.5 excludes the hypothesis of a peak of the space density at z∼4.
The observed differences in the space density of X–ray and radio selected blazars could be ascribed to the interaction of jet electrons with the photons of the CMB, as suggested by Ighina et al. (2019).

3.6 X–ray properties

As described in previous sections, the analysis of the radio spectra of the CLASS objects revealed both truly flat spectrum sources and peaked spectrum objects. An X–ray analysis can provide a more accurate tool to discriminate blazars from non-blazars. Indeed blazars are characterized by a strong, with respect to the optical, and flat X–ray emission which, combined with the other pieces of information, can then be used for a more reliable classification of the CLASS sources. The X–ray analysis of the high-z CLASS sample was performed by Ighina et al. (2019, hereafter

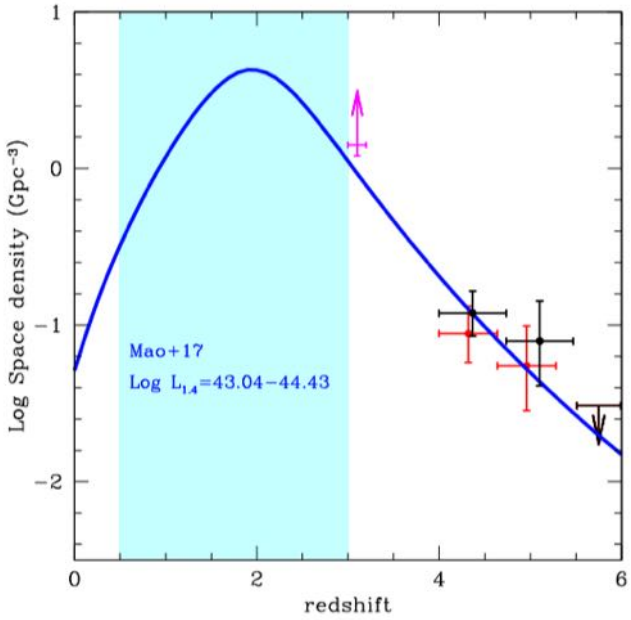

Figure 3.5: Space density versus redshift of the 21 CLASS blazars in the complete sample (black points) and of the 14 objects with a flat radio spectrum (red points). The blue solid line represents the expected densities computed by integrating the radio LF of M17 in the same range of radio luminosities (at 1.4 GHz) observed in the CLASS sample. The shaded area indicates the range of redshift actually sampled by the FSRQs studied by M17 in the indicated range of radio luminosity. The magenta arrow represents the lower limit on the space density derived from CLASS at z∼3. Figure taken from C19.

Ig19). Here we summarize the main steps and results.
Out of the 25 high-z sources in the CLASS sample (Table 3.3), 16 have X–ray data available in the public archives of XMM–Newton, Chandra, and *Swift*–XRT telescopes. In order to complete the X–ray coverage of the sample, we conducted a dedicated *Swift*–XRT (Gehrels et al. 2004) follow-up of the remaining nine objects (P.I. Caccianiga A.). Only one of them (GB6J171103+383016) has not been observed yet, although there is an approved *Swift*–XRT observation (P.I. Belladitta S.). We then carried out the X–ray analysis of all the sources, both the newly observed and the ones already discussed in the literature, in order to have a systematic and up-to-date analysis of the entire sample. We performed the X–ray spectral analysis for each observation independently using the package XSPEC (v.12.9.0i) and by fitting the observed spectra with a simple power law absorbed by the Galactic column density along the line of sight. For about 40% of the sample, we analyzed multiple observations and, even though blazars are known to be highly variable in the X–rays, we decided to combine their best-fitting values with a weighted average, because there are no evidences of strong variability in our data (except for one case). The mean photon index of the whole sample is $\Gamma_X = 1.41^{+0.30}_{-0.28}$. This is significantly flatter than the average value found, for example, in Shemmer et al. (2005), for a sample of RQ AGNs at z>4 ($\Gamma_X = 1.97$), supporting the idea that the majority of the objects selected in C19 are blazars.
Then to identify the bona fide blazars we classified the sources on the basis of the flatness of the X–ray emission and its intensity compared to the optical one.
The α_{ox} parameter (Tananbaum et al. 1979) is commonly used in the literature in order to quantify the relative strength of the X–ray emission with respect to the optical/UV component. This parameter is the two-point spectral index of a fictitious power law connecting 2500Å and

2 keV in the source rest frame. Blazars and misaligned RL AGNs can be distinguished on the basis of the $\alpha_{\rm ox}$ value: sources with an X–ray emission strongly dominated by the relativistic jet have a *flat* $\alpha_{\rm ox}$ index ($\leq$1.50; Donato et al. 2001), while misaligned objects have a steeper (i.e. higher) $\alpha_{\rm ox}$ ($\sim$1.69; Shemmer et al. 2006). We estimated the value of the α_{ox} for the CLASS sample (see Table 3.3) using the relation found in Steffen et al. (2006). The luminosity at 2500Å for the CLASS sources has been computed from the i-band magnitude (PS1) assuming an optical spectral index $\alpha_\nu = 0.44$ (Vanden Berk et al. 2001).
However, for objects with z>4 the 2 keV energy is observed at $\sim$0.3-0.4 keV, where X–ray telescopes are less sensitive, making the estimate of the $\alpha_{\rm ox}$ less accurate and highly dependent on the exact value of the spectral slope. For this reason we decided to consider the X–ray flux at higher energies, where the number of detected photons is larger and the normalization is less affected by a different photon index. To this purpose we introduced the parameter $\tilde{\alpha_{\rm ox}}$ defined at 10 keV rest frame:

$$\tilde{\alpha_{\rm ox}} = -\frac{log(L_{10\ keV}/L_{2500\text{Å}})}{log(\nu_{10\ keV}/\nu_{2500\text{Å}})} = -0.3026\ log(\frac{L_{10\ keV}}{L_{2500\text{Å}}}) \tag{3.6}$$

The second parameter we used for the blazar classification is Γ_X. Indeed a blazar has a flat (<1.8) photon index and a non-blazar source has a relatively steep ($\sim$1.9) Γ_X (e.g., Giommi et al. 2019). In order to calibrate the classification of the CLASS sample, on the basis of Γ_X and $\tilde{\alpha_{\rm ox}}$, we used two reference samples taken from the literature. As first sample, we selected all the FSRQs present in the 5th BZCAT edition (Massaro et al. 2015) with a radio flux density (at 0.843 or 1.4 GHz) above 1.5 Jy. This "radio-cut" has many advantages: first, at such radio fluxes the census of blazars is reasonably complete and the sources can be considered as a well-defined radio flux-limited sample. Second, all these objects have been observed and detected in the X–rays, which excludes any possible bias against particularly X–ray weak sources. For these reasons, this sample should be reasonably representative of the blazar population. Finally, with this flux limit we select objects in a similar range of radio power as the CLASS sources. To have an estimate of X–ray slope and flux of the BZCAT sources, we analyzed all the *Swift*–XRT observations, using the same model adopted for the CLASS objects, that are available for the 47 (out of 105) blazars in this sample that also have an optical counterpart in the PS1 catalog. On the other hand, we considered also the sample of RQ AGNs at z>4 of Shemmer et al. (2005) in order to have a term of comparison also for the coronal X–ray emission. The photon index (Γ_X) as a function of the $\tilde{\alpha_{\rm ox}}$ for these objects is reported in Fig. 3.6. In this figure, we also reported the few confirmed blazars at z>4 with accurate determination of the X–ray parameters (taken from the literature) as red points, together with the the best-fitting values of the faintest high-z (z>5) blazar known so far, i.e. DESJ014132.4-542749.9 (Belladitta et al. 2019, red star, see chapter 4). The difference between the two populations is clear: RQ AGNs occupy only the top right region of the plot, meaning that they have a weak and steep X–ray emission. On the other hand, blazars have a stronger and flat emission and they are located in the bottom left region. Based on this distinction, we set two thresholds to differentiate blazars and non-blazars: $\Gamma_X = 1.8$ and $\tilde{\alpha_{\rm ox}} = 1.355$. These limits include all the confirmed high-z blazars.
We then applied these criteria to the 14 CLASS objects with a reasonable estimate of the photon index ($\rm err_{\Gamma_X} < 0.4$). Among these 14 sources, there is only one object whose Γ_X and $\tilde{\alpha_{\rm ox}}$ are not consistent with a blazar nature (GB6J012126+034646), meaning that its X–ray spectrum is too steep and too weak to be produced by an oriented jet. On the other hand, as expected, the majority of the sources (13) are strong and flat enough to suggest that they are bona fide blazars. Moreover, this method consistently classifies the already confirmed blazars at high redshift, including GB6J090631+693027 in spite having a peaked radio spectrum (see Sect. 3.4).
For the remaining 10 CLASS sources (whose with $\rm err_{\Gamma_X} > 0.4$), the X–ray analysis did not provide

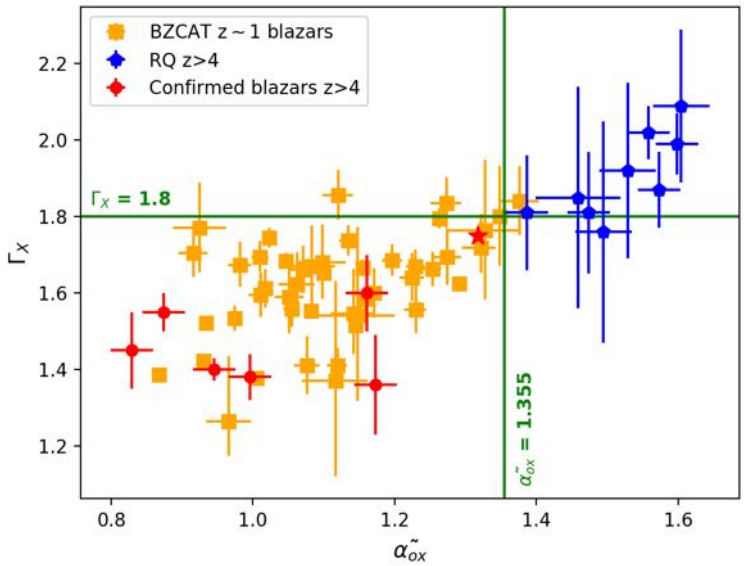

Figure 3.6: Photon index (Γ_X) as a function of the $\tilde{\alpha_{ox}}$ index for the comparison samples. With orange squares we report the BZCAT blazars observed by *Swift*–XRT, with blue pentagons the RQ AGNs at high-z and with red points the few confirmed blazars at high-z for which accurate X–ray observations are available in the literature. The red star represents DESJ014132.4-542749.9 (Belladitta et al. 2019, see chapter 4) the most X–ray weak blazar at high-z. The plot is divided in four areas by a vertical line at $\tilde{\alpha_{ox}} = 1.355$ and a horizontal one at $\Gamma_X = 1.8$, which correspond to the thresholds assumed for the X–ray classification of CLASS sources.

an accurate value of Γ_X. Therefore, in these cases we only used the value of the $\tilde{\alpha_{ox}}$ for the classification. In the specific we considered as blazars the eight sources with an $\tilde{\alpha_{ox}}$ below the threshold of 1.355, while the candidates above the limit as non-blazars (two objects). The final results of this X–ray classification are reported in Table 3.3. In summary, this analysis revealed that 21 CLASS objects have an X–ray emission consistent with a blazar nature, while the remaining three sources do not seem to be powered by a relativistic jet oriented towards us. There is only one source (GB6J164856+460341) that, given the large uncertainty on the $\tilde{\alpha_{ox}}$ value and its proximity to the adopted threshold, we classified as "Blazar?". Also its classification as a flat radio object is uncertain.
This X–ray classification has a relatively good correspondence with the one based on the radio spectra reported in the previous sections. In particular, the majority (∼90 per cent) of the candidates classified as blazars ("flat") has been confirmed also by the X–ray analysis. On the other hand, as mentioned before, the five CLASS sources with a peaked radio spectrum, like the blazar GB6J090631+693027, are classified as blazars by the X–ray analysis.
In this thesis we used this criteria based on X–ray properties (i.e. on Γ_X and on $\tilde{\alpha_{ox}}$) to assess the blazar nature of the newly discovered blazars at z≥5 reported in the other following chapters.

3.7 Summary

In this chapter I described the selection of a complete sample of blazars at 4≤z≤5.5, starting from the cross-match between CLASS (in the radio) and Pan-STARRS PS1 (in the optical). The selection was performed with the *dropout* method (see Sect. 2.3), searching for $g-$, $r-$ and $i-$ dropout sources (i.e. objects with a large $g-r$, $r-i$ and $i-z$ colors respectively). Among the 37 selected candidates, 25 already had a spectroscopic confirmation in the literature, therefore,

the remaining 12 have been spectroscopically observed with TNG and LBT. Only two sources remained unidentified due to the low S/N of their spectra and, therefore they have been not considered for the construction of the sample. Finally, discarding objects with z<4, our sample consists of 25 sources (see Table 3.3), among which 21 are part of the *complete sample*, with a radio flux larger than 30 mJy ad mag<21.
The analysis of the optical spectra of the CLASS sources is in progress, together with the estimation of the mass of the SMBHs hosted by this blazar sample (Diana et al. in prep.)
Regarding the radio properties of the sample, 18 objects (14 of the complete sample) have a genuine flat spectrum on a wide range of frequencies (from 150 MHz to 8.4 GHz, observed frame). The other sources (7), instead, have a spectrum that can considered peaked, i.e. they could be classified as GPS sources. The peaked spectrum does not exclude the blazar nature of the sources, as the most distant object within the CLASS sample (GB6J0906+6930 at z=5.47) has a peaked radio spectrum, but it was already been classified as a blazar in the literature, also thanks to VLBI observations.
A European VLBI Network (EVN) analysis of high-z CLASS blazars is in progress (P.I. Caccianiga A.), to assess the nature of all these sources at mas scale.
24 out of 25 CLASS objects have an available X–ray observation. Therefore, an X–ray spectral classification can be performed on these sources. The adopted parameter of such a classification are: the Γ_X, i.e. the photon index, and the $\tilde{\alpha_{\rm ox}}$, which quantifies the strength of the X–ray emission with respect to the optical one. Based on the values of Γ_X and $\tilde{\alpha_{\rm ox}}$ of low-z and high-z confirmed blazars, the threshold between jet dominated and RQ AGNs has been set at $\Gamma_X = 1.8$ and $\tilde{\alpha_{\rm ox}} = 1.355$. With these two limits, 20 CLASS objects have been classified as blazars, instead only 3 have an X-ray emission that seems to be not powered by a relativistic jet. The X–ray classification of one source remains uncertain.
The radio and the X–ray classification of the CLASS high-z sources are in good agreement. Moreover the X–ray analysis classified as beamed objects the already known blazars from the literature, including GB6J0906+6930 in spite of its peaked radio spectrum.
Finally, thanks to its completeness, the CLASS sample has been used for estimating for the first time the space density of blazars at redshift between 4 and 5.5. The obtained values for the space density are: $\rho_{bl} = 0.13^{+0.05}_{-0.03}$ Gpc^{-3} and $\rho_{all} = 0.17^{+0.05}_{-0.04}$ Gpc^{-3}, for the 14 flat spectrum and the total 21 objects of the complete sample, respectively These results are in good agreement with the theoretical expectation of Mao et al. (2017) who predicted the space density of blazars at all redshifts using a sample of FSRQs at z<3. This consistency allowed us to infer that the FSRQs (and RL in general, since $N_{RL} \sim 2\Gamma^2 N_{bl}$, see chapter 2) has a peak in their evolution at z∼2, similar to the evolution of all the AGN population. This result is in contrast with that found for X–ray selected blazars samples (e.g., Ajello et al. 2009; Toda et al. 2020), which show a peak at higher redshift (z∼4). The possible explanations for this different evolution are under analysis (Ighina et al. in prep.).

Obj name	z	RA (hms)	DEC (dms)	$S_{1.4\ GHz}$ (mJy)	$\alpha_{0.15}^{1.4}$	$Radio_{class}$	Γ_X	flux [0.5-10] keV ($10^{-13} erg/s/cm^2$)	L[2-10] keV (10^{46} erg/s)	α_{ox}	$\tilde{\alpha_{ox}}$	log(XR)	$X\text{–}ray_{class}$
(1)	(2)	(3)	(4)	(5)	(6)	(7)	(8)	(9)	(10)	(11)	(12)	(13)	(14)
GB6J001115+144608[c]	4.96	00:11:15.23	+14:46:01.80	35.8	0.14	flat?	$1.762^{+0.05}_{-0.05}$	3.01±0.16	3.11	$1.28^{+0.01}_{-0.01}$	$1.170^{+0.003}_{-0.002}$	3.05	Blazar
GB6J003126+150729[c]	4.29	00:31:26.79	+15:07:39.52	41.9	−0.53	flat	$2.500^{+0.00}_{-0.59}$	0.278±0.18	0.15	$1.38^{+0.15}_{-0.03}$	$1.404^{+0.003}_{-0.022}$	2.26	non-Blazar
GB6J012126+034646[c]	4.13	01:21:26.13	+03:47:06.76	78.1	−0.88	peaked	$1.794^{+0.18}_{-0.17}$	0.648±0.0932	0.40	$1.57^{+0.03}_{-0.03}$	$1.409^{+0.018}_{-0.009}$	2.68	non-Blazar
GB6J012202+030951[c]	4.0	01:22:01.90	+03:10:02.41	98.4	−0.07	flat	$1.172^{+0.19}_{-0.19}$	14.1±2.11	4.28	$0.95^{+0.03}_{-0.04}$	$0.789^{+0.008}_{-0.013}$	3.05	Blazar
GB6J025758+433837	4.07	02:57:59.08	+43:38:37.71	148.1	−0.28	flat?	$1.425^{+0.36}_{-0.35}$	3.03±0.732	1.40	$1.27^{+0.10}_{-0.09}$	$1.093^{+0.011}_{-0.001}$	2.53	Blazar
GB6J083548+182519[c]	4.41	08:35:49.42	+18:25:20.09	53.2	0.21	flat	$1.337^{+0.26}_{-0.26}$	2.10±0.419	1.00	$1.22^{+0.06}_{-0.05}$	$1.031^{+0.019}_{-0.011}$	2.42	Blazar
GB6J083945+511206[c]	4.4	08:39:46.22	+51:12:02.88	43.1	−0.47	peaked	$1.519^{+0.12}_{-0.11}$	1.59±0.147	0.95	$1.44^{+0.02}_{-0.03}$	$1.247^{+0.005}_{-0.004}$	2.99	Blazar
GB6J090631+693027[c]	5.47	09:06:30.74	+69:30:30.8	92.8	< −0.82	peaked	$1.509^{+0.11}_{-0.11}$	1.30±0.121	1.38	$1.19^{+0.03}_{-0.02}$	$1.048^{+0.005}_{-0.003}$	2.73	Blazar
GB6J091825+063722[c]	4.22	09:18:24.38	+06:36:53.33	30.9	−0.17	flat	$1.260^{+0.35}_{-0.35}$	1.47±0.467	0.59	$1.52^{+0.07}_{-0.07}$	$1.257^{+0.022}_{-0.003}$	1.76	Blazar
GB6J102107+220904	4.26	10:21:07.57	+22:09:21.45	153.0	0.52	flat	$2.258^{+0.24}_{-1.64}$	0.793±0.435	1.00	$0.93^{+0.35}_{-0.01}$	$1.011^{+0.014}_{-0.007}$	2.10	Blazar
GB6J102623+254255[c]	5.25	10:26:23.62	+25:42:59.44	256.9	0.25	flat	$1.243^{+0.26}_{-0.29}$	1.35±0.295	0.67	$1.39^{+0.07}_{-0.06}$	$1.150^{+0.013}_{-0.002}$	1.40	Blazar
GB6J132512+112338[c]	4.42	13:25:12.49	+11:23:29.81	81.4	−0.59	peaked	$1.522^{+0.50}_{-0.48}$	0.646±0.293	0.39	$1.52^{+0.12}_{-0.10}$	$1.308^{+0.031}_{-0.010}$	2.41	Blazar
GB6J134811+193520[c]	4.4	13:48:11.25	+19:35:23.64	51.6	0.00	peaked	$1.825^{+0.55}_{-0.49}$	0.415±0.143	0.36	$1.34^{+0.13}_{-0.04}$	$1.232^{+0.086}_{-0.001}$	2.14	Blazar
GB6J141212+062408[c]	4.47	14:12:09.97	+06:24:06.88	47.2	0.43	flat	$1.620^{+0.50}_{-0.49}$	0.493±0.190	0.32	$1.48^{+0.07}_{-0.08}$	$1.295^{+0.043}_{-0.048}$	1.81	Blazar
GB6J143023+420450[c]	4.72	14:30:23.73	+42:04:36.51	210.6	−0.08	flat	$1.527^{+0.02}_{-0.02}$	18.0±0.335	12.89	$0.90^{+0.01}_{-0.01}$	$0.819^{+0.004}_{-0.004}$	3.10	Blazar
GB6J151002+570256[c]	4.31	15:10:02.92	+57:02:43.40	202.0	0.02	flat	$1.399^{+0.03}_{-0.03}$	5.24±0.151	2.56	$1.08^{+0.01}_{-0.01}$	$0.939^{+0.003}_{-0.003}$	2.40	Blazar
GB6J153533+025419[c]	4.39	15:35:33.88	+02:54:23.38	59.5	0.41	flat	$1.218^{+0.16}_{-0.16}$	6.40±0.905	2.75	$1.12^{+0.05}_{-0.04}$	$0.928^{+0.006}_{-0.005}$	2.68	Blazar
GB6J161216+470311[c]	4.36	16:12:16.75	+47:02:53.63	53.5	0.46	flat	$1.887^{+0.70}_{-0.66}$	0.152±0.0924	0.26	$1.51^{+0.18}_{-0.12}$	$1.387^{+0.035}_{-0.002}$	1.65	non-Blazar
GB6J162956+095959[c]	5.0	16:29:57.28	+10:00:23.49	52.8	0.49	flat	$1.689^{+0.62}_{-0.67}$	0.818±0.455	0.90	$1.20^{+0.19}_{-0.13}$	$1.094^{+0.036}_{-0.003}$	2.06	Blazar
GB6J164856+460341[c]	5.36	16;48:54.53	+46:03:27.3	33.7	−0.47	flat?	$1.088^{+1.69}_{-0.08}$	0.314±0.0917	0.15	$1.67^{+0.11}_{-0.31}$	$1.338^{+0.116}_{-0.002}$	2.19	Blazar?
GB6J171103+383016[c]	4.0	17:11:05.52	+38:30:04.30	45.3	−0.49	peaked?							
GB6J171521+214547	4.01	17:15:21.26	+21:45:31.65	446.4	0.35	flat	$1.140^{+0.30}_{-0.30}$	1.24±0.272	0.39	$1.26^{+0.04}_{-0.06}$	$1.026^{+0.017}_{-0.006}$	0.98	Blazar
GB6J195135+013442	4.11	19:51:36.02	+01:34:42.7	99.1	−0.33	flat	$1.103^{+0.48}_{-0.51}$	2.98±1.12	0.92	$1.31^{+0.05}_{-0.13}$	$1.045^{+0.009}_{-0.006}$	2.55	Blazar
GB6J231449+020146[c]	4.11	23:14:48.71	+02:01:51.08	124.8	−0.05	peaked?	$1.431^{+0.40}_{-0.40}$	0.488±0.223	0.35	$1.47^{+0.10}_{-0.09}$	$1.251^{+0.018}_{-0.006}$	1.83	Blazar
GB6J235758+140205[c]	4.35	23:57:58.55	+14:02:01.83	111.1	0.18	flat	$1.499^{+0.18}_{-0.18}$	3.45±0.530	1.98	$1.16^{+0.05}_{-0.04}$	$1.022^{+0.008}_{-0.003}$	2.43	Blazar

Table 3.3: The CLASS sample of high-z blazars. Col(1): Object name as it is found in the GB6 catalog. Objects marked with *c* are part of the complete sample; Col(2): redshift; Col(3) and Col(4): optical PS1 coordinates; Col(5): flux density at 1.4 GHz taken from NVSS; Col(6): radio spectral index between 150 MHz and 1.4 GHz (in the convention $S_\nu \propto \nu^{-\alpha}$); Col(7): radio classification based on the spectral index; Col(8): photon index; Col(9): X–ray flux in [0.5-10] keV band; Col(10): X–ray luminosity at [2-10] keV; Col(11) and Col(12): α_{ox} between 2500Å and 2 keV and $\tilde{\alpha_{ox}}$ between 2500Å and 10 keV; Col (13): Log_{10} of the X–ray to radio ratio between the X–ray luminosity at [2-10] keV and the radio luminosity at 1.4 GHz (νL_ν); Col(14): X–ray classification. Values taken form C19 and Ig19.

Chapter 4

Searching for 4.5<z<5.5 blazars in SUMSS+DES surveys

This chapter is based on the following paper:
*-**S. Belladitta,** A. Moretti, A. Caccianiga, G. Ghisellini, C. Cicone, T. Sbarrato, L. Ighina and M. Pedani, 2019, A&A, 629, A68*
My contribution to the work: candidates selection, spectroscopic observations in visitor mode at La Silla Observatory, NTT and X-Shooter data reduction, analysis of radio, optical and X–ray properties, virial black hole mass estimation and discussion of the results.

In chapter 3 the first radio flux-limited sample of blazars at high-z (between 4 and 5.5) useful for statistical studies has been presented. Due to the limited number of blazars discovered at z>5 (4 from the literature and 2 from the CLASS sample) we decided to extend the search for more sources at these redshifts, making use of all the radio/optical/IR surveys available.
First we searched for high-z blazar candidates in the southern hemisphere, thanks to the advent of the DES-DR1 (see Sect. 2.4.2). Starting from the combination of SUMSS (Sect. 2.4.1) and DES DR1, which common area covers 3500 deg^2 of the sky (see Fig. 4.1), we searched for blazar candidates at redshift between 4.5 and 5.5 using the *dropout* technique described in Sect. 2.3. For this selection we used a radio limit equal to that of the CLASS selection (i.e. 30 mJy). Powerful radio objects have higher chances to be blazars, as demonstrated in chapter 3. Since DES DR1 is deeper (i-band mag limit equal to 23.4, see Table 2.2.) than mag=21 used for CLASS selection, we decided in this case to extend the optical limit to mag=22.5. Indeed an object with mag=23.4 is not spectroscopically observable in a reasonable amount of time (few hours) with the available southern telescopes. With this magnitude limit DES DR1 allows the detection of objects 4 times less bright than those selected in chapter 3. Starting from the optical and radio properties of the CLASS sample and using the cosmological properties described in Mao et al. (2017), we estimated the number of blazars expected in the DES+SUMSS sky area taking into account the different optical limit. We expected to find about ten objects.
In the following I describe the steps adopted in this specific selection, that led to the discovery of DESJ014132.4-542749.9, a new blazar at z=5.

4.1 Candidates selection

As we were interested in z≥4.5 blazar candidates, we searched for sources with large $r-i$ values (i.e. *r-dropout* objects, see also Fig. 3.3). For the selection a list of 91301 sources from the DES

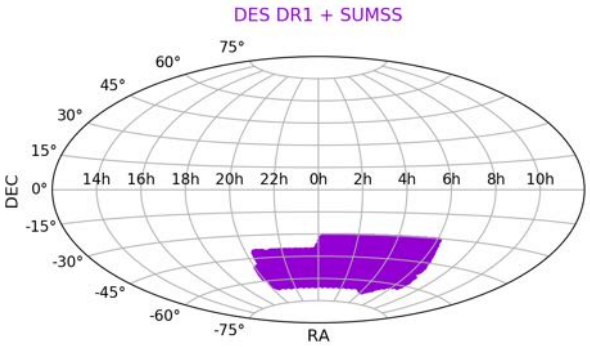

Figure 4.1: The common area between SUMSS and DES DR1, in which we searched for high-z blazars candidates, consists of 3500 deg^2.

DR1 database with the following characteristics has been considered:

- inclusion in the SUMSS catalog: δ < -31°
- observability with ESO/NTT telescope, i.e. mag$_{auto_i}$<22.5
- color selection: mag$_{auto_r}$ - mag$_{auto_i}$>1.5 and mag$_{auto_i}$ - mag$_{auto_z}$<0.5. The $r-i$ threshold adopted here is higher than those used in the CLASS selection ($r-i \geq$1.1, see Sect. 3.1), because, in this case we tailored the threshold on the basis of the dropout values actually observed in the CLASS blazars discovered at z>4.5
- no detection in g band: mag$_{auto_g}$>25.0 and mag$_{aper2_g}$ > 25.0
- reliable magnitudes: magerr$_{auto_z}$<0.2 and magerr$_{auto_i}$<0.2 and magerr$_{auto_y}$<0.3[1]

where mag$_{auto}$ is the magnitude estimate for an elliptical model based on the Kron radius and mag$_{aper2}$ is the magnitude estimate for circular apertures of 2″ (Abott et al. 2018). The complete SQL query performed on the DES DR1 database is reported in Appendix E.
Then we cross-correlated this list with the SUMSS catalog of very bright (S$_{0.8\ GHz}$ > 30 mJy) and relatively compact ($\frac{S_{INT}}{S_{Peak}}^2 < 1.5$) sources (71254 objects), which have higher chances to have their relativistic jet pointing toward us. We used a maximum separation equal to the SUMSS radio positional error (err = $\sqrt{(err_{RA}^2 + err_{DEC}^2)}$) for each source, with a limit of 3″, to guarantee the detection of the real optical counterpart.
With this selection we found three candidates, but only DESJ014132.4−542749.9 (hereafter DES0141−54) has a SED consistent with that of a non-absorbed quasar at high redshift (see Fig. 4.2). Therefore it was considered the only promising candidate for a spectroscopic follow-up observation. Figure 4.2 shows that the other two candidates have a SED better represented by a template of a z∼1 elliptical galaxy or by a template of an absorbed quasar at z∼2, therefore we decided to not propose them for a spectroscopic follow-up. These two types of contamination are indeed common in the selection of high-z RL AGNs (see Sect. 2.3.1).
For the candidate DES0141−54 we reported in Fig. 4.3 the DES DR1 images in the different $grizY$ bands, while the optical DES DR1 magnitude are listed in Table 4.1. DES0141−54 optical coordinates are: RA=25.38517 deg, Dec=-54.46385 deg. The distance between the optical and the SUMSS radio position of DES0141−54 is 2.2″.

[1]This last constraint has been placed to have more reliable colors.
[2]S$_{INT}$ and S$_{Peak}$ are the integrated and the peak flux density respectively.

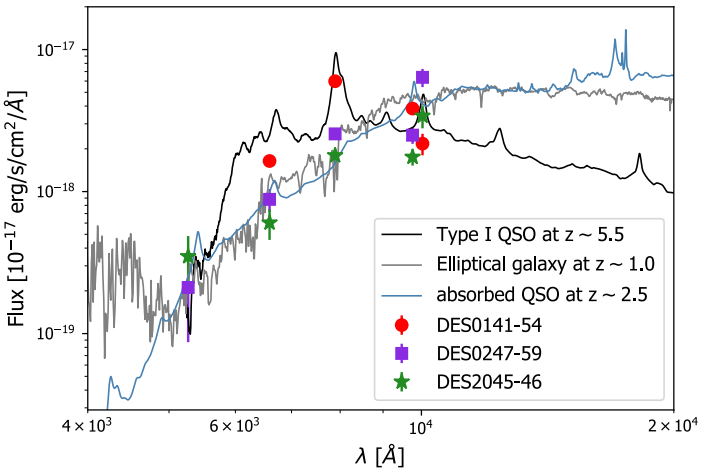

Figure 4.2: SEDs of the three candidates selected from the cross-matching of SUMSS and DES DR1. Red points, violet squares and green stars represent the photometric optical flux densities of our selected candidates. Only DES0141−54 photometric points (in red) are consistent with a non-absorbed quasar template. Instead the other two candidates SEDs are better described by a template of an elliptical galaxy at z∼1 and of an absorbed quasar at z∼2.5. The photometric points are plotted at the effective wavelengths of the DES DR1 filters (see Fig. 2.13). The used templates are from the SWIRE library, Polletta et al. (2007).

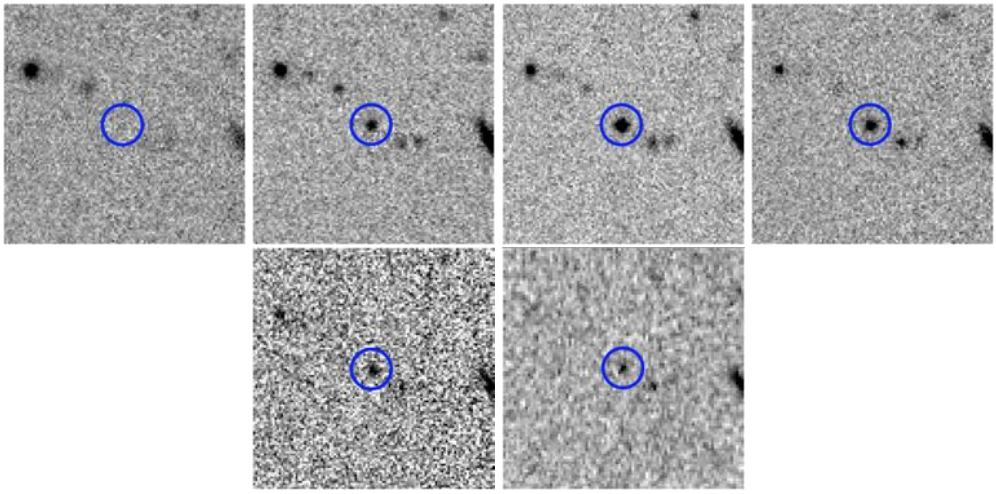

Figure 4.3: $0.5'\times0.5'$ DES g, r, i, z, Y and VHS J cutout images of DES0141−54. The object position is marked in all the images with a blue circle of $2.5''$ of diameter. All images are oriented with north up and east to the left.

4.2 Spectroscopic observations and data reduction

In this section I describe the optical and near-infrared spectroscopic observations of DES0141−54 that allowed the confirmation of the high redshift nature of the source.

filter	λ (μm)	magnitudes	reference survey
(1)	(2)	(3)	(4)
r	0.659	22.96±0.17	DES
i	0.789	21.16±0.12	DES
z	0.976	21.18±0.15	DES
Y	1.003	21.74±0.30	DES
J	1.254	21.14±0.28	VHS
$W1$	3.4	20.24±0.08	WISE
$W2$	4.6	20.80±0.29	WISE

Table 4.1: Optical and near-IR AB magnitude of DES0141−54. Col (1): optical / near-IR filters; Col (2): filter central wavelength in μm; Col (3): observed magnitudes: the J, W1 and W2 WISE magnitude have been converted from Vega to AB system. The WISE magnitude have been also corrected for blending of a nearby source as described in Sect. 4.3; Col (4): reference survey.

4.2.1 NTT observation

After its identification in the DES catalog we performed a dedicated spectroscopic follow-up of DES0141−54 with the ESO Faint Object Spectrograph and Camera (EFOSC2, Buzzoni et al. 1984) mounted at the New Technology Telescope (NTT), located at ESO-La Silla observatory, on 2018 February 9th during the 0100.A-0606(A) observing program (P.I. Moretti A.). We carried out four 15-minutes observations (see Fig. 4.4), with a long-slit of 1.5″ width, for a total exposure time of 1h. The average seeing during the observation was 1.1″ and the average air-mass was

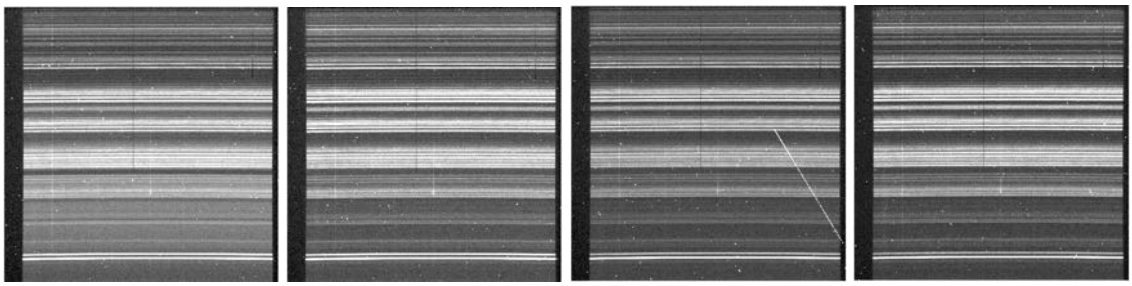

Figure 4.4: Four 15-minutes raw images of DES0141−54, taken at the NTT on the night of 2018 February 9th. In the middle of the four images a clear signal is seen.

1.5. The wavelength calibration was secured by means of frequent exposures of a He-Ar hollow-cathode lamp. The spectrograph response (sensitivity function) was obtained by many exposures of LTT1788 (RA = 03:48:22.17, Dec = −39:08:33.6) spectrophotometric star from the catalog of Hamuy et al. (1992, 1994). The reduction from the two-dimensional images taken with EFOSC2 into a calibrated, one-dimensional spectrum was performed using standard tasks within the IRAF package, and it is described in the following.

Bias and flat-field subtraction:

The first step was to remove the instrumental additive error caused by the *bias*, an electronic noise due to the pre-tensioning of the CCD pixels. Twenty *bias* frames, namely images with the shutter closed and with a null exposure time, have been acquired at the end of the observation. Then a median of these frame was done using the *imcombine* task, obtaining a *master bias frame*

(Fig. 4.5), which is subtracted from all the spectral images using the task *imarith*.
We also acquired different flat-field frames, i.e. images of the sky at the sunset, when the sky is homogeneous enough and free from stars. Flat-fields allow us to evaluate the response of the different pixels of the CCD. We have done a *median* of the flat-fields, using the task *imcombine* generating a *master flat-field*. We computed the mean value of the master flat-field ($<\mathrm{ff}_{med}>$) and then with the task *imarith* the master flat-field was normalized at 1, diving it by the mean value (Fig. 4.5).
Then the single spectral images have been corrected using the following formula:

$$I_{cor} = \frac{Imm - bias}{ff} \times < ff_{med} > \tag{4.1}$$

where $Imm - bias$ is the bias subtracted image, ff is the master flat-field and I_{cor} is the final corrected image.

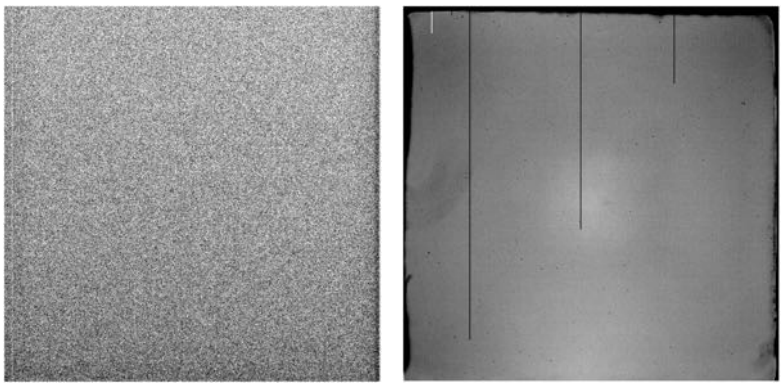

Figure 4.5: *Left*: *Master bias frame* as the mean of 20 bias frames acquired at the beginning of the observing night. *Right*: Normalized *master flat-field frame*.

Cosmic rays removal

After the bias removal and flat-field correction, the images show a contamination due to cosmic rays that collide on the CCD. They can be identified as saturated pixels on the image (see Fig. 4.4). To remove cosmic rays we computed a *median* of the four spectral images to eliminate all the pixels that deviate effectively from the mean value (see Fig. 4.6).

Wavelengths calibration:

To obtain the wavelength calibration frequent short (1-5 sec) exposures of a He-Ar hollow-cathode lamp have been acquired during the same night of observation. Three different tasks have been used to perform th wavelength calibration: $identify$, $reidentify$, $fitcoord$. First of all we $identify$ the emission lines ($\sim$20) of the central column of the lamp spectrum. Then the task proceeds with the automatic identification of the other spectral lines, which can be manually excluded, for example, if a line is saturated. The operation made by $identify$ is extended to the other columns with $reidentify$, for applying a geometric transformation and determining a unique calibration between pixels and wavelengths on the whole image. Finally the task $fitcoord$ determines the geometric transformation between the image coordinates and the wavelength interpolating the output of $reidentify$. A final rms of 3.1 pixel was obtained after the wavelength calibration.
The two dimensional wavelength solution was transferred to the object image by means of the task

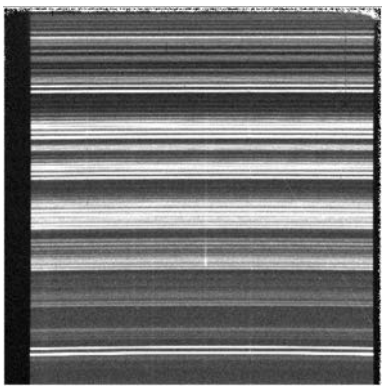

Figure 4.6: Median of the four images of DES0141−54 after the bias subtraction and flat-field correction. Cosmic rays have been removed.

transform. We controlled the goodness of our wavelength calibration by measuring, with the task *splot*, the position of some bright OH sky lines: 6300.30Å, 6863.95Å, 7316.28Å, 7821.50Å. All the lines differs from their laboratory position by <2-3Å. Our wavelength solution can be considered good.

Background subtraction and extraction of the one-dimensional spectrum:

After the wavelengths calibration, we used the task *apall* to extract the one-dimensional wavelength calibrated and background subtracted spectrum of DES0141−54. The algorithm of the task automatically identifies the columns, called *apertures*, which contain the spectrum of the different sources that appear in the slit. We adopted an aperture of 10 pixel width (1.2″) for the source spectrum and we selected the two regions of background on each side of the object emission, which is fitted and subtracted. Figure 4.7 shows the two dimensional background subtracted spectrum of DES0141−54.

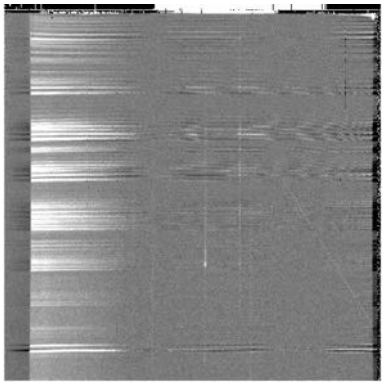

Figure 4.7: Background subtracted image of DES0141−54. In the center of the image the emission of the source is clearly visible.

Flux calibration:

To obtain the flux calibration, namely the spectrograph response, an observation of a spectrophotometric reference star is required. We observed, during the same night, the LTT 1788 star. The image of the star was analyzed with the same procedure of the object image. In addition the

one-dimensional spectrum of the star was analyzed with the task *standard*, which removes the atmospheric absorption lines along the spectrum and produces a sampling of the spectrum. The output of *standard* is then used by the task $sensfunction$ for determining the spectrograph response due to the instrument and to the observational conditions. For this purpose $sensfunction$ compares the star spectrum sampling with a theoretical one: the sensitivity function is therefore constructed. Finally with the task *calibrate* the source spectrum can be flux calibrated and visualized with the task *splot*.
Panel (a) of Fig. 4.8 shows the EFOSC2/NTT spectrum of DES0141−54, with the most important emission lines marked. The good agreement between the DES DR1 photometric points and the spectrum allowed us to infer that the flux calibration is good.

Redshift measurement:

The object redshift has been measured by fitting the Ly-$\alpha\lambda$1216Å line with a single Gaussian profile using the IRAF task *splot*. The resulting value is z=5.00±0.01, confirming the high redshift nature of the selected candidate. DES0141−54 is the first high-z RL AGN discovered in the DES DR1.

4.2.2 X-Shooter follow-up

Since the NTT/EFOSC2 spectrum confirmed the high redshift nature of DES0141−54, we performed a spectroscopic follow-up with X-Shooter (Vernet et al. 2011), the wide band intermediate resolution spectrograph mounted at the ESO Very Large Telescope (VLT). This new observation allowed us to extend the wavelength range in the near-IR band and detect the MgIIλ2798Å emission line, which can be used to estimate the central black hole mass of DES0141−54 (see Sect. 4.6.3). The observation was carried out in a Director's Discretionary Time program (project ID: 2100.A-5039, P.I. Moretti A.) on 2018 February 23 and consisted of 4 exposures of 15 minutes each in nodding mode in the sequence ABBA, with a total integration time of 1h, simultaneously in the UVB (3100-5500 Å), VIS (5500-10150 Å) and NIR (10150-24800 Å) spectroscopic arms. The observation was performed along the parallactic angle in a clear night with an average seeing of 0.8″ and a mean air mass of 1.8. The adopted slit widths were 1.0″ in the UVB and 0.9″ in the VIS and NIR, providing a nominal resolving power ($\lambda/\Delta\lambda$) of 5400, 8900 and 5600, respectively. The spectrophotometric GD71 white dwarf star (R.A = 05:52:27.51, Dec = +15:53:16.6) from the catalog of Moehler et al. (2014) was observed in the same night to ensure the flux calibration, and a series of exposures of a Th-Ar hollow-cathode lamp were done for wavelength calibration.
The data were reduced with the ESO/X-Shooter pipeline v2.5.2 (Modigliani et al. 2010) using the EsoRex interface[3] (Goldoni et al. 2006). We did not reduce the UVB arm, because no signal and/or significant emission line are expected at that wavelengths due to HI absorption clouds along the line of sight. To briefly summarize the reduction routine, the pipeline subtracts the detector bias and dark current, then the spectra are rectified and wavelength-calibrated. Finally the spectroscopic standard star spectrum is used to calculate a flux-calibrated spectrum. However, we noted that the reduced NIR spectrum shows systematically large and frequent sky-subtraction residuals, due to the IR Earth background that is difficult to remove, because it changes in space and time. Consequently, we opted to use some IRAF tasks to improve the reduction. To subtract the background we averaged all the NIR frames in A position (<A>) and B position (<B>) and then we subtracted them, <A>-<B> and <B>-<A>, in which we obtained a positive and a negative spectrum signal. We then aligned at the same y-pixel the positive signals, usign the task $imshift$. Then we used the task *imcombine* to join the two signals and the task *apsum* to extract

[3] http://www.eso.org/cpl/esorex.html.

the mono-dimensional spectrum. Finally for the flux calibration we used *standard*, $sensfunc$ and *calibrate*. After the data reduction we plotted the photometric points on the spectra finding that the flux calibration can be considered good with a level of confidence larger than 95%.
The optical X-Shooter spectrum is shown in the panel (b) of Fig. 4.8. Despite the several residual sky lines in the NIR spectrum, and, therefore, despite to the low S/N (∼2) of the spectrum, we detected the MgIIλ2798Å line. The redshift was measured, as for the EFOSC2/NTT spectrum, fitting a Gaussian profile on the Ly-α line, using the IRAF task *splot*: the extracted value is z=5.005±0.003, confirming the previous value measured in the NTT spectrum. The redshift was also confirmed by fitting the other detected lines with Gaussian profiles: O[VI]λ1035Å, NVλ1242.80Å and the CIVλ1549Å. We obtained z=4.998±0.004, z=4.999±0.002 and z=4.999±0.003 respectively. For our analysis we used as the best estimator the redshift computed from the average of these values: z=5.000±0.002.
From the two spectra shown in Fig. 4.8 it is clear that the Lyman-α line has varied between the two observations (Δ_{t_obs} = 14 days, which, in the source rest frame corresponds to ∼2 days). The observed line flux (Lyα+NV) of DES0141−54 has increased from 3.11×10^{-15} erg s^{-1} cm^{-2} to 3.78×10^{-15} erg s^{-1} cm^{-2}, which corresponds to a variation of 21%. Instead the flux of the AGN continuum has not varied[4] between the two observations. Such a flux variation (∼20%) for the Ly-α line has been already observed in others AGNs, as reported for instance by Woo et al. (2013), Koptelova et al. (2017) and Lira et al. (2018).

4.3 Archival WISE and VHS photometry

DES0141−54 is included in the AllWISE Source Catalog (see Sect. 2.4.3 for details), with clear detections (SNR>4) at λ = 3.4μm (W1) and λ = 4.6μm (W2). The WISE catalog magnitudes have been converted from Vega to AB system using the relations reported in Sect. 2.4.3. The offset between the DES optical and WISE infrared positions is 2.06″. However, the WISE detection is the result of blending of two distinct sources clearly visible in the optical images (see white contours in Fig. 4.9). Therefore we corrected the WISE magnitude for this effect, with the following procedure. We modelled the WISE emission as the sum of two point-like sources at the optical positions of DES0141−54 and of the other object to the south-west (blue and black dashed circles in Fig. 4.9 respectively), leaving the relative normalizations free to vary. As a Point Spread Function (PSF) reference model we used a point-like infrared source nearby in the field of view. We estimated that DES0141−54 contribution to the WISE flux is 60% both in W1 and W2, and we corrected the magnitudes accordingly.
Besides the WISE detection, DES0141−54 has also a J band detection in the Vista Hemisphere Survey (VHS, McMahon et al. 2013), at a distance of 0.073″ from the optical coordinates (right image on the bottom line of Fig. 4.3). Also the VHS J magnitude was converted from Vega to AB system using the relation described on the CASU: $J_{AB} = J_{VHS}+0.916$.
The infrared magnitude of DES0141−54 are listed in Table 4.1 together with the optical ones.

4.4 Archival radio photometry

At radio wavelengths, besides the SUMSS catalog, several radio detections of DES0141−54 are reported in the radio archives. (see Table 4.2 and Table 4.3 for details). In particular, DES0141−54 has been detected by the AT20G$_{follow-up}$ and the ATPMN surveys, both carried out with ATCA

[4]The continuum flux has been computed in the wavelength range 7600-7800 Å where no emission lines and residual sky lines are present. We found a value of ∼3.4×10^{-18} erg s^{-1} cm^{-2} Å^{-1} in both spectra.

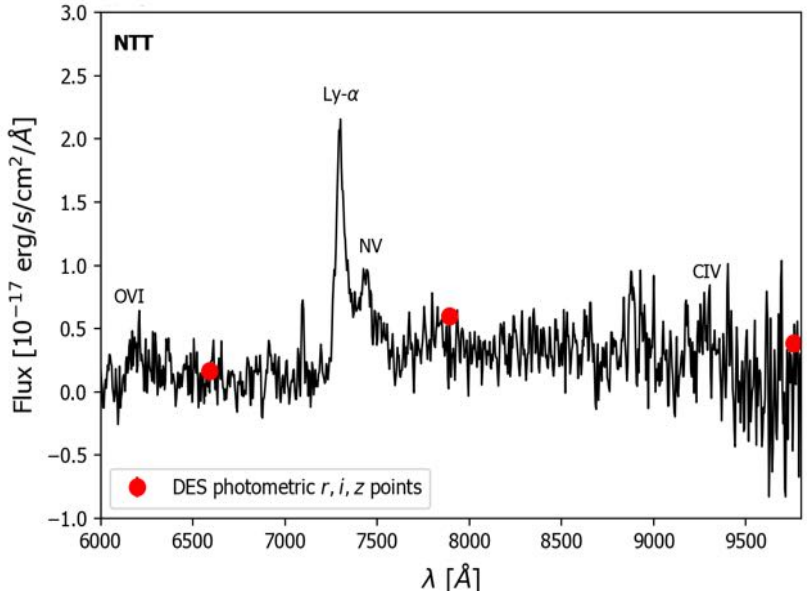

(a)

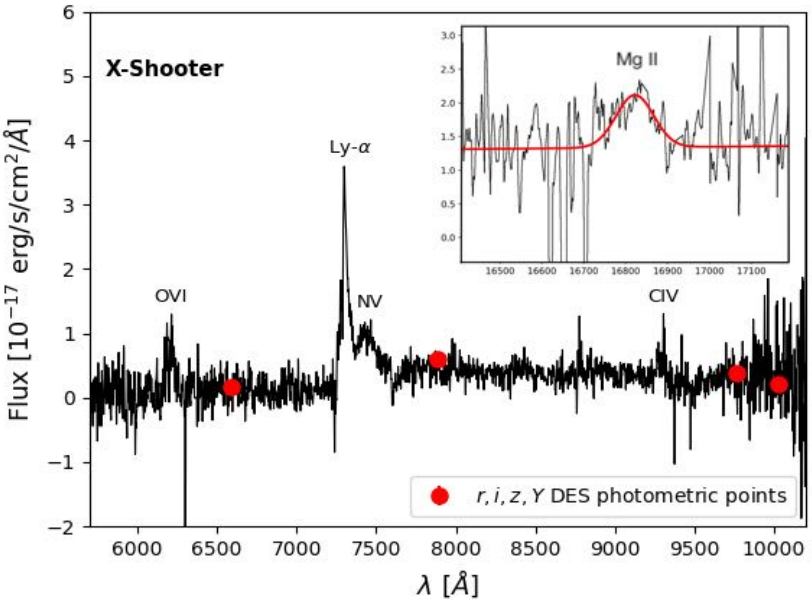

(b)

Figure 4.8: Optical spectra of DES0141−54. Panel (a): EFOSC2/NTT discovery spectrum; panel (b): X–Shooter/VLT follow-up. In the small inset on the right the zoomed-in portion of the NIR spectrum with the Gaussian fit of the MgIIλ2798Å line. In both panels the Ly-$\alpha\lambda$1216Å, the NVλ1242.80Å, the CIVλ1549Å and the O[VI]λ1035Å emission lines are shown We also plot the DES DR1 photometric points that allowed us to infer that the spectra flux calibrations are good in both cases.

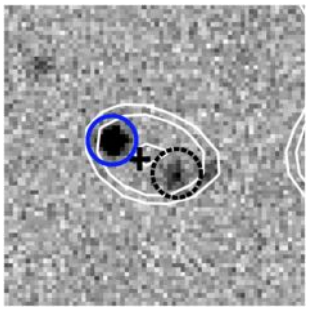

Figure 4.9: WISE W1 contours (in white) overlapped on the DES DR1 i–band $0.3'\times0.3'$ image. The object position is marked with the same blue circle of Fig. 4.3. The central cross marks the position of the WISE detection. The contours illustrate that WISE does not spatially resolve the emission of DES0141−54 and of a south-west source clearly visible in the optical band (black dashed circle). The image is oriented with north up and east to the left.

using the longest baseline (∼6 km), allowing a high angular resolution (<1″ at 8.4 GHz). The distance between the ATCA and the DES0141−54 position is ∼0.15″, allowing us to confirm that the radio-optical association of our source is reliable.

ν_{obs} (GHz) (1)	S_ν (mJy) (2)	reference survey (3)	years of observation (4)
20	43.0±2.0	AT20G	2004-2008
8.6	70.0±4.0	AT20G$_{follow-up}$	2004-2008
8.6	63.0±10.0	ATPMN	1992-1994
8.4	59.5±3.0	CRATES	2005
4.85	100.0±9.0	PMN	1990
4.8	90.0±5.0	AT20G$_{follow-up}$	2004-2008
4.8	82±7.0	ATPMN	1992-1994
0.843	178.3±5.5	SUMSS	2002
0.076-0.231	392.5±69.8 - 241.9±12.3	GLEAM	2013-2014

Table 4.2: Radio detections of DES0141−54 found in the radio archives. Col(1): observed frequency in GHz; Col(2): flux density in mJy; Col(3) reference survey: see section 2.4.1 for details. Col(4) years of the observation. In the last line we report the range of the GLEAM detections, from 76 to 231 MHz. All the GLEAM flux densities can be found in Table 4.3.

4.5 Archival and new X–ray observations

DES0141−54 was serendipitously observed by XMM-Newton in 2005, in the field of Abell 2933 (OBsID:0305060101, revolution 1089), with a 8.7′ of offaxis. The effective exposure times of this observation are 31ks and 23ks for MOS and PN[5], respectively. The source is faint and it is not included in the 3XMM-DR8 catalog (Rosen et al. 2019a,b). We performed the data reduction of the XMM-Newton image using the interactive data analysis task of the XMM-Newton Science Archive (XSA), considering a circular region of 5″ radius centered on the optical position of

[5]MOS and PN are the two types of CCD mounted on the European Photon Imagin Camera (EPIC) onboard XMM-Newton.

ν_{obs} (GHz) (1)	S_ν (mJy) (2)
0.231	241.9±12.3
0.220	251.4±12.6
0.212	260.5±13.1
0.204	259.9±14.5
0.197	266.2±16.9
0.189	258.3±16.5
0.181	292.7±16.1
0.174	271.8±18.0
0.166	273.9±18.9
0.158	275.8±18.1
0.151	252.9±18.9
0.143	267.1±22.0
0.130	231.9±24.4
0.122	252.6±25.3
0.115	281.8±28.3
0.107	361.9±34.8
0.099	293.4±49.9
0.092	343.3±44.9
0.084	342.9±51.3
0.076	392.5±69.8

Table 4.3: Radio flux densities of DES0141−54 found in the GLEAM catalog. Col(1): observed frequency in GHz; Col(2): integrated flux density in mJy.

DES0141−54. The source is detected only in the PN image with 11 counts and a significance of $\sim 3\sigma$. We selected a small region to perform the analysis because of the presence of a nearby bright source (at $\sim 15''$ to the north-east) and of the low counts detected for our object. Flux losses are at the level of 50% and are accounted for the ARF file calculation. Using XSPEC version 12.10.1, we modeled the PN data with a simple absorbed power law with the absorption factor fixed to the Galactic value (2.5×10^{20} cm^{-2}) as measured by the HI Galaxy map (Kalberla et al. 2005). The spectrum was grouped with a minimum of one count for each bin, and the best fit was calculated using the C-statistics. We measured a flux of $7.5\pm2.6\times10^{-15}$ erg s^{-1} cm^{-2} for the [0.5-10] keV energy band, using the best fit value for the photon index (Γ_X=1.75±0.5).
The X–ray flux of DES0141−54 extracted from the XMM-Newton image is faint compared to what we expect from a blazar source at high redshift (see section 4.6.2 for details.). A possibility is that the X–ray flux of the source has varied. Indeed, as described also in Sect. 1.2, blazars are known to be highly variable sources at all wavelengths, including the X–rays. Therefore, in order to check for a possible variability of the X–ray emission of DES0141−54 we asked for a *Swift*–XRT pointed observation, which was carried out with a Target of Opportunity (ToO) request (target ID: 10586, P.I. Moretti A.) on 2018 March 2; the total exposure time was 8340s. The integration time would have been long enough to detect the source if it had an X–ray flux similar to that of the other blazars at z≥5.0 reported in the literature (e.g., Sbarrato et al. 2012b). However, this observation has resulted in a non detection. We computed an upper limit of 1.3×10^{-14} erg s^{-1} cm^{-2} in the [0.5-10] keV energy band, assuming an N_H and a Γ_X equal to those used for the XMM–Newton analysis. This upper limit is consistent with the faint flux computed from the XMM–Newton

image, confirming the weakness of DES0141−54 X–ray emission.

4.6 Results

In this section I report the results of the analysis on the multi-wavelength properties of DES0141−54, by comparing them with those of other high-z RL AGNs. From the literature I collected radio flux densities, optical-IR magnitudes and X–ray band fluxes (whenever possible) of all the jetted AGNs already published with a redshift above 4.5 (see Table C.1).

4.6.1 Radio properties

From the observed optical and radio flux densities we calculated the radio–loudness (R) of DES0141−54 following the definition of Shen et al. (2011): R = $\frac{S_{5\ GHz}}{S_{2500\text{Å}}}$ (rest frame). As already said in Sect. 1.1, this parameter describes how powerful is the non-thermal synchrotron emission with respect to the thermal one. Therefore, a high R supports the idea that the radio emission is boosted along our line of sight.
The rest frame frequency at 5 GHz of DES0141−54 corresponds to an observing frequency of ∼0.83 GHz, therefore similar to the SUMSS frequency. Instead, the rest frame flux density at 2500Å was determined starting from the flux density in the J band and using a power law continuum ($S_\lambda \propto \lambda^{\alpha_\lambda}$) with the spectral index computed from the DES DR1 and WISE photometric points (α_λ=-1.2). We obtained a radio-loudness of 12000±1600.
Figure 4.10 shows the comparison between the radio-loudness of DES0141−54 and that of high-z jetted AGNs from the literature. For all these objects the radio-loudness was calculated using the definition of Shen et al. (2011) as for DES0141−54. The flux at 5 GHz rest frame for these sources was computed starting from the observed flux at 1.4 GHz, found in the reference papers. The radio spectral index was reported in the literature only for few sources, therefore, for the remaining majority we assumed two different spectral indexes, (α_ν = 0.0 and 0.7) and we computed the rest frame flux as the mean of the two. Instead the flux at 2500Å rest frame was extracted from the z band magnitude (the one available for all these sources) and assuming different spectral indexes (α_λ=-1.7 from Selsing et al. 2016 and α_λ=-1.56 from Vanden Berk et al. 2001). Figure 4.10 shows that DES0141−54 has the highest R ever measured at redshift above 5. From Fig. 4.10 we also noticed that the majority of blazars found in the literature (yellow circles) occupies the portion of the plot at very high R (64% have log(R)>2.5), suggesting that DES0141−54 has a high probability of being a blazar. However at z<5 there are two objects with R greater than or equal to that of DES0141−54: J0311+0507 at z=4.51 (Kopylov et al. 2006) and J2102+6015 at z=4.57 (Sowards-Emmerd et al. 2004) respectively. For both of them no evidence of Doppler boosting from VLBI observations is reported in the literature, therefore these sources are not classified as blazars. The first one is a complex multi-component ultra steep spectrum (USS) radio source (Parijskij et al. 2014). The second one is classified by Frey et al. (2018) as a GPS. Therefore, although the high radio-loudness supports the blazar nature of DES0141−54, we cannot exclude the possibility that it is an intrinsically powerful mis-aligned jetted AGN, like J2102+60 and J0311+0507. For this reason we studied the radio spectrum of DES0141−54 to test for a possible GPS nature, as we have already done for the CLASS objects (see Sect. 3.4). Thanks to the large number of radio detections, we computed the wide band radio spectrum of DES0141−54 from 76 MHz up to 20 GHz (Fig. 4.11). We fitted all the photometric radio flux densities with a single power law ($S_\nu \propto \nu^{-\alpha}$) to measure the radio spectral slope. The radio slope between 0.8 and 20 GHz is α=0.45±0.04. By taking into account also the low frequency GLEAM detections, α becomes equal to 0.35±0.02. Therefore, the radio spectrum can be considered flat

(α<0.5). Moreover, the radio slope reported in the GLEAM catalog for this object, computed using only low frequency data, is α=0.259±0.068, confirming the flatness of the spectrum also at low frequencies. These radio spectral properties make the GPS hypothesis very unlikely and support, instead, the idea that DES0141−54 is a beaming dominated object (i.e. a blazar).
This hypothesis is also validated by a radio variability of DES0141−54 at 8.6 GHz and at 4.8 GHz, a characteristic typical of blazars. In fact, as shown in Fig. 4.11 and Table 4.2, DES0141−54 was observed during different years at these two frequencies. This flux variation (∼10% at both frequencies) is consistent with that observed in other high-z blazars (∼14%, Caccianiga et al. 2019).

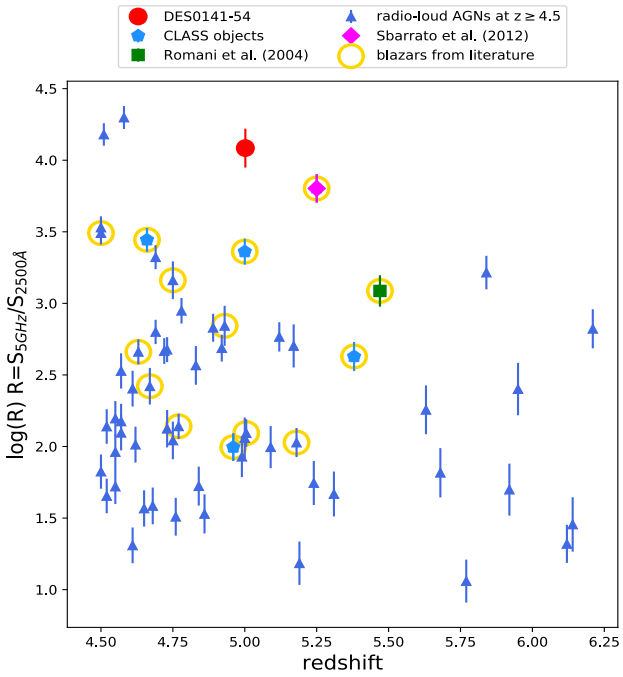

Figure 4.10: Radio-loudness comparison between DES0141−54 (red point) and a sample of z≥4.5 RL AGNs from the literature (blue triangles). DES0141−54 has the highest R at z≥5. It is higher than those of the three most distant blazars discovered up to now (J0906+6930, J1648+4603 and J1026+2542). The objects circled in yellow are all the confirmed blazars found in the literature. We point out that these are only the blazars with a validation in the literature.

4.6.2 X-ray properties

The X–ray flux computed from the XMM-Newton archival image, and the upper limit obtained from the pointed *Swift*-XRT observation, indicate that DES0141−54 is one order of magnitude fainter in the X–rays compared to other confirmed blazars at z≥5.0 (see e.g., Romani et al. 2004; Sbarrato et al. 2012b). To quantify this difference, in Fig. 4.12 we compared the X–ray luminosity at [0.5-10] keV of DES0141−54 with that of the same sample of z≥4.5 RL AGNs from the literature used for the radio comparison (see Table C.1). Figure 4.12 shows the X–ray luminosity as a function of 1.4 GHz luminosity for this sample. DES0141−54 is in the low X–ray luminosity end of the distribution, with an X–ray luminosity >2σ lower than the average of this sample. The statistics of this sample is low, because only few of these high-z objects have been observed in the X–rays up to now.
Moreover we noted that the X–ray luminosity of DES0141−54 is consistent within 1σ with that expected from a RQ quasar with the same optical luminosity (based on the Strateva et al. 2005

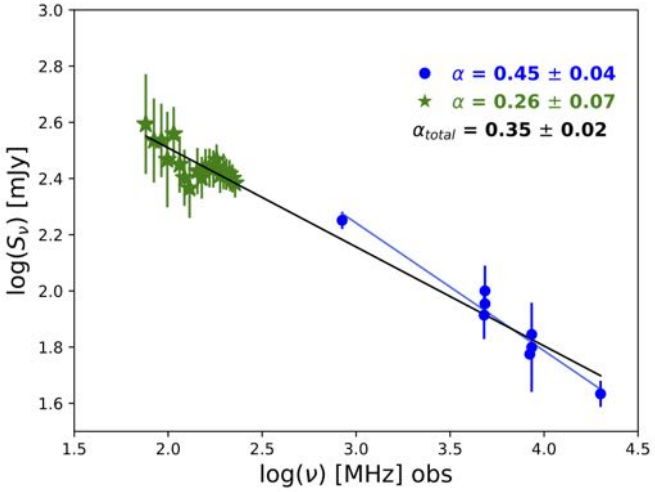

Figure 4.11: Radio spectrum (observed frame) of DES0141−54. Green stars are the GLEAM low frequency detections, while blue points include radio detections from 0.8 GHz (SUMSS) to 20 GHz (AT20G). The corresponding indexes are reported in the legend. Finally in black is reported the total radio spectral index (α_{total}) computed over the whole range of frequencies.

relation). This suggests that the X-ray emission from the relativistic jet must be very weak. Since DES0141−54 is the only RL AGN above redshift 4.5 observed up to now that has a very high radio luminosity but a very weak X–ray luminosity, we looked for similar sources at lower redshifts. To this end, we used the Roma BZCAT-5th edition (Massaro et al. 2015). In particular, we considered only the FSRQs of the BZCAT with a radio flux density (0.843 or 1.4 GHz) above 1.5 Jy, as we have already done in the CLASS sample (see Sect. 3.6). The selected objects have radio luminosities similar to DES0141−54 ($L_{1.4\ GHz}$=1.38±0.11×10^{35} erg s^{-1} cm^{-2} Hz^{-1}), making the comparison more straightforward. With this selection criteria we obtained a sample of 105 FSRQs with a mean redshift of 1.24. For all these objects the X–ray flux reported in the BZCAT at [0.1-2.4] keV was converted to [0.5-10] keV assuming an X–ray spectral index (α_X) equal to 0.5. From this flux, we computed the X–ray luminosity in the same energy band. For the k-correction in the radio band we assumed α_r=0.0. In Fig. 4.13 we show the distribution of the X–ray-to-radio luminosity ratio (XR) for these BZCAT blazars. We overplotted in red the value derived for DES0141−54: log(XR) = 9.96±0.30 Hz. This figure shows that blazars with such a low XR values are very uncommon also at low-z and correspond to the tail of the distribution. In particular, only two blazars (i.e. ∼2% of the total sample) have an XR similar to DES0141−54. The possible origin of such a X–ray weakness will be discussed in Sect. 4.6.4.

4.6.3 Black hole mass estimates

The central black hole mass (M_{BH}) of DES0141−54 has been computed following two different methods: the commonly used virial approach and a method based on the accretion disk emission. Both methods are described in details in Sect. 1.3.

Single epoch mass

The broad CIVλ1549Å and MgIIλ2798Å emission lines detected in the single-epoch VIS and NIR X-Shooter spectra have been used to estimate the M_{BH} of DES0141−54. Although the CIV line is not always considered the best virial estimator, for the reasons mentioned in Sect. 1.3, we decided

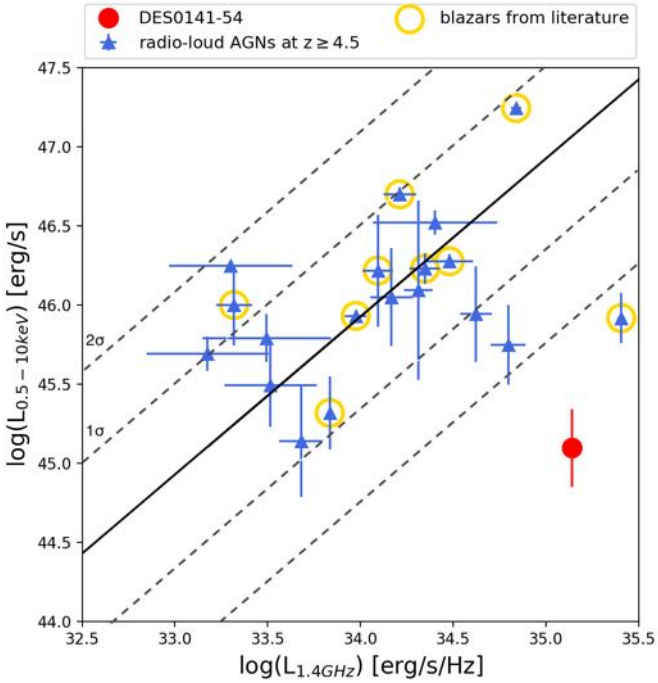

Figure 4.12: Radio versus X–ray luminosity of DES0141−54 (red point) compared to those of z≥4.5 RL AGNs (blue triangles). Yellow circles have the same meaning of Fig. 4.10. The black solid line is the 1:1 relation and the two black dashed lines are the 1σ and 2σ relations. DES0141−54 is one of the most powerful radio high-z AGN ever discovered but it has a very weak X–ray luminosity ($>2\sigma$ out of the mean distribution).

to use it to have a second, independent, SE M_{BH} estimate in addition to the one based on the very noisy MgII line.

We derived M_{BH} by using Eq. 1.13 and Eq. 1.15 reported in Sect. 1.3.1. We computed the FWHMs of the CIV and MgII emission lines through a single Gaussian spectral fit. The rest frame continuum luminosities (λL_λ) at 1350Å and 3000Å have been estimated respectively from the i-band and J-band flux densities, assuming a single power law continuum ($f_\lambda \propto \lambda^{\alpha_\lambda}$) with a slope of α_λ=-1.2, computed from the DES DR1 and WISE photometric points. The FWHM, the continuum luminosities and the computed M_{BH} values are reported in Table 4.4. These M_{BH} virial estimates are affected by large uncertainties intrinsic to the method (∼0.4-0.5 dex, e.g., Shen et al. 2008, 2011), which dominate the total error on the computed SE masses.

In Sect. 1.3.1 we already discussed the possible issue on the SE mass due to the anisotropy of the BLR. Instead in order to evaluate the potential bias related to the jet contamination (see Sect. 1.3.1) we have compared the ratio between the CIV (or MgII) line luminosity (which is not affected by the beaming) and the continuum luminosities at 1350Å (or 3000Å) (which could be affected by the beaming) of DES0141−54 with that of the RQ AGNs at high redshift (z≥4) of the sample of Shen et al. (2011), for which the beaming is not present. We did not find a significant offset between DES0141−54 and that RQs sample, allowing us to infer that the relativistic jet of the source does not strongly contaminates its optical-NIR continuum emission. Therefore the computed virial masses are not overestimated.

To verify the reliability of the SE masses of DES0141−54, we estimated the black hole mass of the source by using an independent method, based on the accretion disk modeling (as discussed in the following).

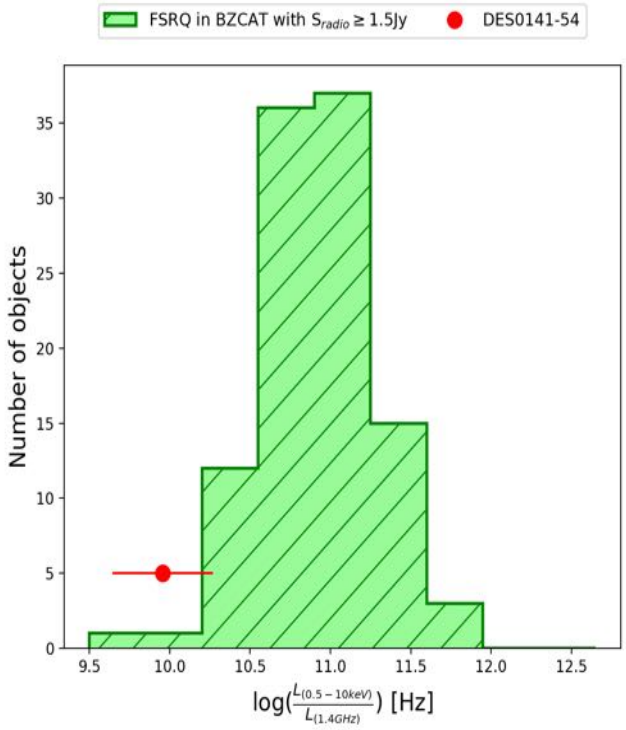

Figure 4.13: Distribution of the X–ray-to-radio luminosity ratio (XR) for the FSRQs with a radio flux greater than 1.5 Jy in the BZCAT. DES0141−54 XR (red point) is similar (within 1σ) to those of a few number (a tail) of low-z blazars. These similarities suggests that DES0141−54 can be the high-z analogue of such rare low redshift blazars.

Bolometric Luminosity and Eddington ratio

We derived the Eddington luminosity (L_{Edd}) and the Eddington ratio ($\lambda_{\rm Edd}$) based on $M_{\rm BH}$. We first estimated the bolometric luminosity (L_{bol}) using the following bolometric corrections:

$$L_{bol} = K_a \times L_{1350\text{Å}}$$
$$L_{bol} = K_b \times L_{3000\text{Å}}$$
$$L_{bol} = K_c \times L_{5100\text{Å}}$$

where $L_{1350\text{Å}}$, $L_{3000\text{Å}}$ and $L_{5100\text{Å}}$ are the continuum luminosities at 1350Å, 3000Å and 5100Å (rest frame) respectively and K are correction factors: K_a is from Shen et al. (2008) and K_b and K_c are from Richards et al. (2006). The estimated values of L_{bol} and their errors, which already take into account the uncertainty on K, are reported in Table 4.4. We then used a mean value of the bolometric luminosity ($<L_{bol}> = 5.2\pm1.7\times10^{46}$ erg s^{-1}) to calculate the mean Eddington ratio from CIV and MgII lines. However, these bolometric corrections are calibrated empirically over low-z RL and RQ Type I AGNs, with a mean expected angle of ∼30°. Therefore, to compute the intrinsic bolometric luminosity of DES0141−54 we have to take into account the inclination factor ($i = \cos(0°)/\cos(30°) = 1.15$) if the source is seen under a small viewing angle ($\theta \sim 0°$) as probably DES0141−54 is, and the fact that the continuum emission from the disk is not isotropic. This inclination factor quantifies the expected difference of orientation between DES0141−54 and the average quasars in the SDSS DR7 sample (Shen et al. 2011), on which the bolometric corrections are computed. Therefore, the $<L_{bol}>$ value aforementioned represents the isotropic bolometric luminosity. The intrinsic value is: $<L_{bol\_int}>=4.5\pm1.5\times10^{46}$ erg s^{-1}. The

corresponding values for the Eddington ratio of CIV and MgII lines are: $\lambda_{\rm Edd\_CIV} = 1.6\pm0.6$ and $\lambda_{\rm Edd\_MgII} = 0.7\pm0.3$. These values indicate that DES0141−54 is accreting very close to the Eddington limit, in agreement with the theoretical models that suggest very high accretion rates (close or even above the Eddington limit) to explain the presence of SMBH at high redshifts (e.g., Lupi et al. 2016; Pezzulli et al. 2016).
Finally, from $<L_{bol}>$ we computed the luminosity emitted isotropically from the accretion disk (see Sect. 1.3.2), following the relation found in Calderone et al. (2013) : $L_{bol}\sim2L_{disk}$. We obtained $L_{disk}\sim2.6\pm0.8\times10^{46}$ erg s^{-1}. In order to check the consistency of our results, we also estimated the isotropic disk luminosity from the line luminosities of Ly-α, NV, CIV and MgII (see Table 4.4), by fitting them with a single Gaussian component. Following Celotti et al. (1997), we computed the total luminosity of the BLR from the CIV and MgII lines, obtaining $L_{BLR} = 1.1\pm0.7\times10^{45}$ erg s^{-1}. If we assume that the BLR intercepts 10% of the disk luminosity (hence a covering factor of 0.1), we estimated an L_{disk} equal to $1.1\pm0.9\times10^{46}$ erg s^{-1}, consistent within the errors with our previous estimate based on $<L_{bol}>$. The error on the isotropic disk luminosity does not take into account the uncertainties on the unknown covering factor.

Parameters related to CIV line.	
FWHM	1934±31
λL_λ at 1350Å	1.2±0.1
M_{BH}	2.18±0.13
Parameters related to MgII line	
FWHM	2447±141
λL_λ at 3000Å	7.3±1.7
M_{BH}	4.7±1.6
Bolometric luminosities (10^{46} erg s^{-1})	
L_{bol} at 1350Å	4.7±1.6
L_{bol} at 3000Å	3.8±1.2
L_{bol} at 5100Å	7.1±1.5
Line luminosities (10^{44} erg s^{-1})	
Ly-α	3.33±0.10
N V	3.71±0.15
C IV	0.66±0.08
Mg II	1.23±0.19

Table 4.4: Optical and near-IR properties of DES0141−54. The FWHM are reported in km s^{-1}; λL_λ is the continuum luminosity near the CIV (1350Å) and the MgII (3000Å) lines in unit of 10^{46} erg s^{-1}; the black hole mass is in unit of 10^8 $M_\odot$. The bolometric luminosities are not corrected for the inclination factor.

Accretion disk models

The optical and IR data can be used to estimate the black hole mass and the accretion rate independently from the virial method (see Sect. 1.3.2). More specifically, we modeled the accretion disk emission with the standard Shakura & Sunyaev model (SS73) and a super-Eddington model (SE, Ohsuga et al. 2002), which is more suited to sources that accrete close to the Eddington limit. The SS73 model that better represents our data is shown in Fig. 4.14 (red dashed line) and describes the emission around a black hole with $M_{BH}= 8\times10^8 M_\odot$ from a disk with a luminosity $L_{disk} = 10^{46}$ erg s^{-1}.

The SS73 model is very well known, but has several limitations. The main problem is related to the possibility for high redshift objects to accrete close to the Eddington limit. Ohsuga et al. (2002) introduced a correction to the standard disk geometry when the disk emission is close to $30\%L_{\rm Edd}$. In this case the radiation pressure affects the geometry and the optical thickness of the disk inner region, hence photons are advected toward the black hole faster than being radiated away. This happens within the so–called photon-trapping radius ($R_{\rm pt}$ already defined in Sect. 1.3.2) where the luminosity emitted by the disk drops dramatically. Outside $R_{\rm pt}$, the disk emits as SS73, and therefore the optical–IR SED can be well approximated by a SS73 truncated at $R_{\rm pt}$, if larger than $3R_{\rm Schw}$. Assuming this correction to mimic a close–to– or SE behavior, our data are best described by a black hole of $3\times10^8 M_\odot$, accreting at $\dot{M}=3.5\times10^{26}$ g s$^{-1}\simeq 8\dot{M}_{\rm Edd}$ and emitting $L_{disk}=10^{46}$ erg s$^{-1}\simeq 24\%L_{\rm Edd}$ (blue solid line in Fig. 4.14).
Figure 4.14 shows that the two best models are very similar but correspond to quite different values of M_{BH}. This difference shows the level of uncertainty on the M_{BH} derived through this method. However the M_{BH} values computed with these two models are both consistent with the values obtained from the virial method, considering the global uncertainties on the used relations (0.4-0.5 dex). Therefore, we can conclude that the SMBH hosted by DES0141−54 has a mass between 3×10^8 and 8×10^8 $M_\odot$.

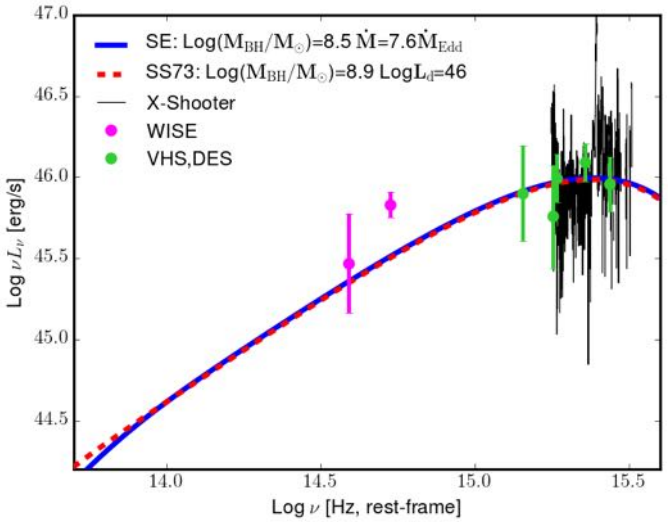

Figure 4.14: Accretion disk models of the optical spectrum and the optical–IR photometric data of DES0141−54. Red dashed line represents the best modeling of SS73, instead the blue line represents the best SE model. We corrected the spectrum and the photometric points for absorption due to intervening HI clouds following Meiksin (2006).

4.6.4 Modelling the Spectral Energy Distribution

As resulted from our analysis, DES0141−54 is, on the one hand, a very radio powerful high-z FSRQ, which strongly supports its blazar nature; on the other hand, it has an X-ray luminosity that is very low compared to most (∼98%) of the blazar population, assuming that the comparison BZCAT sample is representative of the entire blazar population in terms of X–ray-to-radio luminosity ratio. Therefore we tried to reproduce the SED of DES0141−54 with the model fully described in Ghisellini & Tavecchio (2009) to understand whether such a low X–ray luminosity is still compatible with the theoretical predictions of the beaming model.

The model of Ghisellini & Tavecchio (2009) assumes that most of the jet radiation is produced by relativistic electrons located at a distance $R_{\rm diss}$ from the central black hole. The emitting plasma is moving at a relativistic velocity $v = \beta c$ corresponding to the bulk Lorentz factor Γ. The viewing angle θ is small, so that the relativistic Doppler factor δ is >1. This is a one-zone, leptonic model, in which relativistic electrons emit via non–thermal processes: synchrotron, SSC and EC scattering of photons produced externally to the jet, by the accretion disk, the BLR, the dusty torus and by the hot thermal corona. The emitting particle energy distribution is derived through a continuity equation, assuming continuos injection, radiative cooling, possible pair production and pair emission. The injected particle distribution $Q(\gamma)$ [cm^{-3} s^{-1}] is a smoothly broken power law of index s_1 [i.e. $Q(\gamma) \propto \gamma^{-s_1}$] below $\gamma_{\rm b}$ and s_2 above, where $\gamma_{\rm b}$ is the break energy. This particle distribution is assumed to be injected for a light crossing time and the spectrum is calculated at the end of the injection.
The overall rest frame SED (in νL_ν vs ν) of DES0141−54, from radio to X–rays, is shown in Fig. 4.15, together with the model that describes the SED qualitatively, using a small viewing angle (θ), equal to $1/\Gamma$. This is the typical SED of a high-z blazar: the synchrotron emission peaks in the sub–mm band and the iC in the GeV band, leaving the accretion disk component *naked* and thus observable. Table 4.5 lists the parameters of the used model. Some of them are computed independently of the model ($M_{\rm BH}$ from the virial method, L_{disk} from the SS73 disk modeling using the virial mass, R_{BLR} and R_{torus} are computed from L_{disk}[6]) and then used as input parameters. The other input parameters are R_{diss}, Γ, θ, δ, γ_b, γ_{max}, s_1 and s_2 (see Ghisellini & Tavecchio 2009 for details). Finally P_e and B are the output parameters. The values used for this model (all the input parameters and P_e) are rather typical for FSRQs at high redshift (see e.g., Sbarrato et al. 2012b; Ghisellini et al. 2015a). This means that the observed weak X-ray emission of DES0141−54 is still consistent with the blazar hypothesis. However to take into account the very powerful radio emission, a high value of the AGN magnetic field is needed. In our case B∼9 G, which is higher with respect to the typical values (<B> = 4.6 G) found in Ghisellini & Tavecchio (2015) for powerful *Fermi* blazars: only 6% of these powerful FSRQs have a B equal or higher than that of DES0141−54. A large value of the magnetic field is consistent with a relatively small black hole mass, as discussed in Ghisellini & Tavecchio (2009), which derived that the magnetic energy density (U_B) $\propto 1/M_{\rm BH}$, and, therefore, B $\propto M_{\rm BH}^{-1/2}$ (in according also with SS73 model). This can explain why, in our source, the synchrotron process is dominating the overall electromagnetic output. As a consequence, DES0141−54 is expected to be faint in γ–rays, and not detectable by *Fermi* as shown in Fig. 4.15.

$M_{\rm BH}$ (1)	$L_{\rm disk}$ (2)	$L_{\rm disk}/L_{\rm Edd}$ (3)	$R_{\rm diss}$ (4)	$R_{\rm BLR}$ (5)	$R_{\rm torus}$ (6)	$P'_{\rm e,45}$ (7)	B (8)	Γ (9)	$\theta_{\rm V}$ (10)	δ (11)	$\gamma_{\rm b}$ (12)	$\gamma_{\rm max}$ (13)	s_1 (14)	s_2 (15)
4×10^8	8.32	0.16	120	288	5.4e3	0.13	9.63	10	5.7	10.07	2.e2	3e3	1	2.5

Table 4.5: Adopted parameters for the jet model. Col. (1): black hole mass in solar masses; Col. (2): disk luminosity in units of 10^{45} erg s^{-1}; Col. (3): disk luminosity in units of the Eddington luminosity; Col. (4): distance of the dissipation region from the black hole, in units of 10^{15} cm; Col. (5): size of the BLR, in units of 10^{15} cm; Col. (6): size of the torus, in units of 10^{15} cm; Col. (7): power injected in the jet in relativistic electrons, calculated in the comoving frame, in units of 10^{45} erg s^{-1}; Col. (8): magnetic field in G; Col. (9): bulk Lorentz factor; Col. (10): viewing angle in degrees; Col. (11): relativistic Doppler factor; Col. (12): break random Lorentz factor of the injected electrons; Col. (13): maximum random Lorentz factor of the injected electrons; Col. (14): slope of the injected electron distribution before the break; Col. (15): slope of the injected electron distribution beyond the break.

[6] L_{disk}: $R_{BLR}=10^{17}\sqrt{L_{disk,45}}$ cm and $R_{torus}=2.5\times10^{18}\sqrt{L_{disk,45}}$ cm, see Ghisellini & Tavecchio 2009 for details.

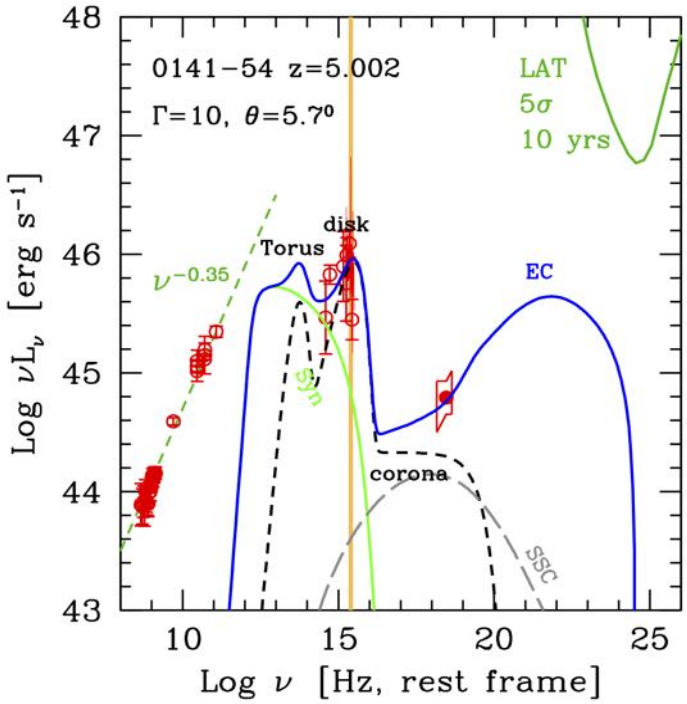

Figure 4.15: SED of DES0141−54 from the radio to X–ray frequencies: the solid blue line shows the theoretical blazar model; the dashed black line is the spectrum of an accretion disk, together with the IR torus radiation and the X–ray emission produced in the hot corona; the solid light green line refers to the synchrotron emission; the grey long dashed line is the SSC component. The vertical orange line marks the position of the Ly-α break. As described in Ghisellini & Tavecchio (2009) the model does not reproduce the radio part of the SED because the jet emitting region that interacts with the external photons is compact and therefore auto–absorbed at low frequencies. We also report in green the *Fermi*-LAT sensitivity curve after 10 years (at 5σ) that shows that our predictions are consistent with a non detection by *Fermi*.

4.7 Summary

In this chapter I presented the selection of $4.5 \leq z \leq 5.5$ (*r-dropout*) blazars in the southern hemisphere, thus extending the results from CLASS survey (chapter 3). The primary aim was to increase of the number of $z \geq 4.5$ blazars discovered so far, by renouncing to the completeness and homogeneity of the selection.

To perform this selection the combination of SUMSS (in the radio) and DES DR1 (in the optical) has been exploited. The intersection between these two surveys covers the largest sky area in the south currently possible (3500 deg^2). The search has led to the discovery one new z=5 blazars, DESJ014132.4−542749.9 (hereafter DES0141−54). As well as DES0141−54 we selected other two candidates, but their SEDs are better represented by an absorbed quasar and an elliptical galaxy at lower redshift. Therefore, they were not spectroscopically observed, to the detriment of reaching a high level of selection completeness.

The discovery of DES0141−54 is in agreement with our expected predictions based on the number of objects in the CLASS sample with a radio flux larger than 100 mJy (similar to that of DES0141−54, 2 objects) and the cosmological evolution presented in Mao et al. (2017).

DES0141−54 is characterized by a flat radio spectrum on a wide range of frequencies, from 76 MHz to 20 GHz, observed frame (456 MHz to 120 GHz in the source rest frame) and a high radio-loudness ($R > 10^4$), which are typical features of blazars, but it has a weak X-ray emission compared to other blazars at low and high redshift. Indeed, DES0141−54 appears to belong to a

minority (2%) of the total blazar population that is characterized by a very weak X–ray luminosity. Using a simple beaming model, we have shown that the very powerful radio luminosity and the weak X–ray emission can be explained with a very high value of the magnetic field (B$\sim$9 G). X–ray data of better quality and at larger energies (above 10 keV observed frame), as well as a long-time scale X–ray monitoring, will be necessary in order to firmly constrain the source orientation and the physical properties of the jet emission.
The X–ray properties of DES0141−54 show an opposite trend with respect to that of other high-z (z>4) blazars, which are characterized by an intense X–ray emission. This fact suggests that a X–ray selection of blazar candidates prevents the selection of such X–ray weak sources.
A high resolution follow-up of DES0141−54 is ongoing in the radio band with the Long Baseline Array (LBA, P.I., Gabányi K., Co. P.I. Belladitta S.) in order to study the radio properties on mas scale, unveiling the parsec-scale emission of this high-z AGN.
Finally, from the analysis of the optical and infrared spectrum, and from the disk modeling, we found that DES0141−54 hosts a small SMBH (M_{BH} = 3-8$\times10^8$ $M_\odot$) with respect to the SMBHs hosted in other RL sources at similar redshift (typically around $10^9 M_\odot$, see e.g., Shen et al. 2011; Trakhtenbrot et al. 2011; Ye et al. 2014). This confirms that using deep photometric catalog (like the DES DR1) we can discover less massive, and therefore less luminous, high-z sources.

Chapter 5

Searching for 4.5<z<5.5 blazars in the NVSS+PS1 surveys

This chapter is based on data not published yet.
My contribution to the work: candidates selection, data reduction and analysis of the TNG spectrum, analysis of the near-IR LBT spectra, of the radio properties, including the VLASS archival image, and of the X–ray properties of the new discovered blazar (PSO J1244+86), P.I. of the $Swift$–XRT observation, virial black hole mass estimation and discussion of the result.

Chapter 4 reports the selection of 4.5≤z≤5.5 blazars in the southern hemisphere and the discovery of an X–ray weak blazar at z=5: DES0141−54. With this source the number of blazar known at z>5 has been increased to 7 sources.
To further increase the number of blazars at 4.5≤z≤5.5, we extended the search also in the northern sky above 75°, a region which is not covered by the CLASS (see Fig. 2.8), by cross-matching the NVSS in the radio band (Sect. 2.4.1) with the PanSTARRS PS1 (Sect. 2.4.2) in the optical. The intersection between these two surveys at declination larger than 75° covers 690 deg^2 (Fig. 5.1). We used the *dropout* technique described in details in Sect. 2.3 to search for z≥4.5

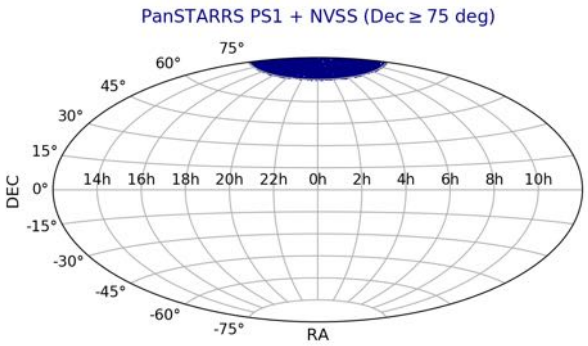

Figure 5.1: The common area of Pan-STARRS PS1 and NVSS at Dec≥75°, in which we searched for 4.5<z<5.5 blazar candidates. It consists of 690 deg^2.

blazars in this area. In particular, we searched for *r-dropout* objects (i.e. with a large $r-i$ and a blue $i-z$ colors). If we had adopted the same radio and optical thresholds used for CLASS selection (radio flux >30 mJy and optical magnitude <21) in 690 deg^2 we would have expected ∼0.3 blazars at redshift between 4.5 and 5.5. To increase the probability of discovery, we decided

to use a magnitude limit of 21.5. This is the faintest magnitude that we can considerer in order to have a reasonable spectroscopic observation (few hours) with the ground based telescopes. This magnitude limit still guarantee that the dropout is significant if the source is not detected in the bluest filters. Therefore, taking into account this optical limit, the radio and optical characteristics of high-z CLASS sources and the cosmological evolution presented in Mao et al. (2017), we expected to find ∼1 blazar at z≥4.5 in the common area of NVSS and Pan-STARRS PS1 at Dec≥75°, i.e. we have a low, but not negligible, probability to find one source. We decided not to reduce the radio flux limit to keep the radio positional error within ∼2″, something that significantly limits the number of radio/optical spurious matches and, therefore, the contamination from stars (see below for details).
In the following I describe the steps adopted in this selection, and the discovery of another powerful RL AGN at z=5.3: PSOJ124413.902+862554.07.

5.1 Candidates selection

From the NVSS catalog we selected only sources with a radio flux density larger than 30 mJy and point-like. These strong radio sources have a higher chance to have the relativistic jet pointed toward us. Moreover, this flux limit allowed us to select only NVSS objects with a low (<2″) radio positional error, thus minimizing the inclusion of contaminants (mainly stars) in the cross-match with the Pan-STARRS database. Finally under this radio threshold we did not expect a significant number of blazars in this area of the sky.
From the NVSS we retrieved a catalog of 118552 sources that we uploaded on the PanSTARRS casjob[1] for the cross-correlation. We searched for all the optical counterparts with a i magnitude brighter than 21.5 in a radius equal to the radio positional error of each radio sources (∼0.7-1.9″). From the cross-correlation we required the following optical parameters: optical coordinates and errors, number of detection in each PS1 filter, PSF, aperture and Kron magnitude for each band[2]. The used SQL query used for the cross-match is reported in Appendix E.
The cross-correlation gave an output catalog of 45251 entries, in which some objects have a multiple detection (the primary and secondary detection of the Pan-STARRS database). For all the sources with no detection in r-band we assumed a magnitude limit (at 5σ) of 23.2. Then all the objects that satisfied the following filters have been selected:

- outside the Galactic Plane: $|b| \geq 20$ ° (to minimize contamination from stars)
- declination above 75°
- no detection in g-band or g magnitude weaker than 22.5 and number of detection in g band equal to 0
- detection in i-band (both PSF and Kron magnitude)
- dropout: rPSFMag-iPSFMag ≥ 1.1 (see Fig. 3.3)
- blue continuum: iPSFMag-zPSFMag ≤ 0.5
- optical stellaricity: iPSFMag-iKronMag < 0.05

After the application of these filters we were left with 6 candidates, which have been cross-correlated with the WISE catalog, searching for all the infrared sources within 1.5″ from their

[1] https://mastweb.stsci.edu/ps1casjobs/
[2] The definition of this type of magnitude can be found at https://outerspace.stsci.edu/display/PANSTARRS/PS1+Source+extracti

optical position. This impact parameter guarantees to find the true mid-IR counterpart of the optical source, without contamination. After this cross-match, we imposed the same filters used for the CLASS sample selection, to remove low-z AGNs contaminants: the objects should be undetected in WISE (W2) or, if detected, z-W2 color has to be $\leq$5 (see chapter 3).
We remained with five objects, on which a visual inspection was performed: two candidates were removed due to the presence of a bright star at few arcsecond from their optical positions. We finally analyzed the SED of the 3 remaining sources and compare them with different templates (high-z quasar, elliptical galaxy, absorbed quasar). We found that only one of the candidates (PSO J124413.902+862554.07, hereafter PSO J1244+86) has the typical SED of a z$\geq$4.5 AGN (see Fig. 5.2). We therefore considered only this object for the spectroscopic follow-up.
The Pan-STARRS PS1 and WISE magnitudes of PSO J1244+86 are reported in Tab. 5.1. The

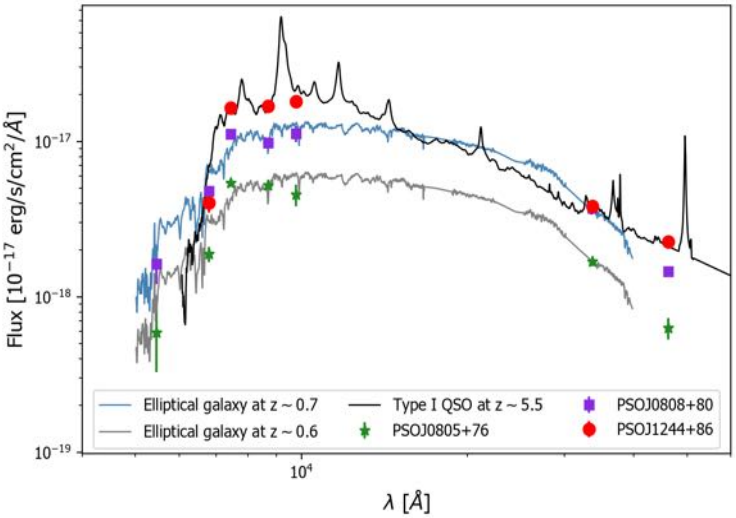

Figure 5.2: SEDs of the three candidates selected form the cross-matching of NVSS and PS1 at Dec $\geq$ 75°. The three candidates are reported with red points, violet squares and green stars. PSO J1244+86 photometric points (in red) are consistent with a template of high-z Type I AGN, while the other two sources are best represented by a template of low-z (0.6-0.7) elliptical galaxy. The photometric points are plotted at the effective wavelengths of the Pan-STARRS filters (see Fig. 2.13).

offset between the Pan-STARRS PS1 optical and WISE mid-IR positions is 0.85″. Figure 5.3 shows the optical images of PSO J1244+86 in the different g, r, i, z, Y bands. The Pan-STARRS PS1 coordinates of the source are: R.A. = 191.05696 deg, Dec = +86.43172 deg.

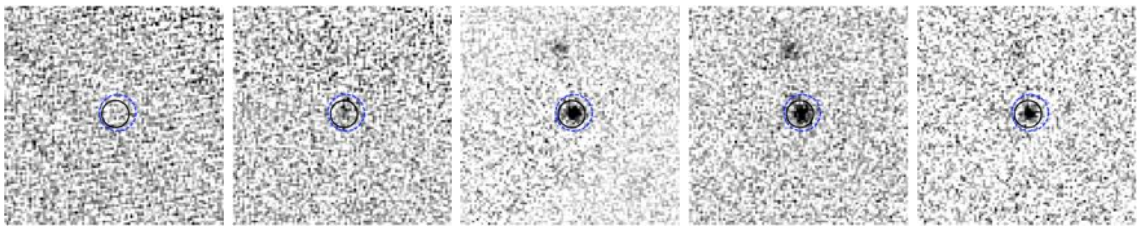

Figure 5.3: 0.4′×0.4′ Pan-STARRS PS1 g, r, i, z, Y cutout images of PSO J1244+86. Its optical position is marked with a black circle of 1.5″ of diameter. The radio NVSS position is marked with a blue dashed circle, as large as the radio positional error reported in the catalog (1.7″). All images are oriented with north up and east to the left.

filter	λ (μm)	mag	Ref. survey
r	0.680	21.92 ± 0.15	PS1
i	0.745	20.21 ± 0.04	PS1
z	0.870	19.83 ± 0.03	PS1
Y	0.978	19.51 ± 0.06	PS1
$W1$	3.4	15.819 ± 0.035	WISE
$W2$	4.6	15.067 ± 0.051	WISE

Table 5.1: Optical and near-IR magnitude of PSO J1244+86. Col (1): optical / near-IR filters; Col (2): filter central wavelength in μm; Col (3): observed magnitude; W1 and W2 WISE are in Vega system; Col (4): reference survey.

5.2 Optical, near-IR observations and data reduction

In this section the spectroscopic data that allowed us to confirm the high-z nature of the selected source, PSO J1244+86, are reported.

5.2.1 TNG observation

After its identification in the Pan-STARRS PS1 database, we performed a dedicated spectroscopic follow-up of PSO J1244+86 with DOLORES installed at the TNG. We confirmed PSO J1244+86 as a high-z AGN the night of the 21 June 2018[3], with a single 30 minutes observation with the LR-R grism and a long-slit of 1″ width (see Fig. 5.4). The data reduction was performed using

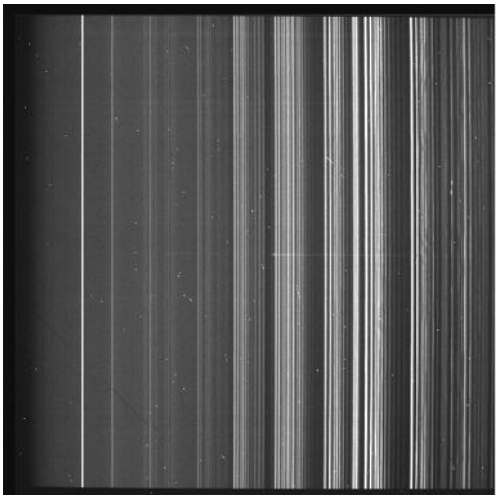

Figure 5.4: 30 minutes image of PSO J1244+86 taken at TNG on the night of 2018 June 21th. The spectrum of PSO J1244v86 is visible in the middle of the image.

IRAF following the same procedures used for DES0141−54 (see Sect. 4.2.1 for all the details). An exposure of a Ar+Ne+Hg+Kr lamp was done to ensure the wavelength calibration and the flux calibration was obtained by observing the G191-B2B (R.A.=05:05:30.62, Dec=+52:49:54.0:) spectrophotometric standard star of the catalogs of Oke (1990). The DOLORES/TNG discovery spectrum of PSO J1244+86 is shown in Fig. 5.5. The object redshift was measured by fitting the Ly-α line with a single Gaussian profile, using the IRAF task *splot*. The resulting value is z = 5.33 ± 0.03, confirming the high redshift nature of the selected candidate.

[3]We thanks Marco Pedani, staff astronomer at the TNG, to have done the observation.

5.2.2 LUCI/LBT follow-up

We performed a spectroscopic follow-up with LUCIFER (LBT NIR Spectroscopic Utility with Camera and Integral Field Unit for Extragalactic Research; Ageorges et al. 2010) at the LBT in order to extend the wavelength range in the near-IR band and detect the CIV and the MgII emission lines, which can be used to estimate the central black hole mass of PSO J1244+86. The observation was carried out on the night of 2019 May 3 (P.I. Moretti A., program ID: LBT2018AC123500-1) and consisted of 12 exposures of 270 second each in nodding mode in the sequence ABBA, with a total integration time of 1h and 48 minutes. The medium seeing along the night was 0.9″ and the mean air mass was 1.7. We decided to use the grism 200 with the zJ and HK filters on LUCI1 and LUCI2 respectively in order to cover all the spectral range and detecting the CIV (LUCI1) and the MgII (LUCI2) simultaneously. Indeed the G200-zJ configuration allowed us to observe the wavelength range from 0.9 to 1.2 μm, where the CIV line is expected (λ_{obs} = 9805Å at z=5.3). Instead the G200-HK configuration covers the range in which the MgII line falls (expected λ_{obs} = 17700Å), from 1.5 to 2.4 μm. The data reduction was performed at the Italian LBT Spectroscopic Reduction Center, through scripts optimized for LBT data, as already done for the CLASS objects (see Sect. 3.1). Each spectral image was independently bias subtracted and flat-field corrected. Sky subtraction was done on 2D extracted, wavelength calibrated spectra. Wavelength calibration was obtained from spectra of arc lamps reaching a rms of 0.25Å on LUCI1 and 0.5Å on LUCI2. In Fig. 5.5 we report the LBT/LUCI1 and the LBT/LUCI2 spectra in which the CIV the CIII] and the MgII lines are detected. By fitting these lines with Gaussian profiles, with the IRAF task *splot*, we confirmed the redshift previously estimated with the TNG data: z_{CIV} = 5.30±0.03, z_{CIII} = 5.32±0.02 and z_{MgII} = 5.32±0.03

5.3 Archival radio photometry

Beside the NVSS detection at 1.4 GHz, PSO J1244+86 has also a detection at 325 MHz in the WENSS (see Sect. 2.4.1 for the survey description). Thanks to these two flux densities, Massaro et al. (2014) included PSO J1244+86 in the LOw frequency Radio CATalog of flat spectrum sources (LORCAT). Moreover it was observed by Healey et al. (2009) at 4.85 GHz with the Effelsberg 100 m telescope.
PSO J1244+86 is also clearly detected at 3 GHz in the VLASS (see Sect. 2.4.1 for the survey description). The survey has not been concluded yet but, to date, quick look images are available from Canadian Astronomical Data Centre (CADC). These quick look images can be used to extract the flux density of PSO J1244+86, after taking into account all the possible source of errors[4] that affected flux densities and radio morphology. PSO J1244+86 has been observed both during the first campaign of the first epoch (VLASS 1.1) in 2017 and the second campaign (VLASS 2.1) in 2020. Since the data of the first epoch suffers from phase errors, i.e. the false impression that an object has a particular morphology or size, we performed the analysis only on second epoch data, the VLASS 2.1 image (top panel of Fig. 5.6). The object appears compact, similar to the beam shape (major axis = 4.372″, minor axis = 2.241″, P.A. = 80.75 deg). Therefore, to quantify the flux density and the size of the source we performed a single Gaussian fit, by using the task IMFIT of the Common Astronomy Software Applications package (CASA, McMullin et al. 2007). We first selected the region on which perform the Gaussian fit[5], which is large enough to contain an area without the source (to compute the noise), but it does not contain other objects

[4]On this web page the list of problematics related to the use of quick look images are reported: https://science.nrao.edu/vlass/data-access/vlass-epoch-1-quick-look-users-guide

[5]We indicated the pixel of the bottom left corner (BLC) and of the top right corner (TRC) of the region: [958-1619]pixels, [1023-1664]pixels.

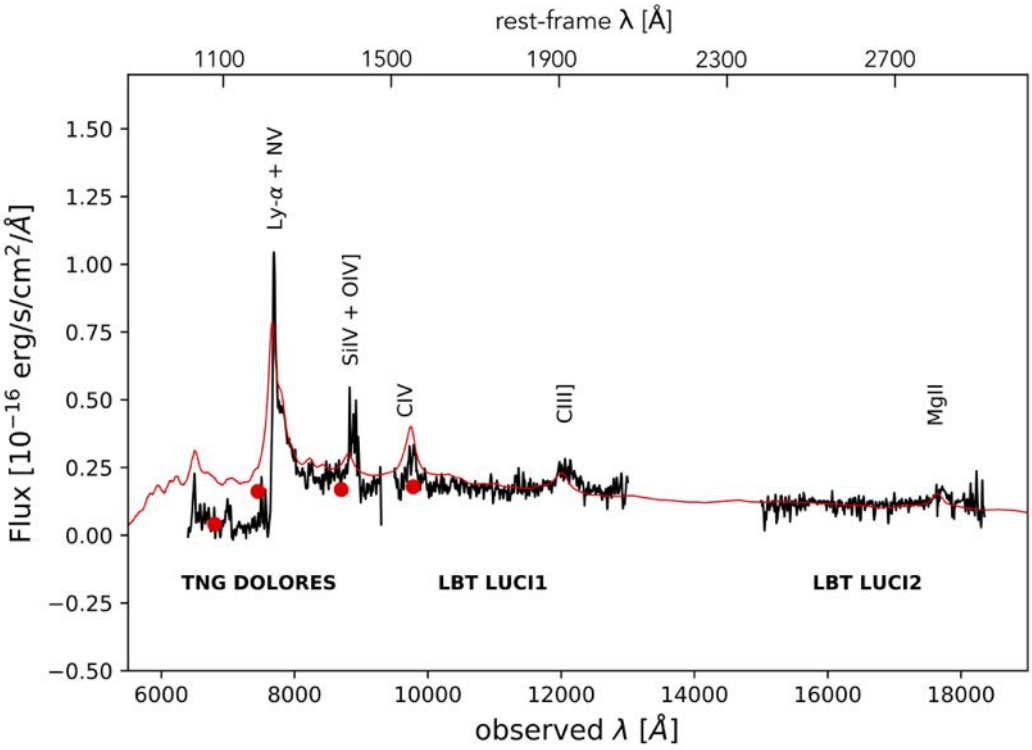

Figure 5.5: Optical and near-IR spectra of PSO J1244+86 taken at TNG and LBT respectively. The most important visible emission lines are marked. In red we overplot the quasar template of Vanden Berk et al. (2001) at the redshift of the quasar for comparison. Red points are the photometric Pan-STARRS PS1 data.

that could contaminate the fit.
The measurements of total and peak flux densities and sizes obtained using by the best fit are listed in Table 5.2, while the model and the residual images are shown in Fig. 5.6 (center and bottom panels). The fact that the residual image is completely cleaned allowed us to infer that the Gaussian fit is good. Also, the residuals are at the thermal noise level, which is a strong indication that the Gaussian fit is robust (χ^2=1.09). The position of the source estimated by the fit is: RA = 12:44:13.57949 ± 0.01239s, Dec = +86:25:54.04861 ± 0.00021s, that is at 0.3″ from the optical PS1 position. By comparing the dimension of the source as estimated by the single

Obs. Freq. (GHz) (1)	Total flux density (mJy) (2)	Peak surface brightness (mJy beam^{-1}) (3)	major axis (arcsec) (4)	minor axis (arcsec) (5)	P.A. (deg) (6)
3.0 (18.9)	40.57±0.32	38.83±0.17	4.5212±0.0274	2.2646±0.0070	83.87±0.17

Table 5.2: Properties of the quick look VLASS 2.1 image of PSO J1244+86. Col (1): observing frequency (rest-frame frequency in parenthesis); Col(2): integrated flux density; Col(3): peak surface brightness; Col(4)-Col(5): major and minor axes of the source; Col(6) position angle (east of north).

Gaussian fit with the beam size, we concluded that our source is point-like and not resolved.
In Table 5.3 all the archival radio flux densities of PSO 1244+86 are reported.

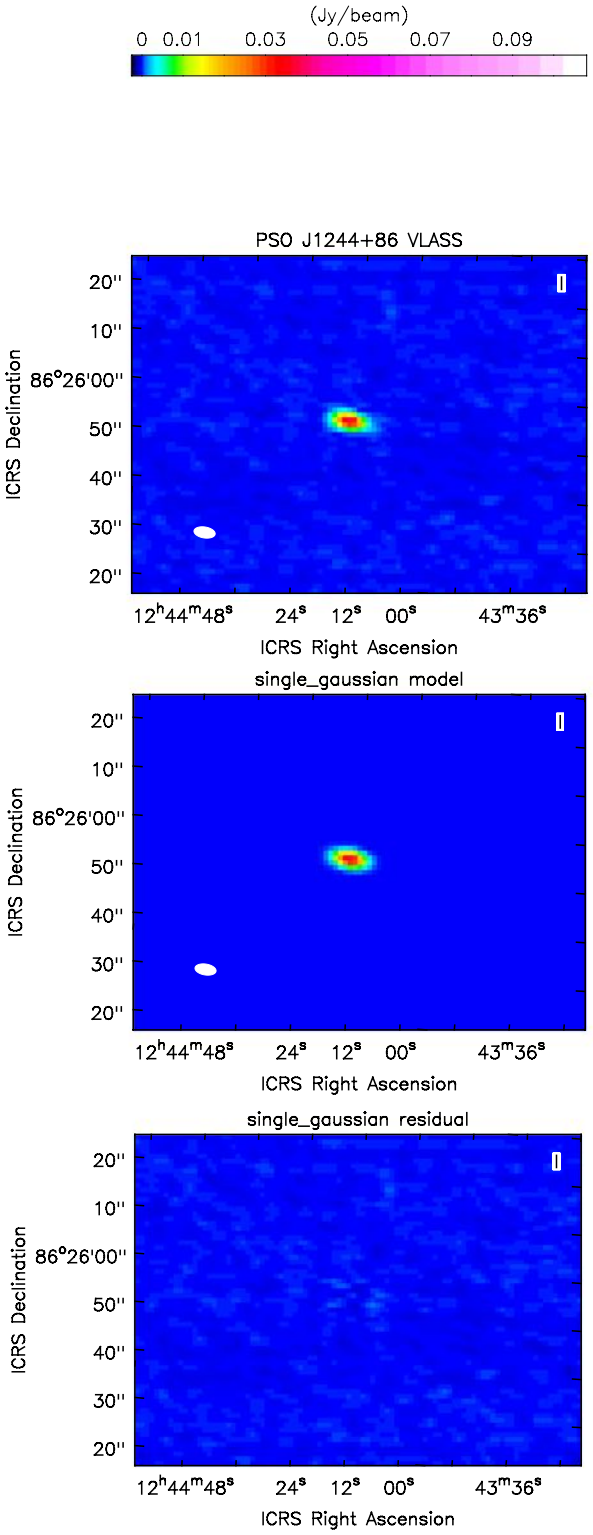

Figure 5.6: VLASS 2.1 quick look image of PSO J1244+86 (*top panel*), Gaussian model (*center*) and residual image (*bottom*). Above the images the color-bar that shows the surface brightness of the source in mJy beam^{-1} is reported; instead at the bottom left corner the beam is shown. North is up, east is left.

Freq (GHz)	S_ν (mJy)	survey
0.325	19.0±3.3	WENSS
1.4	74.2±2.3	NVSS
3.0	40.57±0.32	VLASS
4.85	33.7±1.3	

Table 5.3: Integrated radio flux densities (observed frame) of PSO J1244+86 from archive and from the VLASS 2.1 image analysis. The VLASS integrated flux density are systematically low by 3% (see VLASS quick look webpage for details.

5.4 *Swift*-XRT observation

PSO J1244+86 was observed in X–ray by the *Swift*–XRT telescope (target ID: 3110833; P.I. Belladitta S.). The observations were carried out between September, October and November 2020 and consisted of 44 segments for a total exposure time of 47.81ks. Data have been reduced through the standard data analysis pipeline (Evans et al. 2009), running on the UK *Swift* Science Data Centre web page[6] using HEASOFT v6.26.1. The source is clearly detected with a total of 55 counts and with an expected background of 7 count in [0.5-10] kev energy band. The standard (PSF-fitted) *Swift*–XRT position of the source (Fig. 5.7), calculated by the detected and centroid algorithm is RA = 12:44:12.97, Dec = +86:25:57, with an uncertainty of 3.5″ (90% confidence). This is at 3.0″ from the optical PS1 position. A standard spectral analysis has been performed using XSPEC (v.12.10.1) by fitting the observed spectrum (Fig. 5.8) with a single power law with the absorption factor fixed to the Galactic value (6.46×10^{20} cm^{-2}) as measured by the HI Galaxy map of Kalberla et al. (2005). We measured a photon index (Γ_X) of 1.32 ± 0.22 and a flux of $8.11^{+1.63}_{-1.47}\times10^{-14}$ erg s^{-1} cm^{-2} in the [0.5-10] keV energy band and a luminosity of $5.53^{+1.59}_{-1.35}\times10^{45}$ erg s^{-1} in the [2-10] keV energy band. The value of the photon index is typical of blazars and in line with the value found for the CLASS objects (Γ_X mean $\sim$ 1.4, see Sect. 3.6), suggesting that the X–ray emission of PSO J1244+86 is dominated by the jet emission, i.e. the object is a blazar.

5.5 Results

In this section I report the results on the multi-wavelength analysis (from radio to X–rays) of PSO J1244+86, including the computation of the SMBH mass.

5.5.1 Radio properties

From the radio flux densities listed in Table 5.3 and assuming a power law distribution for the continuum emission ($S_\nu \propto \nu^{-\alpha}$), the radio spectral index of PSO J1244+86 can be computed. We found that the radio spectrum is peaked (see Fig. 5.9). The spectral index between 325 MHz and 1.4 GHz ($\alpha^{1.4}_{0.325}$) is −0.93±0.28 and $\alpha^{4.85}_{1.4}$ (the spectral index between 1.4 and 4.85 GHz) is 0.65±0.09. Therefore PSO J1244+86 can be classified as a GPS, meaning a very young and compact (at arcsecond resolution) radio galaxy with a radio spectrum peaking above ∼1 GHz (observed frame). Healey et al. (2009) already defined this source as a GPS.
As already mentioned in Sect. 3.4, one of the most distant blazar ever discovered, Q0906+6930 (Romani et al. 2004) at z=5.47 shows a clearly peaked radio spectrum (Coppejans et al. 2017), but VLBI data found evidence of Doppler boosting (Zhang et al. 2017, Frey et al. 2018, An et

[6] https://www.swift.ac.uk/index.php

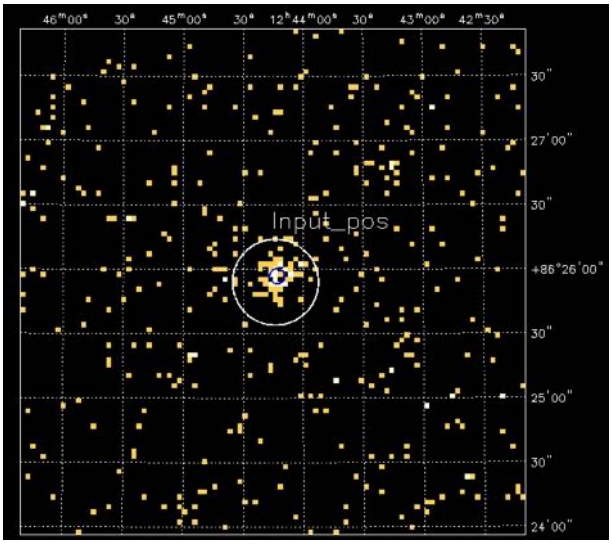

Figure 5.7: *Swift*–XRT image of PSO J1244+86 obtained with the detected and centroid algorithm executed on the UK *Swift* Science Data Centre web page. The white circle is the input position (20″ of radius) in which the algorithm search for the true source position (blue circle in the center, 3.5″ radius).

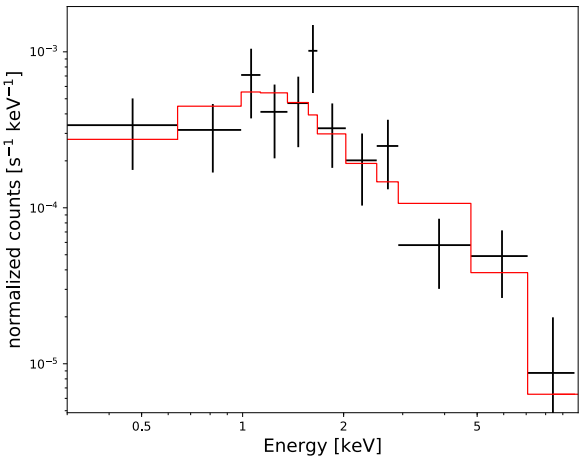

Figure 5.8: *Swift*–XRT observed spectrum of PSO J1244+86.

al. 2020). Therefore, the observation of a peaked radio spectrum does not exclude the presence of beamed jet. Finally we highlighted that the available radio detections are not simultaneous, i.e. they have been taken in different and distant periods (up to 30 years). A simultaneous observation at different radio frequencies (e.g., with the JVLA, from 0.2 to 40 GHz) is necessary to assess the real shape of the radio spectrum of PSO J1244+86.

To test the blazar nature of PSO J1244+86, we computed its radio-loudness (R), the parameter that quantify the level of power of the non-thermal synchrotron radio emission with respect to the thermal one originated in the accretion disk (see Sect. 1.1). As already said in Sect. 4.6.1 the majority of blazars at z≥4.5 has a log(R)>2.5. We calculated the R of PSO J1244+86 from the observed optical and radio flux densities following, as for DES0141−54, the equation of Shen et al. (2011) reported in Sect. 4.6.1. We used this definition for a direct comparison between PSO J1244+86, DES0141−54 and the other RL AGNs at z≥4.5 listed in Tab. C.1.

We estimated the 2500Å flux density directly from the LUCI2 rest-frame spectrum. The radio

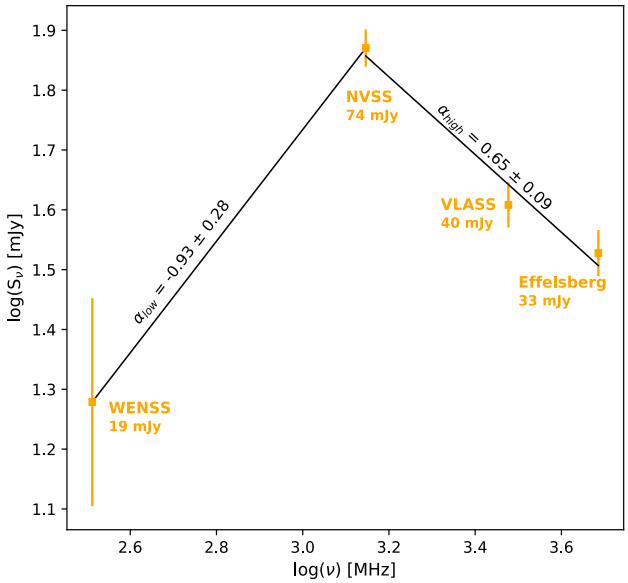

Figure 5.9: Radio spectrum (observed frame) of PSO J1244+86 from 0.325 to 4.85 GHz. The spectrum clearly show a peak around 1 GHz, hence the source can be classified as a GPS. The corresponding indexes of the low and high frequency part of the spectra are reported together with the reference surveys and the integrated flux densities.

flux density at 5 GHz rest-frame was computed from the 4.85 GHz observed flux density and assuming the high frequency spectral slope ($\alpha_{1.4}^{4.85}$). We obtained R = 1014±40. This value is typical of blazars at z≥4.5 (see Fig. 5.10), as already explained in Sect. 4.6.1, suggesting that the radio emission of PSO J1244+86 is beamed along our line of sight.

5.5.2 X–ray properties

In Section 3.6 we introduced a method to classify a source as a blazar using the X–ray properties based on the photon index (Γ_X) and the $\tilde{\alpha_{ox}}$, a parameter that describe the intensity of the X–ray emission with respect to the optical one (see Eq. 3.6). To calculate the $\tilde{\alpha_{ox}}$ of PSO J1244+86, the value of the monochromatic luminosity at 10 keV has been computed from the observed flux density at [0.5-10] keV. The luminosity at 2500Å instead has been measured from the flux density at 2500Å directly obtained from the LUCI 2 rest-frame spectrum: $L_{2500Å} = 5.22\pm0.21\times10^{31}$ erg s^{-1} Hz^{-1}. Therefore, the $\tilde{\alpha_{ox}}$ value for PSO J1244+86 is: 1.316±0.025. This value is typical of blazars both at low and high redshift. In Fig. 5.11 we reported the photon index as a function of $\tilde{\alpha_{ox}}$ for PSO J1244+86 compared to that of CLASS sources. Figure 5.11 shows that the X–ray classification suggests a blazar nature for PSO J1244+86. This is also confirmed by the fact that the X–ray emission of PSO J1244+86 is stronger and flatter with respect than that of a RQ AGN with the same optical luminosity according to the L_X-L_{UV} relation of Just et al. (2007), as shown in Fig. 5.12. This is an indication that the X–ray emission is dominated by the boosted jet component that can largely overwhelm the coronal emission.

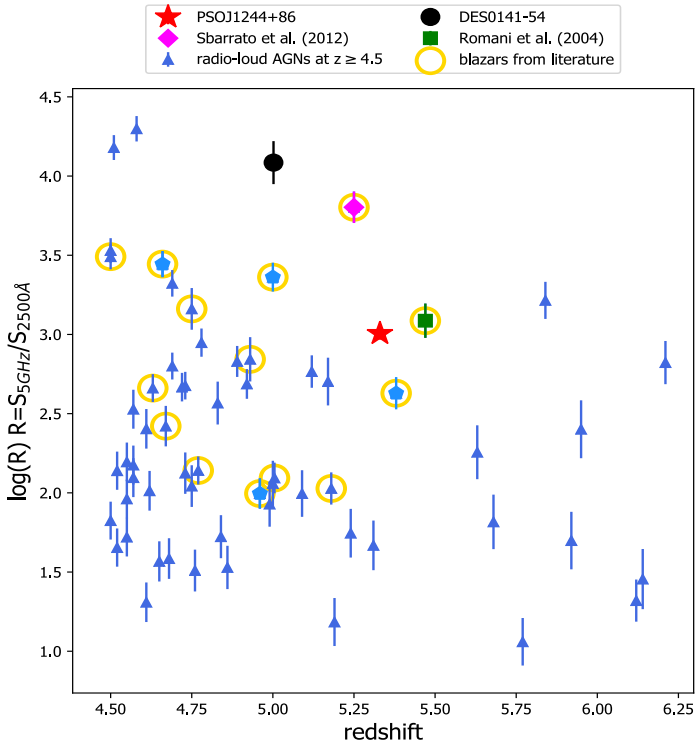

Figure 5.10: Radio-loudness comparison between PSO J1244+86 (red star) and the sample of z≥4.5 RL AGNs from the literature listed in Tab. C.1 (blue triangles). The black point represents DES0141−54 (described in chapter 4). PSO J1244+86 has a R similar to other blazars at the same redshift. The objects circled in yellow are all the confirmed blazars found in the literature. We point out that these are only the blazars with a validation in the literature.

5.5.3 CIV and MgII emission lines properties

This section reports the properties of the two emission lines (CIV and MgII) that can be used to compute the mass of the central SMBH hosted by PSO J1244+86.
Both lines widths have been characterized with the FWHM, by following different steps.

- We shifted the LBT/LUCI 1 and 2 spectra to the source's rest frame, using these two relations: $\lambda_{rest} = \frac{\lambda_{obs}}{1+z_{line}}$ and $F_{\lambda_{rest}} = F_{\lambda_{obs}} \times (1 + z_{line})$, where z_{line} is the redshift of the CIV and MgII emission lines reported in Sect. 5.2.2.

- We linearly fitted the continuum near the lines in two specific intervals free from spectral features and other emission lines. Actually AGNs show a power law spectrum, but in short intervals the linear fit is a good approximation.
  The choice of the continuum intervals depends on specific spectral features of the spectrum. Since the CIV is at the border of the LUCI 1 spectrum, we can use only the continuum on the right side of the line. We selected the interval 1690-1710Å (e.g., Denney et al. 2013) and we computed the mean value: 4.2×10^{-16} erg s^{-1} cm^{-2} A^{-1}. We then subtracted this value to the LUCI 1 spectrum (left panel of Fig. 5.13). In the LUCI 2 spectrum we selected the following two intervals near the MgII line: 2730-2755Å and 2845-2870Å. We verified that there was no contamination of other emission lines in these two intervals. Then we applied a linear fit between these two parts of the spectrum (left panels of Fig. 5.14). Finally we subtracted the continuum to the rest-frame spectra (right panels of Fig. 5.13 and 5.14).

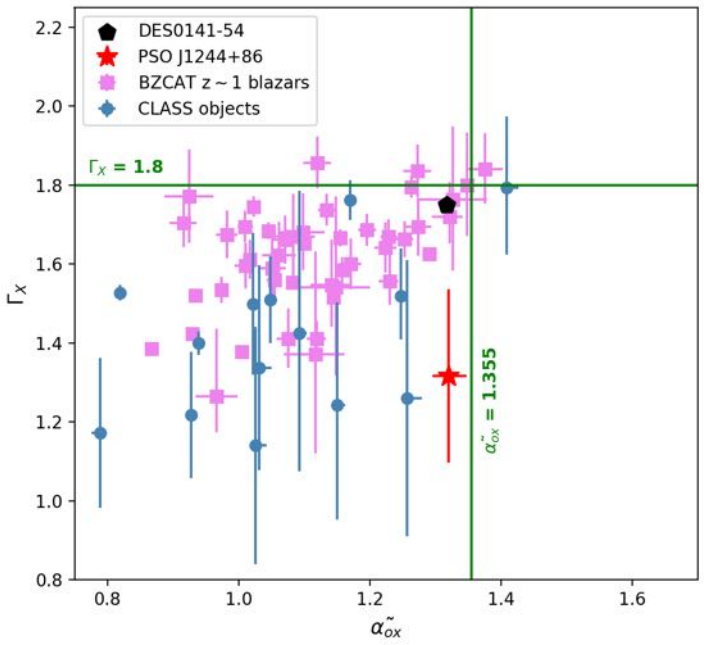

Figure 5.11: X–ray classification of PSO J1244+86 (red star) based on Γ_X and $\tilde{\alpha_{ox}}$. Blue points represent z≥4 CLASS objects. With violet squares we report the z∼1 blazars of the BZCAT sample already used in Fig. 3.6. Black pentagon is DES0141−54. The vertical and horizontal lines, defined in Sect. 3.6, divide blazars from non-blazar sources. This classification set PSO J1244+86 in the same region of the other blazars both at low and high redshift.

- On the LUCI 1 and LUCI 2 pseudo-continuum subtracted spectra we fitted the broad CIV and MgII emission lines with a single Gaussian profile (Fig. 5.15). Many works in the literature (e.g., Wang et al. 2009; Shen et al 2011; Wildy et al. 2018) demonstrated that the inclusion of a narrow component (produced by the NLR) in the MgII line fit leads to negligible effect on the FWHM of broad component. Therefore, we did not include this narrow component in the Gaussian fit. As shown in Fig. 5.14 an absorption feature is present in the middle of the MgII line: we masked it with the IRAF task *splot* before fitting the line profile. Since the existence of a strong narrow component (produced by the NLR) of the CIV line is controversial and difficult to detect (e.g., Wills et al. 1993; Shen & Liu 2012), we did not include this component in the line fit.

- We then computed the FWHM of the lines: FWHM (CIV) = 22.26Å (4310.88 km s^{-1}) and FWHM (MgII) = 26.76Å (2870.15 km s^{-1}).

The uncertainty on these values were evaluated through a Monte Carlo approach, used in other works (e.g., Shen et al. 2011; Shen & Liu 2012; Raiteri et al. 2020; Zuo et al. 2020). Each wavelength of the best fit model was perturbed randomly for 1000 times, according to a Gaussian distribution of the mean rms computed underneath the line profiles on the residual spectra (i.e the pseudo-continuum subtracted spectra from which the best-fit model has been removed). In this way we obtained 1000 different mock spectra of the line profile, from which we measured the line properties with the same procedure used on the real data (see Figs. 5.16 and 5.17). We computed the distribution of FWHM for these 1000 simulated spectra (Fig. 5.18), and the interval that contains 68% of the data in this distribution is taken as the statistical uncertainty on the best fit FWHM value. The obtained values are reported in Table 5.4.

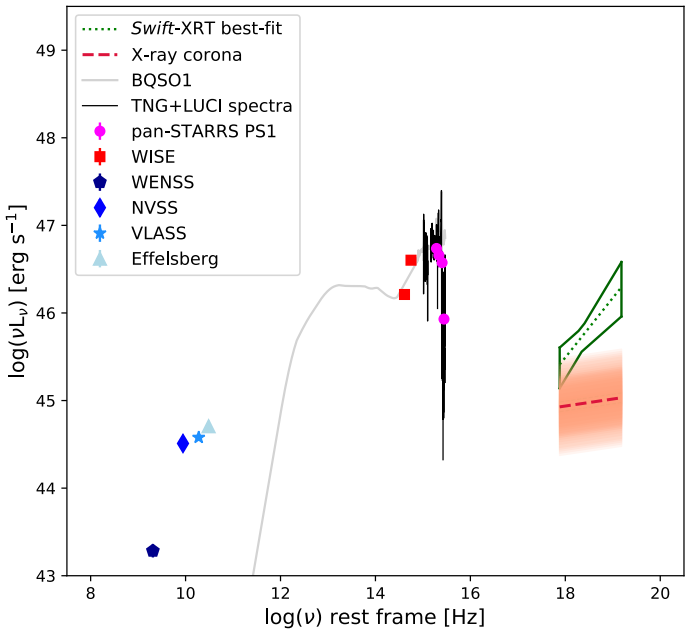

Figure 5.12: Rest-frame SED of PSO J1244+86 from radio to X–ray frequencies. In the X–ray we show the best fit emission in the observed [0.5-10] keV energy band (green dotted line) with its uncertainty. We also report the TNG and LUCI spectra (in black) and a quasar template (Polletta et al. 2007, light-grey line) as guide line. The red dashed line represents the coronal emission expected from a RQ AGN with the same $L_{2500Å}$ of PSO J1244+86 according to the relation of Just et al. (2007), and the orange shaded area is the 1σ uncertainty on this estimate.

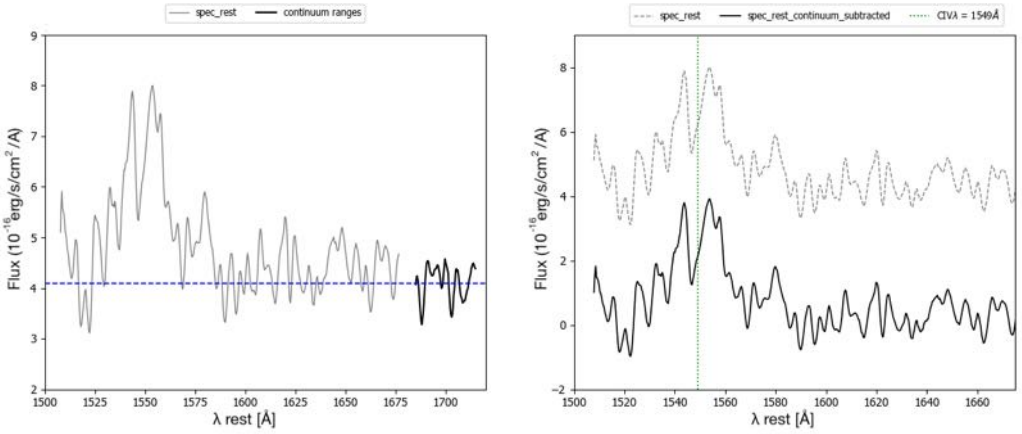

Figure 5.13: *Left panel*: linear fit of the continuum in the LUCI 1 rest-frame spectrum of PSO J1244+86 (blue dashed line). In black we show the continuum interval used for the fit. *Right panel*: in grey the original rest frame LUCI 1 spectrum is reported (dashed spectrum), instead in black we show the continuum subtracted one; the vertical green line represents the position of the rest frame CIV emission line at 1549Å.

5.5.4 Black hole mass estimates

We computed the mass of the SMBH hosted by PSO J1244+86 using the SE method generally described in Sect. 1.3. We followed the same formula used for DES0141−54 and reported in Eqs. 1.13 and 1.15. The rest frame continuum luminosities (λL_λ) at 1350Å and 3000Å have

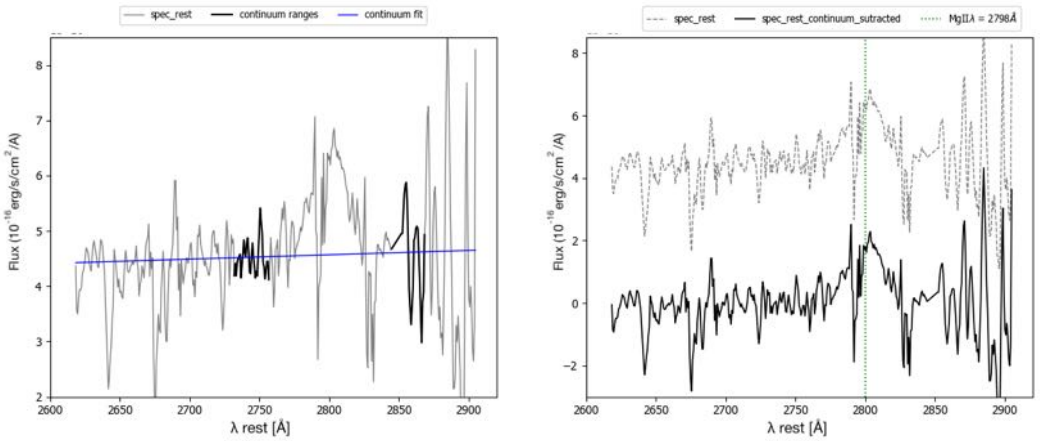

Figure 5.14: *Left panel*: Linear fit of the continuum in the LUCI 2 rest-frame spectrum of PSO J1244+86 (blue line). In black we show the two continuum intervals used for the fit. *Right panel*: the original rest frame LUCI 2 spectrum is reported in grey (dashed spectrum), instead, in black we show the continuum subtracted one; the vertical green line represents the position of the rest frame MgII emission line at 2798Å.

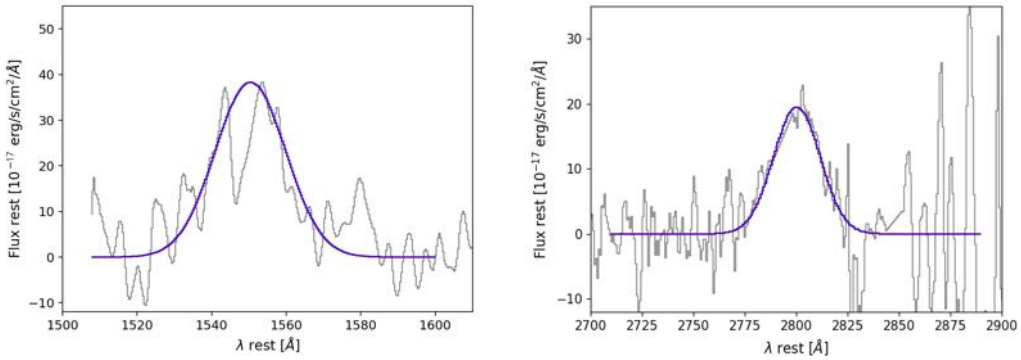

Figure 5.15: Gaussian fit of the CIV (*left*) and MgII (*right*) emission lines. The rest frame LUCI 1 and LUCI 2 spectra are reported in grey in both panels. The absorption feature in the MgII line has been masked.

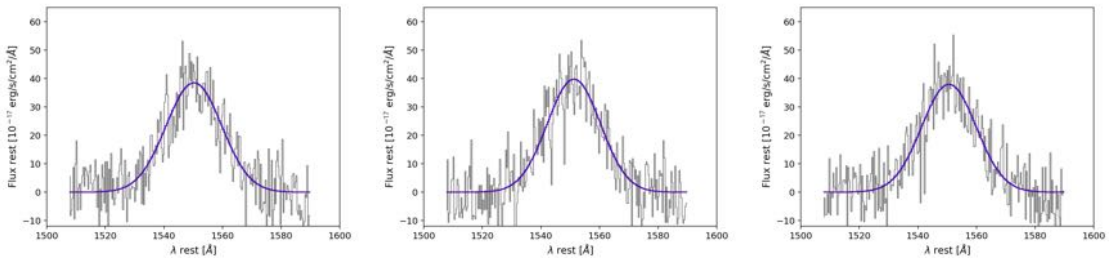

Figure 5.16: Examples of CIV Gaussian fit on mock spectra.

been directly estimated from the TNG and LUCI 2[7] rest frame spectra respectively. Their values are reported in Table 5.4. From the FWHM values estimated in the previous section, we finally

[7]Since the LUCI 2 spectrum at ∼3000Å is noisy, we used the continuum near the MgII line, between 2720Å and 2750Å.

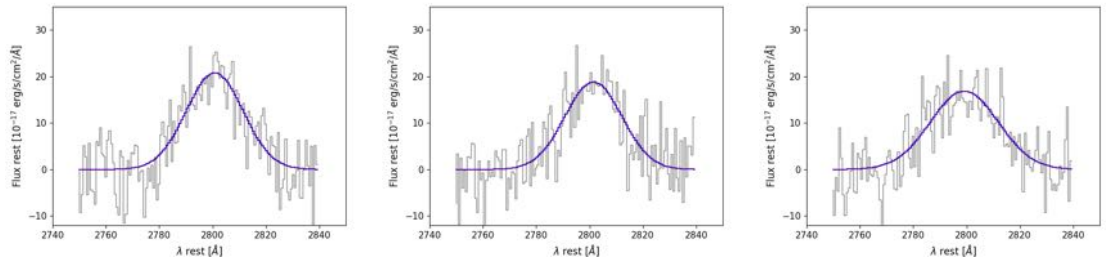

Figure 5.17: Examples of MgII Gaussian fit on mock spectra.

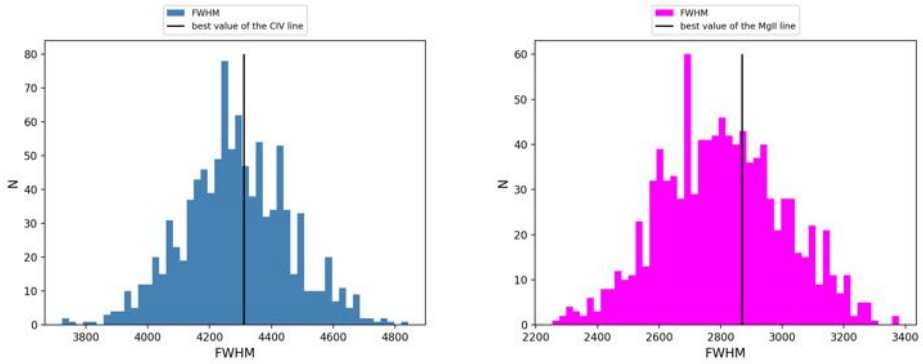

Figure 5.18: Distributions of the FWHM, derived from the fit on CIV (*left*) and MgII (*right*) mock spectra. The vertical lines show the best fit values.

computed the central BH mass of PSO J1244+86 (see Table 5.4). The reported errors are purely statistical. The intrinsic error associated to the used virial relations is 0.4 dex (Shen et al. 2011). As already mentioned in Sect. 1.3.1 the SE masses could be overestimated due to the relativistic jet contamination. To verify this possible bias also for PSO J1244+86 we followed the same approach adopted for DES0141−54 in Sect. 4.6.3. We computed the ratio $L_{CIV}/L_{1350Å}$ (or the $L_{MgII}/L_{3000Å}$)for PSO J1244+86 and we compared them with those of the RQ AGNs at z≥4 of the sample of Shen et al. (2011). The values of line luminosities of PSO J1244+86 are reported in Table 5.4. We did not find a significant offset between our source and the RQ AGNs. Therefore, we can infer that the relativistic jet does not strongly contaminate the optical continuum of PSO J1244+86, and, hence, its SE masses are not overestimated.

Eddington ratio

The values of black hole mass allowed us to derived the Eddington luminosity and the Eddington ratio (λ_{Edd}), which quantifies how fast is the accretion rate with respect to the Eddington limit. First we estimated the bolometric luminosity (L_{bol}) of PSO J1244+86. We used the continuum luminosities at 1350Å and at 3000Å and the following bolometric corrections:

$$L_{bol} = K_a\ L_{1350Å} \qquad L_{bol} = K_b\ L_{3000Å}$$

where K_a and K_b are the two correction factors: K_a = 3.82±1.26 (Shen et al. 2008) and K_b = 5.14±0.19 (Runnoe et al. 2012). The estimated value of L_{bol} are reported in Table 5.4. We have already taken into account the inclination correction factor reported in Sect. 4.6.3. Then we used a mean value of the bolometric luminosity ($<L_{bol}>$=2.41±0.83×10^{47} erg s^{-1}) to compute

the mean Eddington ratio for both CIV and MgII. The obtained values are reported in Table 5.4 and they are in line with those found for other high-z AGNs (both RL and RQ, see chapter 7).

	CIV	MgII
FWHM (km s^{-1})	$4310.88^{+134.59}_{-200.23}$	$2870.15^{+145.98}_{-265.23}$
λL_λ (10^{46} erg s^{-1})	(at 1350Å) 5.5±0.6	(at 3000Å) 6.7±0.4
L_{bol} (10^{47} erg s^{-1})	1.82±0.69 e47	3.0±0.24
M_{BH} ($10^9 M_\odot$)	$2.4^{+0.2}_{-0.3}$	$2.6^{+0.3}_{-0.5}$
λ_{Edd}	0.78±0.33	$0.74^{+0.35}_{-0.43}$
L_{line} (10^{45} erg s^{-1})	2.4±0.1	1.6±0.1

Table 5.4: Best fit parameters for the CIV and MgII emission lines of PSO J1244+86 and virial mass estimates.

5.6 Summary

In this chapter I described the selection of blazar candidates at redshift between 4.5 and 5.5 (*r-dropout*) in the northern hemisphere at declination above 75°. As well as extending the results of CLASS survey, presented in chapter 3, the aim of this selection was primarily increasing the number of blazar at z≥5 (7 in total at the moment, 4 from the literature, 2 from the CLASS sample and DES0141−54). Therefore, as for the selection presented in chapter 4 we were not interested in a complete and homogeneous selection. To perform this selection, the combination between the NVSS radio catalog of bright (>30 mJy) sources and the Pan-STARRS PS1 catalog (in the optical) has been exploited. The common area between these two surveys at Dec≥75° consists of 690 deg^2. This search led to the selection of 3 candidates, but only one, PSOJ124413.902+862554.07 (hereafter PSO J1244+86) was a promising high-z AGN candidate and it was spectroscopically observed at the TNG. Since the SEDs of the other two candidates are well represented by low-z (0.6-0.7) elliptical galaxies, we did not perform a spectroscopic follow-up to assess their real nature.

PSO J1244+86 was confirmed to be a z=5.3 very powerful RL AGNs (74 mJy in the NVSS). The fact that we found only one high-z object in our selection is in agreement with our prediction based on CLASS objects characteristics and the cosmological properties of Mao et al. (2017).

The flat (Γ_X=1.32±0.22) and strong with respect to the optical ($\tilde{\alpha_{ox}}$ = 1.316±0.025) X–ray emission of PSO J1244+86 are typical blazar characteristics. Indeed PSO J1244+86 X–ray features are in line with that of the blazars presented in the CLASS sample (see Table 3.3 for comparison). However the radio spectrum of PSO J1244+86 peaks around 1 GHz (observed frame, i.e., ∼6 GHz in the rest frame). Therefore the source can be classified as a GPS. This does not exclude the blazar nature of PSO J1244+86, as already explained also in Sect. 5.5.1. To finally determinate the real shape of the radio spectrum of PSO J1244+86 a radio observation over a wide range of frequencies (e.g., with the JVLA) is necessary. PSO J1244+86 is not resolved by the VLASS 3 GHz image (2.5″ of resolution), suggesting that any hint of a core-jet structure (typical of blazars) can be revealed only with high-resolution observation, on mas scale.

Finally PSO J1244+86 hosts a SMBH of $2.5\times10^9 M_\odot$. The black hole mass was computed by using the virial approach thanks to the detection of the CIV and the MgII emission lines in a LUCI/LBT spectroscopic follow-up. The value of the SMBH mass of PSO J1244+86 is consistent with those of other AGNs and blazars at similar redshift (see e.g., Trakhtenbrot et al. 2011; Sbarrato et al. 2012b).

Chapter 6

Searching for 5.5<z<6.5 blazars in the NVSS+PS1 surveys: the discovery of the first blazar at z>6

This chapter is based on the following papers:
*- **S. Belladitta**, A. Moretti, A. Caccianiga, C. Spingola, P. Severgnini, R. Della Ceca, G. Ghisellini, D. Dallacasa, T. Sbarrato, C. Cicone et al. (2 more) , 2020, A&A, 635, L7*
*- C. Spingola, D. Dallacasa, **S. Belladitta**, A. Caccianiga, M. Giroletti, A. Moretti and M. Orienti, 2020, A&A, 643, L12 ,*
My contribution to the works: candidates selection, P.I. of the LBT observations, analysis of optical, radio and X–ray properties of the first blazar discovered at z>6 (PSO J0309+27), discussion of the results, P.I. of the radio JVLA observations of PSO J0309+27, discussion of the results of JVLA and VLBA observations.
This chapter is also based on near-IR data not published yet, from which I derived the black hole mass of PSO J0309+27.

Before 2020, the most distant blazar known was the one discovered by Romani et al. (2004): Q0906+6930 at z=5.47. At redshift larger than 5.5 only nine RL AGNs have been discovered (see Table C.2) and none of these have been classified as blazar based on their optical, radio or X–ray properties. To discover the first examples of this rare type of sources it is necessary to explore a large area of sky with a reasonable sensitivity, both in the radio (few mJy) and in the optical (mag∼21.5).
Starting from the results of Sect. 3.5, and using the cosmological evolution presented by Mao et al. (2017), we extrapolated the space density of blazars at 5.5≤z≤6.5 with a radio flux larger than ∼9 mJy and mag≤21.5. In the considered redshift bin, this radio flux limit guarantees a radio luminosity larger than $\sim 10^{43}$ erg s^{-1} for a FSRQ (i.e. a blazar, $\alpha_{\nu r}<0.5$), which is the lower limit for the space density computed in chapter 3. The optical limit was kept equal to that considered in chapter 5 for the same reasons, i.e. it guarantees a reasonable spectroscopic observation and a significant value of the dropout. Therefore, with these radio and optical limits, we expected to discover at 5.5≤z≤6.5 about two/three blazars using the wide field surveys available to date (i.e. the NVSS and Pan-STARRS). For this reason, we performed a systematic search of z≥5.5 blazars combining NVSS, Pan-STARRS PS1 and WISE. The common area of Pan-STARRS PS1 and NVSS in which we search for z≥5.5 blazar candidates is shown in Fig. 6.1 and it consists of ∼ 21000 deg^2, i.e. the northern sky above -30° excluding the Galactic Plane (|b|≥20°).

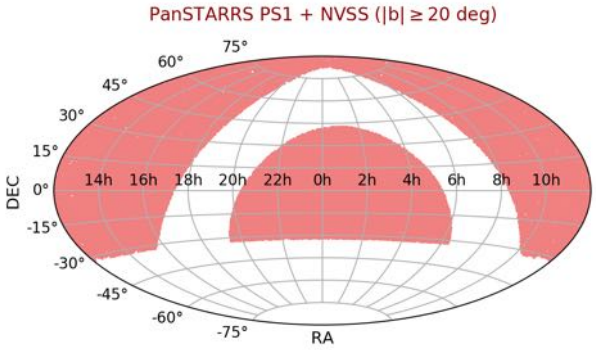

Figure 6.1: The common area of Pan-STARRS PS1 and NVSS, in which we searched for z≥5.5 blazar candidates, is ~ 21000 deg^2.

6.1 Candidate selection

The method used in this selection is similar to that described in chapter 5 but, in this case, we were interested in z≥5.5 candidates, and, therefore, we searched for *i-dropout*, i.e. objects with large $i - z$ values. From the NVSS catalog we selected only sources with a radio flux density larger than 9 mJy and point-like. This radio flux threshold allowed the selection of objects with a relative small (<10″) radio positional error, which minimizes the possible spurious detections. We retrieved a radio catalog of 269215 sources for which, we searched for the optical PS1 counterpart with a z magnitude brighter than 21.5, using an impact parameter equal to the radio positional error of each objects.
From the cross-correlation we required optical coordinates and errors, number of detections in each PS1 filters and magnitudes (PSF, aperture and Kron). The SQL query used for this selection is reported in Appendix E. The output cross-correlated catalog consists of 188942 entries, in which some objects have a multiple detection (the primary and secondary detections of the PS1 database). For all the sources with no detection in i-band we assumed a magnitude limit (at 5σ) of 23.44. Then several filters have been applied to the list, keeping all the objects that satisfied the following criteria:

- outside the Galactic Plane: |b| ≥ 20 ° (to reduce the contamination from stars)
- no detection in g-band and r-band or g and r magnitude fainter than 22.5 and number of detections in both bands equal to 0;
- detection in z-band (both PSF and Kron magnitude)
- dropout: iPSFMag-zPSFMag ≥ 1.1 (see Fig. 3.3)
- blue continuum: zPSFMag-YPSFMag ≤ 0.5
- optical stellaricity: zPSFMag-zKronMag ≤ 0.05

After the application of these filters we were left with a catalog of 305 sources, which have been cross-correlated with the WISE catalog, searching for all the infrared objects within 1.5″ from the optical positions. This impact parameter has been set to guarantee the reliability of the mid-IR counterpart. We then imposed that the objects are either undetected in WISE (W2) or, if detected, we require that z−W2 < 5.0. This is the same filters used in the other selections (chapter 3, 4 and 5), applied for remove the contamination from low-z reddened AGNs. Moreover

two secondary filters have been implemented on the remaining candidates (∼200): we removed 1) objects with Dec≤-29°, i.e. the optical PS1 frames at the border of the surveys that are often problematic and 2) objects very bright in z-band (zPSFMag<18) that are probably stars. After these selection criteria ∼ 150 objects remained, on which a visual inspection were carried-out to remove all the possible corrupted frames or frames with no reliable photometry. From this process, we selected a final sample of 7 candidates. One of this objects is PSO J352.4034−15.3373 at z = 5.84, already discovered by Bañados et al. (2018b), suggesting that our selection method is valid. We proposed the others 6 candidates (see Table 6.1[1]) for a spectroscopic follow-up at the LBT.

candidate	$i-z$	$z-Y$	stellaricity	$S_{1.4\ GHz}$ (mJy)	radio_optical distance (arcsec)	Exp. Time (h)
PSO J0309+27	3.6	0.38	−0.12	23.7	0.66	3
PSO J0944+83	1.1	0.29	−0.19	12.3	1.8	2.6
PSO J1053+16	1.44	−0.45	0.017	17.3	1.4	2.8
PSO J1433−16	1.1	−0.21	−0.12	12.9	1.3	3
PSO J1503+74	3.3	0.43	−0.29	10.7	2.8	3.2
PSO J1752+31	2.42	−0.72	−0.42	21.6	0.23	2.5

Table 6.1: Blazar candidates proposed for the spectroscopic follow-up at LBT. Col (1): candidate name; Col (2) and Col(3): optical colors; Col (4): optical stellaricity; Col (5): flux density at 1.4 GHz (NVSS); Col (6): distance between the radio an optical coordinates; Col (7): exposure time, in hour, asked for the spectroscopic follow-up

6.1.1 Spurious radio/optical matches

To estimate the number of spurious radio/optical matches we generated catalogs of fake sources located at random radio positions, starting from the original NVSS list and moving of ±50″ in RA and Dec. We then applied the same filters on these fake catalogs, finding that the expected number of spurious radio/optical matches is 3±1, i.e. about 50% of the 7 candidates discovered are probably just spurious radio/optical matches (most likely stars).

6.2 LBT spectroscopic follow-up

A spectroscopic follow-up of the 6 candidates was performed at the LBT (program ID IT-2019B-021, P.I. Belladitta S.), using MODS coupled with the red grating G670L (nominal range: 5800-10000 Å). Among these 6 candidates, three (PSO J0309+27, PSO J0944+83 and PSO J1752+31) have been observed between September and December 2019. The data reduction of the observed sources was performed at the Italian LBT Spectroscopic Reduction Center, with the same procedure that has been used also for PSO J1244+86 (chapter 5) and for the CLASS objects (chapter 3). PSO J1752+31 turned out to be a star (likely a spurious radio/optical match), PSO J0944+83 is a low-z galaxy, and the third, PSO J030947.49+271757.31 (hereafter PSO J0309+27), turned out to be a high-z AGN. The spectroscopic follow-up is ongoing for the remaining three candidates.
PSO J0309+27 was observed on the night of the 02 October 2019. We carried out 12 observations of 15-minutes each, with a long-slit of 1.2″ width, for a total observing time of 3 hours. The rms reached with the wavelength calibration were 0.08 Å on MODS1 and 0.07 Å on MODS. The

[1]We report the coordinates of the candidates already spectroscopically observed, since the observations for the other proposed sources are still in progress. PSO J0309+27: RA = 47.447889, Dec = 27.299254; PSO J0944+83: RA = 146.087457, Dec = 83.152069; PSO J1752+31: RA = 268.030219, Dec = 31.724930.

MODS/LBT discovery spectrum of PSO J0309+27 is shown in Fig. 6.3. Since the Ly-$\alpha\lambda$1216Å line is partially absorbed in the blue side by neutral Hydrogen clouds along the line of sight, we estimated the redshift using the O[VI]λ1033Å, the OIλ1304Å and the CIIλ1336Å lines (Fig. 6.3), by fitting them with a single Gaussian profile using the IRAF task *splot*. The resulting mean value is z=6.10±0.03.
We verified that the photometric PS1 points are in good agreement with the optical spectrum; the latter has been used to calculate all the optical properties (e.g., the continuum luminosity) of PSO J0309+27.
Figure 6.2 reports the optical PS1 images of PSO J0309+27 in the 5 filters, while in Table 6.2 its PS1 magnitudes are listed. From Table 6.2 it can be noticed that the source is not detected in the r and i-band of PS1 and in the WISE catalog.

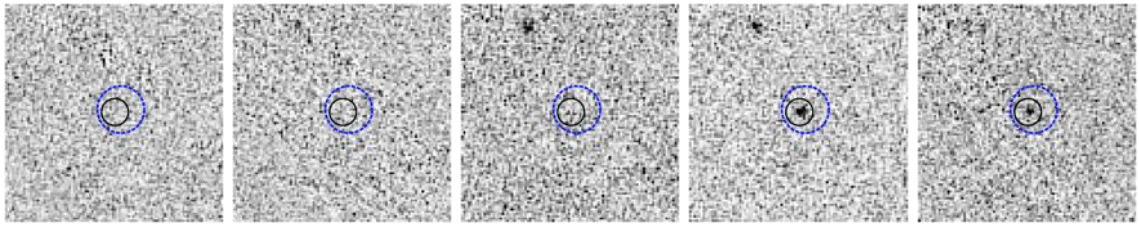

Figure 6.2: $0.4'\times0.4'$ Pan-STARRS PS1 g, r, i, z, Y cutout images of PSO J0309+27. Its optical position is denoted with a black circle of $1.5''$ in diameter. The radio NVSS position is denoted with a blue dashed circle, which is as large as the radio positional error reported in the catalog ($2.4''$). The distance between PS1 coordinates and NVSS position is $0.6''$.All images are oriented with north up and east to the left.

filter	λ	mag
$iPSF$	0.745	24.98 ± 1.51
$zPSF$	0.870	21.37 ± 0.08
$YPSF$	0.978	20.98 ± 0.12
$zKron$	0.870	21.48 ± 0.13

Table 6.2: PS1 magnitude of PSO J0309+27. The source is not detected in the g and r PS1 bands and in the WISE catalog. Col (1): optical PS1 filters; Col (2): filter central wavelength in μm; Col (3): observed magnitude and errors.

6.2.1 LUCI follow-up for PSO J0309+27

The high-z nature of PSO J0309+27 prevents the detection in the optical wavelength range of the CIVλ1549Å and/or the MgIIλ2798Å emission lines usually used for the BH mass estimation. The MgII, at the redshift of the source, falls in an atmospheric absorption band, hence it is not clearly detectable by ground based telescopes. Therefore, we proposed a LBT/LUCI follow-up in order to extend the wavelength range in the near-IR band to detect the CIV emission line. The observation was carried out in a Director's Discretionary Time program (program ID: DDT_2019B_3; P.I. Belladitta S.) on 2019 December 2 and consisted of 12 exposures of 450 seconds each, with a long-slit of $1.2''$ width, in nodding mode in the sequence ABBA, with a total integration time of 3 hours. The medium seeing along the night was $1.1''$ and the mean air mass was 1.2. We used the G200-zJ configuration for both LUCI1 and LUCI2, in order to cover the wavelength range from 0.9 to 1.2 μm, where the CIV was expected to be found. Also in this case the data reduction was performed at the Italian LBT Spectroscopic Reduction Center. A rms of 0.33Å (LUCI1) and of 0.25Å (LUCI2) has been reached during the wavelength calibration. The LBT/LUCI spectrum of

PSO J0309+27 is shown in Fig. 6.3. To plot the spectra together we have normalized the LUCI spectrum to the MODS one, using the region of overlap between the two spectra (9000-10000Å). The analysis of these LUCI/LBT data is described in Sect. 6.6.5.

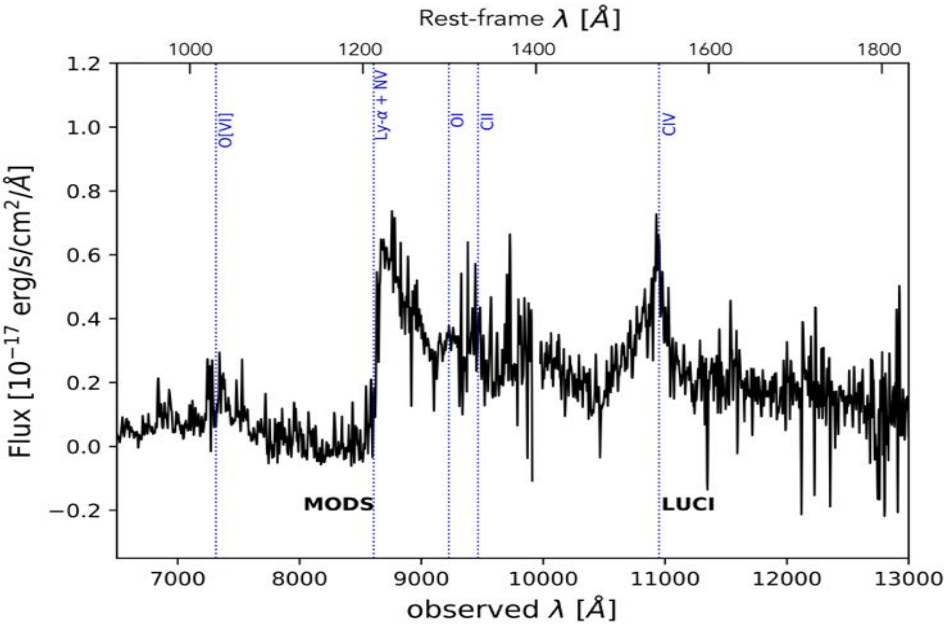

Figure 6.3: LBT MODS and LUCI spectra of PSO J0309+27. The O[VI]λ1033Å, the Ly-$\alpha\lambda$1216Å the OIλ1304Å, the CIIλ1336Å and the CIVλ1549Å lines are marked. In this plot the LUCI spectrum was normalized to the MODS one in the region between 9000Å and 10000Å.

6.3 Archival radio photometry

Besides the NVSS detection at 1.4 GHz, PSO J0309+27 has a detection also at 150 MHz in the TGSS and at 3 GHz in the VLASS 1.1 epoch. The detailed description of these surveys can be found in Sect. 2.4.1. Figure 6.4 shows the overlay of the radio contours on the optical Pan-STARRS PS1 image in z-band. We found that the radio position at 150 MHz is at $\sim 0.5''$ from the Pan-STARRS PS1 coordinates, consistent with the 1.4 GHz position. Instead the separation between the 3 GHz VLASS coordinates and the optical position is $0.31''$. From an elliptical Gaussian fit to the radio images computed with the task IMFIT of the CASA software, we estimated the integrated flux densities at the three radio frequencies (see Table 6.3). The flux densities at 1.4 GHz and at 150 MHz are consistent with those reported in the two radio catalogs.
Moreover, from the Gaussian fit we found that PSO J0309+27 is unresolved at 1.4 GHz as observed by NVSS, while it is resolved at 150 MHz: the TGSS image ($25''$ resolution) shows a slightly elongated structure at 2σ level in the north direction, which may indicate the presence of a jet extended on $\sim$300 kpc at low frequencies (Fig. 6.4, left panel). The source is resolved also in the VLASS image ($2.5''$ resolution), which also revealed the presence of a jet in the same direction than that of TGSS (Fig. 6.4, right panel). This possible extension, which represents about 10% of the total flux density in the TGSS and 5% in the VLASS emission, is commonly observed in blazars (e.g., Antonucci & Ulvestad 1985).

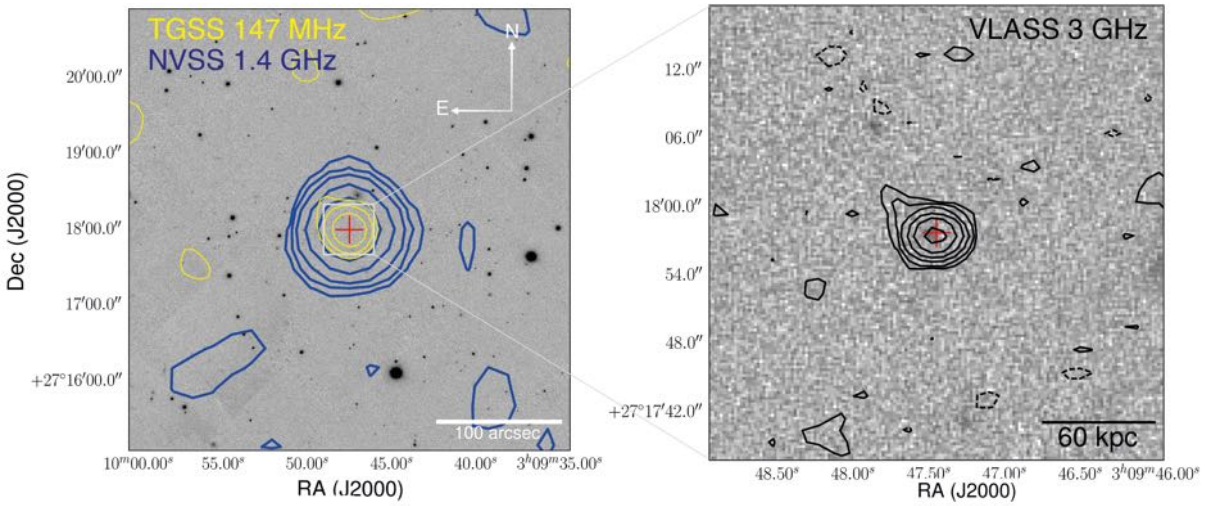

Figure 6.4: *Left*: NVSS (blue) and TGSS (yellow) radio contours overlapped on Pan-STARRS PS1 z-band image (350 arcsec^2 FoV). Contours are at (2, 4, 8, 16, 32) $\times$ the off-source rms, which is 350 μJy beam^{-1} for the NVSS image and 3.5 mJy beam^{-1} for the TGSS image. *Right*: Zoom onto VLASS (black) radio contours. They are at (2, 4, 8, 16, 32, 64) $\times$ the off-source rms, which is 0.13 mJy beam^{-1}. In both panels the red cross indicates the optical position of the source.

Obs. frequency (GHz)	S_ν (mJy)	survey
0.150	64.2 ± 6.2	TGSS
1.4	23.89 ± 0.87	NVSS
3	12.0 ± 1.2	VLASS

Table 6.3: Integrated radio flux densities (observed frame) of PSO J0309+27.

6.4 *Swift*-XRT observation

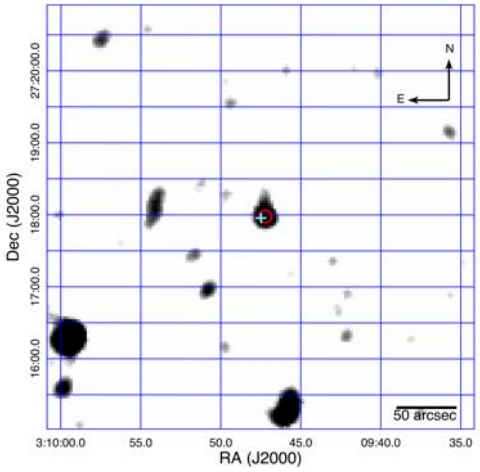

Figure 6.5: 6′×6′ *Swift*–XRT image of PSO J0309+27. The image has been smoothed with a Gaussian filter with σ=6″. The X–ray position is marked with a red circle whose radius (5.2″) is set equal to the XRT positional error. The cyan cross marks the PS1 position of the source.

Few days after the discovery, we also obtained a *Swift*-XRT pointed observation, that was

carried out through two Target of Opportunity (ToO) requests (target ID:12068, P.I. Moretti A.). The total exposure time of the observation was 19.1 ks, distributed in eight segments in the period between October 7 and November 15 2019. Data have been reduced through the standard data analysis pipeline (Evans et al. 2009), running on the UK *Swift* Science Data Centre web page using HEASOFT v6.22. The source was clearly detected with a total of eleven counts and with an expected background of two counts in the [0.5-10] keV energy band. Running a *wavedetect* algorithm (Freeman et al. 2002) the detection significance is 4.4σ. The X–ray position calculated by the `xrtcentroid` HEASOFT task is RA = 03:09:47.22, Dec = +27:17:58.69, with an uncertainty of $5.2''$ (90% confidence). This is at $3.8''$ from the optical PS1 position (Fig. 6.5). Data for the spectral analysis have been extracted from the automatic pipeline, on a circular region of radius of 8 pixel, corresponding to $18.8''$ ($\sim$75% of the PSF). Background has been measured in an annulus with an internal radius of $150''$ and a external radius of $400''$, centered on the source. A standard spectral data analysis has been performed using XSPEC (v.12.10.1), by fitting the observed spectrum (Fig. 6.6) with a simple power law with the absorption factor fixed to the Galactic value (1.16×10^{21} cm^{-2}) as measured by the HI Galaxy map of Kalberla et al. (2005). Due to the limited number of collected photons, we performed the fit using the C-statistic (Cash 1979) on the data. Table 6.4 reports the results of the X–ray analysis, together with the 68 and 90 per cent confidence ranges for the photon index (see also Fig. 6.7), the observed flux in the [0.5-10] keV energy band and the luminosity at [2-10] keV rest frame. The flux error has been computed sampling the parameter pairs (photon index and normalization) within the confidence ellipses and calculating the maximum and minimum of the flux. We noted that the X–ray flux of PSO J0309+27, at 90% level of confidence, is larger than 1×10^{-14} erg s^{-1} cm^{-2}, confirming its very bright emission, supporting the hypothesis of a boosted emission along our line of sight. Due to low number of collected photons, the measured spectral photon index is only poorly constrained: we obtained $\Gamma_X = 1.6\pm0.6$, with a corresponding unabsorbed flux of $3.4^{+5.2}_{-1.9}\times10^{-14}$ erg s^{-1} cm^{-2} in the observed [0.5-10] keV energy band and a luminosity of $4.4^{+6.4}_{-3.0}\times10^{45}$ erg s^{-1} in the [2-10] keV rest-frame energy band.

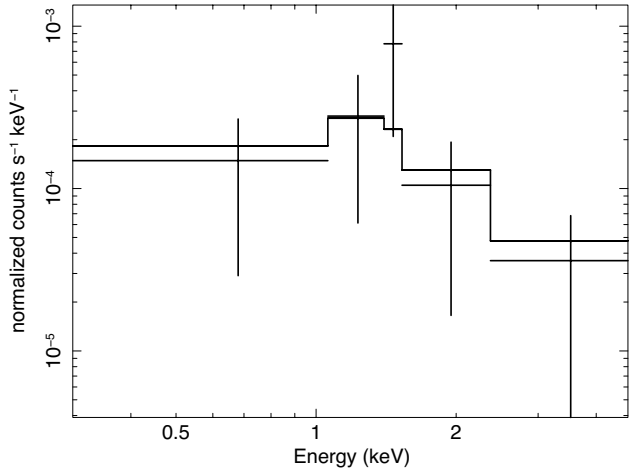

Figure 6.6: *Swift*–XRT spectrum of PSO J0309+27.

6.5 VLA and VLBA observations

We performed a radio follow-up of PSO J0309+27 with the JVLA and the Very Long Baseline Array (VLBA), which aims at constraining the radio spectral properties of PSO J0309+27 and

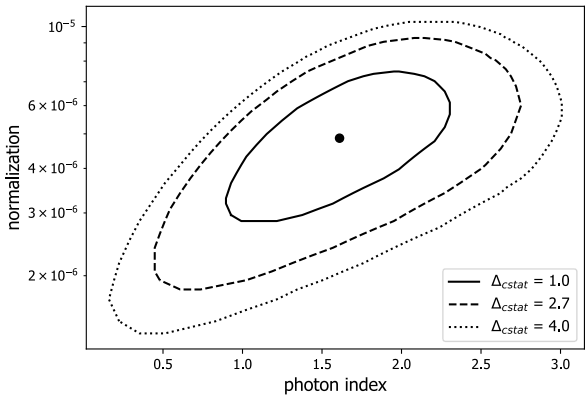

Figure 6.7: Confidence contours plot showing the fitted photon index versus normalization. The contours are drawn for $\Delta_{cstat} = 1.0, 2.7, 4.0$ respectively, corresponding to 68%, 90% and 95% confidence levels for one parameter. The black point represent the best-fitting value.

source	Γ_X	errors	Flux	errors	Luminosity	errors	d.o.f.
(1)	(2)	(3)	(4)	(5)	(6)	(7)	(8)
PSO J0309+27	1.6	±0.6 ±1.1	3.4	$^{+5.2}_{-1.9}$ $^{+9.8}_{-2.4}$	4.4	$^{+6.4}_{-3.0}$ $^{+10.8}_{-3.6}$	9

Table 6.4: Results of the X–ray analysis. Col (1): source name; Col (2): Best fit value on the photon index; Col (4): X–ray flux at [0.5-10] keV (observed frame) in unit of 10^{-14} erg s^{-1} cm^{-2}; Col (6): X–ray luminosity at [2-10] keV (rest-frame) in unit of 10^{45} erg s^{-1}; Col (8): degree of freedom. In columns (3), (5), (7) we report the associated errors at 68% and 90% level of confidence.

simultaneously investigating the morphology and physical conditions from arcsec to mas scales, thus unveiling the parsec-scale emission of this high-z AGN.
Following sections report the observations and data reduction of these radio observations. More details can be found in Spingola et al. (2020, hereafter Sp20).

6.5.1 VLBA

We observed PSO J0309+27 with the VLBA on April 6th, 2020 at central observing frequencies of 1.5, 5 and 8.4 GHz, under the Director's Discretionary Time (DDT) project BS294 (P.I. Spingola C.). The total observing time was of about 2 h for each band. We systematically cycled through the observing frequencies in the 6 h observation in order to obtain the best possible uv-coverage at each band. The correlation was performed using the VLBA DiFX correlator in Socorro (Deller et al. 2011). The data were processed with the Astronomical Image Processing System (`aips`, Greisen 2003) package following the standard VLBA calibration procedure for phase-referenced observations, which are summarized in Sp20. The final self-calibrated images at the three observing frequencies are shown in Fig. 6.8. On VLBI scales PSO J0309+27 is a core plus one-sided jet from 1.5 to 8.4 GHz. We adopted a natural weighting scheme to better recover the most diffuse structure of this source at all frequencies. The properties of the images, such as off-source rms noise level, total flux density, peak surface brightness and restoring beam are listed in Table 6.5. We fit the observed emission using 2D multi-Gaussian fits to the image-plane by using the task IMFIT within the CASA package. The measurements of flux density, peak surface brightness and sizes obtained using this method are listed in Table 6.6, while the identified sub-components are

shown in Fig. 6.9. In addition to the nominal uncertainties of the fit, we consider the uncertainty due to the calibration process of the order of 5%.

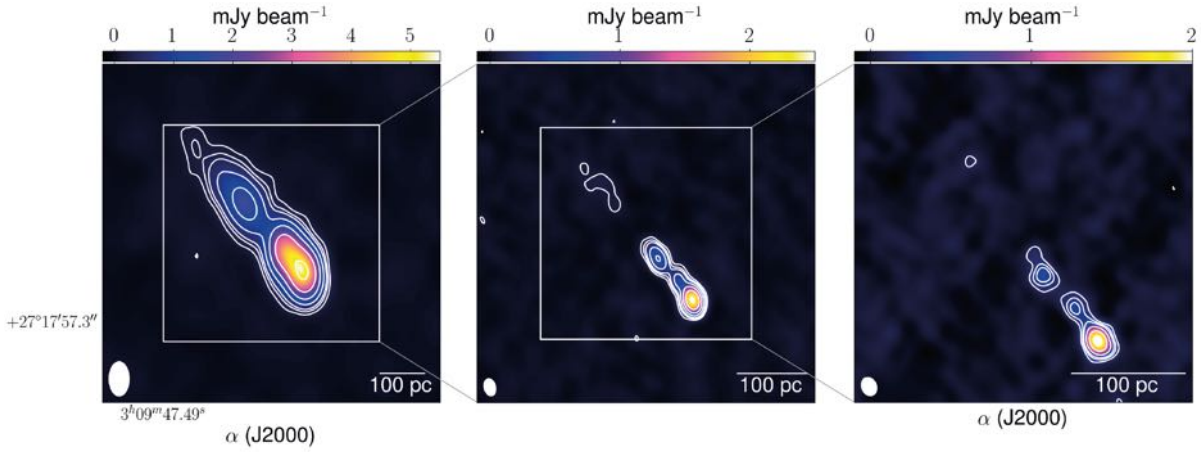

Figure 6.8: Self-calibrated VLBA images of PSO J0309+27 at 1.5 GHz (*left*), 5 GHz (*center*) and 8.4 GHz (*right*). The contours are drawn at (3, 6, 9, 18, 36, 72, 144) × the off-source noise of each map (42, 25, 43 μJy beam^{-1} for 1.5, 5 and 8.4 GHz respectively). The restoring Gaussian beam is shown in white in the bottom left corner of each image; north is up, east is left. Figure taken from Sp20.

Frequency (GHz)	Total flux density (mJy)	Peak surface brightness (mJy beam^{-1})	RMS (μJy beam^{-1})	B$_{maj}$ (mas)	B$_{min}$ (mas)	B$_{PA}$ (mas)
1.5	20 ± 2	7.2 ± 0.7	42	12.8	7.6	0
5.0	7.0 ± 0.7	4.1 ± 0.4	25	4.2	2.9	14
8.4	5.1 ± 0.5	3.2 ± 0.3	43	2.8	2.3	23

Table 6.5: Properties of the self-calibrated VLBA images shown in Fig. 6.8. Col(1): observed frequency in GHz; Col(2): total flux density in mJy; Col(3): peak surface brightness in mJy beam^{-1}; Col(4): off-source rms noise μJy beam^{-1}, Col(5)-Col(6): major and minor axes of the Gaussian restoring beam and Col(7) its position angle (east of north) all in milli-arcsecond.

6.5.2 VLA

PSO J0309+27 was observed with the Jansky VLA (DDT observation, Legacy ID: AB1752, P.I. Belladitta S.) in C configuration on May 15th 2020, from 1.4 to 40 GHz (22 to 0.9″ FWHM), for a total observing time of 1.5 h (50% on source, 50% on calibration). Two antennas were excluded from the observations because of technical issues. We performed imaging (for all bands) and self-calibration (successful for L-, S-, C- and X-bands only) using the `aips` package. The 1.4 and 2.3 GHz observations were the most affected by radio frequency interferences (RFI), causing the loss of a few spectral windows (*flagged* spws in Table 6.7). We obtained separate images for each spw from 1.4 to 15 GHz using natural weights, while we averaged the 64 spws in chunks of 8 spws from 15 to 40 GHz to maximize the sensitivity. From these images we extracted the flux density of the source (unresolved at all frequencies) using a 2D Gaussian fit. The measurements are reported in Table 6.7. In addition to the nominal uncertainties provided by the fit, we considered the uncertainty due to the calibration process (estimated using the scatter on the amplitude gains) of the order of 3-5% from 1.4 to 15 GHz, while it is of 10-15% at 15 and 40 GHz.

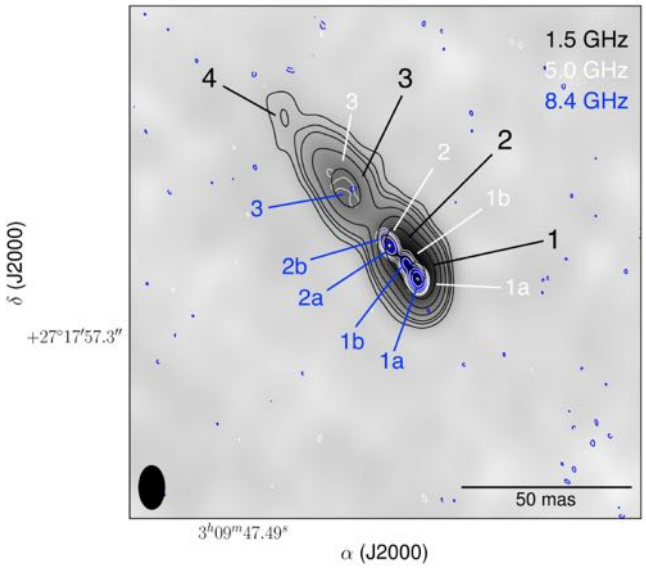

Figure 6.9: Overlay of the 1.5 (black contours), 5 (white contours) and 8.4 GHz (blue contours) emission of PSO J0309+27. We have marked all the different sub-componets that we identified with the Gaussian fit at the three frequencies. The greyscale map is the 1.5 GHz self-calibrated image, and its restoring beam is shown on the bottom left corner; north is up, east is left. Figure taken from Sp20.

Frequency (GHz)	Component	Peak flux density (mJy beam^{-1})	Integrated flux density (mJy)	θ_{maj} (mas)	θ_{min} (mas)	T_B (10^8 K)
1.5 (10.65)	1 (core)	6.83±0.04	8.02±0.08	13.6±0.1	8.3±0.1	2.7±0.2
	2	4.82±0.04	5.80±0.08	13.6±0.2	8.6±0.1	1.9±0.2
	3	1.98±0.04	4.03±0.12	19.2±0.5	10.3±0.5	0.8±0.1
	4	0.30±0.04	1.78±0.25	20.5±0.5	16.1±1.1	0.2±0.1
5 (35.5)	1a (core)	4.18±0.03	4.29±0.05	4.2±0.1	2.9±0.1	>1.19
	1b	0.70±0.03	0.74±0.05	4.2±0.2	2.9±0.1	>0.20
	2	1.02±0.03	1.41±0.06	5.4±0.2	3.0±0.1	0.30±0.02
	3	0.12±0.03	0.60±0.15	12.3±3.1	4.9±0.9	0.03±0.01
8.4 (59.64)	1a (core)	3.21±0.04	3.55±0.08	2.8±0.1	2.3±0.1	>0.67
	1b	0.46±0.04	0.69±0.10	4.4±0.6	2.3±0.2	0.09±0.01
	2a	0.55±0.04	0.71±0.09	3.1±0.3	2.6±0.2	0.11±0.02
	2b	0.23±0.04	0.14±0.05	2.3±0.5	2.0±0.3	0.04±0.02

Table 6.6: Spatially resolved VLBA radio properties of PSO J0309+27 obtained using 2D Gaussian fitting. Col(1): observing (and rest-frame in parentheses) frequency in GHz; Col(2): sub-component identification as labelled in Fig. 6.9; Col(3): peak surface brightness in mJy beam^{-1}; Col(4): integrated flux density in mJy; Col(5)-Col(6): elliptical size convolved by the beam, i.e. major and minor axes (θ_{maj} and θ_{min}) in mas; Col(7): rest-frame brightness temperature T_B in units of 10^8 K. If the subcomponent is unresolved, then only lower limits on its T_B (indicated by > symbol) can be provided.

ν (GHz)	S_ν (mJy)	S_{ν_err} (mJy)	ν (GHz)	S_ν (mJy)	S_{ν_err} (mJy)
1.040	41.61	0.75	12.082	3.81	0.07
1.104	41.25	1.47	12.203	3.66	0.07
1.170	flagged		12.331	3.44	0.07
1.237	29.65	1.5	12.459	3.43	0.07
1.298	flagged		12.587	3.71	0.07
1.362	32.26	0.63	12.716	3.46	0.07

1.424	30.42	0.28	12.843	3.46	0.07
1.487	28.75	0.30	12.971	3.39	0.07
1.541	flagged		13.099	3.53	0.07
1.604	flagged		13.227	3.37	0.07
1.679	24.97	0.32	13.355	3.34	0.06
1.744	23.38	0.29	13.476	3.29	0.06
1.807	22.56	0.29	13.618	3.23	0.06
1.872	19.01	0.27	13.739	3.51	0.06
1.917	11.21	0.15	13.867	3.33	0.06
1.974	12.22	0.49	13.995	3.20	0.06
2.022	21.00	0.21	14.123	3.22	0.06
2.179	flagged		14.251	3.06	0.07
2.307	flagged		14.379	3.20	0.06
2.396	18.10	0.18	14.507	3.16	0.06
2.527	17.82	0.18	14.635	2.83	0.06
2.655	16.59	0.17	14.763	2.92	0.06
2.783	15.81	0.17	14.891	3.12	0.06
2.911	15.39	0.16	15.012	2.69	0.07
3.022	14.76	0.16	15.154	2.90	0.07
3.143	14.05	0.15	15.275	2.69	0.07
3.271	13.66	0.14	15.403	2.77	0.07
3.399	13.38	0.14	15.531	2.81	0.07
3.527	12.64	0.08	15.658	2.70	0.07
3.655	11.94	0.09	15.787	2.69	0.07
3.783	11.56	0.10	15.915	2.51	0.07
3.947	flagged		16.043	2.77	0.08
4.522	9.44	0.13	16.171	2.57	0.07
4.643	9.70	0.06	16.299	2.51	0.07
4.771	9.58	0.08	16.427	2.53	0.07
4.899	8.99	0.08	16.548	2.74	0.07
5.027	9.04	0.08	16.690	2.64	0.07
5.155	8.82	0.08	16.810	2.48	0.08
5.283	8.46	0.09	16.939	2.48	0.08
5.411	8.28	0.08	17.067	2.48	0.08
5.522	7.94	0.10	17.195	2.50	0.08
5.643	7.97	0.08	17.323	2.32	0.08
5.773	flagged		17.451	2.37	0.09
5.899	7.99	0.08	17.579	2.27	0.08
6.026	7.62	0.09	17.707	2.14	0.08
6.154	flagged		17.834	2.16	0.09
6.282	7.04	0.09	17.963	2.22	0.10
6.413	7.47	0.09	18.084	2.17	0.10
8.051	5.64	0.06	18.695	2.13	0.05
8.179	5.80	0.06	19.703	2.06	0.05
8.307	5.57	0.06	20.695	2.01	0.05
8.435	5.44	0.06	21.703	1.69	0.06
8.563	5.37	0.06	22.695	1.68	0.06
8.691	5.18	0.06	23.703	1.58	0.06
8.819	5.06	0.06	24.695	1.52	0.06
8.947	5.03	0.07	25.701	1.19	0.06
9.058	5.08	0.06	30.995	1.05	0.07
9.179	4.93	0.06	32.003	0.90	0.08
9.303	4.93	0.06	32.995	1.02	0.08
9.435	4.88	0.06	34.003	0.96	0.08
9.563	4.83	0.06	34.995	0.93	0.08

9.692	4.81	0.06	36.003	0.77	0.10
9.819	4.81	0.06	36.995	0.89	0.10
9.940	4.40	0.07	38.003	0.69	0.13

Table 6.7: PSO J0309+27 flux densities from the VLA observation. Observing frequency (Col 1), flux density (Col 2) and nominal uncertainty on flux density from 2D Gaussian fit (Col 3).

6.6 Results

In this section I report the main results obtained from the multi-wavelength analysis of PSO J0309+27 from radio to X–ray bands.

6.6.1 Radio spectral index and radio-loudness

The radio spectral index is a fundamental parameter in the study of AGNs jets, as it allows to clearly separate the optically thick base of the jet (the "core"), which is the part closest to the SMBH, from the steep-spectrum components associated with the more external part of the radio jets.
From the NVSS and TGSS radio flux densities (Table 6.3) and assuming a single power law distribution for the continuum emission ($S_\nu \propto \nu^{-\alpha_{\nu r}}$) we computed the radio spectral index of PSO J0309+27 between 1.4 GHz and 150 MHz, finding $\alpha_{\nu r} = 0.44\pm0.11$. Using the peak flux densities, which better describe the core emission, we obtained a slightly flatter spectral index ($\alpha_{\nu r} = 0.39\pm0.12$). This value can be considered flat within the uncertainties ($\alpha_{\nu r}<0.5$) and represents an indication of the presence of a beamed jet.
From the observed optical (Table 6.2) and radio flux densities (Table 6.3) we calculated the radio-loudness (R) of PSO J0309+27. In this case we used the definition of Kellermann et al. (1989) already reported in Sect. 1: $R = \frac{S_{1.4\ GHz}}{S_{4400\text{Å}}}$. We used this definition for comparing the R value of PSO J0309+27 with the value already reported in the literature for the other RL AGNs discovered at z≥5.5 (see Table C.2). We estimated the flux density at 4400Å by extrapolating the 1350Å flux density from the optical spectrum, assuming a power law continuum with an optical spectral index of 0.44 (Vanden Berk et al. 2001). We obtained R=2500±500, suggesting that PSO J0309+27 is a beaming dominated source. This high value of R is typical of high-z blazars (see for example Fig. 4.10).
In Fig. 6.10 we compared the radio spectral index and the radio-loudness of PSO J0309+27 with those of other RL AGNs discovered so far at z≥5.5 for which a measurement of the radio spectral index is available in the literature (Table C.2). For comparison we also plotted the values of R and $\alpha_{\nu r}$ of the CLASS objects at 4.0≤z≤5.5 (see Table 3.3). We found that at z≥5.5 PSO J0309+27 has the highest R ever measured and it is the only one with a flat radio spectrum. Indeed, none of the other RL AGNs at z≥5.5 is classified as blazar, based on high resolution VLBI observations (Frey et al. 2003, 2005, 2008, 2010, 2011; Momjian et al. 2008, 2018; Cao et al. 2014; Coppejans et al. 2016).

6.6.2 Radio spectrum from VLBA and VLA

In Fig. 6.11 we show the radio spectrum for all of the sub-components of PSO J0309+27 resolved using VLBI (see Fig. 6.9). In this case Sp20 adopted the convention $S_\nu \propto \nu^{\alpha_{\nu r}}$ for the power law distribution. We identified the brightest component (1 or 1a in Fig. 6.9) as the radio core region, because it shows a flatter synchrotron spectral index between 1.5 and 5 GHz than the other sub-components ($\alpha_{\nu r}=-0.52\pm0.03$). Also, its spectral index becomes flatter between 5 and

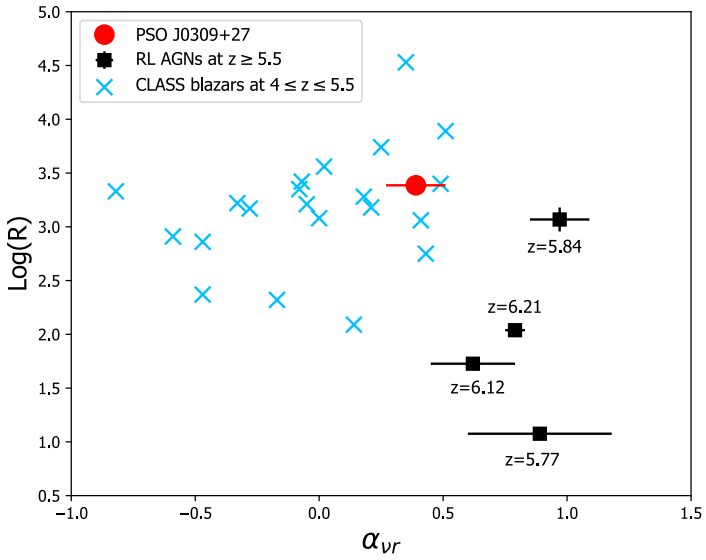

Figure 6.10: Radio-loudness (R) versus the radio spectral index ($\alpha_{\nu r}$) of PSO J0309+27 (red point) compared to RL AGNs discovered at z≥5.5 (black squares) for which a measure of $\alpha_{\nu r}$ in the literature is available. For PSO J0309+27 we report the value of $\alpha_{\nu r}$ computed from the peak flux densities. Light-blue crosses represent the CLASS high-z (4≤z≤5.5) blazars. Among z≥5.5 RL AGNs PSO J0309+27 has the highest R ever measured and it is the only one with a flat $\alpha_{\nu r}$.

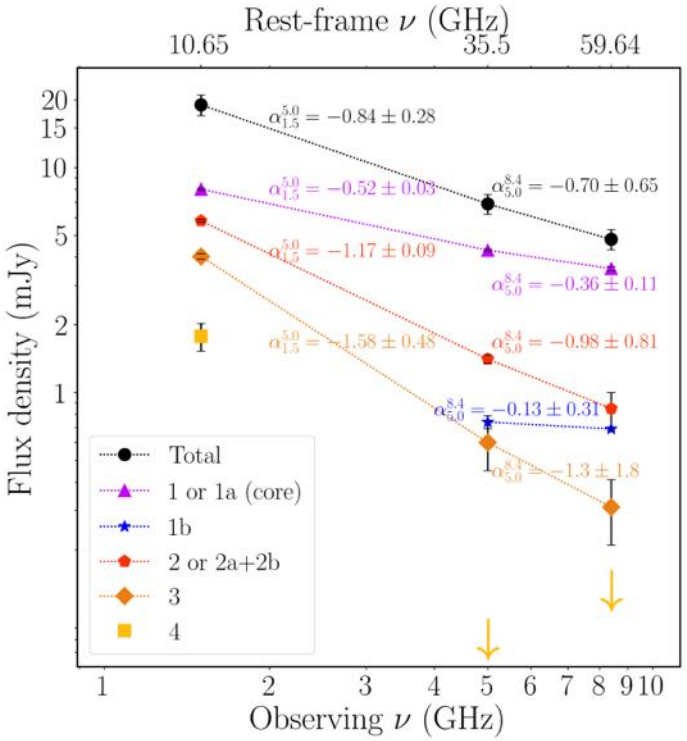

Figure 6.11: Radio spectrum of all the sub-components of PSO J0309+27 spatially resolved by the multi-frequency VLBA observations. The arrows indicate the 3 detection limit for sub-component 4 at 5 and 8.4 GHz, estimated as three times the flux density within the same area of the 1.5 GHz detection of that sub-component. Figure taken from Sp20.

8.4 GHz ($\alpha_{\nu r}$=−0.36±0.11). Nevertheless, our 2D Gaussian fit does not associate component 1a with a point-like source, indicating that the actual source radio core is blended with the innermost optically thick part of the jet. Component 1b also shows a flat spectrum between 5 and 8.4 GHz ($\alpha_{\nu r}$=−0.13±0.31), and it is among the faintest sub-components. All of the other sub-components have steep spectral index (see Fig. 6.11), but the uncertainties on the integrated flux density for some of them are quite large.
The broad-band radio spectrum as measured by the VLA (shown in Fig. 6.12) is consistent with the steep-spectrum trend measured with the VLBA. By fitting the VLA data with a single power law model ($S_\nu \propto \nu^{\alpha_{\nu r}}$) we found a spectral index of α= −0.98±0.05 between 1 and 40 GHz. As there is an indication for a steepening in the spectrum from the 15 GHz data (Fig. 6.12), we also fitted the VLA observations using a broken power law, which found a break at ν_{break} = 14.5±0.5 GHz (rest-frame 103 GHz), a spectral index of α= −0.96±0.03 before ν_{break} and α= −1.39±0.09 after ν_{break}. Both the single and broken power law models provide a good representation of the data, as they have similar reduced chi-square values (1.8 and 2.2, respectively). This is also shown in Fig. 6.12: both fits are consistent with the observations within the uncertainties. Finally, in Fig. 6.12 we observed a flattening of the spectrum at low frequencies (between 0.150 and 1.4 GHz). Therefore, the spectral turnover must be at low frequencies, as the flux density at 150 MHz is higher than at 1.4 GHz. Low-frequency observations (with LOFAR) are in program to assess the presence of this turnover.

Radio variability

By comparing the VLA data at 1.4 and 3 GHz with the archival observations of NVSS (at 1.4 GHz in 1993) and VLASS (at 3 GHz in 2017) we found an indication for a 20-30% variability in this source. This kind of 20-30% variability on scales of several months to a few years in the radio has been observed in other RL AGNs, but we cannot exclude that PSO J0309+27 had a much more pronounced variability on shorter time scales, which is typical of blazars (e.g., Hovatta et al. 2008). A future long-term monitoring is needed to assess the amplitude and the time scale of the variability in this AGN.

6.6.3 Jet physical properties

In the VLBI images we did not find any evidence for a counter-jet, which indicates that this AGN is seen under a relatively small viewing angle, as expected if PSO J0309+27 is a blazar. To estimate the possible ranges of viewing angles (θ) and of the bulk velocity (v_{bulk}) in terms of speed of light (β_{bulk}) we used the jet/counter-jet brightness ratio J (Giovannini et al. 1994) and the core-dominance value (Giovannini et al. 1988, 1994; Giroletti et al. 2004). For details on this computation see Sp20. The computed valued for θ and β_{bulk} are reported in Fig. 6.13. The maximum value allowed by the core-dominance relation is β_{bulk} = 0.98 (corresponding to a minimun θ of ∼10 deg). This implies a value of Γ equal to ∼5 or less (see Eq. 1.8). Finally from Eq. 1.9 we computed the Doppler factor, finding δ ∼6.
We note that a value of Γ of ∼5 would be in good agreement with what proposed by Volonteri et al. (2011) to reconcile the significant deficit of observed high-z blazars with respect to the expected number of blazars at z∼3.

We estimated the source brightness temperature of each sub-component with the following equation (e.g., Kovalev et al. 2005):

$$T_B(\lambda) = \frac{2ln2}{\pi k}\frac{S_\lambda \lambda^2 (1+z)}{\theta_{maj}\theta_{min}}[K] \quad (6.1)$$

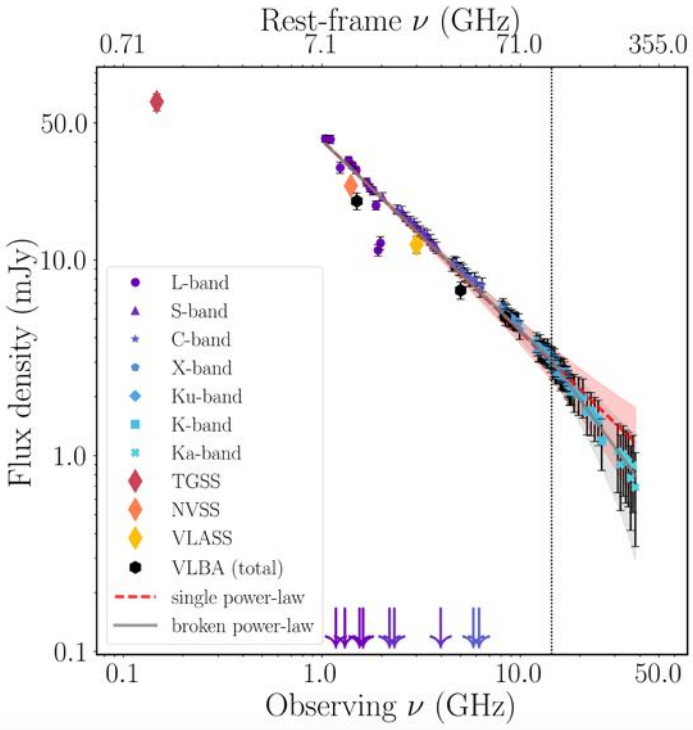

Figure 6.12: Radio spectrum of PSO J0309+27 from 0.150 up to 40 GHz. The VLA observations from 1.4 to 40 GHz are represented with different symbols for each band as indicated in the legend (bottom left corner). Archival TGSS, NVSS and VLASS observations are indicated with diamonds, while the total flux density of the VLBA observations is reported using black filled circles. The arrows indicate flagged spws. The red (dashed) and grey (solid) lines stand for the single and broken power law fits, respectively, where the shaded areas represent the uncertainties of the fits (same color coding). The vertical dotted line indicates the frequency break of the broken power law fit (14.5 GHz). Figure taken from Sp20.

where k is the Boltzmann constant, S_λ is the integrated flux density of each sub-component at the observing wavelength (λ), θ_{maj} and θ_{min} are the FWHMs of the elliptical 2D Gaussian fits along the major and the minor axes, all in cgs units. The computed values of T_B are reported in Table 6.6. The brightness temperature of the sub-components of PSO J0309+27 is of the order of 10^8 K at 1.5 and 5 GHz, and 10^7 K at 8.4 GHz. Similar values for T_B associated with bright extended steep-spectrum jets (from a few to hundreds of parsecs in projection) has been measured also in other RL AGNs at redshifts z>4 (Frey et al. 2011; Gabányi et al. 2015; Cao et al. 2017; Bañados et al. 2018b; Momjian et al. 2018; An et al. 2020, but see Frey et al. 2015 for higher T_B values at z∼5). These T_B estimates are also 2-3 orders of magnitude lower than what measured for low-z blazar samples (e.g., MOJAVE blazars, Kovalev et al. 2005 and the VLBA-BU-BLAZAR sample, Jorstad et al. 2017).

Overall, the jet physical properties of PSO J0309+27 point to a moderately beamed jet. However, our observational constraints deriving from a single epoch observation are too loose to obtain stringent values for parameters like the bulk velocity and the viewing angle of the jet, so that we could mainly put upper (or lower) limits. Nevertheless, if PSO J0309+27 is a blazar then in Fig. 6.13 it should lie below the dashed line, which is the typical value to discern between aligned ($< 1/\Gamma$) and misaligned ($> 1/\Gamma$) RL AGNs, and below the maximum value allowed by the core-dominance relation ($\beta_{bulk} = 0.98$).
Finally, we highlight that our findings cannot exclude that PSO J0309+27 is seen under a larger

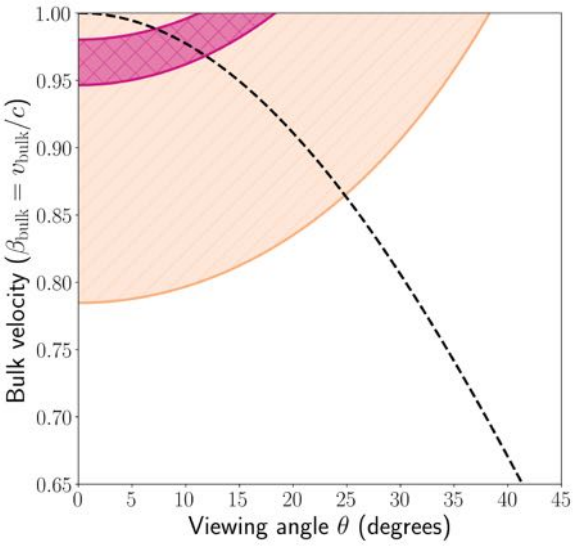

Figure 6.13: Allowed values on the jet viewing angle (θ) and its bulk velocity (v_{bulk}) in units of the speed of light (β_{bulk}=v_{bulk}/c). The orange hatched area corresponds to the allowed parameter space in the β-θ plane using the jet/counter-jet brightness ratio, while the magenta area traces the parameter space allowed by the core dominance. The black dashed line corresponds to $1/\Gamma$, which is the typical value to discern between aligned ($<1/\Gamma$) and misaligned ($>1/\Gamma$) AGNs. Figure taken from Sp20.

viewing angle. In such case, the values for Γ could be higher than 5, but the bright X–ray emission (described in the following section) would need a boost, which could be due to the ic/CMB effect.

6.6.4 X–ray properties

Blazars are characterized by a strong X–ray emission with respect to the optical thermal emission from the accretion disk. Following Ighina et al. (2019), we computed the $\tilde{\alpha_{\rm ox}}$ parameter of PSO J0309+27, which quantifies the relative strength of the X–ray emission with respect to the optical/UV component (see Sect. 3.6). We estimated the $\tilde{\alpha_{\rm ox}}$ assuming two different values of Γ_X: 2.0 (typical of z>6 RQ AGNs, e.g., Nanni et al. 2017, Vito et al. 2019) and 1.5 (typical of blazars, e.g., Giommi et al. 2019). Indeed, although the value of the Γ_X measured in Sect. 6.4 is consistent with a flat index ($\Gamma_X \sim 1.5$), typical of blazars sources, it is also consistent, within 1σ, with that of RQ or misaligned RL AGNs ($\Gamma_X \sim 2$). As expected the value of $\tilde{\alpha_{\rm ox}}$ does not depend significantly on the choice of Γ_X and it is equal to $1.09^{+0.07}_{-0.04}$. According to Ighina et al. (2019) this value is typical of high-z blazars (see Fig. 3.6 and Fig. 5.11).
We also compared the $\tilde{\alpha_{\rm ox}}$ of PSO J0309+27 with those reported in Vito et al. (2019, hereafter V19), which includes all the z>6 RQ AGNs observed in the X–rays at the time of PSO J0309+27 discovery. By doing this comparison we wanted to establish whether the X–ray emission of PSO J0309+27 is significantly more luminous compared to what is observed in non-blazar AGNs at similar redshifts. Indeed in a FSRQ the optical/UV emission has the same origin as in RQ AGNs (the accretion disk), while the X–ray emission is dominated by the boosted jet component that can largely overwhelm the coronal emission. To convert the values of $\alpha_{\rm ox}$ reported in V19 into $\tilde{\alpha_{\rm ox}}$ we used the relation found in Ighina et al. (2019): $\tilde{\alpha_{\rm ox}} = 0.789\alpha_{\rm ox} + 0.212(\Gamma_X - 1.0)$. We found that PSO J0309+27 has a much flatter $\tilde{\alpha_{\rm ox}}$ compared to the average value of the V19 sample (1.09 vs $<\tilde{\alpha_{\rm ox}}> = 1.54$), corresponding to an X–ray emission (at 10 keV) a factor $\sim$30 larger, on average, than that of the V19 AGNs, for the same UV luminosity. Considering the standard deviation of the values of $\tilde{\alpha_{\rm ox}}$ in the V19 sample (σ=0.11) and the uncertainty of our

measure (0.04), the $\tilde{\alpha_{ox}}$ of PSO J0309+27 is 3.7σ away from the mean value. Even considering the dependence between α_{ox} and $L_{2500Å}$, commonly observed in RQ AGNs, found in Just et al. (2007), the value of $\tilde{\alpha_{ox}}$ of PSO J0309+27 remains significantly ($\geq 2\sigma$) flatter compared to z>6 RQ AGNs. This confirms that PSO J0309+27 is different from the AGNs currently discovered at z>6 in terms of X–ray emission (see also Fig 6.14). This fact, combined with the radio properties unveiled from VLBI, convincingly supports the idea that the radio and X–ray emission of PSO J0309+27 is produced by a relativistically boosted jet, i.e. that the object is a blazar.

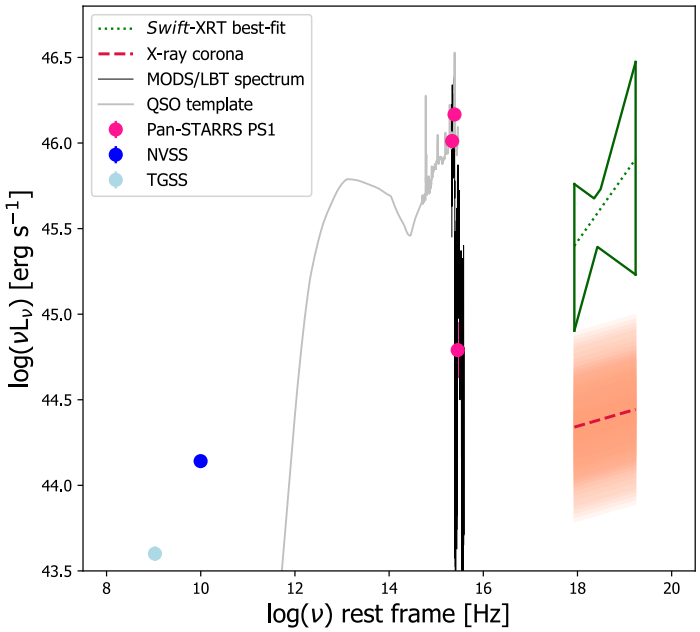

Figure 6.14: Rest-frame SED of PSO J0309+27 from radio to X–ray frequencies. In addition to the radio and optical photometric points, in the X–rays we show the best-fit emission in the observed [0.5-10] keV energy band (green dotted line) with its uncertainty. We also report the optical MODS/LBT spectrum (in black) and a quasar template (Polletta et al. 2007, grey solid line) for guide-line. The red dashed line represents the coronal emission expected from a RQ AGN with same $L_{2500Å}$ of PSO J0309+27 according to Just et al. (2007) relation, and the orange shaded area is the 1σ uncertainty on this estimate.

6.6.5 CIVλ1549Å emission line properties

Following the approach described in Sect. 5.5.3, we characterized the CIVλ1549Å line profile of PSO J0309+27, which we used to compute the mass of the central SMBH.
We parametrized the line width using both the FWHM and the line dispersion (σ_{line}, see also Eq. 1.11). We computed both by fitting the line profile, following different steps, similar to those described in Sect. 5.5.3.

- We shifted the LBT/LUCI spectrum to the source's rest frame: $\lambda_{rest} = \lambda_{obs}/(1+z_{CIV})$ and $F_{\lambda_{rest}} = F_{\lambda_{obs}} \times (1+z_{CIV})$, where z_{CIV} is the redshift of the peak of the CIV emission line: z = 6.063±0.003.

- We linearly fitted the continuum near the line in two specific intervals free from spectral features and other emission lines. We chose different intervals with respect to those proposed by Denney et al. (2013), i.e. 1435-1465Å and 1690-1710Å due to the fact that at $\lambda \sim$1435Å and at $\lambda \sim$1700Å there are many spikes due to the background. Therefore the the adopted

continuum intervals are: 1445-1465 Å and 1655-1685Å. Then we applied a linear fit between these two parts of the spectrum (see left panel of Fig 6.15) and we subtracted the continuum to the rest-frame spectrum (see right panel of Fig 6.15).

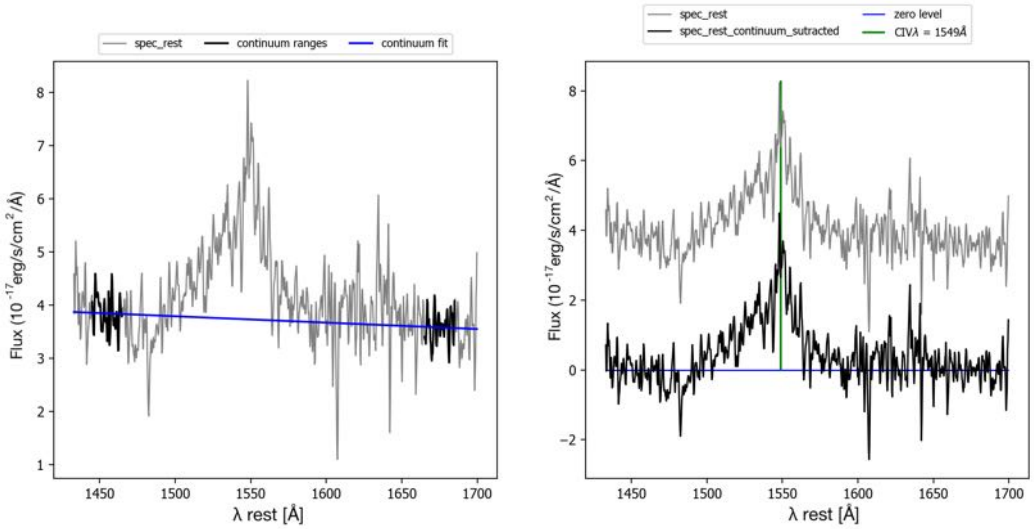

Figure 6.15: *Left panel*: Linear fit of the continuum (blue line) on the LUCI spectrum. In black we show the two continuum intervals used for the fit. *Right panel*: in grey the original rest frame LUCI spectrum (*top*), in black (*bottom*) the continuum subtracted one; the horizontal blue line is the *zero* level and the vertical green line represents the position of the rest frame CIV emission line at 1549Å.

- On the pseudo-continuum subtracted spectrum we fitted the CIV emission line with a double Gaussian profile (see Fig 6.16). The profile of the CIV broad emission line is usually fitted using at least two Gaussians (e.g., Shen et al. 2008; Tang et al. 2012). As already mentioned in Sect. 5.5.3 we did not include in the fit the CIV component due to the NLR. Moreover we decided not to include the FeII features, because, as mentioned in previous studies (e.g., Shen et al. 2011; Trakhtenbrot & Netzer 2012, Zuo et al. 2020), the contribution from FeII around the CIV line is expected to be small.

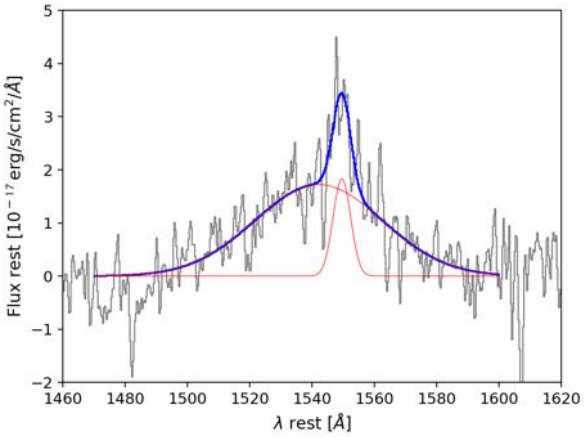

Figure 6.16: Double Gaussian fit of the CIV emission line. The rest frame LBT/LUCI spectrum is reported in grey, the two Gaussians in red and the sum of these two in blue.

- We computed the total FWHM, as we did for PSO J1244+86 (see Sect. 5.5.3), finding: FWHM = 14.71 Å = 2850.06 km s^{-1}. The FWHMs of the two single Gaussians are ∼6.6 Å (1286 km s^{-1}) and ∼48.3 Å (9350 km s^{-1}).
  Through Eq. 1.11 we estimated the second momentum of the line profile (σ_{line}). Discretizing the integral in the σ_{line} definition, using small intervals, we found: $\sigma^2_{line} = 347.43$ Å^2. Hence $\sigma_{line} = \sqrt{\sigma^2_{line}} = 18.64$ Å = 3609.97 km s^{-1}. Since we fitted the CIV line with a complex Gaussian profile, the relation FWHM = $2.355\sigma_{line}$ is not valid (Peterson et al. 2004).

- From the best fit model we also measured the rest-frame equivalent width (REW) and the line luminosity ($L_{CIV} = 4\pi D_L^2 F_{CIV}$, where F_{CIV} is the rest frame line flux). All these estimates and their uncertainties are listed in Table 6.8.

FWHM	$2850.06^{+801.26}_{-622.21}$ km s^{-1}	$M_{BH} = 4.3^{+3.6}_{-2.3} \times 10^8 M_\odot$ $\lambda_{Edd} = 0.62^{+0.58}_{-0.40}$
σ_{line}	$3609.97^{+120.24}_{-115.48}$ km s^{-1}	$M_{BH} = 8.1^{+1.6}_{-1.5} \times 10^8 M_\odot$ $\lambda_{Edd} = 0.33 \pm 0.16$
REW	$26.49^{+0.58}_{-0.73}$ Å	
F_{CIV}	$9.90^{+0.21}_{-0.28} \times 10^{-16}$ erg s^{-1} cm^{-2}	
L_{CIV}	$4.0 \pm 0.1 \times 10^{44}$ erg s^{-1}	
Δ_v	$1847.10^{+117.08}_{-134.09}$ km s^{-1}	

Table 6.8: Best fit parameters for the CIV emission line of PSO J0309+27 and single epoch black hole mass estimates. Δ_v is the line blueshift as defined in Sect. 6.6.5.

The uncertainties on these parameters are evaluated through a Monte Carlo approach as already done for PSO J1244+86 (see Sect. 5.5.3). In Figure 6.17 we report three example of double Gaussian fit on mock spectra. Instead Fig. 6.18 shows the distributions of FWHM, σ_{line} and REW for the 1000 simulated spectra, from which we computed the statistical uncertainty on the best fit values that has been propagated to the other estimates.

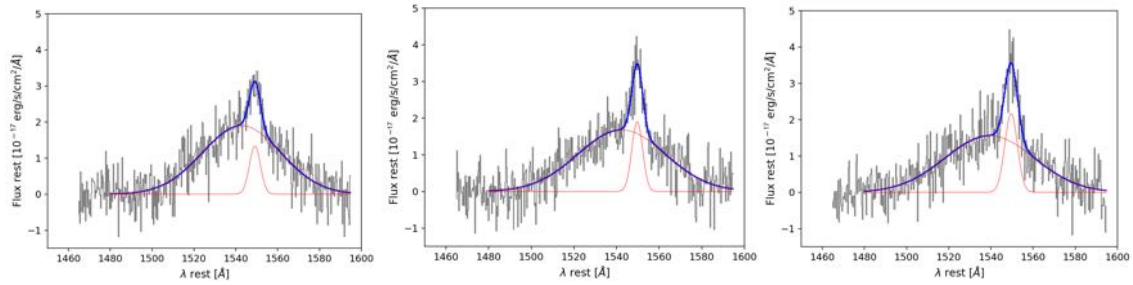

Figure 6.17: Examples of double Gaussian fit on mock spectra.

CIV blueshift and asymmetry

The CIV emission line is known to show asymmetry and blueshift with respect to the low ionization lines (e.g., Gaskell 1982; Richards et al. 2011; Coatman et al. 2017; Vietri et al. 2018; Zuo et al. 2020), independently from the source orientation (e.g., Kimball et al. 2011; Runnoe et al. 2014). Specifically, both a low-velocity core component and a blue excess can be present (Denney 2012). These characteristics suggest that the CIV clouds are affected by non gravitational effects, such

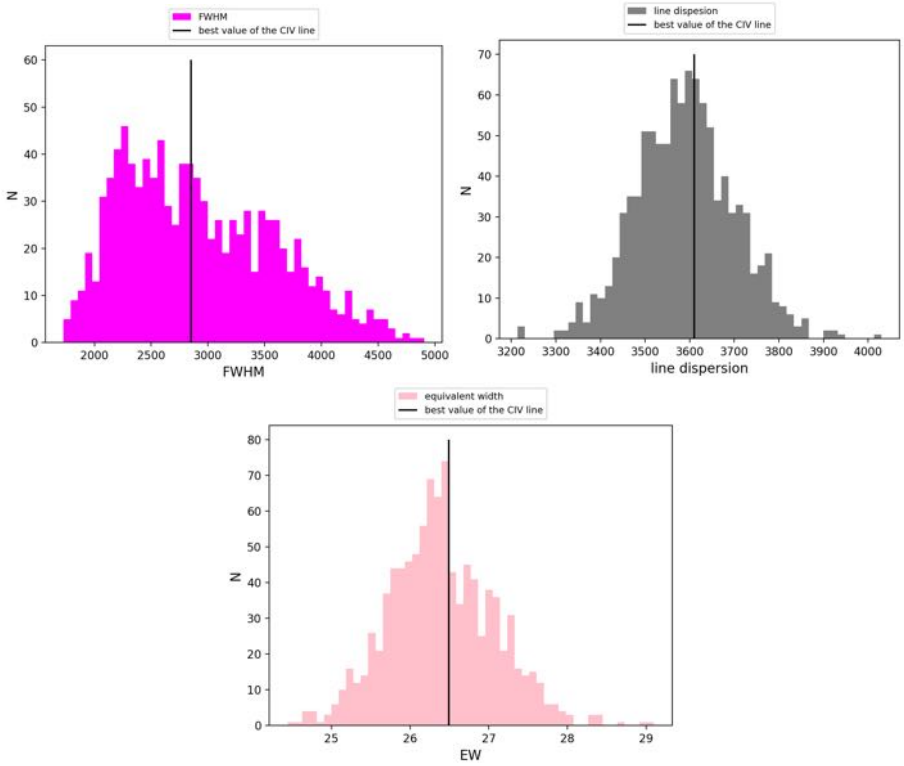

Figure 6.18: Distributions of the FWHM, σ_{line} and REW derived from the fit on mock spectra. Vertical black lines show the best fit values.

as outflows, most likely originated in disk winds. Largest CIV blueshifts indicate that non-virial motions have a significant effect on the observed emission velocity profile.
We computed the CIV blueshift of PSO J0309+27 following the equation of Coatman et al. (2017): Δ_v (km s^{-1}) = c$\frac{1549.48-\lambda_{half}}{1549.48}$, where c is the speed of light, 1549.48 is the rest-frame wavelength for the CIV and λ_{half} is the line centroid[2]. Positive blueshift values indicate an excess of emitting materials in the observed direction (i.e. an outflow). The value of the estimated Δ_v is reported in Table 6.8. This value is not high (Δ_v<2000 km s^{-1}), indicating that the outflows component is weak with respect to the emission of virialized gas. This is consistent with the results found in the literature (e.g., Shen & Liu 2012; Coatman et al. 2016): for small values of FWHM and σ_{line}, a low value of blueshift (Δ_v<2000 km s^{-1}) is usually observed. The largest blueshifts have been discovered to date in the so-called weak emission line quasars (WELQs, Diamond-Stanic et al. 2009), which exhibit a REW $<$ 10Å and a more asymmetric line profile (see e.g., Vietri et al. 2018 and reference therein). With a REW of ∼30Å PSO J0309+27 does not belong to this quasar population.

6.6.6 Black hole mass estimation

We computed the central black hole mass (M_{BH}) of PSO J0309+27 following two different and independent methods, as we have already done for DES0141−54 in Sect. 4.6.3. The first method is the single epoch (SE) approach and the second method is based on the accretion disk emission.

[2]The line centroid is defined as the wavelength that bisect the line in two equal part. We used the definition of Dalla Bontá et al. (2020): $\lambda_{half} = \frac{\int \lambda P(\lambda) d\lambda}{\int P(\lambda) d\lambda}$. We computed the λ_{half} parameter on the LUCI spectrum reported to rest-frame with the z_{syst}=6.10±0.03 computed from the emission lines in the LBT/MODS discovery spectrum.

Single epoch mass

We estimated the black hole mass of PSO J0309+27 from the single-epoch NIR LUCI spectrum by using the the CIV emission line and by following the scaling relationship of Vestergaard & Peterson (2006)[3] already reported in Eq. 1.13 and 1.14 of Sect. 1.3. The continuum luminosity at 1350Å ($\lambda L\lambda_{1350Å}$) has been computed directly from the rest frame optical LBT/MODS spectrum: $\lambda L\lambda_{1350Å} = 1.02\pm0.19\times10^{46}$ erg s^{-1}. In Table 6.8 we reported the virial black hole mass derived both from FWHM and σ_{line}.
Denney et al. (2013) and Dalla Bontá et al. (2020) find better agreement between CIV-based and Hβ-based mass estimates by using σ_{line} rather than FWHM, in particular when the spectrum has a high S/N. Since the value of S/N of the LBT/LUCI spectrum of PSO J0309+27 (∼8) is close to the required limit to ensure a reliable measure of σ_{line} (S/N=10), according to Denney et al. (2013), we considered the mass derived from this parameter as more reliable compared to the one based on the FWHM. Therefore, we used as the best value of the black hole mass of PSO J0309+27 the one computed from σ_{line}: $8.1^{+1.6}_{-1.5}\times10^8M_\odot$. In Table 6.8 we also reported the measurement uncertainties of the virial black hole mass, derived by propagating the errors of the CIV line width and of the monochromatic continuum luminosity. However we have to take into account the large intrinsic scatter of the CIV relations of the SE method (0.3 dex, e.g., Vestergaard & Peterson 2006; Jun et al. 2017) that affects the M$_{\rm BH}$ estimates.
As we have already done in Sect. 4.6.3 and Sect. 5.5.4, also in the case of PSO J0309+27 we have to take into account the possibility that the continuum emission could be contaminated by the relativistic jet. By comparing the ratio between the CIV line luminosity and the continuum luminosities at 1350Å of PSO J0309+27 with that of the RQ AGNs at high redshift of the sample of Shen et al. (2011) we did not find a significant offset between our blazar and that sample. This allow us to infer that the relativistic jet of PSO J0309+27 does not strongly contaminates its optical-NIR continuum emission.
Without taking into account the intrinsic uncertainty on the virial relation, we found that PSO J0309+27 hosts the smallest black hole among $z > 6$ RL objects ever discovered (see Fig. 7.1). Indeed Shen et al. (2019) reports the virial mass of J1427+3312 (z=6.12, McGreer et al. 2006, M$_{\rm BH}$ = $1.1\pm0.2\times10^9$M$_\odot$) of J1609+3041[4] (z=6.16, Bañados et al. 2015, M$_{\rm BH}$ = $4.3\pm0.3\times10^9$M$_\odot$) and of J1429+5447 (z=6.21, Willott et al. 2010a, M$_{\rm BH}$ = $1.8\pm2.5\times10^9$M$_\odot$).

Eddington Ratio

From the values of black hole mass, we derived the Eddington luminosity (L$_{Edd}$) and the Eddington ratio (λ_{Edd}). To compute λ_{Edd} we first estimated the bolometric luminosity (L$_{bol}$) of PSO J0309+27 using a bolometric correction (e.g., Richards et al. 2006): L$_{bol}$ = L$_{1350Å}$ × K$_{bol}$. In this case we used the correction factor of Shen et al. (2008): K$_{bol}$ = 3.81±1.26. However we have to remind that this K$_{bol}$ is calibrated empirically over RL and RQ Type I AGNs, with a mean expected angle of 30° (see also Sect. 4.6.3). Since PSO J0309+27 is a source probably observed under a small viewing angle ($\theta \sim 0°$) and that the continuum emission from the disk is not isotropic, we have to take into account the inclination factor ($i=\frac{\cos 0°}{\cos 30°} = 1.15$), to compute the intrinsic bolometric luminosity. This led to a final estimate of: L$_{bol}$ = 3.38±1.52 × 10^{46} erg s^{-1}. We obtained a similar value for L$_{bol}$ (3.57×10^{46} erg s^{-1}) using more recent non-linear relations

[3]We did not use black hole mass estimators that correct the effect of the CIV line blueshift (e.g., Coatman et al. 2017) first because the blueshift value for PSO J0309+27 is not high and second because the application of the blueshift correction factor, calibrated on z<4 AGNs may be inappropriate for high-z sources (e.g., Kim et al. 2018).

[4]Actually, Liu et al. (2021) showed with deep radio observations that the quasar J1609+3041 is not RL.

between K_{bol} and the continuum luminosity (e.g., Runnoe et al. 2012; Netzer 2019)[5]. Then we computed λ_{Edd} as the ratio between the bolometric luminosty and the Eddington luminosity both from the σ_{line} and the FWHM (see Table 6.8). In the following sections we always use the λ_{Edd} estimated from the σ_{line}, which we considered the best black hole mass estimator. The obtained value of 0.33±0.16 is similar to those found in other high-z AGNs (both RL and RQ) at the same redshift (see chapter 7).

6.6.7 Accretion disk model

Assuming that the disk emission of PSO J0309+27 is well described by a geometrically thin and optically thick SS73 model, we can estimate, in an independent way, the black hole mass of our source. We already used this approach in Sect. 4.6.3. The detailed description of the method can be found in Sect. 1.3.2. M_{BH}, $\dot{M}$ and η are the free parameters of the model. If we assume η=0.1 and if we measure L_{disk} (hence $\dot{M}$, because $L_{disk} = \eta \dot{M} c^2$), we are left with M_{BH} as the only remaining free parameter of the model. To estimate the value of the L_{disk} of PSO J0309+27 we followed the procedure described in Calderone et al. (2013, hereafter C13), based on the CIV line luminosity. From L_{CIV} we computed the disk luminosity for an isotropic BLR: $L_{disk\_iso} = 74.1 \times L_{CIV}$ (this relation has an intrinsic scatter of 0.3 dex)[6]. This equation is calibrated on Type I AGNs of the sample of Shen et al. (2011), therefore on a sample of objects oriented randomly, with an expected mean angle of 30°. For an AGN observed face on we have taken into account the inclination factor reported in Sec. 6.6.6. We therefore obtained: $L_{disk} = 1.71^{+2.12}_{-1.30} \times 10^{46}$ erg s^{-1}. Using this value and using as a guide line optical-UV spectrum of PSO J0309+27 and the photometric points at rest-frame wavelengths larger than the Ly-α line, we can finally constrain the black hole mass. The SS73 model that better represents our data is shown in Fig. 6.19 and describes the emission around a black hole with $M_{BH} = 2.6^{+2.1}_{-0.9} \times 10^8 M_\odot$ and $\dot{M} = 2.35 \pm 0.56 \times 10^{26}$ g s^{-1}.
From L_{disk} we also calculated L_{bol} as $\sim 2 L_{disk}$ (C13), obtaining 3.42×10^{46} erg s^{-1}, consistent within the errors with the value obtained in Sect. 6.6.6. The errors reported here for these quantities, are purely statistical.
The M_{BH} value computed with this accretion disk model is consistent with the values obtained from the virial method, considering the global uncertainties. We highlight that our method does not perform a statistical fit on the data, and we merely reproduce the rest-frame optical-UV SED following a qualitative approach.

6.7 Summary

In this chapter I reported the selection of blazar candidates at redshift between 5.5 and 6.5 ($i-dropout$ sources) using the combination between the widest field surveys available to date (NVSS in the radio, Pan-STARRS PS1 in the optical and WISE in the mid-IR), which their common area cover ∼21000 deg^2. Before this selection only 9 RL AGNs have been discovered at z≥5.5 but none of them has been classified as a blazar. We selected 7 $i-dropout$ objects, one of which has been already discovered by Bañados et al. (2018b). The 6 new candidates have been proposed for a spectroscopic follow-up at LBT. Three sources have been already observed in

[5] In the specific we adopted the non linear relation of Runnoe et al. (2012): $\log(L_{bol}) = A + B \times \log(L_{1350Å})$, with A = 4.745 and B=0.910. The author demonstrated that a non linear relation between L_{bol} and $L_{1350Å}$ provides a moderate improvement over using other standard bolometric corrections.

[6] L_{disk_iso} is the isotropic equivalent luminosity of L_{disk}, that is the actual luminosity integrated along all directions. The two quantities are related to each other by: $L_{disk\_iso} = 2\cos(\theta)\, L_{disk}$, where θ is the viewing angle of the source.

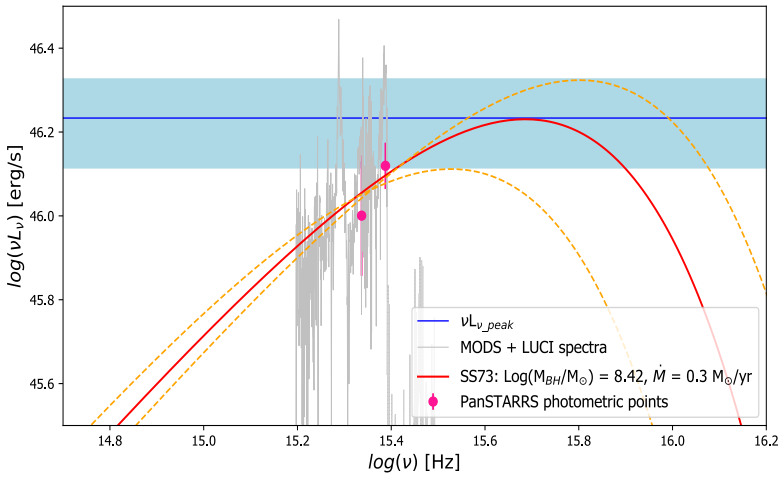

Figure 6.19: Accretion disk model of optical and NIR spectra (in grey) and PanSTARRS z and Y photometric data (magenta points) of PSO J0309+27. The red line represents the best modeling of SS73, while the horizontal blue line shows the disk peak emission. The statistical error on the peak luminosity is shown by the light blue shaded area and the two orange dashed lines represent the black hole mass range corresponding to the maximum and the minimum peak luminosity.

Septembre-December 2019: one turned out to be a star (likely a spurious ratio/optical match), one is a low-z galaxy, and the third is PSO J030947.49+271757.31 (hereafter PSO J0309+27), that has been confirmed to be at z=6.10±0.10. The spectroscopic follow-up is ongoing for the remaining three candidates, among which another one is a very promising high-z RL AGN.
Therefore, we have studied the multi-wavelength properties of PSO J0309+27, the first blazar at z>6. It is the brightest AGN in the radio band discovered to date above redshift 6 (23 mJy as measured in the NVSS). PSO J0309+27 is also the second brightest AGN in the X–ray band discovered at z>6 (with the brightest being CFHQS J142952+544717 from recent SRG/e-ROSITA observations, Medvedev et al. 2020).
The very high radio-loudness (R>2000) and the strong X–ray emission compared to the optical ($\tilde{\alpha_{ox}}$=1.09), strongly support the hypothesis that PSO J0309+27 is a jet dominated object, i.e. a blazar. Moreover on mas scale PSO J0309+27 reveals a core plus one-sided jet structure, a typical feature of oriented sources. The jet extends for hundred of kpc at low frequencies (150 MHz, observed frame) and it is in the same direction at all scales. Overall the physical parameters of the jet (low bulk Lorentz factor, ∼5, moderately small viewing angle, $\theta < 20$ deg, and small brightness temperature, $T_B \sim 10^8$) point to a mild beaming, that can be explained as a relatively slow jet. The radio spectrum at arcsecond scale is steep and seems to peak at low frequencies (<150 MHz, observed frame, i.e., <1 GHz in the rest frame) making PSO J0309+27 a MegaHertz Peaked Spectrum source (MPS).
The radio properties of this first blazar at z>6 are consistent with those already found in the literature: several brightest X–ray blazars at z>4 observed with VLBI show prominent jets extended on hundreds of parsecs in projection, a steep integrated spectrum in the GHz and low brightness temperatures of the core (i.e. $T_B < 10^{10}$ K), indicating mild beaming (e.g., Cao et al. 2017).
PSO J0309+27 has been recently observed with EVN+eMERLIN at 1.4 and 22 GHz (P.I. Spingola C.). These observations will allow us to investigate both intermediate and small scales emission and the radio flux densities variability of PSO J0309+27. Moreover we have approved

Low Frequnecy Array (LOFAR) observations (P.I. Spingola C.) to investigate the jet emission at low radio frequencies and the possible turnover in the radio spectrum and to test the interaction between the relativistic jet and the interstellar medium.
On the other hand, a *Swift*–XRT observation, despite of the low number of collected photons (11), revealed that PSO J0309+27 is characterized by a strong X–ray emission with respect to that of a RQ AGN with the same optical luminosity. The $\tilde{\alpha_{ox}}$ of the source is typical of blazars and it is flatter compared to the average value of the z>6 RQ AGNs presented in the sample of Vito et al. (2019, $<\tilde{\alpha_{ox}}> = 1.54$). This confirms that the X–ray emission of PSO J0309+27 is dominated by a beamed jet.
We have already obtained Chandra observations (100 ks, Ighina et al in prep.) for confirming the previous *Swift*–XRT result. The high-resolution Chandra follow-up will also allow us to investigate if PSO J0309+27 is characterized by a kpc X–ray jet, as suggested by several authors for z>4 powerful RL AGNs (e.g., Schwarz 2002; Marshall et al. 2018). Such a X–ray jet can be the consequence of the interaction between the jet electrons and the photons of the CMB (iC/CMB model, e.g., Tavecchio et al. 2000). In Fig. 6.20 I report a preliminary result of this 100 ks Chandra observation. A clear signal in the N-E direction (indicated with the two solid red line in the figure) at hundred of kpc from the central X–ray emission, is clearly detected. This emission could represent the X–ray jet of PSO J0309+27 and it is in the same direction of the radio jet detected by the VLBI.
Finally, with a LUCI/LBT spectroscopic follow-up in the near-IR we detected the CIVλ1549Å emission line, from which we computed the black hole mass of PSO J0309+27. We found a M_{BH} of $8.1^{+1.6}_{-1.5}\times10^{8}M_{\odot}$ using the virial method. This result is consistent, considering both statistical and intrinsic uncertainties, with that obtained independently with a method based on accretion disk modelling. From the value of the black hole mass we computed the Eddington ratio of the source, finding λ_{Edd}=0.33±0.16. The properties derived from the optical and near-IR spectra of PSO J0309+27 (i.e. black hole mass, Eddington ratio, bolometric luminosity) are consistent with those of other AGNs, both RQ and RL, at similar redshift, as we show in the next chapter.

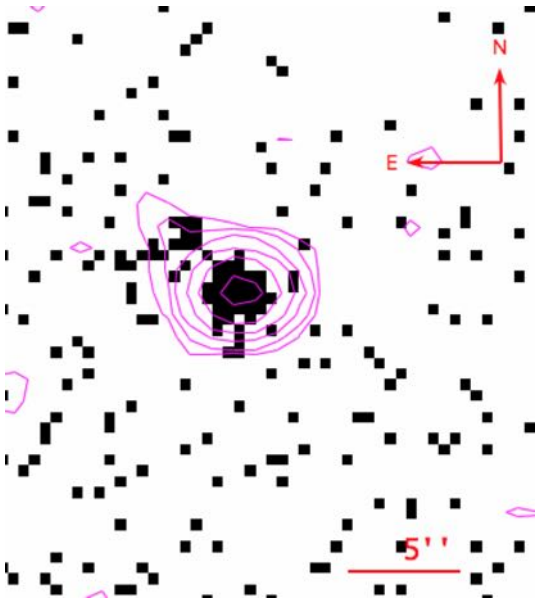

Figure 6.20: $0.4'\times0.4'$ 100 ks Chandra observation of PSO J0309+27. On the detected X–ray emission we over plotted the radio contours from VLASS. In the same direction of the radio jet (NE direction) a hint of a possible X–ray jet is observed. Courtesy of A. Moretti.

Chapter 7

Discussions and conclusion

In this thesis I presented the search, the discovery and the multi-wavelength study of high-z (z≥4) blazars, including the discovery of the first blazar at z>6.
In chapter 2 I mentioned the importance of finding blazars at high-z: they permit the unbiased (free from obscuration effects) census of the entire population of RL AGNs, including the dust reddened and obscured (Type 2) sources: $N_{RL} = \sim 2\Gamma^2 N_{blazar}$, where Γ is the bulk Lorentz factor of the jet relativistic plasma. The selection of blazar samples at high-z (z≥4) suitable for statistical studies and the discovery of more blazars at the highest redshift (until z∼6) represent the two best ways to study the RL AGN population in the early Universe. In chapter 3 I described the selection of a statistical radio flux limited sample of blazars at 4.0≤z≤5.5 (21 sources in total). This is, to date, the largest statistically complete radio flux-limited sample of high-z blazars available in the literature. In chapter 4, 5 and 6 I extended the selection to find more blazars at z>5.
In each chapter I described the method used to select the blazar candidates, based on the cross-match between radio, optical and mid-IR wide field surveys and on the *dropout* technique. Different combinations of radio and optical surveys (CLASS+PS1, SUMSS+DES, NVSS+PS1) have been exploited to select blazar candidates all over the sky.
The objects in the CLASS sample and the sources discovered individually at z≥5 (DES0141−54 at z=5.0, PSO J1244+86 at z=5.3 and PSO J0309+27 at z=6.1) represent a significant increase (∼50%) in the total number of detected blazar in the early Universe (see Table 7.1). At redshift between 5.5 and 6 no blazars have been found with the selection method presented in this work. This redshift range is part of the so-called *quasar redshift gap* (z between ≃5.3 and ≃5.7; e.g., Yang et al. 2019a). Moreover the null increment at redshift between 4.5 and 5 is due to the fact that the 2 CLASS blazars in this redshift range were already known in the literature before this thesis (see Table A.1).

Number of blazars		
z	Before this work	After this work
4-4.5	15	23 (53%)
4.5-5	8	8 (0%)
5-5.5	4	8 (50%)
5.5-6	0	0
6-6.5	0	1 (100%)

Table 7.1: Number of blazar before and after this thesis. The sources are divided in the same redshift bin used in Fig. 2.2. In parenthesis the percentage of newly discovered blazars in each redshift bin is reported.

Radio and X–ray properties

The objects of the CLASS sample at redshift between 4 and 5.5, PSO J1244+86 and PSO J0309+27 have been confirmed to be blazars mainly from their X–ray emission, which is stronger and flatter with respect to that of RQ AGNs with same optical luminosities. This is an indication of the presence of a beamed jet, whose emission overwhelms that of the X–ray corona. Instead, DES0141−54 shows a very weak X-ray emission compared to the other blazars described in this thesis. Its X–ray emission is also consistent with the coronal one, suggesting that the power of the relativistic jet must be very weak. However the flatness of its radio spectrum on a wide range of frequencies and the very high value of radio-loudness (the highest ever measured at z≥5) support the blazar nature of this source. As well as DES0141−54, there are also 15 CLASS blazars that show a flat radio spectrum. However the other sources studied in this work present differences in the shape of the radio spectrum. 5 CLASS sources and PSO J1244+86 show a peak in the radio spectrum around 1 GHz (observed frame), while for other 5 CLASS objects the classification is uncertain. RL AGNs with a peaked radio spectrum are commonly observed at high-z (e.g., Coppejans et al. 2017). Finally in the case of PSO J0309+27 the spectrum becomes steeper at very high frequencies. It has already been highlighted that a not genuine flat radio spectrum does not prevent the blazar nature of the sources, as the case of Q0906+6930 (see e.g., Sect. 3.4).
High-z powerful X–ray AGNs, as the blazars studied in this thesis, could be also the suitable objects for investigating the presence of kpc X–ray jets arising from the interaction between jet electrons and CMB photons, as already highlighted in Sect. 6.7 for PSO J0309+27.

Black hole mass and bolometric luminosity

From the analysis of the CIV and/or the MgII emission lines in the optical/near-IR spectra of DES0141−54, PSO J1244+86 and PSO J0309+27, we found that they host a SMBH of 10^8-10^9 solar masses. The analysis of the optical properties of the CLASS blazars is still in progress (Diana et al. in prep.), but a preliminary result revealed that they also host such massive black holes (see Table D.1[1]).
In Figure 7.1 we show L_{bol} versus M_{BH}, for DES0141−54, PSO J1244+86, PSO J0309+27 and for the CLASS objects compared to RQ and RL AGNs from the literature. Following De Rosa et al. (2011) we considered a low-z comparison sample from the SDSS DR7 quasar catalog of Shen et al. (2011), selecting only objects (both RQ and RL) with a redshift range 0.35<z<2.25, a measure of the virial black hole mass, bolometric luminosity and Eddington ratio. We also considered as a comparison sample all the AGNs discovered at 4≤z≤6.5 with a measure of the SE black hole mass from CIV or MgII lines and L_{bol}. This sample consists of ∼990 objects taken from different works[2] and includes both high- and low-luminous AGNs. For all these objects, we used the most recent measurements of black hole mass and bolometric luminosity when more than one exists in the literature.
From Fig. 7.1 it is clear that the z≥4 blazars discovered in this thesis occupy a region in the parameter space similar to those of high-z AGNs (both RL and RQ) already discovered. The similar range of masses is likely just a consequence of the fact that all these high-z sources have been selected from similar optical/IR surveys.

[1] We do not have the optical/near-IR spectrum of the source GB6J090631+693027 at z=5.47, but a measurement of its black hole mass, based on the virial method, is available in An & Romani(2018): $4.2\times10^9 M_\odot$

[2] Jiang et al. (2007), Willott et al. (2010b), De Rosa et al. (2011), Shen et al. (2011), (2019), Ikeda et al. (2017), Mazzucchelli et al. (2017), Eilers et al. (2018), Kim et al. (2018), Onoue et al. (2019), Andika et al. (2020). Willott et al. (2010b) is the only work that used a slightly different cosmology. However the black hole mass derived from Willott et al. (2010b) and the one derived adjusting the cosmology are consistent within the errors, therefore for Fig. 7.1 the published values have been used.

It should be noted that, as discussed in Sect. 1.3.1 and Sect. 4.6.3, the source orientation may bias the derived physical parameters, like the black hole mass and the Eddington ratio. In principle, this problem may affect a direct comparison between blazars and other classes of AGNs (both RQs and RLs). However, as discussed in the previous Chapters, we do not have evidence that black hole masses are significantly affected by this problem. As far as the L_{bol}/L_{Edd} ratio is concern, we have already taken into account the orientation bias, by correction the bolometric luminosities for the inclination angles (see Sect. 4.6.3, Sect. 5.5.4, Sect. 6.6.6 and Table D.1).

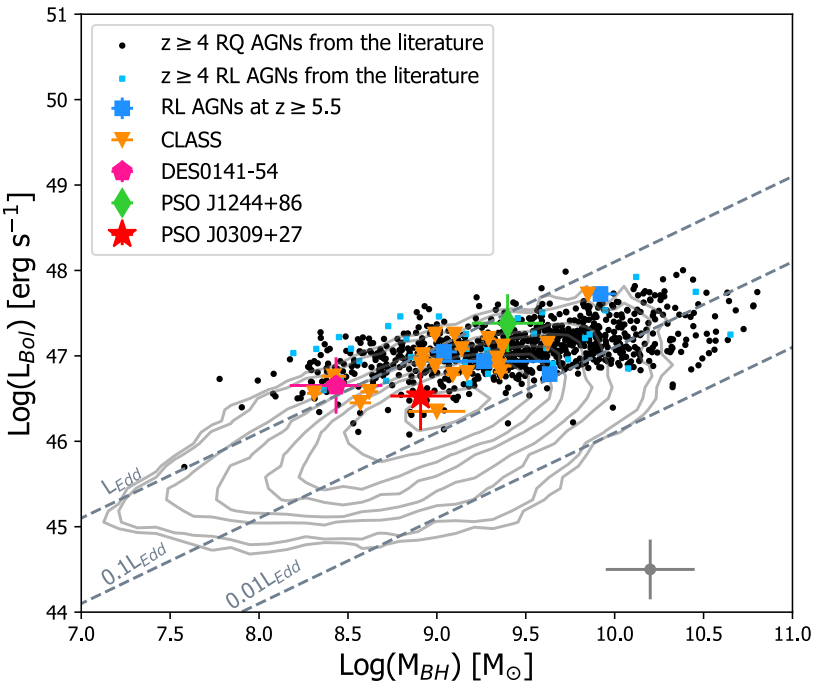

Figure 7.1: The SMBH mass-luminosity plane for DES0141−54 (magenta pentagon), PSO J1244+86 (green diamond), PSO J0309+27 (red star) and CLASS blazars (orange triangles), compared to other AGNs samples for which a virial black hole mass estimation is available in the literature: black points are 4.0≤z≤6.5 RQ AGNs, little blue and large blue squares are RL AGNs at z≥4 and z≥5.5 respectively and grey contours show the distribution of low redshift SDSS AGNs from Shen et al. (2011), both RL and RQ. The diagonal lines show constant Eddington ratio (λ_{Edd} = 1, 0.1, 0.01). The grey cross represent the statistical uncertainty on the virial black hole mass and a representative mean error on the bolometric luminosity of the high-z sample. Our high-z blazars occupy the same parameter space of the other RL and RQ AGNs at high redshift, with the majority of our blazars being as massive as the other RL AGNs at high-z (blue squares). Instead DES0141−54, PSO J0309+27 and 5 CLASS blazars show lower BH masses.

Tracing back the BH seed

Accurate measurements of black hole masses and Eddington ratios of high-z AGNs help to constrain formation scenarios of the first seed black holes. In particular, as already mentioned in Sect. 1.4, the discovery of jetted-AGNs in the early Universe represents a serious challenge to our understanding of black hole growth, especially if the presence of the jet is associated with a rapidly spinning black hole, which is expected to have a large radiation efficiency and, therefore, a longer growth time with respect to black holes hosted by RQ AGNs (see Eq. 1.21).

We applied the black hole growth model[3] described by Eq. 1.21 to derive the initial mass of the black hole seed required to observe the mass of DES0141−54 at z=5, PSO J1244+86 at z=5.3, PSO J0309+27 at z=6.1 (1.186, 1.103 and 0.922 Gyr after the Big Bang respectively) and of the CLASS sources in the redshift range 4-5.5. Figure 7.3 shows the estimated growth history of these black holes according to this model. These results depend of the assumptions made, i.e. on the redshift of the seed formation, on the accretion rate and on the radiative efficiency. We trace the mass back to z=30, when the first stars and galaxies are thought to have formed (e.g., Bromm & Larson 2004; Bromm & Yoshida 2011). For the three z≥5 blazars (DES0141−54, PSO J1244+86 and PSO J0309+27) we assumed that the seed black holes accrete constantly with the observed Eddington ratio for each sources (see Sect. 4.6.3, Table 5.4 and Table 6.8) or with λ_{Edd} equal to 1, the maximum accepted value in a Eddington limited accretion scenario. Instead for CLASS blazars we assumed only a growth at the observed Eddington ratio (see Table D.1), to produce a clearer plot for the entire sample. The efficiency parameter is believed to depend on black hole spin (e.g., King & Pringle 2006) and can be as high as ∼30-40% in case of spinning black hole (e.g., Thorne 1974). The spin parameter has been observationally measured only in ∼20 sources in the local universe (through the relativistic broadening of the Fe-Kα line; e.g., Brenneman et al. 2011; Reynolds 2014). Current semianalytical models place only weak constraints on the spin values at z>5, which depend on the gas accretion mode, the morphology of the host galaxy and black hole mass (e.g., Sesana et al. 2014). Therefore as no stringent constraints on black hole spin are reported to date for high-z AGNs, we assume both an efficiency of 0.1 (expected for not rapidly spinning black holes) and 0.3 (expected for Kerr black holes). Finally all the uncertainties on the virial black hole mass, both statistical errors and the intrinsic scatter of the SE method, have been taken into account. For DES0141−54 we computed the weighted mean of the two virial masses (from CIV and MgII lines). Then we considered the scatter on the black hole mass estimate of 0.4 dex reported in Shen et al. (2011), obtaining $M_{BH} = 2.7^{+4.27}_{-1.62}\times10^8 M_\odot$. The same intrinsic scatter has been taken into account in the case of PSO J1244+86, for which we computed the mean of the two SE masses: $M_{BH} = 2.5^{+3.7}_{-1.5}\times10^9 M_\odot$. Finally for PSO J0309+37 we used the virial mass based on the σ_{line} parameter and the intrinsic scatter of 0.36 dex reported in Peterson et al. (2004), obtaining: $M_{BH} = 8.14^{+9.01}_{-4.49}\times10^8 M_\odot$. These total errors were propagated also to the Eddington ratios. Instead for CLASS sources, for illustrative purpose, the best fit values of the black hole masses reported in Table D.1 have been used.

Figure 7.3 shows that only in the case of DES0141−54 and of 6 CLASS blazars an efficiency of 0.3 reproduced a seed black hole consistent with those predicted by current theoretical models (see Sect. 1.4). For DES0141−54 this is due to its low black hole mass, the high observed accretion rate and the fact that is the least distant object. For the two other sources (one more massive, PSO J1244+86, and one more distant, PSO J0309+27) and for the bulk population (13) of CLASS blazars, only η=0.1 can reproduce a theoretically accepted seed mass. Alternative scenarios assuming a higher efficiency (η=0.3), instead, would require more massive seeds ($M_{seed}\geq10^6 M_\odot$) as progenitors of PSO J1244+86 and PSO J0309+27 and of the 13 CLASS objects. These expected seeds are even more massive than what the direct collapse (DCBH) models predict ($M_{seed}\sim10^4$-$10^6 M_\odot$, e.g., Latif & Ferrara 2016). This results suggests that such high values of efficiency are not probably realistic, not even in RL AGNs.

Alternatively, super-Eddington accretion episodes must occur for a significant fraction of the growth time. To date, there have been no clear examples of such super-Eddington SMBHs at z>5, although this scenario has been suggested for J1205−0000, a mildly obscured AGN at z=6.699 (Onoue et al. 2019) and for PSO J006+39 at z=6.621 (Tang et al. 2019) that are two RQ AGNs.

[3]In this work, the value of the duty cycle ($f_{act}(M,t)$) is assumed to be equal to 1, meaning that the AGN has been active for all the time.

Indeed SE accretion episodes are often taken into consideration also for the growth of black holes hosted in RQ AGNs, even if, to date, this scenario has been discussed mainly for objects at z≥6.5 (e.g., Mazzucchelli et al. 2017; Bañados et al. 2018a; Onoue et al. 2019; Wang et al. 2021). The model described in Eq. 1.21 applied to z∼6.5-7.5 RQ AGNs hosting $10^9 M_\odot$ black holes predicts at z∼30 seed black holes with masses similar to those expected from DCBH models, while it rules out lighter seeds, i.e. those derived from stellar Pop III remnants. Such types of progenitors can be a valid possibility only if hyper-Eddington accretion episodes occurs during the black hole growth or if the efficiency is low (η<0.1). It has been suggested that maintaining super-Eddington accretion might be possible in specific environments (e.g., Inayoshi et al. 2016), but whether or not this type of accretion is sustainable remains an important open question for the growth of both RL and RQ AGNs.
Another possible solution taken into consideration for the growth of black holes in RL AGNs has been proposed by Jolley & Kunzic (2008), Jolley et al. (2009) and Ghisellini et al. (2010): when a jet is present, not all the gravitational energy of the infalling matter is transformed into heat and then radiation, but can be transformed in other forms, such as amplifying the magnetic field energy of the inner disk, a necessary ingredient for launching the jet (Blandford & Znajek 1977). In this case the total accretion efficiency can be $\eta = 0.3$, but only a fraction of it (η_d) goes to heat the disk, while the rest ($\eta - \eta_d$) goes to amplify the magnetic field necessary to launch the jet. Therefore disk luminosity becomes Eddington limited for a larger accretion rate, making the black hole growing faster. This possible solution has been discussed for the first time in Ghisellini et al. (2015) for the powerful blazar SDSS 0131−0321 at z=5.18. The authors predict a reasonable seed for this blazar making different assumptions on the value of η_d. Without taking into account this possible solution the seed black hole required to reproduce the mass of SDSS 0131−0321 would be too large, exceeding those predicted from DCBH models.
Cosmological simulations of seeds black holes growth (e.g., Di Matteo et al. 2008; Booth & Schaye 2009,; Alexander & Hickox 2012; Feng et al. 2014a) are fundamental to understand what are the main ingredients of the seed evolution besides the accretion process (e.g., mergers, AGN or stellar feedback, different duty cycles).

Space densities of high-z blazars

In Section 3.5, we have computed for the first time the space density of blazars at redshift between 4 and 5.5, using the CLASS sample. By comparing the CLASS sample space densities with the theoretical expectation of Mao et al. (2017), we found that FSRQs (and hence the RL AGNs, if we consider $N_{RL}=2\Gamma^2 N_{blazar}$) have a peak in their evolution at z∼2, which is in agreement with the peak estimated for the total (RQ + RL) AGN population (e.g., Hopkins et al. 2007). Instead this is in contrast with the results obtained from X–ray selected blazar samples (e.g., Ajello et al. 2009; Toda et al. 2020). We are now investigating the possible origin of this discrepancy (Ighina et al. in prep).
Thanks to the newly discovered blazars at z∼5 presented in chapter 4 and 5 (i.e., DES0141−54 at z=5 and PSO J1244+86 at z=5.3), we can update the space density of blazars at 4.5≤z≤5.5 computed in Sect. 3.5. Moreover thanks to the discovery of PSO J0309+27 we can infer the first unbiased measurement of the space density of FSRQs at z∼6. These three sources have the same characteristics of the blazars of the CLASS sample in term of radio and optical luminosity[4]. However, as explained in chapter 4, 5 and 6, we did not spectroscopically identify all the selected candidates, and, therefore, the derived space densities at z=4.5-6 should be more properly con-

[4] $\log(L_{1.4\ GHz}) = 43.04\text{-}44.43$ and $M_{1450\text{Å}}$ between −24.8 and −28.1 are the range of radio and optical luminosity covered by the CLASS sample.

sidered as lower limits (although we do not expect that the actual values are very different from these lower limits).
To derive the space density, we followed the same procedure and formulas described in Sect. 3.5 (i.e. Eqs. 3.1, 3.2 and 3.3). In the redshift bin between 4.5 and 5.5 there are 6 CLASS blazars and two new blazars. We divided this range of redshift in two bins (4.5-5 and 5-5.5). In both bins 4 objects are present[5]. CLASS blazars were selected in a sky area of 13120 deg^2, DES0141−54 in the southern sky (3500 deg^2) and in the 690 deg^2 at Dec≥75° we selected PSO J1244+86. The computed values of the space density at redshift 4.5-5 and 5-5.5 are reported in Table 7.2. They are consistent with the prediction of Mao et al. (2017, see Fig. 7.2. Instead at z>5.5 the only known blazar is, to date, PSO J0309+27. It was selected in an area of ∼21000 deg^2 corresponding to a comoving volume between redshift 5.5 and 6.5 of 359 Gpc^3. This implies a space density of $5.5^{+11.2}_{-4.6}$ ×10^{-3} Gpc^{-3} (see Table 7.2) in this redshift bin. This estimate agrees with the expectations based on the cosmological evolution presented by Mao et al. (2017), which predicts a space density at the same redshift of ∼0.012 Gpc^{-3} (Fig. 7.2).

In order to reduce the statistical uncertainty on these space densities estimates, statistically

redshift bin	N blazars	Total area (deg^2)	ρ_{bl} (Gpc^{-3})
4.5-5	4	16620	$0.045^{+0.035}_{-0.021}$
5-5.5	4	13810	$0.057^{+0.045}_{-0.027}$
5.5-6.5	1	21000	$0.0055^{+0.0112}_{-0.0046}$

Table 7.2: Space densities of blazars in three different redshift bins, computed using CLASS sources at z>4.5 and the other three newly discovered blazars at z≥5 (DES0141−54, PSO J1244+86 and PSO J0309+27). Col (1): redshift bin; Col (2): number of blazars; Col (3): total areas on which the space densities reported in Col (5) have been calculated.

complete and larger samples of blazars, and more blazars at the higher redshift are needed.

Future developments

To date the most critical difficulties in the selection of larger sample of blazars suitable for statistical studies at the highest redshift, are:

- the low accuracy of the radio positions of the available radio surveys, that lead to the inclusion of tens of spurious radio/optical matches (i.e. stars) in the selection process;
- the magnitude limit of the optical wide field surveys (∼22 for Pan-STARRS and SDSS), which prevents from the selection of low luminous AGNs;
- the spectroscopic limit of current largest 8-10 m telescopes;

The advent of the Large Synoptic Survey Telescope (LSST, Vera C. Rubin Observatory, Ivezic et al. 2008) data in the next decade, combined with future radio surveys (e.g., the Evolutionary Map of the Universe, EMU, Norris et al. 2011, or the surveys performed with the Square Kilometer Array, SKA) will allow the selection of larger samples of blazars at the highest redshift (z>7). For example, by taking into account the cosmological evolution of Mao et al. (2017) and the radio and optical characteristics of the CLASS high-z sample, we expect to find 10 blazars above redshift 6 and a handful of blazars (∼5) above redshift 7 in the common area of EMU and LSST. Indeed the

[5]GB6J0011+1446, GB6J1430+4204, GB6J1629+0959 and DES0141−54 at z=4.5-5 and GB6J1026+2542, PSO J1244+86 GB6J1648+4603 and GB6J0906+6930 at z>5.

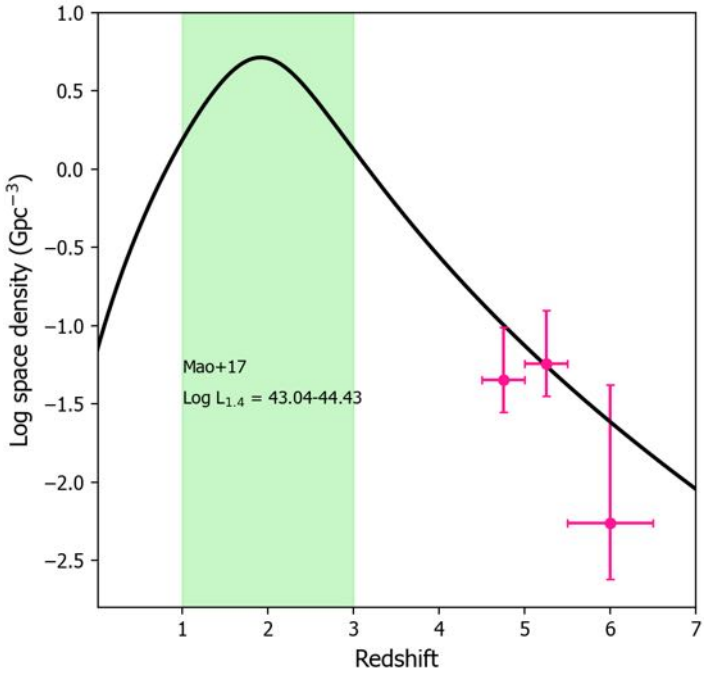

Figure 7.2: Space densities versus redshift of the blazars at z≥4.5 presented in this thesis (magenta points, Table 7.2). As explained in the text, this values should be properly considered as lower limits. The black solid line represents the expected space density at all redshift computed by integrating the LF of Mao et al. (2017, reported in Sect. 3.5) in the same range of radio luminosity (at 1.4 GHz) observed in these blazars. The shaded area indicates the range of redshift sampled by the FSRQs of Mao et al. (2017) in this range of radio luminosity.

new generation of radio surveys not only will be deeper (e.g., a 5σ limit of ∼50 μJy in the case of EMU) but they will provide more accurate positions of the detected sources, thus minimizing the inclusion of spurious radio/optical matches. These surveys in combination with LSST, which will reach a magnitude limit of 24-26, will allow the discovery of fainter RL AGNs up to z∼7.2, i.e. within the so-called re-ionization epoch (z>6-7). Sources with a optical magnitude of ∼24-25 could be then spectroscopically observed with the next generation of optical/near-IR telescopes with ∼30-40 m of diameter (as the Extremely Large Telescope, ELT).
I am already participating to the EMU-pilot survey with a project focused on the search of misaligned RL AGNs in the southern sky (thanks to the combination with the optical DES). Moreover, I joined the italian LSST collaboration with a project[6], supported by INAF, dedicated to the high-z- RL AGNs. Finally I became part of an Advanced Telescope for High ENergy Astrophysics (Athena, Nandra et al. 2013) working group for a projetc focused on exploring the RL population in the re-ionization era.

[6]project title: *High-z AGN and galaxies into the Re-ionization Epoch with LSST*

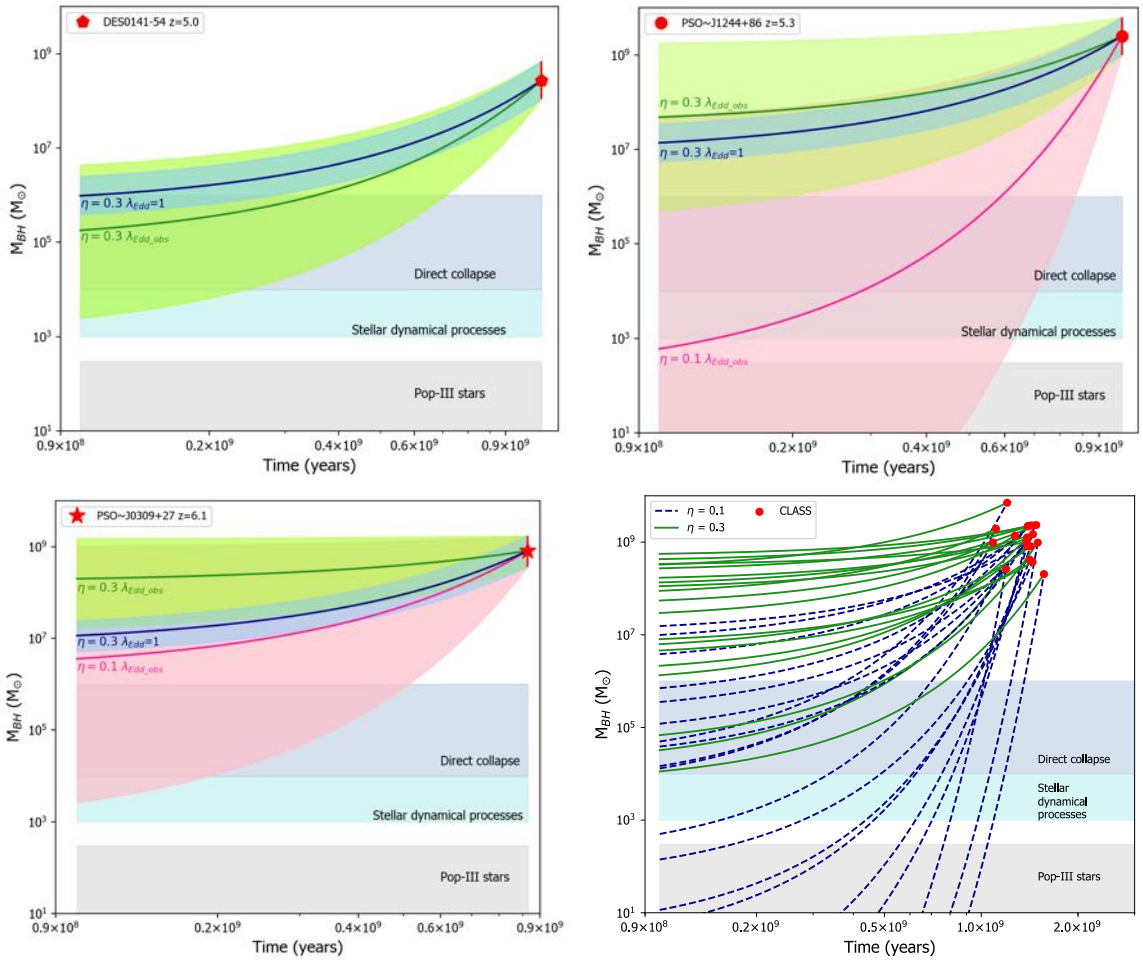

Figure 7.3: Estimated growth history of DES0141−54 (*upper left panel*, red pentagon at z=5), PSO J1244+86 (*upper right panel*, red point at z=5.3), PSO J0309+27 (*bottom left panel*, red star at z=6.1). Solid lines represent the best fit cases, under which the corresponding λ_{Edd} and η are reported; while the uncertainties are shown with colored shaded areas. The *bottom right panel* show the black hole growth of the CLASS sources. Here the solid and the dashed lines represent the growth at $\eta = 0.3$ and η=0.1 respectively. On the x-axis of all the panels the time since the Big Bang is reported. The shaded horizontal regions correspond to the expected mass ranges of Pop III remnants BHs ($M_{seed} \leqslant 10^2 M_\odot$, grey), stellar dynamical processes ($M_{seed} \geqslant 10^3$-$10^4 M_\odot$, cyan) and direct collapse BHs ($M_{seed} \sim 10^4$-$10^6 M_\odot$, dark cyan). The values of the different seed black holes are taken from Valiante et al. (2016).

Appendix A

Blazars from the literature

Here I report the list of the z≥4 sources classified as blazars in the literature before 2018. The criteria used to classify a source as a blazar are different, and based both on radio and X–ray properties. Here I considered all the sources with a validation in the literature.

name	z	RA (hms)	Dec (dms)	blazar identification
J012202+030951	4.0	01:22:01.90	+03:10:02.41	1
J171521+214547	4.01	17:15:21.26	+21:45:31.65	2
J142048+120545	4.02	14:20:48.01	+12:05:45.9	3
J222032+002537	4.2	22:20:32.49	+00:25:37.5	3
J195135+013442	4.11	19:51:36.02	+01:34:42.7	4
J102838−084438	4.276	10:28:38.80	−08:44:38.6	5
J091824+063653	4.22	09:18:24.38	+06:36:53.3	6
J130940+573309	4.28	13:09:40.70	+57:33:09.9	2
J115503−310758	4.3	11:55:03.16	−31:07:58.7	7
J151002+570243	4.31	15:10:02.92	+57:02:43.4	8
J213412−041909	4.334	21:34:12.02	−04:19:09.7	3
J052506−334305	4.383	05:25:06.18	−33:43:05.5	9
J083946+511202	4.4	08:39:46.22	+51:12:02.8	10
J132512+112329	4.42	13:25:12.49	+11:23:29.8	2
J125359−405930	4.464	12:53:59.53	−40:59:30.7	7
J094004+052630	4.5	09:40:04.8	+05:26:30.99	11
J032444−291821	4.63	03:24:44.29	−29:18:21.22	7
J172026+310431	4.67	17:20:26.68	+31:04:31.6	11
J143023+420450	4.72	14:30:23.73	+42:04:36.51	9
J101335+281119	4.75	10:13:35.44	+28:11:19.24	11
J021043−001818	4.77	02:10:43.16	−00:18:18.4	11
J145459+110927	4.93	14:54:59.30	+11:09:27.89	11
J001115+144601	4.96	00:11:15.24	+14:46:01.8	12
J114657+403708	5.0	11:46:57.79	+40:37:08.66	13
J013127−032100	5.18	01:31:27.34	−03:21:00.2	14
J102623+254259	5.25	10:26:23.62	+25:42:59.44	15
J090630+693030	5.47	09:06:30.75	+69:30:30.80	16

Table A.1: Sources classified as blazars in the literature before 2018. Col (1): object name; Col (2): redshift; Col (3) and Col (4): optical coordinates; Col (5): Reference for blazar classification: 1=Sowards-Emmerd et al. (2003); 2=Ghisellini et al. (2015b); 3=Sbarrato et al. (2015); 4=Healey et al. (2008); 5=Yuan et al. (2000); 6=Massaro et al. (2015); 7=Massaro et al. (2009); 8=Yuan et al. (2003); 9=Worsley et al. (2004); 10=Sbarrato et al. (2013); 11=Coppejans et al. (2016); 12=Shemmer et al. (2006); 13=Ghisellini et al. (2014); 14=Ghisellini et al. (2015a); 15=Sbarrato et al. (2012b); 16=Romani et al. (2004).

Appendix B

CLASS spectra

In this Appendix I report the optical spectra taken at the LBT and TNG telescopes for 10 out of 12 CLASS candidates without a spectroscopic identification in the literature and without an optical spectra in the SDSS database. The low value of the S/N of the other two sources prevents a clear identification of the two objects, therefore I do not report their spectra here.

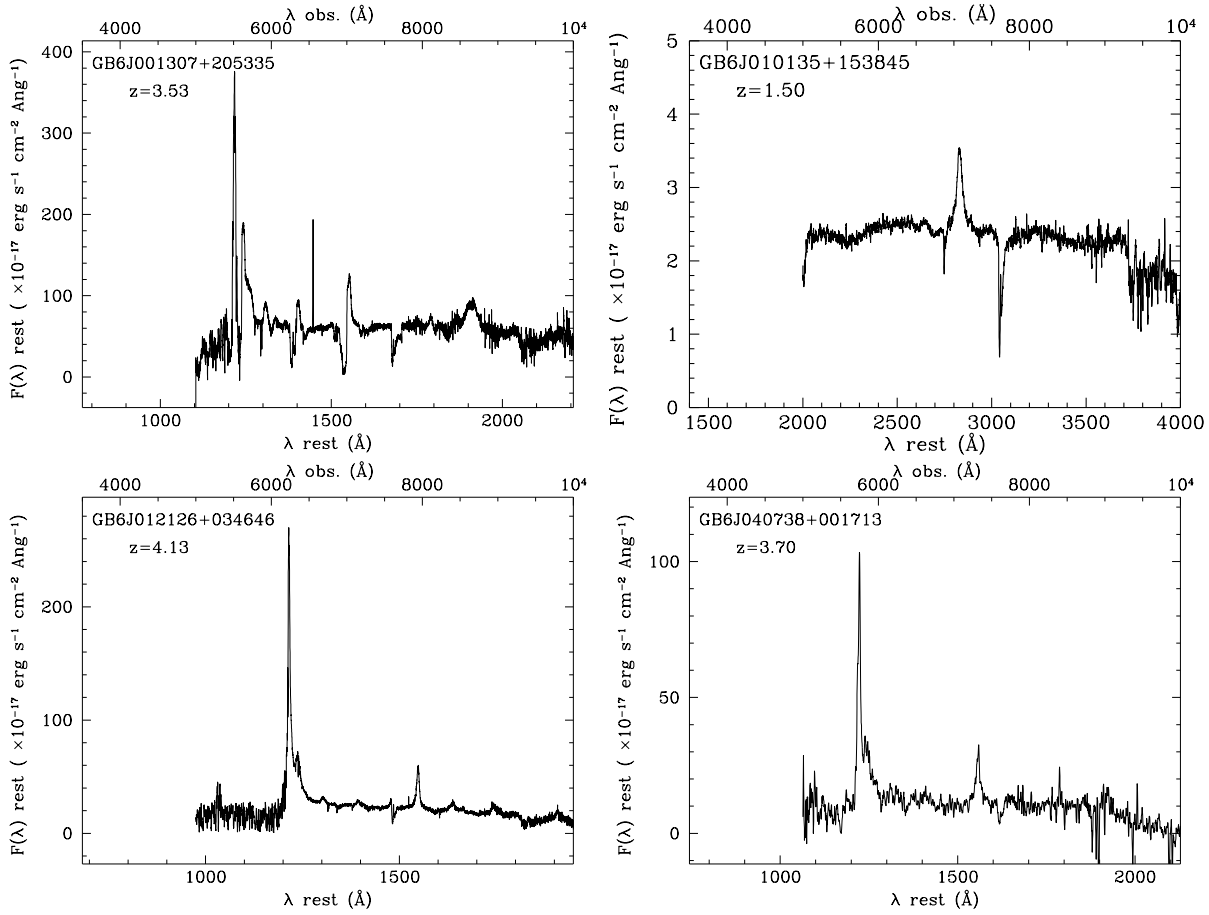

Figure B.1: Spectra taken at TNG and LBT for 10 out of 12 CLASS candidates. For each source the name and the redshift are reported. On the *bottom* x-axis the observed wavelengths (in Å) are shown, while the rest frame wavelengths (in Å) are reported on the *top* x-axis. The y-axis shows the rest frame flux density of each object in unit of 10^{17} erg s^{-1} cm^{-2} Å^{-1}.

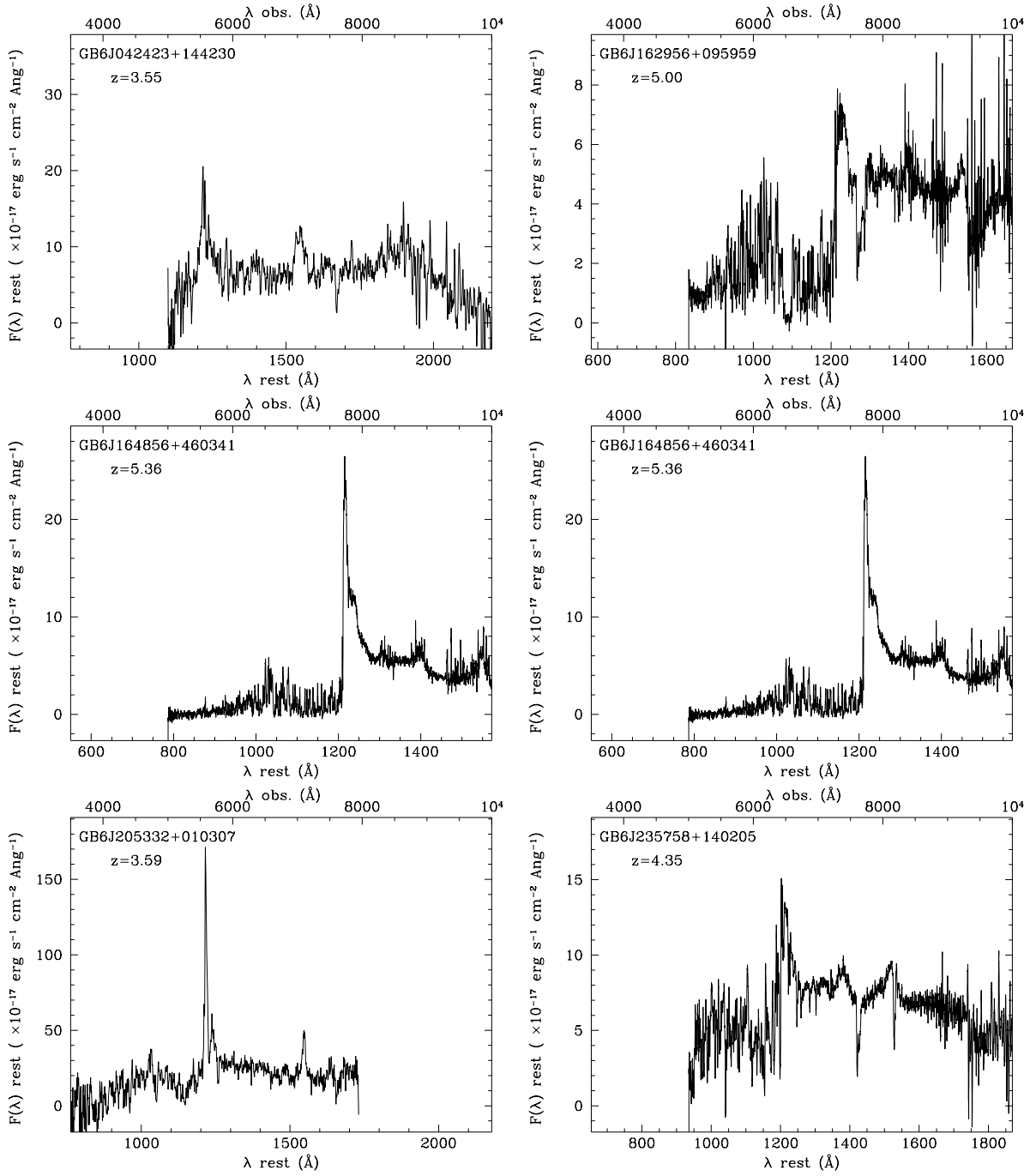

Figure B.2: Same caption as Fig. B.1.

Appendix C

Comparison samples

In this appendix I report the tables of the different samples used for comparison with the blazars discovered in this work. Table C.1 includes all the RL AGNs at z≥4.5 used for the radio-loudness comparison with DES0141−54 and PSO J1244+86. Instead in Table C.2 we list the z≥5.5 RL AGNs used for radio-loudness and $\alpha_{\nu r}$ comparison with PSO J0309+27.

Object name (1)	z (2)	Coordinates (3)	$S_{1.4\ GHz}$ (4)	z mag (5)	$S_{[0.5-10]\ keV}$ (6)	ref. (7)
J001115+144601^{+}	4.96	00:11:15.24 +14:46:01.8	24.3±1.2 / 35.8±1.5	18.14	3.01±0.16	1,2
J013127-032100^{b}	5.18	01:31:27.34 −03:21:00.8	33.7±1.7 / 31.4±1.0	18.10	1.30±0.56	3,4
J020138+032203	4.57	02:01:38.95 +03:22:03.4	9.8±0.6 / 9.6±0.5	19.31		5,6
J021043-001818*	4.77	02:10:43.16 −00:18:18.4	8.46 / 9.9±0.5	19.34	0.52±0.04	7,8
J031147+050703	4.51	03:11:47.96 +05:08:03.87	508.32 / 500±15.0	19.96		9
J032444-291821	4.63	03:24:44.29 −29:18:21.22	- / 236.5±7.1	17.75	1.23±0.13	10,11,8
J034141-004812	5.68	03:41:41.86 −00:48:12.7	2.09±0.14 / -	20.31		12
J074154+252029	5.19	07:41:54.72 +25:20:29.6	2.97 / -	18.33	0.92±0.31	13,14
J081333+350810*	4.92	08:13:33.32 +35:08:10.8	37.45 / 35.6±1.1	19.15	0.71±0.16	1,15
J083643+005453	5.77	08:36:43.86 +00:54:53.23	1.11±0.15 / 2.5±0.5	18.77	0.25±0.05	16,17
J090132+161506	5.63	09:01:32.65 +16:15:06.8	3.99 / 3.9±0.5	20.73		12
J090630+693030^{+b}	5.47	09:06:30.75 +69:30:30.80	- / 92.80±2.8	19.86	1.32±0.12	18,2
J091316+591921*	5.12	09:13:16.55 +59:19:21.6	17.55 / 17.7±0.7	20.73	0.05±0.03	19,20
J092132+185654	4.52	09:21:32.57 +18:56:54.5	4.37 / 3.0±0.4	20.68		21
J094004+052630	4.50	09:40:04.8 +05:26:30.95	58.48 / 61.7±1.9	20.59		22
J100303+112209	4.57	10:03:03.44 +11:22:09.7	2.79 / -	20.85		21
J101335+281119	4.75	10:13:35.44 +28:11:19.24	14.43 / 15.8±0.6	21.44		23
J102623+254259^{*+b}	5.25	10:26:23.61 +25:42:59.5	239.44 / 256.9±7.7	20.02	1.04±0.29	24,2
J103418+203300	4.99	10:34:18.65 +20:33:00.2	3.85 / 4.0±0.5	19.86		24
J105511+481848	4.57	10:55:11.40 +48:18:48.9	4.67 / 6.0±1.2	20.90		6
J114657+403708*	5.00	11:46:57.79 +40:37:08.6	12.4±0.6 / 12.5±0.5	19.55	0.94±0.22	25,26
J121329+181029	4.50	12:13:29.07 +18:10:29.1	3.02 / 2.3±0.4	20.18		21
J123237+520343	4.62	12:32:37.49 +52:03:43.8	4.54 / 3.5±0.5	20.20		6
J123503-000331*	4.72	12:35:03.03 −00:03:31.7	18.35 / 18.1±0.7	20.04	0.70±0.5	27,8
J123604+030341	4.55	12:36:04.19 +03:03:41.8	2.10 / -	20.02		22
J124230+542257*	4.73	12:42:30.58 +54:22:57.3	20.21 / 19.7±0.7	19.90	0.28±0.08	1,15
J130002+011823	4.61	13:00:02.16 +01:18:23.1	2.52 / 2.4±0.4	18.85		28
J131121+222738*	4.61	13:11:21.32 +22:27:38.6	6.53 / 7.5±0.5	20.35		24
J131814+341805	4.86	13:18:14.03 +34:18:05.6	3.10 / 3.5±0.4	19.00		13
J135135+284014	4.73	13:51:35.71 +28:40:14.8	3.42 / 6.1±1.3	19.88		13
J140025+314910	4.69	14:00:25.41 +31:49:10.68	20.51 / 21.9±0.8	20.19		22
J142634+543622	4.84	14:26:34.85 +54:36:22.8	4.36 / 2.5±0.4	19.85		13
J142738+331241	6.12	14:27:38.58 +33:12:41.93	1.03±0.05 / -	19.68		29
J142952+544717	6.21	14:29:52.17 +54:47:17.63	2.95 / 3.8±0.5	21.89		30
J143003+144354*	4.83	14:30:03.96 +14:43:54.8	6.07 / 12.4±0.9	20.22		24

J143023+420436^{+b}	4.7	14:30:23.74 +42:04:36.49	215.62 / 210.6±6.3	19.57	18.0±0.33	10,2
J144231+011055	4.52	14:42:31.71 +01:10:55.3	1.87 / -	19.98	0.24±0.06	19,31
J145143-151216	4.76	14:51:43.74 −15:12:16.4	- / 28.5±1.0	16.67	2.42±0.43	11,32
J145212+023526*	4.89	14:52:12.86 +02:35:26.3	5.63 / 16.8±1.3	20.30		28
J145459+110927	4.93	14:54:59.30 +11:09:27.89	15.07 / 9.8±0.5	21.17		23
J150149+592252	4.65	15:01:49.05 +59:22:52.2	5.68 / 4.6±0.5	18.79		6
J150545+433827	4.68	15:05:45.12 +43:38:27.9	4.52 / 4.5±0.5	18.86		6
J152028+210039	4.55	15:20:28.16 +21:00:39.7	1.75 / 6.1±0.5	20.05		24
J154824+333500	4.69	15:48:24.01 +33:35:00.09	37.84 / 38.2±1.2	20.75		22
J160937+304147	6.14	16:09:37.27 +30:41:47.78	0.48±0.14 / -	21.02		12
J161105+084435	4.55	16:11:05.65 +08:44:35.48	8.82 / 8.7±0.5	19.08		25
J161425+464029	5.31	16:14:25.14 +46:40:29.0	2.16 / -	19.89		1
J162830+115403	4.5	16:28:30.46 +11:54:03.47	40.98 / 42.2±1.3	21.02		23
J162957+100023^{+}	5.00	16:29:57.28 +10:00:23.5	53.81 / 52.8±1.6	20.58		34
J164854+460327^{+}	5.36	16:48:54.53 +46:03:27.4	32.28 / 33.7±1.1	19.85	0.17±0.09	34,2
J165913+210115*	4.78	16:59:13.23 +21:01:15.8	28.81 / 29.3±1.0	20.06	0.58±0.12	25
J172026+310431*	4.67	17:20:26.68 +31:04:31.6	10.56 / 11.3±0.5	19.95		24
J205321+004706	5.92	20:53:21.77 +00:47:06.8	0.43±0.14 / -	21.74		35,12
J210240+601509	4.58	21:02:40.21 +60:15:09.84	- / 318.0±9.5	21.17		36
J222843+011031	5.95	22:28:43.53 +01:10:31.91	1.32 / -	22.28		37
J223907+003022	5.09	22:39:07.56 +00:30:22.6	1.22 / -	21.32		13
J224524+002414	5.17	22:45:24.27 +00:24:14.2	3.72 / -	21.88		10,38
J232741-002803	4.75	23:27:41.35 −00:28:03.9	1.38 / -	21.29		13
J232936-152016	5.84	23:29:36.81 −15:20:16.5	- / 14.9±0.7	21.22		39
J232939+300350	5.24	23:29:39.30 +30:03:50.8	- / 4.9±0.4	19.19		5,40
J234433+165316	5.00	23:44:33.46 +16:53:15.3	- / 15.3±0.6	18.73		5,40

Table C.1: RL AGNs at z≥4.5 collected from the literature. Col(1): Object name: objects marked with an $*$ and a + are also part of the sample of Sbarrato et al. (2013) and Caccianiga et al. (2019) respectively, objects marked with a *b* are the confirmed blazar in the literature; Col(2): Redshift (for J121329 and J144231 we have computed the redshift because on the SDSS it is wrong); Col(3): Coordinates (hms, dms, J2000); Col(4): $S_{1.4\ GHz}$ from FIRST and/or from NVSS in unit of mJy; for J2228+01 and J2245+00 the flux is taken from VLA SDSS STRIPE82 (Hodge et al. 2011); Col(5): PSF *z* mag from Pan-STARRS PS1; for J0311+05, J1427+33, and J2228+01 the value is taken from their reference papers and converted where necessary; for J1505+43 the magnitude is taken from SDSS DR14 Quasar Catalog (Pâris et al. 2018); Col(6): Observed X–ray flux at [0.5-10] keV in unit of 10^{-13} erg s^{-1} cm^{-2}; Col(7): reference for redshift, radio identification and X–ray flux: 1=Schneider et al. (2005), 2=Ighina et al. (2019), 3=Yi et al. (2014), 4=Ghisellini et al. (2015a), 5=Wang et al. (2016), 6=Pâris et al.(2018), 7=Fan et al. (2001a), 8=Rosen et al. (2016a,b), 9=Kopylov et al.(2006), 10=Véron-Cetty et al. (2001), 11=Hook et al. (2002), 12=Bañados et al.(2015), 13=McGreer et al. (2009), 14=Wu et al. (2013), 15=Zhu et al. (2019), 16= Fan et al. (2001b), 17=Bechtold et al. (2003) 18=Romani et al. (2004), 19=Anderson et al. (2001), 20=Vignali et al. (2003), 21=Pâris et al.(2014), 22=Pâris et al.(2012), 23=Titov et al.(2013), 24=Schneider et al.(2010), 25=Schneider et al.(2007), 26=Ghisellini et al. (2014), 27=Fan et al.(2000), 28=Schneider et al.(2003), 29=McGreer et al. (2006), 30=Willott et al. (2010a), 31=Shemmer et al. (2006), 32=Lopez et al. (2006), 33=Healey et al. (2008), 34=Caccianiga et al. (2019), 35=Jiang et al. (2009), 36=Sowards-Emmerd et al. (2004), 37=Zeimann et al. (2011), 38=McGreer et al. (2013), 39=Bañados et al.(2018b), 40=Yang et al. (2016).

name	z (ref)	$S_{1.4\ GHz}$	$\alpha_{\nu r}$ (ref)	R
(1)	(2)	(3)	(4)	(5)
J034141−004812	5.68 (1)	2.09	0.75* (1)	178.0±40.5
J083643+005453	5.77 (2)	1.11	0.89±0.29 (8)	11.9±0.3
J090132+161506	5.63 (1)	3.90	0.75* (1)	91.4±8.8
J142738+331241	6.12 (3)	1.03	0.62±0.17 (8)	53.3±4.1
J142952+544717	6.21 (4)	2.95	0.79±0.04 (8)	109.2±8.9
J160937+304147	6.14 (1)	0.48	0.75* (1)	28.3±8.6
J205321+004706	5.92 (5)	0.43	0.75* (1)	44.1±18.7
J222843+011031	5.95 (6)	1.32	0.8 (1)	61.3±20.9
J232936−152016[a]	5.84 (7)	14.90	0.97±0.12 (7)	1169.5±300.5

Table C.2: RL AGNs discovered to date at z≥5.5. Col (1): object name; For the object marked with *a* the reported values of $\alpha_{\nu r}$ and R are the median of the results of Bañados et al. (2018b); Col (2): redshift from the literature and reference; Col (3): observed radio flux density at 1.4 GHz in mJy; Col (4): radio spectral index and reference. For objects marked with an $*$, $\alpha_{\nu r}$ have been assumed by Bañados et al. (2015); Col (5): radio-loudness as defined in Kellerman et al. (1989). List of references: 1=Bañados et al. (2015), 2=Fan et al. (2001), 3=McGreer et al. (2006), 4=Willott et al. (2010a), 5=Jiang et al. (2009), 6=Zeimann et al. (2011), 7=Bañados et al. (2018b); 8=Coppejans et al. (2017).

Appendix D

M_{BH} of the CLASS high-z blazars

In this appendix I report the black hole masses, bolometric luminosities and Eddington ratio of the CLASS high-z blazars. These data are not already published and are reported in Diana et al. (in prep). The black hole masses have been computed with the SE method, by fitting the CIV emission line for the sources with a optical/near-IR spectra available (19 among 25 objects) and by using the relations of Vestergaard & Peterson 2006 based on σ_{line} (see Eq. 1.14).

name	M_{BH}	L_{bol}	λ_{Edd}
	$10^9 M_\odot$	10^{47} erg s^{-1}	
(1)	(2)	(3)	(4)
GB6J001115+144608	7.08	5.25	0.54
GB6J003126+150729	2.29	0.64	0.20
GB6J012126+034646	0.98	1.77	1.32
GB6J083548+182519	1.00	0.22	0.16
GB6J083945+511206	1.26	1.78	1.02
GB6J091825+063722	2.34	1.29	0.40
GB6J102107+220904	0.37	0.28	0.55
GB6J102623+254255	1.95	1.58	0.59
GB6J132512+112338	0.83	1.02	0.89
GB6J134811+193520	2.24	0.76	0.24
GB6J141212+062408	2.19	0.93	0.31
GB6J143023+420450	1.38	1.20	0.63
GB6J151002+570256	0.81	0.79	0.71
GB6J153533+025419	1.23	0.60	0.35
GB6J161216+470311	0.42	0.38	0.66
GB6J162956+095959	0.26	0.57	1.59
GB6J164856+460341	0.98	0.76	0.56
GB6J171103+383016	0.20	0.36	1.29
GB6J235758+140205	1.48	0.63	0.31

Table D.1: Black hole masses, bolometric luminosities and Eddington ratio of the CLASS high-z blazars. Col (1): object name; Col (2): M_{BH}, in unit of $10^9 M_\odot$. Col (3): bolometric luminosity in unit of 10^{47} erg s^{-1}, corrected for the inclination factor i defined in Sect. 4.6.3; Col (4): Eddington ratio defined as L_{bol}/L_{Edd}.

Appendix E

SQL queries on DES and PS1 casjob

In this appendix I report the queries made on DES DR1[1] and Pan-STARRS PS1[2] casjob, which have been used for the selection of high-z blazars in this thesis.

DES DR 1 query:
SELECT ALPHAWIN_J2000 RAP,DELTAWIN_J2000 DECP,
mag_auto_g, magerr_auto_g, wavg_mag_psf_g, wavg_magerr_psf_g,
mag_aper2_g, magerr_aper2_g,
mag_auto_r, magerr_auto_r, wavg_mag_psf_r, wavg_magerr_psf_r,
mag_aper2_r, magerr_aper2_r,
mag_auto_i, magerr_auto_i, wavg_mag_psf_i, wavg_magerr_psf_i,
mag_aper2_i, magerr_aper2_i,
mag_auto_z, magerr_auto_z, wavg_mag_psf_z, wavg_magerr_psf_z,
mag_aper2_z, magerr_aper2_z,
mag_auto_y, magerr_auto_y, wavg_mag_psf_y, wavg_magerr_psf_y,
mag_aper2_y, magerr_aper2_y
FROM DR1_MAGNITUDE WHERE
DELTAWIN_J2000 < -31.0
and magerr_auto_z < 0.2 and magerr_auto_i < 0.2 and magerr_auto_y < 0.3
and mag_auto_r-mag_auto_i > 1.5
and mag_auto_i-mag_auto_z < 1.0
and mag_auto_i between 18.0 and 22.5
and mag_auto_g > 25.0 and mag_aper_2_g > 25.0

The detailed description of the parameters can be found at
https://des.ncsa.illinois.edu/releases/dr1/dr1-faq or in Abbott et al. (2018).

PS1 query for the selection of $4.5 \leq z \leq 5.5$ blazars:
SELECT m.ra, m.dec, m.err, nb.distance, nb.objID,
s.objID, s.raStack, s.decStack, s.raStackErr, s.decStaackErr,
s.raMean, s.decMean, s.raMeanErr, s.decMeanErr, s.l, s.b,
s.nStackDetections, s.nDetections, s.ng, s.nr, s.ni, s.nz, s.ny, s.primaryDetection,
s.gPSFMag, s.gPSFMagErr, s.gApMag, s.gApMagErr, s.gKronMag, s.gKronMagErr,
s.rPSFMag, s.rPSFMagErr, s.rApMag, s.rApMagErr, s.rKronMag, s.rKronMagErr,

[1] https://des.ncsa.illinois.edu/releases/dr1/dr1-access
[2] https://mastweb.stsci.edu/ps1casjobs/

s.iPSFMag, s.iPSFMagErr, s.iApMag, s.iApMagErr, s.iKronMag, s.iKronMagErr,
s.zPSFMag, s.zPSFMagErr, s.zApMag, s.zApMagErr, s.zKronMag, s.zKronMagErr,
s.yPSFMag, s.yPSFMagErr, s.yApMag, s.yApMagErr, s.yKronMag, s.yKronMagErr
INTO myDB.ps1xnvss_over30 from MyDB.nvss_over30 as m
CROSS APPLY fGetNearbyObjEq(m.ra, m.dec, m.err) as nb
inner JOIN StackObjectView as s on nb.objID = s.objID
WHERE s.iPSFMag≤21.5

PS1 query for the selection of 5.5≤z≤6.5 blazars:
SELECT m.ra, m.dec, m.err, nb.distance, nb.objID,
s.objID, s.raStack, s.decStack, s.raStackErr, s.decStaackErr,
s.raMean, s.decMean, s.raMeanErr, s.decMeanErr, s.l, s.b,
s.nStackDetections, s.nDetections, s.ng, s.nr, s.ni, s.nz, s.ny, s.primaryDetection,
s.gPSFMag, s.gPSFMagErr, s.gApMag, s.gApMagErr, s.gKronMag, s.gKronMagErr,
s.rPSFMag, s.rPSFMagErr, s.rApMag, s.rApMagErr, s.rKronMag, s.rKronMagErr,
s.iPSFMag, s.iPSFMagErr, s.iApMag, s.iApMagErr, s.iKronMag, s.iKronMagErr,
s.zPSFMag, s.zPSFMagErr, s.zApMag, s.zApMagErr, s.zKronMag, s.zKronMagErr,
s.yPSFMag, s.yPSFMagErr, s.yApMag, s.yApMagErr, s.yKronMag, s.yKronMagErr
INTO myDB.ps1xnvss_over9 from MyDB.nvss_over9 as m
CROSS APPLY fGetNearbyObjEq(m.ra, m.dec, m.err) as nb
inner JOIN StackObjectView as s on nb.objID = s.objID
WHERE s.zPSFMag≤21.5

Detailed information about the used PS1 parameters can be found at
https://outerspace.stsci.edu/display/PANSTARRS/PS1+FAQ+-+Frequently+asked+questions

Bibliography

[1] Abbott, T. M. C., Abdalla, F. B., Allam, S., et al. 2018, ApJS, 239, 18.

[2] Abdo, A. A., Ackermann, M., Ajello, M., et al. 2010, ApJ, 722, 520.

[3] Abramowicz, M. A., Czerny, B., Lasota, J. P., et al. 1988, ApJ, 332, 646.

[4] Abramowicz, M. A. & Lasota, J.-P. 1995, Comments on Astrophysics, 18, 141

[5] Abramowicz, M. A. & Fragile, P. C. 2013, Living Reviews in Relativity, 16, 1.

[6] Ackermann, M., Ajello, M., Allafort, A., et al. 2011, ApJ, 741, 30.

[7] Ageorges, N., Seifert, W., Jütte, M., et al. 2010, SPIE, 7735, 77351L.

[8] Ajello, M., Costamante, L., Sambruna, R. M., et al. 2009, ApJ, 699, 603.

[9] Ajello, M., Shaw, M. S., Romani, R. W., et al. 2012, ApJ, 751, 108.

[10] Ajello, M., Romani, R. W., Gasparrini, D., et al. 2014, ApJ, 780, 73.

[11] Alexander, D. M. & Hickox, R. C. 2012, NewAR, 56, 93.

[12] Aller, M. F., Aller, H. D., & Hughes, P. A. 2011, Journal of Astrophysics and Astronomy, 32, 5.

[13] Amirkhanyan, V. R. & Mikhailov, V. P. 2006, Astrophysics, 49, 184.

[14] An, H. & Romani, R. W. 2018, ApJ, 856, 105.

[15] An, T., Mohan, P., Zhang, Y., et al. 2020, Nature Communications, 11, 143.

[16] Anderson, S. F., Fan, X., Richards, G. T., et al. 2001, AJ, 122, 503.

[17] Andika, I. T., Jahnke, K., Onoue, M., et al. 2020, ApJ, 903, 34.

[18] Antonucci, R. R. J. & Ulvestad, J. S. 1985, ApJ, 294, 158.

[19] Antonucci, R. R. J. & Miller, J. S. 1985, ApJ, 297, 621.

[20] Antonucci, R. R. J., Kinney, A. L., & Ford, H. C. 1989, ApJ, 342, 64.

[21] Antonucci, R. 1993, ARA&A, 31, 473.

[22] Assef, R. J., Denney, K. D., Kochanek, C. S., et al. 2011, ApJ, 742, 93.

[23] Bai, J. M. & Lee, M. G. 2001, ApJ, 548, 244.

[24] Baldi, R. D., Capetti, A., & Giovannini, G. 2015, A&A, 576, A38.

[25] Baldi, R. D., Capetti, A., & Massaro, F. 2018, A&A, 609, A1.

[26] Baldwin, J. A. & Netzer, H. 1978, ApJ, 226, 1.

[27] Bañados, E., Venemans, B. P., Morganson, E., et al. 2015, ApJ, 804, 118

[28] Bañados, E., Venemans, B. P., Mazzucchelli, C., et al. 2018, Natur, 553, 473.

[29] Bañados, E., Carilli, C., Walter, F., et al. 2018, ApJL, 861, L14.

[30] Batiste, M., Bentz, M. C., Raimundo, S. I., et al. 2017, ApJL, 838, L10.

[31] Bechtold, J., Siemiginowska, A., Shields, J., et al. 2003, ApJ, 588, 119.

[32] Becker, R. H., White, R. L., & Helfand, D. J. 1994, Astronomical Data Analysis Software and Systems III, 61, 165

[33] Begelman, M. C., Volonteri, M., & Rees, M. J. 2006, MNRAS, 370, 289.

[34] Begelman, M. C. & Volonteri, M. 2017, MNRAS, 464, 1102.

[35] Belladitta, S., Moretti, A., Caccianiga, A., et al. 2019, A&A, 629, A68.

[36] Belladitta, S., Moretti, A., Caccianiga, A., et al. 2020, A&A, 635, L7

[37] Benn, C. R., Vigotti, M., Pedani, M., et al. 2002, MNRAS, 329, 221.

[38] Bennett, A. S. 1962, MmRAS, 68, 163

[39] Bentz, M. C., Peterson, B. M., Pogge, R. W., et al. 2006, ApJ, 644, 133.

[40] Bentz, M. C., Denney, K. D., Grier, C. J., et al. 2013, ApJ, 767, 149.

[41] Bicknell, G. V. 1995, ApJS, 101, 29.

[42] Blandford, R. D. & Znajek, R. L. 1977, MNRAS, 179, 433.

[43] Blandford, R. D. & Rees, M. J. 1978, PhyS, 17, 265.

[44] Blandford, R. D. & Königl, A. 1979, ApJ, 232, 34.

[45] Blandford, R. D. & McKee, C. F. 1982, ApJ, 255, 419.

[46] Blandford, R. D. & Payne, D. G. 1982, MNRAS, 199, 883.

[47] Blandford, R., Meier, D., & Readhead, A. 2019, ARA&A, 57, 467.

[48] Bock, D. C.-J., Large, M. I., & Sadler, E. M. 1999, AJ, 117, 1578.

[49] Bond, J. R. 1984, Stellar Nucleosynthesis, 297.

[50] Booth, C. M. & Schaye, J. 2009, The Monster's Fiery Breath: Feedback in Galaxies, Groups, and Clusters, 1201, 21.

[51] Brenneman, L. W., Reynolds, C. S., Nowak, M. A., et al. 2011, ApJ, 736, 103.

[52] Bromm, V. & Larson, R. B. 2004, ARA&A, 42, 79.

[53] Bromm, V. & Yoshida, N. 2011, ARA&A, 49, 373.

[54] Browne, I. W. A., Wilkinson, P. N., Jackson, N. J. F., et al. 2003, MNRAS, 341, 13.

[55] Buzzoni, B., Delabre, B., Dekker, H., et al. 1984, The Messenger, 38, 9

[56] Caccianiga, A., Moretti, A., Belladitta, S., et al. 2019, MNRAS, 484, 204.

[57] Calderone, G., Ghisellini, G., Colpi, M., et al. 2013, MNRAS, 431, 210.

[58] Campitiello, S., Ghisellini, G., Sbarrato, T., et al. 2018, A&A, 612, A59.

[59] Cao, H.-M., Frey, S., Gurvits, L. I., et al. 2014, A&A, 563, A111.

[60] Cao, H.-M., Frey, S., Gabányi, K. É., et al. 2017, MNRAS, 467, 950

[61] Carballo, R., González-Serrano, J. I., Benn, C. R., et al. 2008, MNRAS, 391, 369.

[62] Carnall, A. C., Shanks, T., Chehade, B., et al. 2015, MNRAS, 451, L16.

[63] Cash, W. 1979, ApJ, 228, 939.

[64] Celotti, A., Padovani, P., & Ghisellini, G. 1997, MNRAS 286, 415.

[65] Celotti, A., Ghisellini, G., & Chiaberge, M. 2001, MNRAS, 321, L1.

[66] Chambers, K. C., Magnier, E. A., Metcalfe, N., et al. 2016, arXiv:1612.05560

[67] Chandra, S., Baliyan, K. S., Ganesh, S., et al. 2011, ApJ, 731, 118.

[68] Chen, Y. Y., Zhang, X., Zhang, H. J., et al. 2015, MNRAS, 451, 4193.

[69] Chhetri, R., Ekers, R. D., Jones, P. A., et al. 2013, MNRAS, 434, 956.

[70] Ciaramella, A., Bongardo, C., Aller, H. D., et al. 2004, A&A, 419, 485.

[71] Coatman, L., Hewett, P. C., Banerji, M., et al. 2016, MNRAS, 461, 647.

[72] Coatman, L., Hewett, P. C., Banerji, M., et al. 2017, MNRAS, 465, 2120.

[73] Condon, J. J., Cotton, W. D., Greisen, E. W., et al. 1998, AJ, 115, 1693.

[74] Coppejans, R., Frey, S., Cseh, D., et al. 2016, MNRAS, 463, 3260.

[75] Coppejans, R., van Velzen, S., Intema, H. T., et al. 2017, MNRAS, 467, 2039.

[76] Cutri, R. M., Wright, E. L., Conrow, T., et al. 2012, Explanatory Supplement to the WISE All-Sky Data Release Products

[77] Czerny, B., Modzelewska, J., Petrogalli, F., et al. 2015, Advances in Space Research, 55, 1806.

[78] Dalla Bontà, E., Peterson, B. M., Bentz, M. C., et al. 2020, ApJ, 903, 112.

[79] Davies, M. B., Miller, M. C., & Bellovary, J. M. 2011, ApJL, 740, L42.

[80] D'Elia, V., Padovani, P., Giommi, P., et al. 2015, MNRAS, 449, 3517.

[81] De Breuck, C., van Breugel, W., Röttgering, H., et al. 2001, AJ, 121, 1241.

[82] De Rosa, G., Decarli, R., Walter, F., et al. 2011, ApJ, 739, 56.

[83] Decarli, R., Labita, M., Treves, A., et al. 2008, MNRAS, 387, 1237.

[84] Decarli, R., Dotti, M., & Treves, A. 2011, MNRAS, 413, 39.

[85] Deller, A. T., Brisken, W. F., Phillips, C. J., et al. 2011, PASP, 123, 275.

[86] Denney, K. D. 2012, ApJ, 759, 44.

[87] Denney, K. D., Pogge, R. W., Assef, R. J., et al. 2013, ApJ, 775, 60.

[88] Devecchi, B. & Volonteri, M. 2009, ApJ, 694, 302.

[89] Diamond-Stanic, A. M., Fan, X., Brandt, W. N., et al. 2009, ApJ, 699, 782.

[90] Di Matteo, T., Colberg, J., Springel, V., et al. 2008, ApJ, 676, 33.

[91] Donato, D., Ghisellini, G., Tagliaferri, G., et al. 2001, A&A, 375, 739.

[92] Done, C., Gierliński, M., Sobolewska, M., et al. 2007, The Central Engine of Active Galactic Nuclei, 373, 121

[93] Edge, D. O., Shakeshaft, J. R., McAdam, W. B., et al. 1959, MmRAS, 68, 37

[94] Eilers, A.-C., Hennawi, J. F., & Davies, F. B. 2018, ApJ, 867, 30.

[95] Elvis, M. 2000, ApJ, 545, 63.

[96] Evans, P. A., Beardmore, A. P., Page, K. L., et al. 2009, MNRAS, 397, 1177.

[97] Fabian, A. C. 2012, ARA&A, 50, 455.

[98] Fan, X., Strauss, M. A., Schneider, D. P., et al. 2000, AJ, 119, 1.

[99] Fan, X., Strauss, M. A., Richards, G. T., et al. 2001, AJ, 121, 31.

[100] Fan, X., Narayanan, V. K., Lupton, R. H., et al. 2001, AJ, 122, 2833.

[101] Fan, X., Carilli, C. L., & Keating, B. 2006, ARA&A, 44, 415.

[102] Fanaroff, B. L. & Riley, J. M. 1974, MNRAS, 167, 31P.

[103] Feng, Y., Di Matteo, T., Croft, R., et al. 2014, MNRAS, 440, 1865.

[104] Ferrarese, L. & Merritt, D. 2000, ApJL, 539, L9.

[105] Fine, S., Jarvis, M. J., & Mauch, T. 2011, MNRAS, 412, 213.

[106] Flaugher, B. 2005, International Journal of Modern Physics A, 20, 3121.

[107] Flesch, E. W. 2015, PASA, 32, e010.

[108] Fosbury, R. A. E. 2006, Physics of Active Galactic Nuclei at all Scales, 121.

[109] Francis, P. J., Hewett, P. C., Foltz, C. B., et al. 1991, ApJ, 373, 465.

[110] Freeman, P. E., Kashyap, V., Rosner, R., et al. 2002, ApJS, 138, 185.

[111] Frey, S., Mosoni, L., Paragi, Z., et al. 2003, MNRAS, 343, L20.

[112] Frey, S., Paragi, Z., Mosoni, L., et al. 2005, A&A, 436, L13.

[113] Frey, S., Gurvits, L. I., Paragi, Z., et al. 2008, A&A, 484, L39.

[114] Frey, S., Paragi, Z., Gurvits, L. I., et al. 2010, A&A, 524, A83.

[115] Frey, S., Paragi, Z., Gurvits, L. I., et al. 2011, A&A, 531, L5.

[116] Frey, S., Paragi, Z., Fogasy, J. O., et al. 2015, MNRAS, 446, 2921.

[117] Frey, S., Titov, O., Melnikov, A. E., et al. 2018, A&A, 618, A68.

[118] Gabányi, K. É, Cseh, D., Frey, S., et al. 2015, MNRAS, 450, L57.

[119] Gaskell, C. M. 1982, ApJ, 263, 79.

[120] Ghisellini, G. & Madau, P. 1996, MNRAS, 280, 67.

[121] Ghisellini, G. & Tavecchio, F. 2009, MNRAS, 397, 985.

[122] Ghisellini, G., Tavecchio, F., Foschini, L., et al. 2010, MNRAS, 402, 497.

[123] Ghisellini, G., Tavecchio, F., Foschini, L., et al. 2011, MNRAS, 414, 2674.

[124] Ghisellini, G., Haardt, F., Della Ceca, R., et al. 2013, MNRAS, 432, 2818.

[125] Ghisellini, G., Sbarrato, T., Tagliaferri, G., et al. 2014, MNRAS, 440, L111.

[126] Ghisellini, G., Tagliaferri, G., Sbarrato, T., et al. 2015, MNRAS, 450, L34.

[127] Ghisellini, G., Haardt, F., Ciardi, B., et al. 2015, MNRAS, 452, 3457.

[128] Ghisellini, G. & Tavecchio, F. 2015, MNRAS, 448, 1060.

[129] Ghisellini, G. & Sbarrato, T. 2016, MNRAS, 461, L21.

[130] Ghisellini, G., Righi, C., Costamante, L., et al. 2017, MNRAS, 469, 255.

[131] Giommi, P., Padovani, P., Polenta, G., et al. 2012, MNRAS, 420, 2899.

[132] Giommi, P., Brandt, C. H., Barres de Almeida, U., et al. 2019, A&A, 631, A116.

[133] Giovannini, G., Feretti, L., Gregorini, L., et al. 1988, A&A, 199, 73

[134] Giovannini, G., Feretti, L., Venturi, T., et al. 1994, ApJ, 435, 116.

[135] Giroletti, M., Giovannini, G., Feretti, L., et al. 2004, ApJ, 600, 127.

[136] Glikman, E., Bogosavljević, M., Djorgovski, S. G., et al. 2010, ApJ, 710, 1498.

[137] Goldoni, P., Royer, F., François, P., et al. 2006, SPIE, 6269, 62692K.

[138] Greene, J. E., Peng, C. Y., & Ludwig, R. R. 2010, ApJ, 709, 937.

[139] Gregory, P. C., Scott, W. K., Douglas, K., et al. 1996, ApJS, 103, 427.

[140] Greisen, E. W. 2003, Information Handling in Astronomy - Historical Vistas, 109.

[141] Gunn, J. E. & Peterson, B. A. 1965, ApJ, 142, 1633.

[142] Haardt, F. & Maraschi, L. 1991, ApJL, 380, L51.

[143] Haehnelt, M. G. & Rees, M. J. 1993, MNRAS, 263, 168.

[144] Hamuy, M., Walker, A. R., Suntzeff, N. B., et al. 1992, PASP, 104, 533.

[145] Hamuy, M., Suntzeff, N. B., Heathcote, S. R., et al. 1994, PASP, 106, 566.

[146] Hardcastle, M. J. & Croston, J. H. 2011, MNRAS, 415, 133.

[147] Healey, S. E., Romani, R. W., Taylor, G. B., et al. 2007, APjS, 171, 61.

[148] Healey, S. E., Romani, R. W., Cotter, G., et al. 2008, ApJS, 175, 97.

[149] Healey, S. E., Fuhrmann, L., Taylor, G. B., et al. 2009, AJ, 138, 1032.

[150] Hodge, J. A., Becker, R. H., White, R. L., et al. 2011, AJ, 142, 3.

[151] Homan, D. C., Kovalev, Y. Y., Lister, M. L., et al. 2006, ApJL, 642, L115.

[152] Honscheid, K. & DePoy, D. L. 2008, arXiv:0810.3600

[153] Hook, I. M., McMahon, R. G., Patnaik, A. R., et al. 1995, MNRAS, 273, L63.

[154] Hook, I. M. & McMahon, R. G. 1998, MNRAS, 294, L7.

[155] Hook, I. M., McMahon, R. G., Shaver, P. A., et al. 2002, A&A, 391, 509.

[156] Hopkins, P. F., Richards, G. T., & Hernquist, L. 2007, ApJ, 654, 731.

[157] Hopkins, P. F., Hernquist, L., Cox, T. J., et al. 2008, ApJS, 175, 356.

[158] Hurley-Walker, N., Callingham, J. R., Hancock, P. J., et al. 2016, VizieR Online Data Catalog, VIII/100

[159] Ighina, L., Caccianiga, A., Moretti, A., et al. 2019, MNRAS, 489, 2732.

[160] Ikeda, H., Nagao, T., Matsuoka, K., et al. 2017, ApJ, 846, 57.

[161] Inayoshi, K., Haiman, Z., & Ostriker, J. P. 2016, MNRAS, 459, 3738.

[162] Intema, H. T., Jagannathan, P., Mooley, K. P., et al. 2017, A&A, 598, A78.

[163] Isler, J. C., Urry, C. M., Coppi, P., et al. 2017, ApJ, 844, 107.

[164] Ivezić, Ž., Menou, K., Knapp, G. R., et al. 2002, AJ, 124, 2364.

[165] Ivezic, Z., Axelrod, T., Brandt, W. N., et al. 2008, Serbian Astronomical Journal, 176, 1.

[166] Jarvis, M. J. & McLure, R. J. 2006, MNRAS, 369, 182.

[167] Jiang, L., Fan, X., Vestergaard, M., et al. 2007, Aj, 134, 1150.

[168] Jiang, L., Fan, X., Ivezić, Ž., et al. 2007, ApJ, 656, 680.

[169] Jiang, L., Fan, X., Bian, F., et al. 2009, AJ, 138, 305.

[170] Jiang, L., McGreer, I. D., Fan, X., et al. 2016, ApJ, 833, 222.

[171] Jolley, E. J. D. & Kuncic, Z. 2008, MNRAS, 386, 989.

[172] Jolley, E. J. D., Kuncic, Z., Bicknell, G. V., et al. 2009, MNRAS, 400, 1521.

[173] Jorstad, S. G., Marscher, A. P., Smith, P. S., et al. 2013, ApJ, 773, 147.

[174] Jorstad, S. G., Marscher, A. P., Morozova, D. A., et al. 2017, ApJ, 846, 98.

[175] Jun, H. D., Im, M., Kim, D., et al. 2017, ApJ, 838, 41.

[176] Just, D. W., Brandt, W. N., Shemmer, O., et al. 2007, ApJ, 665, 1004.

[177] Kaiser, N., Aussel, H., Burke, B. E., et al. 2002, SPIE, 4836, 154.

[178] Kaiser, N., Burgett, W., Chambers, K., et al. 2010, SPIE, 7733, 77330E.

[179] Kalberla, P. M. W., Burton, W. B., Hartmann, D., et al. 2005, A&A, 440, 775.

[180] Kaspi, S., Smith, P. S., Netzer, H., et al. 2000, ApJ, 533, 631.

[181] Kaspi, S., Brandt, W. N., Maoz, D., et al. 2007, ApJ, 659, 997.

[182] Kellermann, K. I. 1988,
https://ned.ipac.caltech.edu/level5/Sept04/Kellermann2/paper.pdf

[183] Kellermann, K. I., Sramek, R., Schmidt, M., et al. 1989, AJ, 98, 1195.

[184] Kellermann, K. I. 2016, Star Clusters and Black Holes in Galaxies across Cosmic Time, 312, 3.

[185] Kim, Y., Im, M., Jeon, Y., et al. 2018, ApJ, 855, 138.

[186] Kimball, A. E., Ivezić, Ž., Wiita, P. J., et al. 2011, AJ, 141, 182.

[187] King, A. R. & Pringle, J. E. 2006, MNRAS, 373, L90.

[188] Koptelova, E., Hwang, C.-Y., Yu, P.-C., et al. 2017, Scientific Reports, 7, 41617.

[189] Kopylov, A. I., Goss, W. M., Pariĭskiĭ, Y. N., et al. 2006, Astronomy Letters, 32, 433.

[190] Kormendy, J. & Ho, L. C. 2013, ARA&A, 51, 511.

[191] Kovalev, Y. Y., Kellermann, K. I., Lister, M. L., et al. 2005, AJ, 130, 2473.

[192] Krolik, J. H. & Begelman, M. C. 1988, ApJ, 329, 702.

[193] Kurk, J. D., Walter, F., Fan, X., et al. 2007, ApJ, 669, 32.

[194] Lacy, M., Baum, S. A., Chandler, C. J., et al. 2020, PASP, 132, 035001.

[195] Laing, R. A. & Bridle, A. H. 2002, MNRAS, 336, 328.

[196] Latif, M. A. & Schleicher, D. R. G. 2015, A&A, 578, A118.

[197] Latif, M. A. & Ferrara, A. 2016, PASA, 33, e051.

[198] Lira, P., Kaspi, S., Netzer, H., et al. 2018, ApJ, 865, 56.

[199] Liu, T., Tozzi, P., Wang, J.-X., et al. 2017, ApJS, 232, 8.

[200] Liu, Y., Wang, R., Momjian, E., et al. 2021, ApJ, 908, 124.

[201] Lopez, L. A., Brandt, W. N., Vignali, C., et al. 2006, AJ, 131, 1914.

[202] Lupi, A., Haardt, F., Dotti, M., et al. 2016, MNRAS, 456, 2993.

[203] Lusso, E. & Risaliti, G. 2016, ApJ, 819, 154.

[204] Madau, P. & Rees, M. J. 2001, ApJL, 551, L27.

[205] Magorrian, J., Tremaine, S., Richstone, D., et al. 1998, AJ, 115, 2285.

[206] Mainzer, A., Bauer, J., Cutri, R. M., et al. 2014, ApJ, 792, 30.

[207] Mao, P., Urry, C. M., Marchesini, E., et al. 2017, ApJ, 842, 87.

[208] Maraschi, L., Ghisellini, G., & Celotti, A. 1992, ApJL, 397, L5.

[209] Maraschi, L. & Rovetti, F. 1994, ApJ, 436, 79.

[210] Marscher, A. P. 1996, Energy Transport in Radio Galaxies and Quasars, 100, 45

[211] Marscher, A. P., Jorstad, S. G., Aller, M. F., et al. 2004, X-ray Timing 2003: Rossi and Beyond, 714, 167.

[212] Marshall, H. L., Gelbord, J. M., Worrall, D. M., et al. 2018, ApJ, 856, 66.

[213] Massaro, E., Giommi, P., Leto, C., et al. 2009, A&A, 495, 691.

[214] Massaro, F., Giroletti, M., D'Abrusco, R., et al. 2014, ApJS, 213, 3.

[215] Massaro, E., Maselli, A., Leto, C., et al. 2015, Ap&SS, 357, 75.

[216] Matsuoka, Y., Onoue, M., Kashikawa, N., et al. 2019, ApJL, 872, L2.

[217] Matthews, T. A. & Sandage, A. R. 1963, ApJ, 138, 30.

[218] Mauch, T., Murphy, T., Buttery, H. J., et al. 2003, MNRAS, 342, 1117.

[219] Mazzucchelli, C., Bañados, E., Venemans, B. P., et al. 2017, ApJ, 849, 91.

[220] McConnell, D., Sadler, E. M., Murphy, T., et al. 2012, MNRAS, 422, 1527.

[221] McGreer, I. D., Becker, R. H., Helfand, D. J., et al. 2006, ApJ, 652, 157

[222] McGreer, I. D., Helfand, D. J., & White, R. L. 2009, AJ, 138, 1925.

[223] McGreer, I. D., Jiang, L., Fan, X., et al. 2013, ApJ, 768, 105.

[224] McLure, R. J. & Dunlop, J. S. 2002, MNRAS, 331, 795.

[225] McLure, R. J. & Jarvis, M. J. 2002, MNRAS, 337, 109.

[226] McMahon, R. G., Banerji, M., Gonzalez, E., et al. 2013, The Messenger, 154, 35

[227] McMullin, J. P., Waters, B., Schiebel, D., et al. 2007, Astronomical Data Analysis Software and Systems XVI, 376, 127

[228] Medvedev, P., Sazonov, S., Gilfanov, M., et al. 2020, MNRAS, 497, 1842.

[229] Meiksin, A. 2006, MNRAS, 365, 807.

[230] Mejía-Restrepo, J. E., Lira, P., Netzer, H., et al. 2017, Frontiers in Astronomy and Space Sciences, 4, 70.

[231] Merloni, A. 2016, Lecture Notes in Physics, Berlin Springer Verlag, 101.

[232] Modigliani, A., Goldoni, P., Royer, F., et al. 2010, SPIE, 7737, 773728.

[233] Moehler, S., Modigliani, A., Freudling, W., et al. 2014, A&A, 568, A9.

[234] Momjian, E., Carilli, C. L., & McGreer, I. D. 2008, AJ, 136, 344.

[235] Momjian, E., Carilli, C. L., Bañados, E., et al. 2018, ApJj, 861, 86.

[236] Moran, E. C. 2007, The Central Engine of Active Galactic Nuclei, 373, 425

[237] Mortlock, D. J., Warren, S. J., Venemans, B. P., et al. 2011, Natur, 474, 616.

[238] Murphy, T., Sadler, E. M., Ekers, R. D., et al. 2010, MNRAS, 402, 2403.

[239] Myers, S. T., Jackson, N. J., Browne, I. W. A., et al. 2003, MNRAS, 341, 1.

[240] Nandra, K., Barret, D., Barcons, X., et al. 2013, arXiv:1306.2307

[241] Nanni, R., Vignali, C., Gilli, R., et al. 2017, A&A, 603, A128.

[242] Narayan, R. & Yi, I. 1994, ApJL, 428, L13.

[243] Narayan, R. & Yi, I. 1995, ApJ, 444, 231.

[244] Narayan, R. & Yi, I. 1995, ApJ, 452, 710.

[245] Nenkova, M., Sirocky, M. M., Ivezić, Ž., et al. 2008, ApJ, 685, 147.

[246] Nenkova, M., Sirocky, M. M., Nikutta, R., et al. 2008, ApJ, 685, 160.

[247] Netzer, H. 2019, MNRAS, 488, 5185.

[248] Ni, Y., Wang, M.-Y., Feng, Y., et al. 2019, MNRAS, 488, 5551.

[249] Norris, R. P., Hopkins, A. M., Afonso, J., et al. 2011, PASA, 28, 215.

[250] Novikov, I. D. & Thorne, K. S. 1973, Black Holes (Les Astres Occlus), 343

[251] O'Dea, C. P. 1998, PASP, 110, 493.

[252] Oke, J. B. 1990, AJ, 99, 1621.

[253] Onken, C. A., Ferrarese, L., Merritt, D., et al. 2004, ApJ, 615, 645.

[254] Onoue, M., Kashikawa, N., Matsuoka, Y., et al. 2019, ApJ, 880, 77.

[255] Ohsuga, K., Mineshige, S., Mori, M., et al. 2002, ApJ, 574, 315.

[256] Ohsuga, K., Mori, M., Nakamoto, T., et al. 2005, ApJ, 628, 368.

[257] Padovani, P. & Urry, C. M. 1990, ApJ, 356, 75.

[258] Padovani, P. & Giommi, P. 1995, ApJ, 444, 567.

[259] Padovani, P. 2017, Nature Astronomy, 1, 0194.

[260] Paliya, V. S., Domínguez, A., Cabello, C., et al. 2020, ApJL, 903, L8.

[261] Parijskij, Y. N., Thomasson, P., Kopylov, A. I., et al. 2014, MNRAS, 439, 2314.

[262] Pâris, I., Petitjean, P., Aubourg, É., et al. 2012, A&A, 548, A66.

[263] Pâris, I., Petitjean, P., Aubourg, É., et al. 2014, A&A, 563, A54.

[264] Pâris, I., Petitjean, P., Ross, N. P., et al. 2017, A&A, 597, A79.

[265] Pâris, I., Petitjean, P., Aubourg, É., et al. 2018, A&A, 613, A51.

[266] Péroux, C., Storrie-Lombardi, L. J., McMahon, R. G., et al. 2001, AJ, 121, 1799.

[267] Peterson, B. M. 1993, PASP, 105, 247.

[268] Peterson, B. M., Ferrarese, L., Gilbert, K. M., et al. 2004, ApJ, 613, 682.

[269] Peterson, B. M. 2014, SSRv, 183, 253.

[270] Pezzulli, E., Valiante, R., & Schneider, R. 2016, MNRAS, 458, 3047.

[271] Pian, E. 2002, PASA, 19, 49.

[272] Pian, E., Falomo, R., & Treves, A. 2005, MNRAS, 361, 919.

[273] Pogge, R. W., Atwood, B., Brewer, D. F., et al. 2010, SPIE, 7735, 77350A.

[274] Polletta, M., Tajer, M., Maraschi, L., et al. 2007, ApJ, 663, 81.

[275] Raiteri, C. M., Acosta Pulido, J. A., Villata, M., et al. 2020, MNRAS, 493, 2793.

[276] Rajput, B., Stalin, C. S., & Rakshit, S. 2020, A&A, 634, A80.

[277] Ramos Almeida, C., Martínez González, M. J., Asensio Ramos, A., et al. 2016, MNRAS, 461, 1387.

[278] Readhead, A. C. S. 1994, ApJ, 426, 51.

[279] Rengelink, R. B., Tang, Y., de Bruyn, A. G., et al. 1997, A&AS, 124, 259.

[280] Retana-Montenegro, E. & Röttgering, H. J. A. 2017, A&A, 600, A97.

[281] Reynolds, C. S. 2014, SSRv, 183, 277.

[282] Richards, G. T., Lacy, M., Storrie-Lombardi, L. J., et al. 2006, ApJS, 166, 470.

[283] Richards, G. T., Kruczek, N. E., Gallagher, S. C., et al. 2011, AJ, 141, 167.

[284] Romani, R. W., Sowards-Emmerd, D., Greenhill, L., et al. 2004, ApJL, 610, L9.

[285] Rosen, S. R., Webb, N. A., Watson, et al. 2016, VizieR Online Data Catalog, IX/46

[286] Rosen, S. R., Webb, N. A., Watson, M. G., et al. 2016, VizieR Online Data Catalog, IX/50

[287] Rosen, S. R., Webb, N. A., Watson, M. G., et al. 2019, VizieR Online Data Catalog, IX/54

[288] Rosen, S. R., Webb, N. A., Watson, et al. 2019, VizieR Online Data Catalog, IX/55

[289] Ruan, J. J., Anderson, S. F., Plotkin, R. M., et al. 2014, ApJ, 797, 19.

[290] Runnoe, J. C., Brotherton, M. S., & Shang, Z. 2012, MNRAS, 422, 478.

[291] Runnoe, J. C., Brotherton, M. S., DiPompeo, M. A., et al. 2014, MNRAS, 438, 3263.

[292] Saikia, P., Körding, E., & Falcke, H. 2016, MNRAS, 461, 297.

[293] Sbarrato, T., Ghisellini, G., Maraschi, L., et al. 2012, MNRAS, 421, 1764.

[294] Sbarrato, T., Ghisellini, G., Nardini, M., et al. 2012, MNRAS, 426, L91.

[295] Sbarrato, T., Ghisellini, G., Nardini, M., et al. 2013, MNRAS, 433, 2182.

[296] Sbarrato, T., Ghisellini, G., Tagliaferri, G., et al. 2015, MNRAS, 446, 2483.

[297] Schneider, D. P., Fan, X., Hall, P. B., et al. 2003, AJ, 126, 2579.

[298] Schneider, D. P., Hall, P. B., Richards, G. T., et al. 2005, AJ, 130, 367.

[299] Schneider, D. P., Hall, P. B., Richards, G. T., et al. 2007, AJ, 134, 102.

[300] Schneider, D. P., Richards, G. T., Hall, P. B., et al. 2010, AJ, 139, 2360.

[301] Schwartz, D. A. 2002, ApJL, 571, L71.

[302] Schmidt, M. 1963, Natur, 197, 1040.

[303] Selsing, J., Fynbo, J. P. U., Christensen, L., et al. 2016, A&A, 585, A87.

[304] Sesana, A., Barausse, E., Dotti, M., et al. 2014, ApJ, 794, 104.

[305] Shakura, N. I. & Sunyaev, R. A. 1973, A&A, 500, 33

[306] Shapiro, S. L. 2005, ApJ, 620, 59.

[307] Shaver, P. A., Wall, J. V., & Kellermann, K. I. 1996, MNRAS, 278, L11.

[308] Shemmer, O., Brandt, W. N., Vignali, C., et al. 2005, ApJ, 630, 729.

[309] Shemmer, O., Brandt, W. N., Schneider, D. P., et al. 2006, ApJ, 644, 86.

[310] Shen, Y., Greene, J. E., Strauss, M. A., et al. 2008, ApJ, 680, 169.

[311] Shen, Y., Richards, G. T., Strauss, M. A., et al. 2011, ApJS 194, 45.

[312] Shen, Y. & Liu, X. 2012, ApJ, 753, 125.

[313] Shen, Y., Brandt, W. N., Dawson, K. S., et al. 2015, ApJS, 216, 4.

[314] Shen, Y., Wu, J., Jiang, L., et al. 2019, ApJ, 873, 35.

[315] Sikora, M. 1994, ApJS, 90, 923.

[316] Sowards-Emmerd, D., Romani, R. W., & Michelson, P. F. 2003, ApJ, 590, 109.

[317] Sowards-Emmerd, D., Romani, R. W., Michelson, P. F., et al. 2004, ApJ, 609, 564.

[318] Spingola, C., Dallacasa, D., Belladitta, S., et al. 2020, A&A, 643, L12.

[319] Stacy, A., Greif, T. H., & Bromm, V. 2012,MNRAS, 422, 290.

[320] Steffen, A. T., Strateva, I., Brandt, W. N., et al. 2006, AJ, 131, 2826.

[321] Stern, D., Djorgovski, S. G., Perley, R. A., et al. 2000, AJ, 119, 1526.

[322] Stickel, M., Padovani, P., Urry, C. M., et al. 1991, ApJ 374, 431.

[323] Strateva, I. V., Brandt, W. N., Schneider, D. P., et al. 2005, AJ, 130, 387.

[324] Stocke, J. T., Perlman, E. S., Wurtz, R., et al. 1991, The Space Distribution of Quasars, 21, 218

[325] Sulentic, J. W., Bachev, R., Marziani, P., et al. 2007, ApJ, 666, 757.

[326] Tananbaum, H., Avni, Y., Branduardi, G., et al. 1979, ApJL, 234, L9.

[327] Tang, B., Shang, Z., Gu, Q., et al. 2012, ApJS, 201, 38.

[328] Tang, J.-J., Goto, T., Ohyama, Y., et al. 2019, MNRAS, 484, 2575.

[329] Tavecchio, F., Maraschi, L., Sambruna, R. M., et al. 2000, ApJL, 544, L23.

[330] Tchekhovskoy, A., Narayan, R., & McKinney, J. C. 2011, MNRAS, 418, L79.

[331] Tchekhovskoy, A. & Bromberg, O. 2016, MNRAS, 461, L46.

[332] Thorne, K. S. 1974, ApJ, 191, 507.

[333] Titov, O., Stanford, L. M., Johnston, H. M., et al. 2013, arXiv:1305.3017

[334] Toda, K., Fukazawa, Y., & Inoue, Y. 2020, ApJ, 896, 172.

[335] Tody, D. 1993, Astronomical Data Analysis Software and Systems II, 52, 173

[336] Torresi, E., Grandi, P., Capetti, A., et al. 2018, MNRAS, 476, 5535.

[337] Trakhtenbrot, B., Netzer, H., Lira, P., et al. 2011, ApJ, 730, 7.

[338] Trakhtenbrot, B. & Netzer, H. 2012, MNRAS, 427, 3081.

[339] Tran, H. D. 2003, ApJ, 583, 632.

[340] Turk, M. J., Abel, T., & O'Shea, B. 2009, Science, 325, 601.

[341] Ueda, Y., Akiyama, M., Ohta, K., et al. 2003, ApJ, 598, 886.

[342] Urry, C. M., Padovani, P., & Stickel, M. 1991, ApJ, 382, 501.

[343] Urry, C. M. & Padovani, P. 1995, PASP, 107, 803.

[344] Valiante, R., Schneider, R., Volonteri, M., et al. 2016, MNRAS, 457, 3356.

[345] Vanden Berk, D. E., Richards, G. T., Bauer, A., et al. 2001, AJ, 122, 549.

[346] Vernet, J., Dekker, H., D'Odorico, S., et al. 2011, A&A, 536, A105.

[347] Véron-Cetty, M.-P. & Véron, P. 2001, A&A, 374, 92.

[348] Vestergaard, M. & Peterson, B. M. 2006, ApJ, 641, 689.

[349] Vietri, G., Piconcelli, E., Bischetti, M., et al. 2018, A&A, 617, A81.

[350] Vignali, C., Brandt, W. N., Schneider, D. P., et al. 2003, AJ, 125, 418.

[351] Vito, F., Brandt, W. N., Bauer, F. E., et al. 2019, A&A, 630, A118.

[352] Volonteri, M., Haardt, F., & Madau, P. 2003, ApJ, 582, 559.

[353] Volonteri, M. & Rees, M. J. 2005, ApJ, 633, 624.

[354] Volonteri, M. 2010, A&ARv, 18, 279.

[355] Volonteri, M., Haardt, F., Ghisellini, G., et al. 2011, MNRAS, 416, 216.

[356] Volonteri, M., Silk, J., & Dubus, G. 2015, ApJ, 804, 148.

[357] Volonteri, M., Habouzit, M., Pacucci, F., et al. 2016, Galaxies at High Redshift and Their Evolution Over Cosmic Time, 319, 72.

[358] Wang, J.-G., Dong, X.-B., Wang, T.-G., et al. 2009, ApJ, 707, 1334.

[359] Wang, F., Wu, X.-B., Fan, X., et al. 2016, ApJ, 819, 24.

[360] Wang, F., Yang, J., Fan, X., et al. 2018, ApJL, 869, L9.

[361] Wang, F., Yang, J., Fan, X., et al. 2021, ApJL, 907, L1.

[362] Wildy, C., Czerny, B., & Kuźmicz, A. 2018, ApJ, 861, 54.

[363] Willott, C. J., Delorme, P., Reylé, C., et al. 2010, AJ, 139, 906

[364] Willott, C. J., Albert, L., Arzoumanian, D., et al. 2010, Aj, 140, 546.

[365] Wills, B. J., Netzer, H., Brotherton, M. S., et al. 1993, ApJ, 410, 534.

[366] Wilson, A. S. & Colbert, E. J. M. 1995, American Astronomical Society Meeting Abstracts 186

[367] Woo, S. C., Turnshek, D. A., Badenes, C., et al. 2013, MNRAS, 434, 1411.

[368] Worsley, M. A., Fabian, A. C., Celotti, A., et al. 2004, MNRAS, 350, L67.

[369] Wright, A. E., Griffith, M. R., Burke, B. F., et al. 1994, ApJS, 91, 111.

[370] Wright, E. L., Eisenhardt, P. R. M., Mainzer, A. K., et al. 2010, AJ, 140, 1868.

[371] Wu, J., Brandt, W. N., Miller, B. P., et al. 2013, ApJ, 763, 109.

[372] Wu, X.-B., Wang, F., Fan, X., et al. 2015, Natur, 518, 512.

[373] Wu, J., Ghisellini, G., Hodges-Kluck, E., et al. 2017, MNRAS, 468, 109.

[374] Yang, J., Wang, F., Wu, X.-B., et al. 2016, ApJ, 829, 33.

[375] Yang, J., Wang, F., Fan, X., et al. 2019, ApJ, 871, 199

[376] Yang, J., Wang, F., Fan, X., et al. 2019, AJ, 157, 236.

[377] Yang, J., Wang, F., Fan, X., et al. 2020, ApJL, 897, L14.

[378] Yi, W.-M., Wang, F., Wu, X.-B., et al. 2014, ApJL, 795, L29.

[379] York, D. G., Adelman, J., Anderson, J. E., et al. 2000, AJ, 120, 1579.

[380] Young, S., Packham, C., Hough, J. H., et al. 1996, MNRAS, 283, L1.

[381] Yuan, W., Matsuoka, M., Wang, T., et al. 2000, ApJ, 545, 625.

[382] Yuan, W., Fabian, A. C., Celotti, A., et al. 2003, MNRAS, 346, L7.

[383] Zeimann, G. R., White, R. L., Becker, R. H., et al. 2011, ApJ, 736, 57.

[384] Zensus, J. A. & Pearson, T. J. 1987, Journal of the British Astronomical Association, 98, 48

[385] Zickgraf, F.-J., Voges, W., Krautter, J., et al. 1997, A&A, 323, L21

[386] Zhang, Y., An, T., Frey, S., et al. 2017, MNRAS, 468, 69.

[387] Zhu, S. F., Brandt, W. N., Wu, J., et al. 2019, MNRAS, 482, 2016.

[388] Zuo, W., Wu, X.-B., Fan, X., et al. 2020, ApJ, 896, 40.

Ringraziamenti

Come alla fine di ogni viaggio, bisogna lasciare anche un po' di spazio per ringraziare tutte le persone che mi hanno aiutato e appoggiato in questi tre anni e che hanno condiviso con me ogni singolo momento di questo lungo e bellissimo percorso.
Innanzitutto, desidero ringraziare di cuore i miei relatori, Alberto e Alessandro, per avermi seguito in questi tre anni. Grazie per avermi dato la possibilitá di lavorare con voi, per tutti i vostri insegnamenti, per avermi trasmesso la passione per la ricerca, per non avermi mai fatto mancare le occasioni di poter crescere, partecipare a conferenze, meeting, scuole internazionali e per avermi dato la magnifica possibilitá di andare ad osservare in Cile. Grazie a entrambi, perché é soprattutto per merito vostro che mi posso considerare super soddisfatta di tutto questo enorme lavoro!
Particular thanks go to the referees of this manuscript, Dr. Eduardo Bañados and Dr. Alessandro Capetti, for their very useful comments and suggestions and for the positive judgment on the whole thesis.
Ringrazio poi Gianpiero, direttore dell'Osservatorio di Brera in questi tre anni, per avermi dato la possibilitá di svolgere la mia attivitá di ricerca proprio in Osservatorio. Grazie anche a tutti gli altri colleghi di Brera-Merate (Paola, Roberto, Claudia, Gabriele, Tullia, Luca) e dell'Istituto di radio astronomia di Bologna (Cristiana, Daniele, Marcello, Monica) con cui ho condiviso il mio lavoro di ricerca e da cui ho imparato moltissimo. Un ringraziamento particolare e molto forte va a Cristiana, che ha creduto in questo progetto e con enorme entusiasmo e tanta grinta mi ha trascinato nel magnifico mondo della radioastronomia, nonostante "she doesn't share!" (cit.)! Grazie per tutto, senza di te e senza le tue capacitá alcune parti di questa tesi non sarebbero mai state possibili. Ringrazio moltissimo anche Daniele che é sempre stato l'Esperto per eccellenza in tutte le questioni radio-astronomiche che abbiamo affrontato insieme, dalle osservazioni JVLA, all'interpretazione dei dati.
Grazie a tutti gli altri ricercatori di Brera-Milano, ai colleghi del POE (Stefano grazie per i mille caffé mattutini, i libri consigliati, gli aneddoti di vita) e a tutto il personale dell'osservatorio che in questi tre anni sono stati una seconda famiglia, ogni giorno. Grazie a Laura, Gianlu, Fabio e Chiara per essere stati dei fantastici compagni di ufficio e a Roberto per aver portato un po' di sana romanitá *tra noi.*
Grazie ad Arianna, mia grande amica e fedele compagna di dottorato, con cui ho condiviso la maggior parte delle gioie e delle ansie!
Grazie a tutti gli astro-amici, Mery, Gabri, Andre, Tullia (a Tati, Fabio e Sarah che hanno preso una strada diversa) e a Fede (l'infliltrato teorico), per essere rimasti nel mio campo gravitazionale anche in questi tre anni, sopportandomi sempre, e dandomi qualche badilata quando serviva! E come non ringraziare gli astro-amici al di lá dell'oceano che ogni tanto mi ricordano di guardare le cose da una prospettiva diversa: Riccardo (il Nanni) e Alessandro (il Peca) conosciuti su una piccola isola greca ad una conferenza.

Tutti questi tre anni di ricerca peró non sarebbero stati possibili senza l'appoggio delle mie amiche di una vita, Nene, Vero ed Elisa, della Cumpa (grazie sopratutto a Doson per aver condiviso con me questi tre anni di dottorato nella stessa universitá ma in dipartimenti diversi), dei Guidos, di Cesare e Vale, di Flavia e Marco (grazie a voi due per gli interminabili viaggi con Trenord!) e di Roby e Marco. Grazie per ogni aperitivo, cena, pranzo, camminata in montagna, per ogni risata, per ogni pettegolezzo, per avermi sempre sopportato e sprondato ad andare avanti, anche quando le difficoltá si facevano sentire.
Grazie alla mia splendida famiglia, i miei genitori, mio fratello Marco, gli zii tutti e Gió, per essermi sempre stati vicini in ogni momento di questi tre lunghi anni, nonostante la strada che mi avete aiutato ad intraprendere vi sembri a volte strana e difficile.
E infine, e soprattutto, grazie a Simone, la mia roccia, la metá della mela, che mi ha sempre sostenuta incondizionatamente, nonostante il mio caratteraccio, che ha raccolto i pezzi quando era necessario, che ha festeggiato con me per ogni articolo pubblicato e per ogni traguardo, anche il piú piccolo, che in tutti i suoi gesti e con la sua praticitá da quel bravo ingegnere che é ha sempre trovato il modo di supportarmi (e soprattutto SOpportarmi).
Grazie, per tutta la felicitá che mi regali ogni giorno.
Ora il Nepal ci aspetta.

Stars
In your multitudes
Scarce to be counted
Filling the darkness
With order and light!
You are the sentinels
Silent and sure
Keeping watch in the night
Keeping watch in the night